The Search for Exotic Baryons at the HERMES Experiment

by

Wouter Deconinck

A dissertation submitted in partial fulfillment
of the requirements for the degree of
Doctor of Philosophy
(Physics)
in The University of Michigan
2008

Doctoral Committee:

Professor Wolfgang B. Lorenzon, Chair
Professor Gordon L. Kane
Professor Michael J. Longo
Professor Jianming Qian
Associate Professor Arthur M.F.W. Verhoogt

ABSTRACT

The Search for Exotic Baryons at the HERMES Experiment

by
Wouter Deconinck

Chair: Wolfgang B. Lorenzon

One of the interesting questions of Quantum Chromodynamics, the theory that governs the interactions between quarks and gluons, has been whether it is possible to observe hadrons which can not be explained as a combination of only two or three valence quarks. In numerous searches the existence of these exotic hadrons could not be confirmed. Recently, calculations based on the quark soliton model predicted the narrow exotic baryons Θ^+ and Ξ^{--}. A narrow resonance identified as the Θ^+ was observed by several experiments at the predicted mass of 1540 MeV, but later followed by several dedicated experiments that could not confirm these positive results.

At the HERMES experiment a search for the quasi-real photoproduction of the exotic baryon Θ^+ on a deuterium target and the subsequent decay through $pK^0_S \rightarrow p\pi^+\pi^-$ revealed a narrow resonance in the pK^0_S invariant mass distribution at 1528 MeV. In the search for the corresponding antiparticle Θ^- the result is consistent with zero events.

In this thesis we present the search for the exotic baryon Ξ^{--} on a deuterium target in the data sample used for the observation of the Θ^+. An upper limit on the cross section of the exotic baryon Ξ^{--} is determined. The search for the exotic baryon Θ^+ on hydrogen and deuterium targets at the HERMES experiment is extensively discussed. The event mixing method can be used to estimate the distribution of background events. Several difficulties with this method were addressed, but the background description in the case of the exotic baryon Θ^+ remains unconvincing. Between the years 2002 and 2005 the HERMES experiment operated with a magnetic holding field around the hydrogen target. A method for the reconstruction of displaced vertices in this field was developed. The data collected during the years 2006 and 2007 offer an integrated luminosity that is several times higher than in previous data sets. After investigating all data sets collected with the HERMES experiment on hydrogen and deuterium targets, we are not able to observe a resonance peak at an invariant mass of 1540 MeV consistent with the exotic baryon Θ^+.

ACKNOWLEDGEMENTS

This dissertation would not have been possible without the help of numerous faculty, colleagues, friends and family. Perhaps unknowingly, many individuals contributed to the successful completion of this dissertation, through their expressions of support or concrete assistance in solving problems. Importantly, this also includes a large number of educators, teachers, and mentors who helped shape my approach to this research project before I entered the graduate program at the University of Michigan. I would like to express my gratitude to all of them. Several individuals deserve special mention for their contributions to this dissertation.

Wolfgang Lorenzon has been an exceptional advisor, a constant source of support and inspiration. He put great trust in my independence and always left me the freedom to explore, but was careful to remind me when I was losing sight of my goals. Whenever I asked Wolfgang for his opinion on my work, he offered his insights and comments quickly and accurately. His strategical advice transcended my graduate career; he provided me with opportunities to connect with other academics and was crucial in the formation of my post-doctoral plans. I am very grateful for having had the opportunity to work with Wolfgang. During my future career I can only hope to be as good a mentor as Wolfgang.

My thanks go out to the other members of my dissertation committee for their interest in my work, for the different viewpoints they provided, and for their suggestions for improvement and changes. Gordy Kane provided me with the theoretical background in standard model physics (and beyond) in several courses on particle physics, and continued to be a source of enlightening insight. Mike Longo's perspective on pentaquarks inspired me to carefully review the assumptions underlying this dissertation research, leading to the interesting discovery of ghost tracks in the HERMES data. One of the most interesting courses of my graduate track was taught by Jianming Qian on experimental collider physics. He introduced many of the experimental techniques, from particle detection to statistical analysis, and his lecture notes remain a handy reference. Arthur Verhoogt gracefully accepted the "challenge" of being the ever cheerful cognate member on my dissertation committee after a rather long time away from physics. His questions made me think more about the meaning of the presented results on a very fundamental level.

The original idea of dissertation research at the HERMES experiment was suggested by the spokesperson at the time, Dirk Ryckbosch. His course on medium energy physics at the University of Gent was what sparked my interest in subnuclear physics. Without the inspiration of Dirk I would not have pursued a graduate program at the University of Michigan.

I am very much indebted to my colleague and supervisor Avetik Airapetian. In our office "container" at DESY he was always there (as a walking encyclopedia or even analysis guru) to answer questions and to direct me to the right path when solving problems. Together with Riccardo Fabbri, we spent many evenings in the East Hall, trying to solve odd hardware or software malfunctions in the LPOL system. I want to thank my LPOL friends Avetik and Riccardo not only for being such great colleagues, but also for reminding me of the joys of good Italian food and *caffè*. Or course, I should have put on my soccer shoes more regularly to join Avetik and Riccardo...

I wish to thank all of my colleagues and friends at the HERMES experiment for the interesting discussions, for the critical observations, and for valuable suggestions. In particular the regulars at the "offsite" meetings, arguably more useful than any other meeting, will be missed. Many thanks to Caro and Charlotte for the numerous conversations that had nothing to do with physics, and for the ones that did. Many of the ideas in this dissertations resulted from suggestions by Achim, Alex, Beni, Brian, Caro, Charlotte, Dominik, Elke, Jim, Josh, Larry, Markus, Rebecca, Roberto, Steve, and Yves. Any mistakes result from my misinterpretations of their great ideas. A special thank you goes to Evelyn and Sabine for all their practical advice on wrestling with the German bureaucracy.

I would like to thank my parents, Hilde and Johan, for giving me the opportunities to study and explore, for teaching me to keep an open mind, and for providing me with an example of how to live.

Finally, I most want to thank Susanne who was always there for me, even while we were separated by oceans and time zones. Without her constant support I would not have been able to accomplish this.

TABLE OF CONTENTS

LIST OF FIGURES

Figure

LIST OF TABLES

Table

CHAPTER I

Introduction

In the Standard Model of particle physics the fundamental fermionic constituents of matter are organized in three progressively more massive generations. Each generation of particles consists of two quarks with electromagnetic charge $+\frac{2}{3}$ and $-\frac{1}{3}$ (up u and down d, charm c and strange s, top t and bottom b), a lepton with by definition electromagnetic charge -1 (electron e, muon μ, tau τ), and the corresponding neutral neutrino (ν_e, ν_μ, ν_τ). The particles are subjected to the four fundamental forces: the gravitational force, the electromagnetic interaction responsible for electricity and magnetism, the weak interaction which is important in nuclear processes such as β-decay, and the strong interaction that binds the protons and neutrons in the atomic nucleus. Even though gravity is the most apparent force at macroscopic scales, it is much weaker than the other forces at microscopic scales and will be ignored here.

The fundamental forces act by the exchange of force-mediating particles or gauge bosons. The massless photon γ mediates the electromagnetic force between electrically charged particles. The theory of Quantum Electrodynamics (QED) describes the interactions mathematically as the abelian $U(1)_{em}$ gauge theory. Because of the small value of the electromagnetic coupling constant $\alpha \approx \frac{1}{137}$, the theory of QED lends itself well to perturbative expansion. This allows for the calculation of experimental observables to a very high precision.

The weak force is carried by the three massive vector bosons $W^\pm$ and Z^0 and acts on all fermionic fundamental particles listed above.[1] Because the $W^\pm$ bosons are charged, they are affected by the electromagnetic interaction. The masses of vector bosons are generated by spontaneous symmetry breaking at energies below approximately 10^2 GeV. Above this energy the electromagnetic interaction and the weak interaction are unified in the electroweak interaction with the symmetry group $SU(2) \otimes U(1)_Y$, where Y is the hypercharge. Just as the electromagnetic charge, the hypercharge of a particle indicates how strongly it will couple to the electroweak gauge bosons. At lower energies the electroweak symmetry is spontaneously broken down to $U(1)_{em}$ by the Higgs mechanism, which not only generates the masses of the Goldstone bosons $W^\pm$ and Z^0 but also of all other fermions in the Standard Model, because the interaction of the Higgs field is proportional to the fermion mass.

In addition to the electromagnetic charge and the hypercharge, the quarks (but not the leptons and neutrinos) carry a color charge which can take on one of the values red r, green g, or blue b, the sum of which cancels out. The antiquarks carry an anticolor charge $\overline{r}$, $\overline{g}$, or $\overline{b}$. The eight massless and electromagnetically neutral gluons g mediate the strong force by coupling to the color charge of the quarks. The gluons carry a combined color-anticolor charge. The interaction of the gluons with the quarks, and of the gluons with each other, is described by the theory of Quantum Chromodynamics (QCD), a non-abelian gauge theory with color symmetry group $SU(3)_c$ (for a review see reference [1]).

The self-interaction of gluons, a feature of the $SU(3)$ group structure of QCD that is not present in the simpler $U(1)$ structure of QED (at least at tree level), causes the interaction between two quarks to become weaker when the quarks are closer to each other, and stronger when they are further apart. This is opposite to the behavior of QED, where the effect of electromagnetic charge screening reduces the interaction at larger distances. This particular effect of QCD is called asymptotic freedom, because at short distances the quarks are quasi-free. Similarly, due to the

[1] Naively the strength of the interaction is inversely proportional to the squared mass of the mediating boson. The larger mass of the weak bosons is responsible for the weakness of the weak force.

increase of the interaction at large distances, it is impossible to remove a colored object from a colorless bound state, a property known as color confinement. QCD only allows colorless free objects; all colored objects have to be in a bound state such that their total color charge is canceled.

1.1 Mesons and baryons

The colorless bound states of quarks, antiquarks and gluons in QCD are called hadrons. The simplest colorless combinations of quarks and antiquarks are the *mesons* consisting of a quark and an antiquark ($q\overline{q}$) and the *baryons* composed of three quarks (qqq). These two or three quarks, which carry most of the hadron's momentum, are called the valence quarks. Solely these two or three valence quarks determine the physical observable quantum numbers of the bound state (such as the spin J and the strangeness S). In addition, the valence quarks are embedded in a sea of $q\overline{q}$ pairs, which have no net contribution to the quantum numbers of the bound state, but which can be probed in deep-inelastic scattering experiments. For example, a proton consists of one d and two u valence quarks but $s\overline{s}$ pairs are created and disappear constantly in the quark sea.

Because the masses of the c, b and t quarks are large compared to the masses of the u, d and s quarks ($m_u \approx 3\,\text{MeV}$, $m_d \approx 6\,\text{MeV}$, $m_s \approx 100\,\text{MeV}$, $m_c \approx 1.24\,\text{GeV}$, the masses for the b and t quarks are even larger [1]), they are usually ignored in treatments of the lightest hadrons. When only the three lightest quarks u, d and s are considered, the flavor symmetry group $SU(3)_f$ describes the hadronic bound states. All hadronic states in a perfect symmetry group are expected to have the same energy. $SU(3)_f$ is not an exact symmetry owing to the larger mass of the s quark, but very useful as an approximation. When we also include the c quark, we obtain the badly broken $SU(4)_f$ flavor symmetry. In this work we will limit ourselves to the light quarks only and consider the flavor symmetry group $SU(3)_f$.

Following the group-theoretical relation $\mathbf{3} \otimes \mathbf{3} = \mathbf{8} \oplus \mathbf{1}$ in the flavor symmetry group $SU(3)_f$, the nine possible quark-antiquark combinations $q\overline{q}$ can be grouped in a singlet and an octet of light mesons. Because the s quark has a larger mass than the u and d quarks, the symmetry is not perfect and the mesons with non-zero strangeness are heavier than the mesons without strangeness.[2] Mesons with equal strangeness are approximately degenerate in mass, because of the $SU(2)$ isospin symmetry between u and d quarks. When we include the c quark, we obtain a 15-plet according to $\mathbf{4} \otimes \mathbf{4} = \mathbf{15} \oplus \mathbf{1}$. The mass splittings are now even larger, and the states with charm content are largely independent of the states already obtained in the $SU(3)_f$ singlet and octet.

If we limit ourselves to the ground states without orbital excitations, in other words to bound states with $\ell = 0$, the total spin $J = \ell + s$ of the mesons can be $J = 0$ or $J = 1$ for antiparallel or parallel quarks spins (the sum of the spins is represented by the lower case s, to avoid confusion with the strangeness S). In both spin configurations the meson states can be classified in a singlet and an octet. In figure 1.1 the $J = 0$ states or pseudoscalar mesons are shown in the left panel and the $J = 1$ states or vector mesons are shown in the right panel. The isoscalar singlet state and the two isoscalar states at the center of the octet mix with each other because they have identical quantum numbers (*i.e.* $Q = 0$, $S = 0$).

The multiplets for the baryons consisting of three quarks are determined similarly to the classification scheme of the mesons. The relation $\mathbf{3} \otimes \mathbf{3} \otimes \mathbf{3} = \mathbf{10}_S \oplus \mathbf{8}_M \oplus \mathbf{8}_M \oplus \mathbf{1}_A$, however, does not produce separate ground state multiplets with and without angular momentum ℓ. By treating the quarks with spin up and spin down independently the flavor-spin symmetry group $SU(6)_{fs}$ can be used to determine the ground state multiplets. The baryons are now described by the relation $\mathbf{6} \otimes \mathbf{6} \otimes \mathbf{6} = \mathbf{56}_S \oplus \mathbf{70}_M \oplus \mathbf{70}_M \oplus \mathbf{20}_A$ and the ground state 56-plet decomposes according to $\mathbf{56} = \mathbf{10} \oplus \mathbf{8}$ in an octet with spin $J = \frac{1}{2}$ and a decuplet with spin $J = \frac{3}{2}$. In figure 1.2 the ground state baryon octet is shown on the left and the decuplet on the right. As in the case of mesons, the masses of baryons with the same strangeness S are almost identical because of isospin symmetry. The differences between the masses of baryons with different strangeness is larger.

Because the strong coupling constant α_S is of the order of unity at the energies of the lightest bound quark states, a perturbative approach to QCD is not applicable to calculate the masses of the lightest mesons and baryons.[3] At higher energies (and thus shorter distance scales) the strong coupling constant decreases and reaches a value $\alpha_S(M_Z) = 0.12$ at the mass of the Z boson. At higher energies perturbative QCD can be used for high-precision tests of QCD, similar

[2] The strangeness S of a hadron is proportional to the number of strange quarks. It follows the convention that the flavor of a quark has the same sign as its electromagnetic charge. Because the strange quark has negative electromagnetic charge $-\frac{1}{3}$, the strangeness of the s quark itself is $S = -1$.

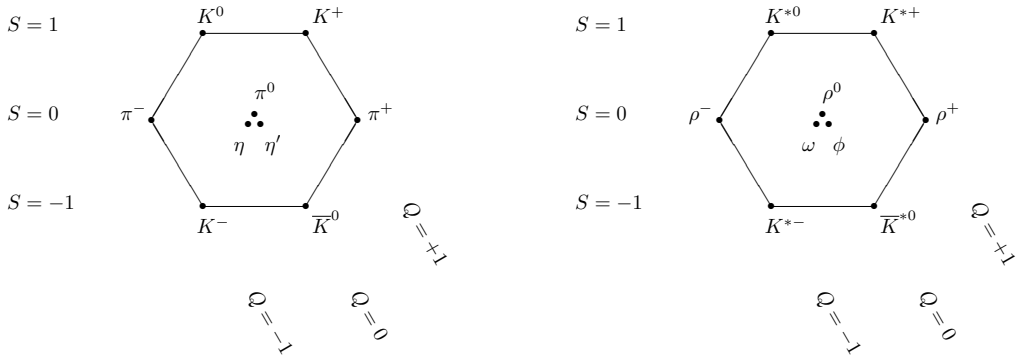

Figure 1.1: The ground state singlets and octets of the light $J = 0$ pseudoscalar mesons (left panel) and $J = 1$ vector mesons (right panel) made of only u, d and s quarks without angular momentum ($\ell = 0$).

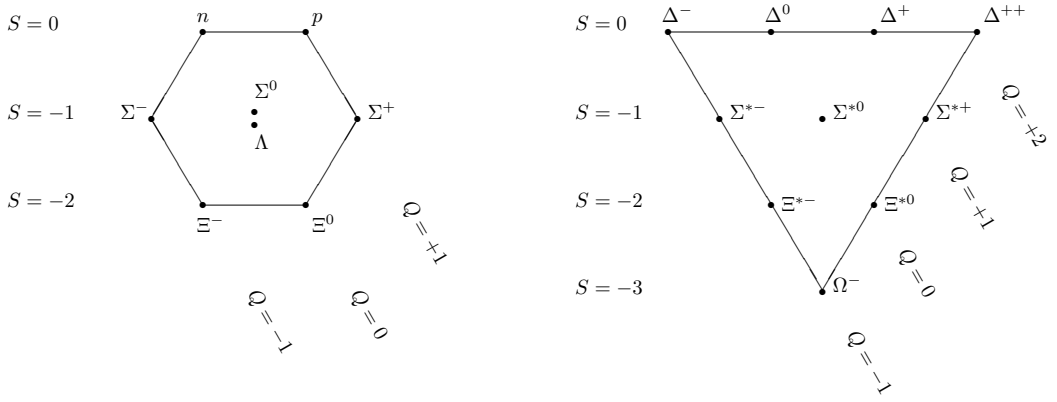

Figure 1.2: The ground state $J = \frac{1}{2}$ octet (left panel) and $J = \frac{3}{2}$ decuplet (right panel) of the light baryon states made of only u, d and s quarks without angular momentum ($\ell = 0$).

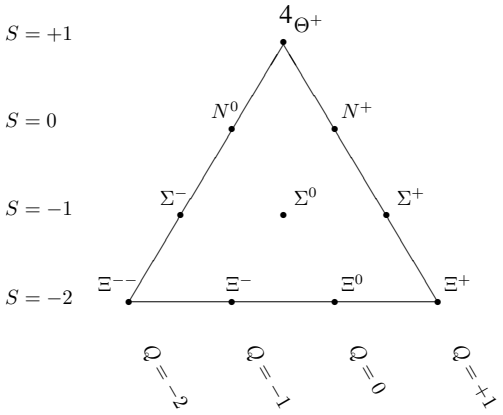

Figure 1.3: The ground state antidecuplet of the exotic $J = \frac{1}{2}$ baryon states, as predicted by the chiral quark soliton model (see section 2.2.4).

to what is possible in QED. In the non-perturbative region several phenomenological approaches can be used for the determination of the hadronic masses. In the constituent quark model (CQM) the quarks are 'dressed' or given a larger mass ($m_{u/d,CQM} \approx 350\,\text{MeV}$, $m_{s,CQM} \approx 470\,\text{MeV}$) and their interaction in a hadronic potential is determined [2].

1.2 Exotic hadrons

QCD does not prohibit the existence of colorless hadronic states with more than two or three quarks. In fact, studies of the nucleon structure point to a significant contribution from quark-antiquark pairs to the total momentum and spin of the nucleon. The naive quark model with bound states of only two or three valence quark seems incomplete. When one realizes that the quarks in mesons and baryons are bound together by the gluons, also gluons should play an important role in the description of bound states.

The hadrons that fall outside of the expectations of the naive quark model are called manifestly exotic hadrons. Their quantum numbers can not be explained by a bound state of only two or three quarks. Crypto-exotic hadrons are composed of more than two or three quarks, but mix with a regular hadron with the same quantum numbers. The exotic mesons can be classified as glue balls (gg), hybrids ($q\bar{q}g$), and tetraquarks ($q\bar{q}q\bar{q}$). Pentaquarks ($qqqq\bar{q}$) are examples of exotic baryon states.

For mesons the quantum numbers for the total spin J, the parity P, and the charge conjugation eigenvalue C are only allowed to have a limited set of values. The configurations $J^{PC} = 0^{--}$, 0^{-+}, 1^{-+}, 2^{+-},... cannot be obtained in the naive quark model. The observation of several states with $J^{PC} = 1^{-+}$ since the 90s points unambiguously to the existence of exotic mesons, although the exact nature of these exotic mesons is still unknown.[4]

The charge conjugation eigenvalue C is not a good quantum number for baryons, and all combinations of the total spin J and the parity P are allowed. However, an exotic baryon can be identified with a combination of the charge Q and the strangeness S. Since no three-quark baryons with positive strangeness exist, a baryon with charge $Q = +1$ and strangeness $S = +1$ must have the minimal quark configuration $uudd\bar{s}$. This exotic baryon will be referred to as Θ^+. Similarly, the minimal quark content of the exotic baryon Ξ^{--} with charge $Q = -2$ and strangeness $S = -2$ is $ssdd\bar{u}$. In the chiral quark soliton model, discussed in section 2.2, the lightest exotic baryons with spin $J = \frac{1}{2}$ are organized in an antidecuplet, shown in figure 1.3. Due to mixing of the internal member of this antidecuplet with a non-exotic octet, the only manifestly exotic baryons are located on the corners of this antidecuplet.

[3]The advances in lattice QCD calculations make it possible to determine the masses of the bound states directly from the $SU(3)$ Lagrangian of QCD. This is however not up to par yet with the results from phenomenological quark models.

[4]If each of the reported 1^{-+} state were confirmed, it would result in an overpopulation of the 1^{-+} hybrid multiplet. The experiment GlueX at JLab is proposed to investigate exotic mesons [3].

So far, experimental searches for exotic baryons have been unsuccessful. Early experiments in the 1970s were not able to confidently prove the existence of exotic baryons, although a number of (often contradictory) results in kaon-nucleon scattering reported positive results. In recent years a new wave of positive experimental results and contrasting null results about the exotic baryons Θ^+ and Ξ^{--} has revitalized the discussion, but it is too early to draw conclusions about the existence of these exotic baryons.

At the HERMES experiment in Hamburg, Germany, a search for the exotic baryons Θ^+ and Ξ^{--} was performed [4, 5]. A resonance peak in the decay channel corresponding to the Θ^+ was observed at a mass of $M = 1528\,\text{MeV}$, but no Ξ^{--} resonance could be found. Since these result were published in 2003 and 2004, a large amount of additional data has been collected. This dissertation investigates the search for exotic baryons in these data.

1.3 Overview

In chapter II an overview will be given of the experimental and theoretical efforts to observe, refute or more broadly understand exotic baryons. The evidence in favor of the recently observed exotic baryons Θ^+ and Ξ^{--} is examined and critically compared with null results. The theoretical efforts in hadronic physics have lead to a number of different approaches in calculating the mass and the width of exotic baryons. The most well-known approach is without doubt the chiral quark soliton model, but the diquark model and the diquark-triquark model are also presented.

The HERMES experiment is introduced in chapter III. It is located in the East Hall of the HERA collider at the DESY laboratory, where energetic electrons or positrons are collided on a fixed gas target. The scattered lepton and the collision fragments are detected in a conventional forward spectrometer with good particle identification capabilities. Although the polarization of the lepton beam is not relevant for the analysis of exotic baryons, the longitudinal polarimeter is discussed in the light of proposed future lepton polarimeter designs.

The analysis of the exotic baryons at the HERMES experiment is presented in chapter IV. Similar to the original analyses of the exotic baryons Θ^+ and Ξ^{--} at the HERMES experiment [4, 5], a search for the exotic baryon Ξ^{--} is presented. The photoproduction cross section ratio of the $\Lambda(1520)$ and $\overline{\Lambda}(1520)$ hyperons is used to determine the expected number of observed Θ^- baryons. For the analysis of the data collected with a transversely polarized hydrogen target, a tracking algorithm was developed for displaced vertices in a homogeneous field. Finally, the technique of event mixing for the determination of distributions of background events is discussed.

In the final chapter V the results of this work are summarized. The analysis method, involving several novel aspects, is critically reviewed. The observation of exotic baryons at the HERMES experiment, in particular of the Θ^+ and the Ξ^{--}, is assessed.

CHAPTER II

The Search for Exotic Baryons

The search for exotic baryons knows a long history, starting immediately after the formulation of the quark model and development of the mathematical structure of QCD. The assumedly lightest five-quark exotic baryon, with a quark configuration $uudd\bar{s}$ and with positive strangeness $S = +1$, has been the focus of the majority of the experimental searches, and it receives therefore also an important position in the theoretical models. In early searches exotic baryons with strangeness $S = +1$ were referred to as Z^* resonances, but in the recent results the symbol Θ^+ has become the accepted notation. The other manifestly exotic baryons in the antidecuplet composed of only u, d and s quarks are denoted by Ξ^{--} for the $ddss\bar{u}$ quark configuration and by Ξ^+ for the $uuss\bar{d}$ quark configuration.[1] Currently only one experiment reported evidence for these states, in contrast with numerous null results.

In this chapter we review the experimental and theoretical results about the light exotic baryons, consisting of only u, d and s quarks.[2] In section 2.1 the older KN partial wave analyses and several recent spectroscopic results are discussed, comparing the positive and null results where possible. In section 2.2 we review the theoretical predictions for exotic baryons and the recent developments that aim to reconcile the seemingly contradictory experimental results.

2.1 Experimental results

Since the early days of QCD, experimental searches for baryons composed of more than three quarks have been performed. In particular, the observation of a baryon with a positive strangeness S would be a clear signature of an exotic baryon, because such a baryon can only be explained by the combination of five or more quarks.

2.1.1 Early controversy about exotic baryons

Using secondary charged kaon beams, a large amount of data has been collected in scattering of kaons on protons and deuterons in the late 60s and 70s. Several indications for baryon resonances with positive strangeness, identified as Z^* resonances at that time,[3] were observed in the partial wave analysis of these data, but none of the reports was ever sufficiently significant to stand beyond the doubt created by contradicting experimental results [6]. The widths of the observed Z^* resonances were usually of the order of 100 MeV, both for the isoscalar resonances Z_0^* around 1800 MeV and for the isovector resonances Z_1^* at 1900 MeV and higher. Due to these large widths, the resonances are now understood as non-exotic pseudo-resonances induced by the opening of $K\pi N$ channels [7].

Starting with its 1986 edition of the Review of Particle Physics [8], the Particle Data Group decided to omit the experimental results for the exotic baryons Z^*. The "general prejudice against baryons not made of three quarks" and

[1] The Particle Data Group [1] refers to the exotic baryons Ξ^{--} and Ξ^+ with the symbol Φ, but this notation has not found a lot of adoption in the experimental community. In this work we will continue to use the symbol Ξ to avoid inconsistencies with the cited sources.

[2] After the first reports of the observation of the exotic baryon Θ^+ in 2003, similar exotic states with c or b quarks instead of the s quark were predicted [9, 10, 11]. The experimental observation of a resonance decaying to $D^{*-}p$ at the H1 experiment was interpreted as evidence for the charmed exotic baryon Θ_c^0 [12], but in subsequent searches no other experiment was able to confirm this observation. This charmed exotic baryon Θ_c^0 will not be discussed in this work.

[3] The isospin of the resonance is often indicated as a subscript, *i.e.* Z_0^* or Z_1^*.

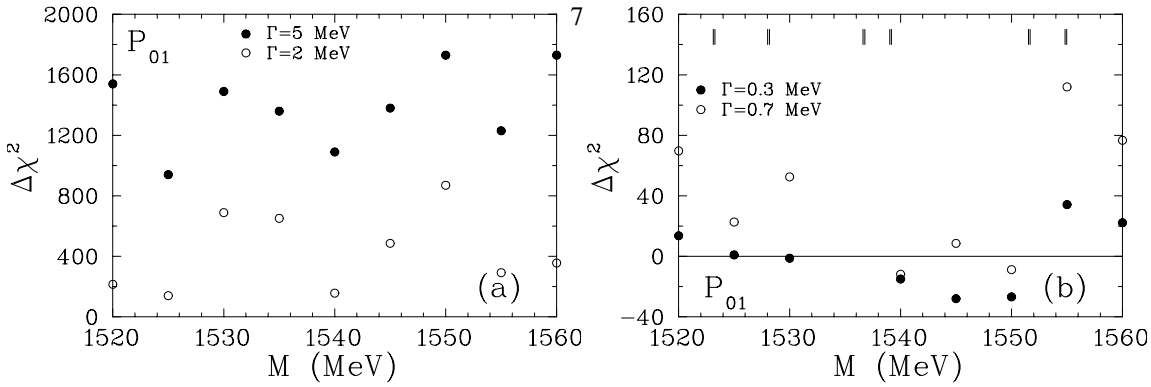

Figure 2.1: Change of the overall χ^2 when including a narrow P_{01} resonance in a global partial wave analysis of the KN scattering data is only acceptable for resonance widths Γ below a few MeV. The small vertical lines in the right panel indicate the position of experimental observations of the exotic baryon $\Theta^+(1540)$. In the right panel the values for $\Delta\chi^2$ at 1535 MeV are off-scale. Taken from reference [13].

"lack of experimental activity" were cited as reasons why a decision on the existence of exotic baryons was not to be expected in the foreseeable future. The discussion indeed lay dormant for more than 15 years, until the first of the most recent results was presented in 2003.

The K^+p and K^+d scattering databases were recently re-examined in the light of the evidence for a surprisingly narrow exotic baryon resonance Θ^+ with a mass of approximately 1540 MeV. An upper limit on the width of the exotic baryon Θ^+ of a few MeV was derived, based on fluctuations in the measured cross sections [14, 15, 16]. In a re-examination of the partial wave analysis of the KN scattering data, the new narrow exotic baryons were included and the difference in the goodness-of-fit parameter χ^2 was determined [13]. In figure 2.1 the change of the overall χ^2 of a global fit to the KN scattering data is shown when including a narrow P_{01} resonance. For intrinsic resonance widths Γ above 2 MeV, the increase of the total χ^2 is too large, and only for widths below a few MeV the inclusion of a narrow resonance is possible. Similarly, when including a narrow S_{01} or P_{03} resonance only a width below 1 MeV is consistent with the KN scattering data. This puts a strong constraint on the theoretical models trying to explain the observed exotic baryons.

2.1.2 Experimental results since 2003

Prompted by the theoretical predictions of the chiral quark soliton model [17], a new series of experimental results claiming the observation of the exotic baryon Θ^+ at a mass of approximately 1540 MeV has been published since 2003. This resonance with positive strangeness $S = +1$ can only be explained as a five-quark state with configuration $uudd\bar{s}$, and corresponds to the Z^* resonances discussed in the 70s. Following common practice for baryons, the determined mass is added to the symbol of the resonance to distinguish it from other resonance with the same structure and thus the same symbol, but with a different mass due to orbital excitations. When discussing the observed exotic resonance state around 1540 MeV we will therefore write $\Theta^+(1540)$. The isospin structure of the exotic resonance $\Theta(1540)$ has not been determined conclusively experimentally, with most experiments unable to observe a possible isopartner $\Theta^{++}(1540)$ but some results pointing to the existence of the isospin partner [18]. In the chiral quark soliton model the exotic baryon Θ was predicted to be an isoscalar (as the Z_0^* state).

Initially, the positive results created a lot of enthusiasm in the hadron spectroscopy community. The number of theoretical papers published on the subject, trying to reconcile the different observed masses and attempting to determine the possible production mechanisms rose quickly. However, slowly null results began to trickle in, most of them with better statistical precision and placing strict limits on the allowed cross section or intrinsic width. The apparent disagreement between the positive results and the null results turned around the initial enthusiasm for the experiments that presented evidence in favor. A few experiments could not repeat their previous results with data

collected in very similar conditions. Only a small number of experiments has presented additional data in different reaction channels or kinematic regimes in which they confirmed their earlier sightings.

Now, when looking back at the large amount of experimental results, some positive, several null, we can draw some conclusions. Some experimental results were already discarded as invalid, others are in the process of being confirmed or refuted. In this section some experimental results are discussed in more detail. Completeness was not pursued, only experimental results deemed interesting or significant in the eyes of the author were included. Since it is difficult to order the experiments consistently according to any experimental characteristic, they are presented chronologically. But because some experiments published several results, the chronological line has been broken at several points.

2.1.3 Photoproduction on neutrons at the LEPS experiment

In the beginning of 2003, the first recent claim for the observation of the exotic baryon $\Theta(1540)$ was presented by the Laser-Electron Photon experiment at SPring-8 (LEPS) in Japan. At the LEPS experiment high-energetic photons are produced by Compton back-scattering of laser photons from the 8 GeV electrons in the SPring-8 synchrotron [19]. The frequency of the 351 nm Ar laser limits the Compton photon energy to values below 2.4 GeV. The photon energy is determined by measuring the momentum of the scattered electrons using one of the bending magnets of the SPring-8 storage ring. Only for photons with an energy above 1.5 GeV, the scattered electron can be detected.[4]

The photons strike a fixed target cell and the reaction products are detected by the LEPS spectrometer. The design of the spectrometer is optimized for the detection of photoproduced ϕ mesons at forward angles. A silicon strip vertex detector and three drift chambers are used to track charged particles in a magnetic dipole field and determine their momentum. A time-of-flight (TOF) scintillator detector and a Čerenkov counter are used to distinguish electrons from pions.

For the first publication on exotic baryons at the LEPS experiment [20], a 0.5 cm thick plastic scintillator (SC) with an approximately equal number of hydrogen and carbon nuclei was used as the target for the photon beam. This scintillator target was located downstream from the actual liquid hydrogen (LH_2) target for the study of the photoproduction of ϕ mesons. In 2003 the LH_2 target was replaced by a longer target cell which could also hold liquid deuterium (LD_2), to allow for the study of reactions on neutrons without the need for a complicated Fermi motion correction [21, 22].

First results on the scintillator target

For the analysis of the first data sample, collected on the SC target, events with a K^+K^- pair in the detector were considered [20]. The scattered nucleon was reconstructed from the missing mass $MM(\gamma K^+K^-)$, and a veto on a scattered proton track was used to suppress the photo-nuclear reaction $\gamma p \to K^+K^-p$ off protons in the H or C atoms. Assuming the reaction $\gamma n(^{12}\mathrm{C}) \to K^+K^-(n)$ the missing mass $MM(\gamma K^{\pm})$ corresponds now to the invariant mass $M(nK^{\mp})$. The Fermi motion of the target neutron in the atomic nucleus leads to smearing of the kinematic variables and is corrected for.[5]

In the distribution of the missing mass $MM(\gamma K^+)$, shown in the left panel of figure 2.2, the $\Lambda(1520)$ resonance is not visible in the sample with the proton veto (solid lines), but becomes visible when a proton hit is required (dashed lines) as expected for the reaction $\gamma p(^{12}\mathrm{C}) \to \Lambda(1520)K^+ \to pK^-K^+$. The distribution of the missing mass $MM(\gamma K^-)$, shown in the right panel of figure 2.2, for events originating in the SC target (solid lines) exhibits a peak at a mass of 1540 ± 10 GeV with a width smaller than 25 MeV and a naive significance of $\frac{S}{\sqrt{B}} = 4.6\,\sigma$.[6] The structure disappears when the events are not required to originate in the SC target, but instead in the LH_2 target (dotted lines).

[4] Because of energy conservation, photons with a lower energy correspond to scattered electrons with an energy closer to the beam energy. The separation between the scattered electron and the electron beam after the first dipole magnet in the synchrotron is then too small and the electron is outside the acceptance of the tagging counter.

[5] Only after the Fermi motion correction a clean separation of the Λ hyperon at 1115 MeV and the Σ^- hyperon at 1190 MeV, both decaying to $K^+\pi^-$, is possible due the improvement in the resolution.

[6] Several expressions are used to calculate the statistical significance of experimental results. The statistical significance of a hypothesis represents the probability that the observation is a random fluctuation, and is usually expressed in units of standard deviations for a normal distribution. The naive estimator $\frac{S}{\sqrt{B}}$ for the significance of a peak with S events on top of B background events is only valid when the background B is known

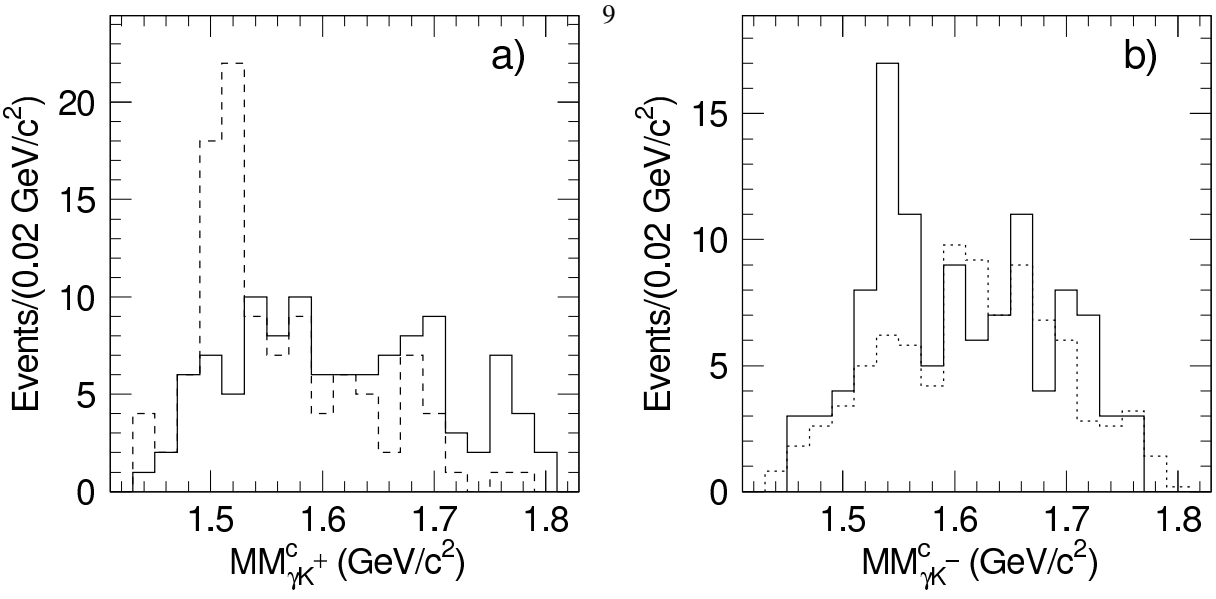

Figure 2.2: The distribution of the missing masses $MM(\gamma K^+)$ (left panel) and $MM(\gamma K^-)$ (right panel) for events originating in the SC target and corrected for Fermi motion in the C nucleus (solid line in both panels). When an additional proton track is required in the final state, the $\Lambda(1520)$ resonance becomes visible in the left panel (dashed line). In the right panel, the background contribution is estimated using events with the initial vertex in the LH_2 target (dotted line). Taken from reference [20].

Dedicated setup with the liquid deuterium target

In 2003 the target system at the LEPS experiment was upgraded to allow for data collection on liquid hydrogen and liquid deuterium targets with increased thickness [22]. The hydrogen target allowed to estimate the background distributions for reactions on the neutrons, and coherent reactions on deuterons could now be studied without the need for a complicated Fermi motion correction.

The original result for photoproduction on neutrons was confirmed with higher statistical precision, as shown in figure 2.3. This result still depends on the correction for the Fermi motion of the neutron in the deuterium atom. In the left panel the distribution of the missing mass $MM(\gamma K^+)$ with a prominent $\Lambda(1520)$ peak is shown. The distribution of the missing mass $MM(\gamma K^-)$ is shown in the right panel with an excess of events at 1.53 GeV. The dashed line represents the mixed event background, presumably normalized in the invariant mass region below 1.5 GeV.

Inspired by the analysis method used at the CLAS experiment (see section 2.1.6), the LEPS experiment also searched for the $\Theta(1540)$ in the coherent reaction $\gamma d \rightarrow pK^-X$ on a deuterium target using the missing mass $MM(\gamma pK^-)$. When only events are selected with an invariant mass $M(pK^-)$ in the region corresponding to the $\Lambda(1520)$ hyperon, the distribution for the missing mass $MM(\gamma K^- p)$ in figure 2.4 is obtained. The total background (indicated by the red line) has a component modeled by the sidebands of the $\Lambda(1520)$ hyperon (blue line) and a component from $\Lambda(1520)$ production estimated from the LH_2 data (green line). A peak structure at 1.53 GeV and a broad bump at 1.6 GeV are observed.

In summary, the LEPS experiment currently claims evidence for the exotic baryons $\Theta(1540)$ in several different reaction channels. The results seem to indicate simultaneous production of the non-exotic $\Lambda(1520)$ hyperon and the

and large. It overestimates the true statistical significance by assuming that the resonance is there, by ignoring the uncertainty in the background description and the change from Gaussian to Poisson distributions for a low number of events. The alternative expression $\frac{S}{\sqrt{B+S}}$ is sometimes used to avoid the assumption that the resonance exists. Only a fully correlated statistical treatment of peak and background allows to calculate the expression $\frac{S}{\delta B}$, where δB is now the uncertainty in the number of background events in the peak region.

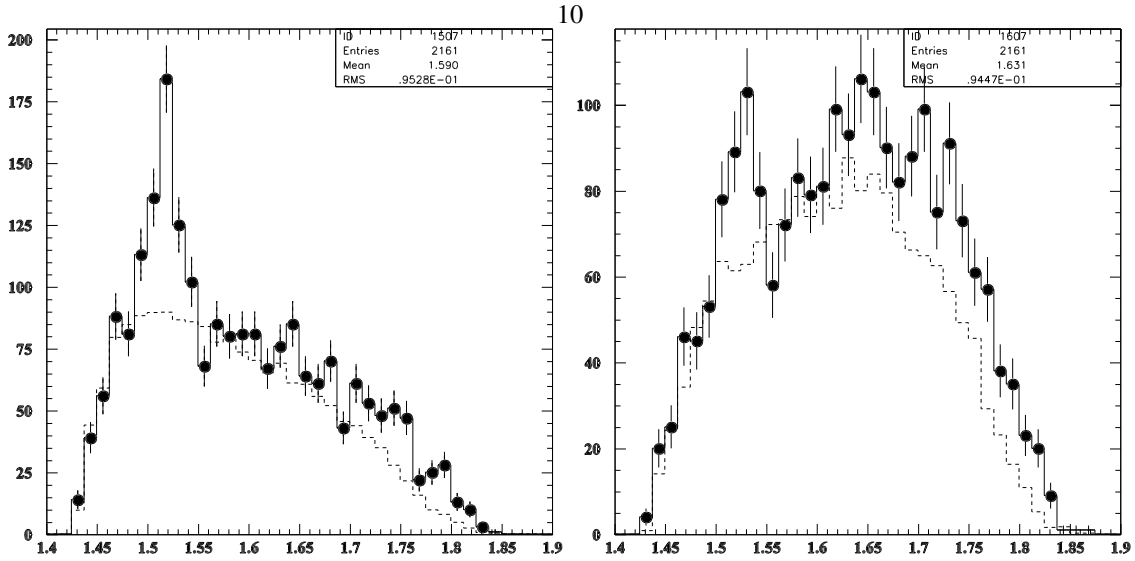

Figure 2.3: The missing mass distributions of $MM(\gamma K^+)$ (left panel) and $MM(\gamma K^-)$ (right panel) in the new data, corrected for Fermi motion in the deuterium nuclei of the LD_2 target (solid lines). The values on the horizontal axis are in GeV, with unspecified bin size. The mixed-event background is shown as the dashed line. Taken from references [22, 23].

exotic baryon $\Theta(1540)$.

2.1.4 Charge-exchange reaction $K^+\mathrm{Xe} \rightarrow K^0_S p\mathrm{Xe}'$ at the DIANA experiment

The bubble chamber of the DIANA experiment is filled with liquid Xe and is exposed to a beam of positive kaons K^+ with an energy of 850 MeV separated from the ITEP proton synchrotron. Charged particles are photographically detected by the ionized tracks they leave in the bubble chamber. Using special stereo-projectors the tracks can be fully reconstructed. The momentum of the particles is derived from the range the track covers in the liquid Xe. The strangeness of the final state is fixed to $S = +1$ by the incoming kaon K^+.[7]

First half of the available data sample

The invariant mass $M(K^0_S p)$ was measured using to the charge-exchange reaction $K^+ n(\mathrm{Xe}) \rightarrow K^0_S p(\mathrm{Xe}')$ where the neutral kaon decays inside the chamber to two pions, $K^0_S \rightarrow \pi^+\pi^-$ [24]. Rescattering in the Xe nucleus was suppressed by requiring the proton p and neutral kaon K^0 to be in the forward direction and in opposite azimuthal regions with respect to the incoming kaon K^+. A narrow resonance was found at a mass of 1539 ± 2 MeV with a width smaller than 9 MeV, visible in the left panel of figure 2.5. The naive statistical significance was determined to be $4.4\,\sigma$.

Full data sample

In 2006 the DIANA collaboration finished the analysis of the full data sample [25]. The new results confirm the earlier results (see right panel in figure 2.5), and increase the naive statistical significance of the observed $\Theta(1540)$

[7]The decay of the neutral kaon K^0 does not allow to determine the sign of the strangeness, since both the neutral kaon K^0 and antikaon $\overline{K}^0$ decay to a pion pair $\pi^+\pi^-$.

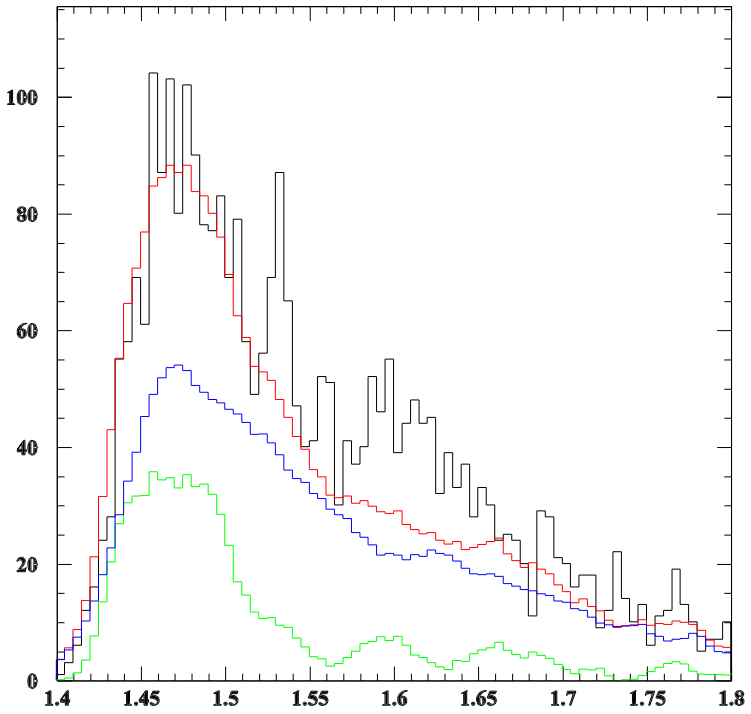

Figure 2.4: The missing mass distribution of $MM(\gamma K^- p)$ on the deuterium target. A peak structure at 1.53 GeV and a broad bump at 1.6 GeV are observed above the background (indicated by the red lines). The values on the horizontal axis are in GeV, with unspecified bin size. For a description of the background model refer to the text. Taken from references [22, 23].

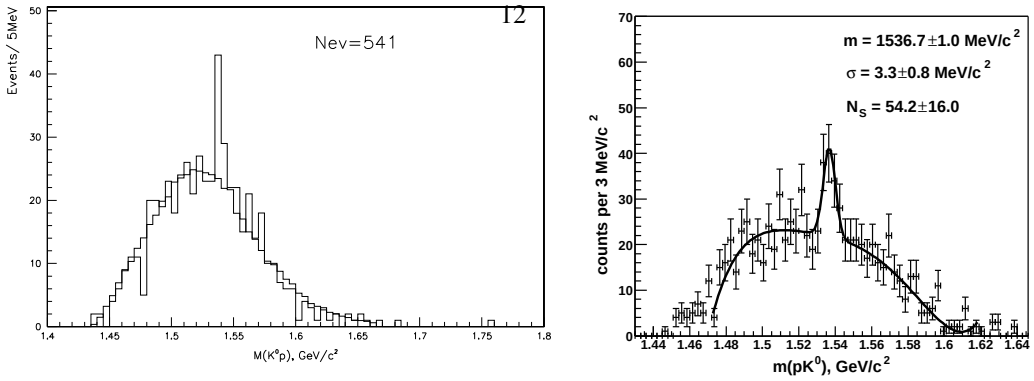

Figure 2.5: The distributions of the invariant mass $M(pK^0)$ for the charge-exchange reaction $K^+n(\mathrm{Xe}) \to pK^0\mathrm{Xe}$' at the DIANA experiment. Rescattering in the Xe nucleus is suppressed. The original data sample (left panel) was expanded by a factor two and re-analyzed (right panel). The distribution of the background events is obtained from a fit to the data. Taken from references [24, 25].

peak. The intrinsic width of the $\Theta(1540)$ resonance peak could be determined from the ratio of resonant and non-resonant events as $\Gamma = 0.36 \pm 0.11$ MeV.

The upper limits on the intrinsic width Γ of an exotic baryon, as determined from the re-analysis of the NK scattering data, is consistent with the width determined at the DIANA experiment.

2.1.5 Photoproduction on protons to $nK^+K^0_S$ at the SAPHIR experiment

At the SAPHIR experiment [26], similar to the CLAS experiment below, energetic photons are produced by bremsstrahlung when 2.8 GeV electrons from the continuous mode Electron Stretcher Accelerator (ELSA) strike a copper foil radiator. The energies of the scattered electrons are measured in the tagging system, and allow the determination of the photon energies between 0.9 GeV and 2.7 GeV. The photon beam then passes through a liquid hydrogen target.

The hydrogen target is located in the center of a cylindrical drift chamber. The momentum of charged particles is determined from their motion in the field of a C-shaped magnet. The central drift chamber is surrounded by a scintillator wall to measure the time-of-flight. In the forward direction a planar drift chamber is used for tracking.

In the reaction $\gamma p \to \Theta^+ K^0_S \to nK^+\pi^+\pi^-$ the kinematic parameters of the neutron were determined from missing energy and momentum. In the distribution of the invariant mass $M(nK^+)$ a peak is observed at $1540 \pm 4(\mathrm{stat}) \pm 2(\mathrm{sys})$ MeV with a width smaller than 35 MeV. The cross section is estimated to be similar to that of ϕ photoproduction, but a factor 4 smaller than final states with open strangeness [27], or around 0.2 μb [28].

Recent null results in the same reaction channel by the CLAS experiment [29, 30], with a very similar geometrical acceptance and a statistical precision far exceeding that of the SAPHIR results, have cast a shadow of doubt on the result of the SAPHIR experiment. The upper limit for this reaction channel determined at the CLAS experiment is 0.8 nb, almost three orders of magnitude smaller than the value determined at the SAPHIR experiment.

2.1.6 Photoproduction on protons and deuterons at the CLAS experiment

At the CEBAF Large Acceptance Spectrometer (CLAS) experiment on the 6 GeV CEBAF race-track accelerator at the Thomas Jefferson National Accelerator Facility (JLab) high-energetic electrons or tagged photons are scattered on fixed, light nuclear targets [31]. The tagged photons are produced by colliding the accelerated electron beam with an energy of up to 6 GeV on a thin bremsstrahlung radiator. The tagged photons have energies from 3 to 5.5 GeV.

The detector is, as indicated by its name, a large acceptance device with a toroidal magnetic field and drift chambers for particle tracking, and Čerenkov counters and scintillation time-of-flight detectors for particle identification.

Electromagnetic calorimeters are used to detect electrons, photons, and neutrons (although neutron detection is not used in the analyses described here).

The CLAS experiment has published several results on exotic baryons, all in photoproduction reactions on light nuclei. The first two positive results contributed largely to the initial acceptance of the $\Theta(1540)$ baryon, whereas the later null results were considered by some as the proverbial 'nail in the coffin' of the $\Theta(1540)$ baryon.

Photoproduction on deuterons (g2a and g10)

The CLAS experiment obtained its first exotic baryon results with the reaction $\gamma d \to K^+K^-p(n)$ [32]. In this reaction on the neutron, the proton can be regarded as a spectator. It has only a small transverse momentum and is normally not detected by the CLAS spectrometer. Relying on the spectator model for the determination of the neutron momentum is an approximation that increases the number of background events. Therefore, only those events were used where the proton and the K^- have a final state interaction (FSI) and the proton is scattered into the acceptance of the detector by the K^-. This technique allowed for a reduction of the background.

The kinematic parameters of the neutron were reconstructed from the missing energy and momentum of the reaction. In the distribution of the invariant mass $M(nK^+)$ a resonance with a naive significance of $5.2\,\sigma$ was found at 1542 ± 5 MeV, with a width compatible with the experimental resolution. The background was modeled with a Gaussian function.

A repetition of this measurement at the CLAS experiment, with more than six times higher statistical precision and in very similar conditions,[8] could not confirm the existence of a resonance peak in this channel. The background had been underestimated substantially in the first result. In the left panel of figure 2.6 the data points of the original g2a result are compared to the newer results, represented by the solid line. The upper limit of the cross section in the channel $\gamma n \to K^-\Theta^+$ was estimated at 3 nb [33].

In the newer data sample, a search for exotic resonances was also performed in the distribution of the invariant mass $M(K^+n)$ in the reaction $\gamma d \to \Lambda K^+(n)$. The requirement of a Λ hyperon in the final state explicitly tags the strangeness of the reaction. As shown in the right panel of figure 2.6, no resonance was observed and an upper limit on the cross section of 5 nb was determined.

To summarize the results of the CLAS experiment on a deuterium target, we conclude that no exotic resonances could be observed in different reaction channels, and strict upper limits on the production were determined.

Photoproduction on the proton (g6)

A second analysis investigated the reaction channel $\gamma p \to \pi^+K^-K^+(n)$ on a proton target [34]. Again, the neutron was reconstructed from the missing energy and momentum, and in the distribution of the invariant mass $M(nK^+)$ a resonance peak at a mass of 1555 ± 10 MeV with a naive significance $7.8\,\sigma$ was found, as shown in figure 2.7. The inset of figure 2.7 was obtained with relaxed event selection requirements. The experimental resolution was also here dominant over the width of the resonance. No resonance structure corresponding to the decay $\Theta^{++} \to pK^+$ was found.

A repetition of this positive experiment is scheduled for the first half of 2008. The g12 run will collect a higher number of photoproduction events on protons, and should either confirm this result with high precision or refute it with a strict upper limit on the allowed cross section.

Photoproduction on the proton with increased statistics (g11)

In 2005, new results on a proton target were presented by the CLAS experiment, once again with very high statistical precision. In the reaction channels $\gamma p \to \overline{K}^0K^0p$ [29] and $\gamma p \to \overline{K}^0K^+(n)$ [30] a search was performed for a resonance with decay channels $\Theta^+ \to K^0_Sp$ and $\Theta^+ \to K^+n$, but no resonance could be observed. The results are reproduced in figure 2.8. A combined analysis of both channels allows to estimate an upper limit on the production

[8] One substantial difference was the movement of the target 25 cm upstream of the center of the spectrometer. For one half of the data collection, a lower value for the magnetic field of the CLAS spectrometer was chosen. This was done to increase the acceptance for forward angle, negatively charged tracks. For the comparison with the previous results, only the half of the data set taken at the same magnetic field value was used.

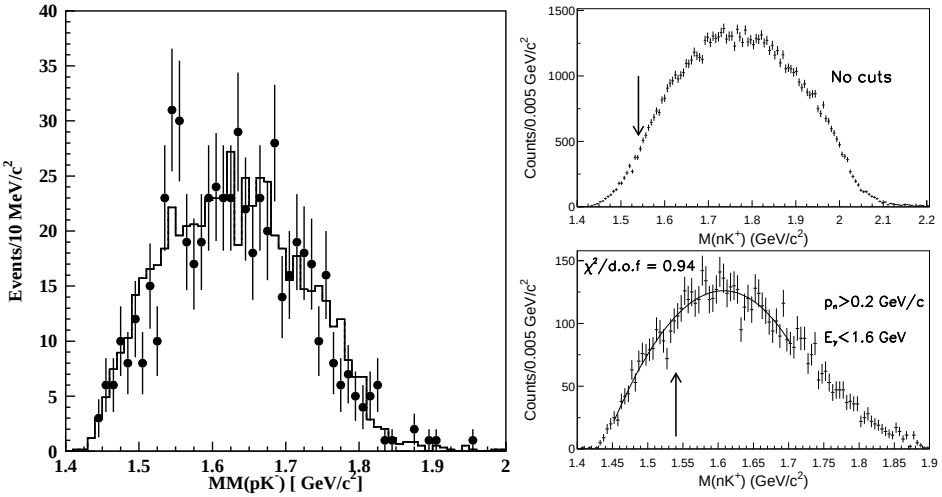

Figure 2.6: The results of the g10 run at the CLAS experiment. The data points collected during the g2a run are compared to the distribution obtained in the g10 run, represented by the solid line (left panel). In the search for associated production of the exotic baryon $\Theta(1540)$ and a Λ hyperon, no resonance could be observed (right panel). Taken from references [33, 35].

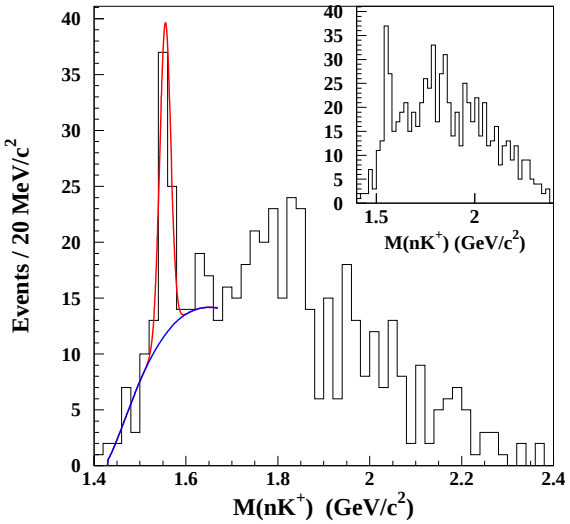

Figure 2.7: The distributions of the invariant mass $M(nK^+)$ in the reaction $\gamma p \to \pi^+ K^- K^+(n)$ for data collected at the CLAS experiment. The neutron was reconstructed from the missing energy and momentum. The inset shows the distribution with relaxed event selection requirements. Taken from reference [34].

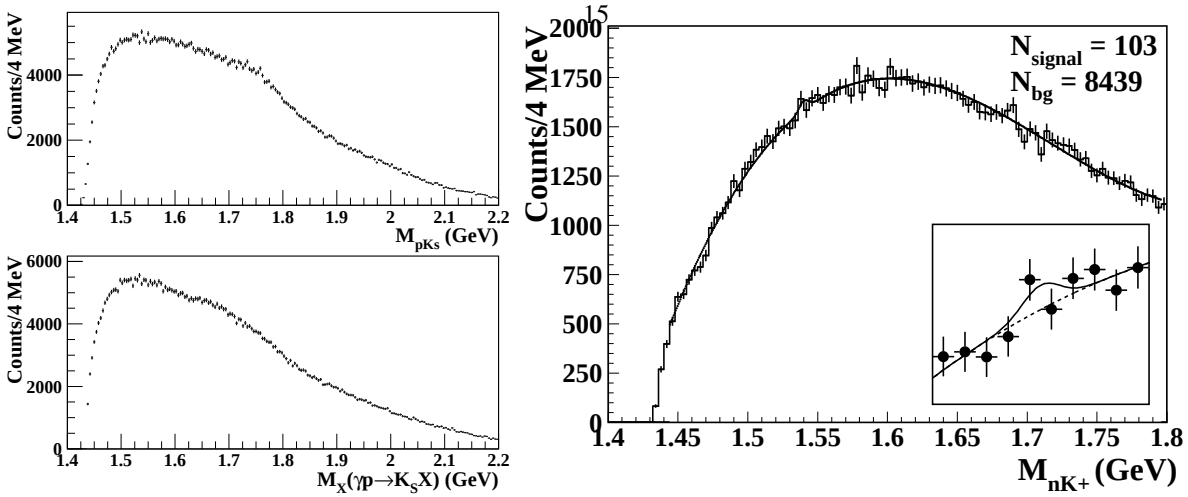

Figure 2.8: The distributions of the invariant mass $M(K^0_S p)$ (left, top) and $M(K^+ n)$ (right) in the reaction channels $\gamma p \to \overline{K}^0 K^+(n)$ and $\gamma p \to \overline{K}^0 K^0 p$ at the CLAS experiment. The missing mass of the second reaction, when only a K^0_S is required in the final state, is shown in the left, bottom panel. No resonances are visible, and upper limits on the photoproduction cross section are estimated. Taken from references [29, 30].

cross section $\gamma p \to \overline{K}^0 \Theta^+$ of 0.7 nb. Using several theoretical models, the width of a possible resonance is limited to values below 3.2 MeV.

Due to the implemented hardware triggers and the lower photon energy, this data sample can not be used to confirm or refute the earlier, positive result on a proton target in the reaction channel $\gamma p \to \pi^+ K^- K^+(n)$.

The previous results seem to be in disagreement with the results of the LEPS experiment. A detailed analysis, taking into account the small differences in acceptance and kinematic coverage, indicates that the results are still consistent for several possible theoretical scenarios for the exotic baryons [36].

It is possible that seemingly unrelated changes to the analysis method or selection criteria reduce the number of observed exotic events, due to the interference with another process. A recent development in the search for exotic baryons at the CLAS experiment exploits the interference between different reactions with identical final states [37, 38].

2.1.7 Quasi-real photoproduction at the HERMES experiment

The HERMES experiment will be described in detail in chapter III. Here we summarize the published evidence for a narrow resonance compatible with the exotic baryon Θ^+ in quasi-real photoproduction on a deuterium target through the decay channel $pK^0_S \to p\pi^+\pi^-$ [4].

The distribution of background events is modeled using a simulation with the PYTHIA Monte Carlo generator, which does not include several excited Λ^* hyperon resonances that thus have to be added in by hand. The shape of the mixed event background distribution agrees with the non-resonant contribution of the Monte Carlo simulation, providing further justification of this method.[9] In the left panel of figure 2.9 the distribution of the invariant mass $M(pK^0_S)$ is shown with a fit of a Gaussian resonance shape on a background model composed of the Monte Carlo simulation, mixed event distribution, and additional Λ^* hyperon resonances. In the right panel of figure 2.9 the data is fitted with the sum of a third order polynomial function and a Gaussian resonance shape, effectively reducing the assumptions on the understanding of the distribution of background events.

A search for the exotic antibaryon Θ^- was also performed at the HERMES experiment, but did not result in an observation. In figure 2.10 the distribution of the invariant mass $M(\overline{p}K^0_S)$ is shown. The number of events was

[9] The event mixing method that was used for this analysis is known to be incorrect. For a detailed discussion, refer to section 4.7.

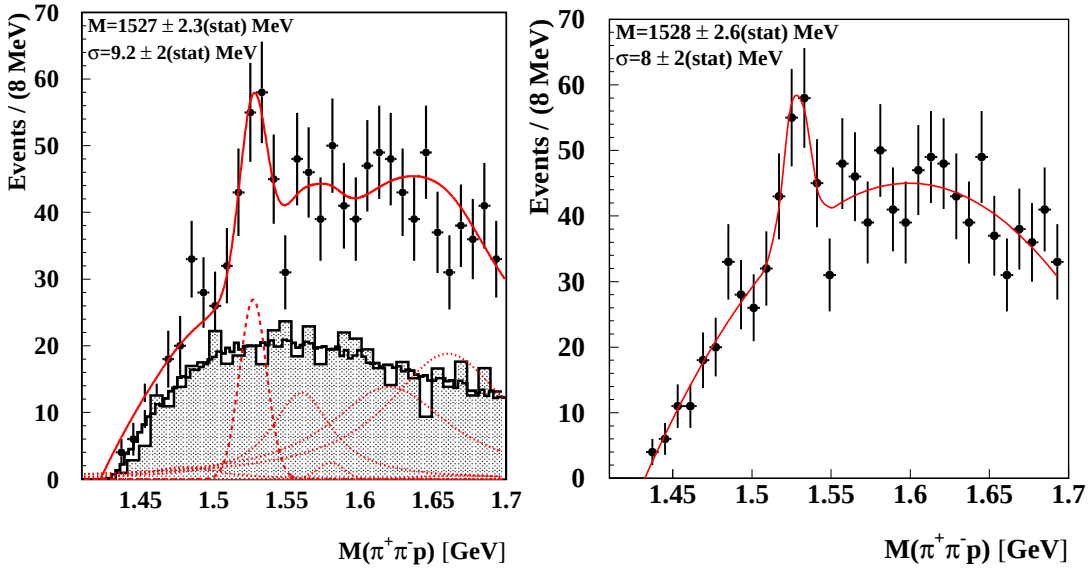

Figure 2.9: Observation of the exotic baryon Θ^+ at the HERMES experiment. In the left panel the background events in the distribution of the invariant mass $M(pK^0_S)$ are modeled using the mixed event background distribution (solid black line) normalized to the non-resonant contribution determined in a PYTHIA Monte Carlo simulation (shaded histogram). In addition the excited Λ^* hyperon resonances (dotted lines) and a Gaussian resonance shape corresponding to the exotic baryon Θ^+ (dashed line) are added. In the right panel the sum of third order polynomial function and a Gaussian resonance shape is used. Taken from reference [4].

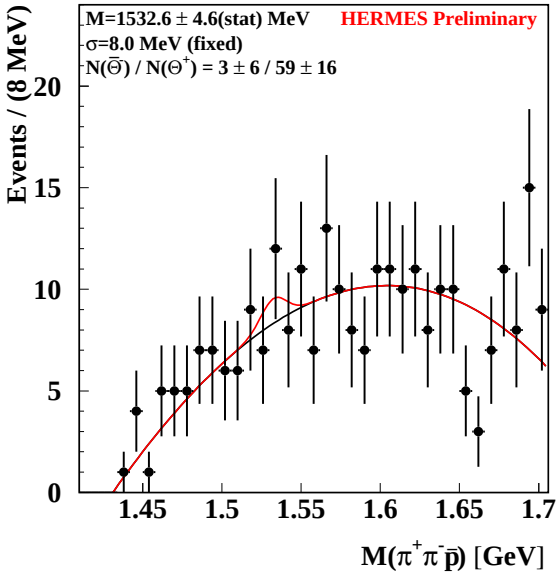

Figure 2.10: Search for the exotic baryon Θ^- at the HERMES experiment. The distribution of the invariant mass $M(\bar{p}K^0_S)$ is fitted with the sum of a third order polynomial function and a Gaussian resonance shape.

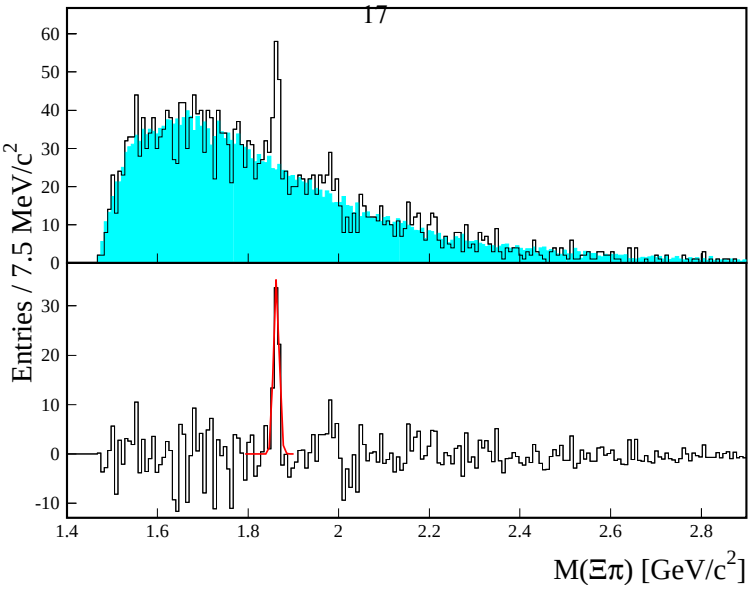

Figure 2.11: Evidence for the exotic baryon Ξ^{--} at the NA49 experiment is found in the decay channel to $\Xi^{--} \rightarrow \Xi^-\pi^- \rightarrow \Lambda\pi^-\pi^-$. The normalized mixed event background (shaded histogram) is subtracted from the invariant mass distribution in the top panel. A narrow peak is visible at a mass of 1862 MeV in the subtracted distribution in the bottom panel. Taken from reference [39].

determined using the sum of a third order polynomial function and a Gaussian resonance shape. The result of 3 ± 6 events is consistent with zero.

2.1.8 Fixed-target proton-proton collisions with the COSY-TOF experiment

The COSY-TOF experiment is a time-of-flight detector at the cooler synchrotron proton storage ring COSY at FZ-Jülich. Protons of 2.95 GeV are focused on a liquid hydrogen target and the reaction products are detected in several time-of-flight hodoscopes. The momentum is reconstructed geometrically, without the use of a spectrometer magnet. The investigation of the predictions of the chiral quark soliton model [17] was already in 1998 one of the objectives of the COSY-TOF experiment.

In the exclusive reaction channel $pp \rightarrow \Sigma^+ K^0_S p$, a narrow resonance was observed in the distribution of the invariant mass $M(pK^0_S)$ at 1530 ± 5 MeV, with a width compatible with the experimental resolution [40]. The cross section was estimated as $0.4 \pm 0.1(\text{stat}) \pm 0.1(\text{sys})\,\mu$b.

More data was collected by the COSY-TOF experiment at marginally higher beam energy. Using three different analysis methods, no $\Theta(1540)$ resonance could be observed in the new data with high statistical precision. An upper limit on the cross section of $\sigma(pp \rightarrow \Sigma^+\Theta^+) < 0.15\,\mu$b was determined (at 95% confidence level) [41].

2.1.9 Proton-proton collisions at the NA49 experiment

At the NA49 experiment at the CERN SPS accelerator complex protons with an energy of 158 GeV were collided on a liquid hydrogen target. The reaction fragments were detected with four large time projection chambers. Particle identification is achieved using the energy loss dE/dx.

By reconstructing the particles in the decay channel to $\Xi^-\pi^-$ and further to $\Lambda\pi^-\pi^-$, the invariant mass distribution in figure 2.11 is obtained. After subtracting the background determined by event mixing, a narrow peak is visible at a mass of 1862 MeV. This resonance was interpreted as the exotic baryon Ξ^{--} [39].

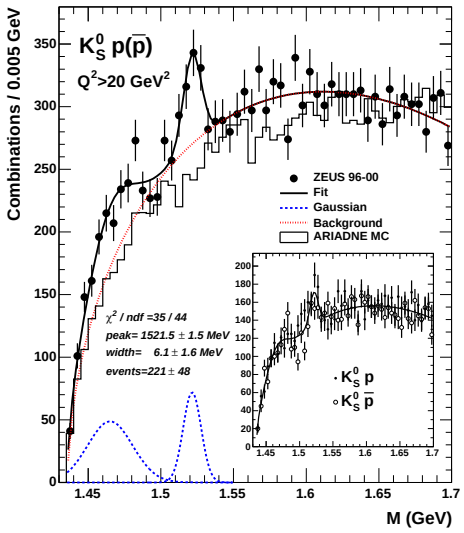

Figure 2.12: The distribution of the invariant mass $M(pK^0_S)$ for inclusive DIS events at the ZEUS experiment. A clear peak is visible at 1521.5 MeV.

2.1.10 Inclusive deep-inelastic scattering at the ZEUS experiment

The ZEUS experiment was the first collider experiment to provide evidence for the existence of the $\Theta(1540)$ state. At the ZEUS experiment inclusive deep-inelastic scattering of electrons and protons at a center-of-mass energy of about 310 MeV is studied. In the analysis at the ZEUS experiment resonance decays to $K^0_S\overline{p}$ are considered as well. They can only be explained as an exotic baryon $\overline{\Theta}$ with minimal quark content $(\overline{uudds})$. A resonance at $1521.5 \pm 1.5(\text{stat}) \pm 2.8(\text{sys})$ MeV is observed. The width is consistent with the experimental resolution of 2 MeV [42].

2.1.11 Hadronic interactions at the SVD-2 experiment

At the SVD-2 experiment, the 70 GeV proton beam of the IHEP accelerator in Protvino, Russia, collides on a fixed C, Si, or Pb target. The spectrometer was designed to study charm hadroproduction near threshold. It consists of a high-precision microstrip vertex detector, a large-aperture spectrometer magnet with multi-wire proportional chambers, and a threshold Čerenkov counter for separation of pion and proton tracks between 4 and 21 GeV. A narrow resolution for several established resonances could be demonstrated.

The search for exotic baryons at the SVD-2 experiment concentrated on the inclusive scattering of protons from nuclei $pA \rightarrow pK^0_S X$. Two results have been presented by the SVD collaboration, with partly overlapping data samples. The first result presents a resonance in the distribution of the invariant mass $M(pK^0_S)$ at $1526 \pm 3(\text{sys}) \pm 3(\text{stat})$ MeV [43]. One could argue that the resonance seems to exist of only a single data point.

A more recent analysis, with improved tracking algorithms, confirmed the earlier indications. An increase of a factor 3 to 4 in total number of K^0_S events was obtained. Moreover, the full data sample was separated in two distinct kinematic regimes, depending on the location of the K^0_S decay vertex. Even without event selection criteria, both subsamples exhibit a peak at $1522.2 \pm 3(\text{stat})$ MeV or 1523.6 ± 3.1 MeV (see figure 2.13). The total proton-nuclear cross section is estimated as 6 μb.

2.1.12 Secondary kaons in the BELLE detector

Using the interaction of secondary kaons with the detector material of the BELLE experiment at the KEKB e^+e^- collider, production of the exotic baryon $\Theta(1540)$ was studied [44]. Interactions in the inner Si vertex detectors were

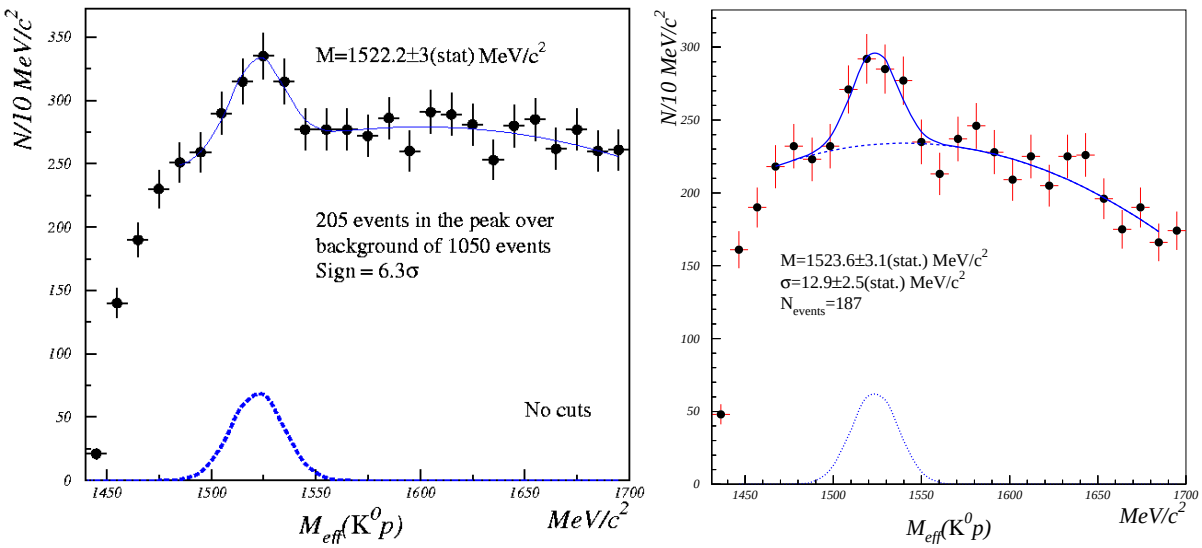

Figure 2.13: Recent results of the SVD-2 experiment. Both figures were obtained with statistically independent subsamples.

used, and both inclusive and exclusive reaction channels were investigated. The result of the inclusive search for pK^0 decays are shown in the left panel of figure 2.14. No structure is observed in the distribution of the invariant mass $M(pK^0_S)$, but the $\Lambda(1520)$ hyperon is clearly visible in the distribution of the invariant mass $M(pK^-)$. The estimated upper limit on the ratios of the inclusive $\Lambda(1520)$ and $\Theta(1540)$ cross sections is 2.5%.

Exclusive production of $\Theta(1540)$ baryons is studied in the reaction $K^+n \to pK^0_S$. Since the (secondary kaon) projectile is not reconstructed, assumptions have to be made about the contribution of other reaction channels to the same final state. Destructive interference between different reaction channels is expected to be negligible, though. The resulting distribution of $M(pK^0_S)$ is shown in the right panel of figure 2.14, but does not indicate any structure at the position of the reported $\Theta(1540)$ baryon. The expected yield is indicated by the open points, and the signal expected from the results of the DIANA experiment are indicated by the solid line. These results do not seem to confirm the results of the DIANA experiment. The upper limit on the width of the $\Theta(1540)$ resonance is estimated as $\Gamma < 0.64\,\text{MeV}$.

2.1.13 Exotic baryons in e^+e^- annihilation at the BABAR experiment

At the BABAR experiment electrons and positrons are collided at a center of mass energy of $\sqrt{s} = 10.58\,\text{GeV}$. An inclusive search for the $\Theta(1540)$ and for most of the other members of the exotic antidecuplet was performed on the very expansive data set with an integrated luminosity of $123\,\text{pb}^{-1}$. Clear signals are observed for the known baryon resonances, but no evidence is found for the production of exotic baryons.

In the left panel of figure 2.15 the distribution of the invariant mass $M(pK^0_S)$ is shown for events satisfying the decay channel $\Theta(1540) \to pK^0_S$. No $\Theta(1540)$ resonance is observed at a mass of 1540 MeV or anywhere else in the distribution. Similarly, the existence of the exotic $\Xi^{--}(1860)$, $\Xi^-(1860)$ and $\Xi^0(1860)$ resonances could not be confirmed.

For the manifestly exotic baryons $\Theta^+(1540)$ and $\Xi^{--}(1860)$ upper limits on the production rate per $e^+e^- \to q\bar{q}$ interaction are determined to allow comparison with the regular baryons [45]. The comparison between regular baryons (at two different center-of-mass energies) and the determined upper limits on the production rate for the manifestly exotic baryons (for two assumptions on the width) is shown in the right panel of figure 2.15.

Although baryon production in e^+e^- collisions is known for the democratic production of hadrons with nonzero strangeness (and other heavier quark constituent), depending only on the mass and the spin of the produced hadron

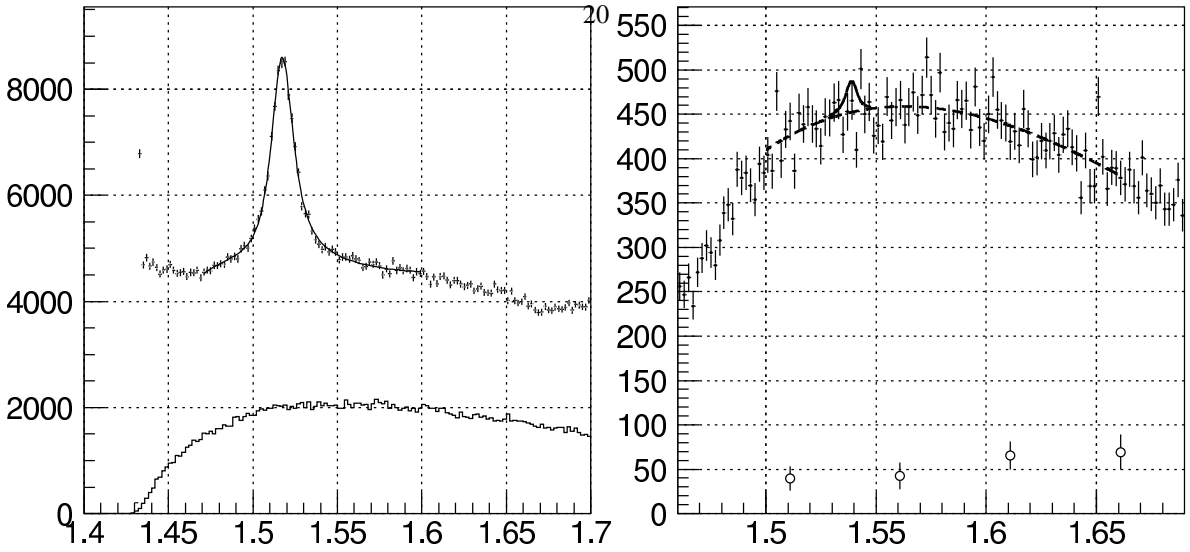

Figure 2.14: Secondary kaon scattering with the Si vertex detectors at the BELLE experiment is used to study the reaction $K^+n \rightarrow pK^0$. In the left panel, the distributions of the invariant mass $M(pK^-)$, represented by the data points with error bars with a prominent $\Lambda(1520)$ resonance peak, and the invariant mass $M(pK^0)$, represented by the solid histogram, are shown for inclusive events. In the right panel, the distribution of the invariant mass $M(pK^0)$ for exclusive events is shown, with the expected yield indicated by the open symbols. Taken from reference [44].

but not directly on the specific quark content, the production of an exotic baryon such as the $\Theta^+(1540)$ requires the creation of five $q\overline{q}$ pairs out of the vacuum compared to only three for regular baryons. Comparing the production rates of exotic hadrons to the expectations for regular hadrons could therefore appear unmotivated.

More recently an inclusive search for the $\Theta^+(1540)$ was performed using the interactions of secondary hadrons and of electrons or positrons in the beam halo with the beam pipe and the material of the inner tracking detectors [46, 47]. Again no evidence for the exotic baryon $\Theta^+(1540)$ was found, but the results allow for a comparison with other photo-, electro-, and hadroproduction (see figure 2.16).

2.1.14 Fixed target proton-tungsten collisions at the HyperCP experiment

The HyperCP experiment at Fermilab was designed to study CP symmetry violation in the decays of the cascade hyperons Ξ^- and Ξ^+ [48]. A secondary beam is produced by 800 GeV protons striking a copper target, and the collimator channel immediately downstream of the target and embedded in a dipole magnet is used to select a positively charged beam, consisting of mainly protons and pions with approximately 5% kaons, with a broad momentum distribution between 120 and 220 GeV. Events produced in the tungsten exit region of the collimator were used in a search for the exotic baryons $\Theta^+(1540)$ [49].

The HyperCP experiment does not have dedicated particle identification detectors. For the identification of the K^0_S mesons the signature of their decay to two oppositely charged pions with a reconstructed invariant mass $M(\pi^+\pi^-)$ consistent with the K^0 mass allows for a clean selection. Charged particles with more than 50% of the total momentum were assumed to be protons, motivated by the high probability of being protons for these events. Thus, the search was restricted to the exotic baryon decay $\Theta^+(1540) \rightarrow pK^0_S$.

In the distribution of the invariant mass $M(pK^0_S)$ no peak was observed, as shown in figure 2.17. The distribution is fitted with the expected resonance shape obtained in a Monte Carlo simulation. At most 0.3% of the pK^0_S candidate events could come from the decays of exotic Θ^+ baryons. The same data sample contained over 140,000 combined Ξ^- and Ξ^+ decays.

The high value and broad spread of beam momentum avoids the possibility of peaks generated by kinematic

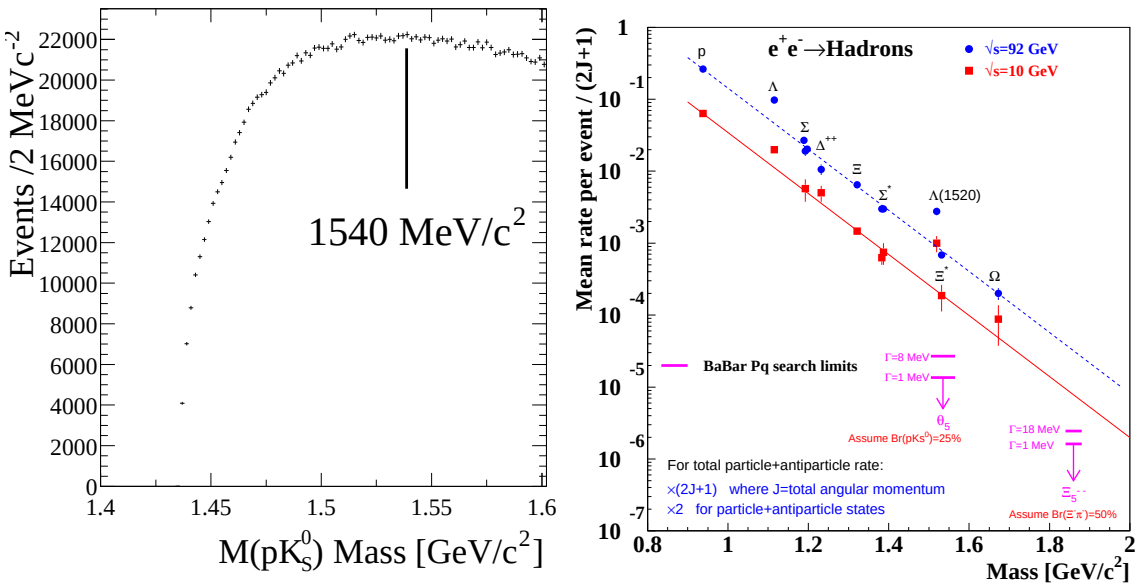

Figure 2.15: Production of exotic baryons in e^+e^- annihilation at the BABAR experiment. In the left panel the distribution of the invariant mass $M(pK^0_S)$ is shown. The expected position of the $\Theta^+(1540)$ peak is indicated but no structure is visible. In the right panel the production rates per $e^+e^- \to q\bar{q}$ interaction are compared for the regular baryons and for the determined upper limits on the production of the exotic baryons $\Theta^+(1540)$ and $\Xi^{--}(1860)$. Taken from reference [45].

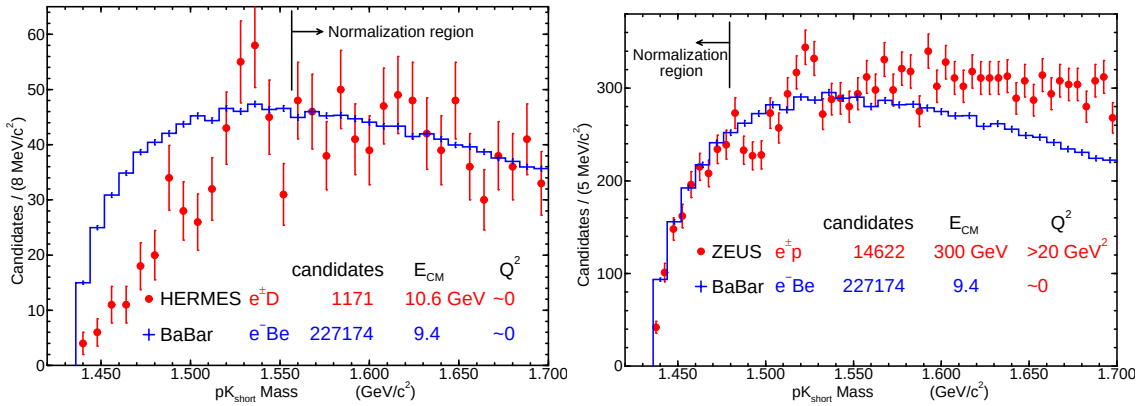

Figure 2.16: Electro- and hadroproduction of exotic baryons at the BABAR experiment. The results of the BABAR experiment are compared with the results of the HERMES experiment (left panel) and the ZEUS experiment (right panel). Taken from reference [47].

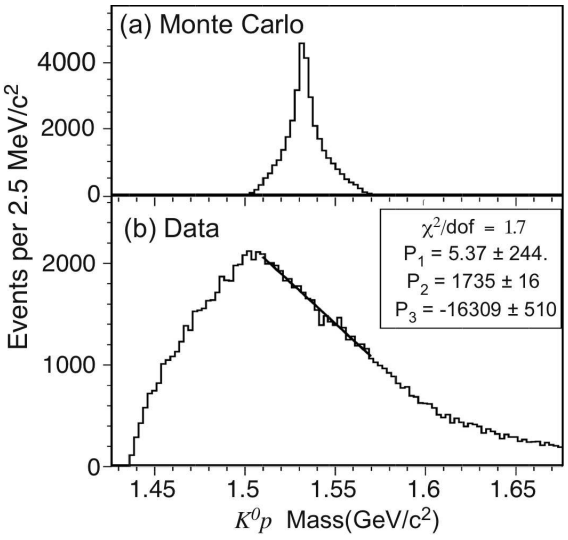

Figure 2.17: The search for $\Theta^+(1540)$ decays at the HyperCP experiment. The expected resonance shape is shown in the upper panel, and used in a fit to the distribution of the invariant mass $M(pK^0_S)$ in the lower panel. At most 0.3% of the pK^0_S candidates could come from an exotic decay $\Theta^+(1540) \to pK^0_S$. Taken from reference [49].

reflections. Unfortunately, together with the mixed beam composition it precludes the estimation of limits on the production cross section of the $\Theta(1540)$ baryons.

2.1.15 High-energetic proton-nucleus interactions at the HERA-B experiment

At the HERA-B experiment collisions of high-energetic protons in the halo of the 920 GeV HERA proton beam with the nuclei of atoms in target wires were studied. The HERA-B detectors has a large acceptance, precision silicon vertex detectors and particle identification detectors. The resonance decays $K^0_S \to \pi^+\pi^-$, $\Lambda \to p\pi^-$, $\Lambda(1520) \to pK^-$, and $\Xi^- \to \Lambda\pi^-$ are cleanly identified and reconstructed. In the selected momentum region between 22 and 55 GeV the misidentification of protons is less than 1%.

Using the decay channel to pK^0_S an inclusive search for the exotic baryon $\Theta^+(1540)$ was performed in the data samples collected on carbon, titanium and tungsten wires. The three obtained invariant mass distributions are shown in top panels of figure 2.18. Any structures in the distributions are consistent with statistical fluctuations. The upper limits on the cross section for the production of $\Theta(1540)$ baryons are between 4 and 20 μb per nucleon. The ratio of the production rates of the exotic Θ^+ to other hyperons is five times smaller than the value observed at the ZEUS experiment, and two orders of magnitude smaller than the value observed at the HERMES experiment.

A search for the exotic baryon $\Xi(1860)$ was performed in the decay channels to $\Xi^-\pi^-$ and $\Xi^-\pi^+$ and the corresponding antiparticle channels, but also there upper limits stronger than 4 μb per nucleon could be determined. The distributions of the invariant mass $M(\Xi\pi)$ for the $\Xi^0(1860)$ and $\Xi^{--}(1860)$ combinations (and their charge conjugates) are shown in the bottom panels of figure 2.18. A clear excess is visible at 1530 MeV corresponding to the well-established $\Xi^{0*}(1530)$ hyperon.

2.1.16 Discussion

In this experimental overview several observations of the exotic baryons Θ^+ and Ξ^{--} have been discussed. Among the original observations of the Θ^+ there are several that are not valid anymore (SAPHIR, CLAS on deuterons, COSY-TOF), and only the LEPS and SVD-2 experiments have been able to confirm the original analysis with additional data, although these results have only been shown at conferences or published in proceedings. The observation of the exotic

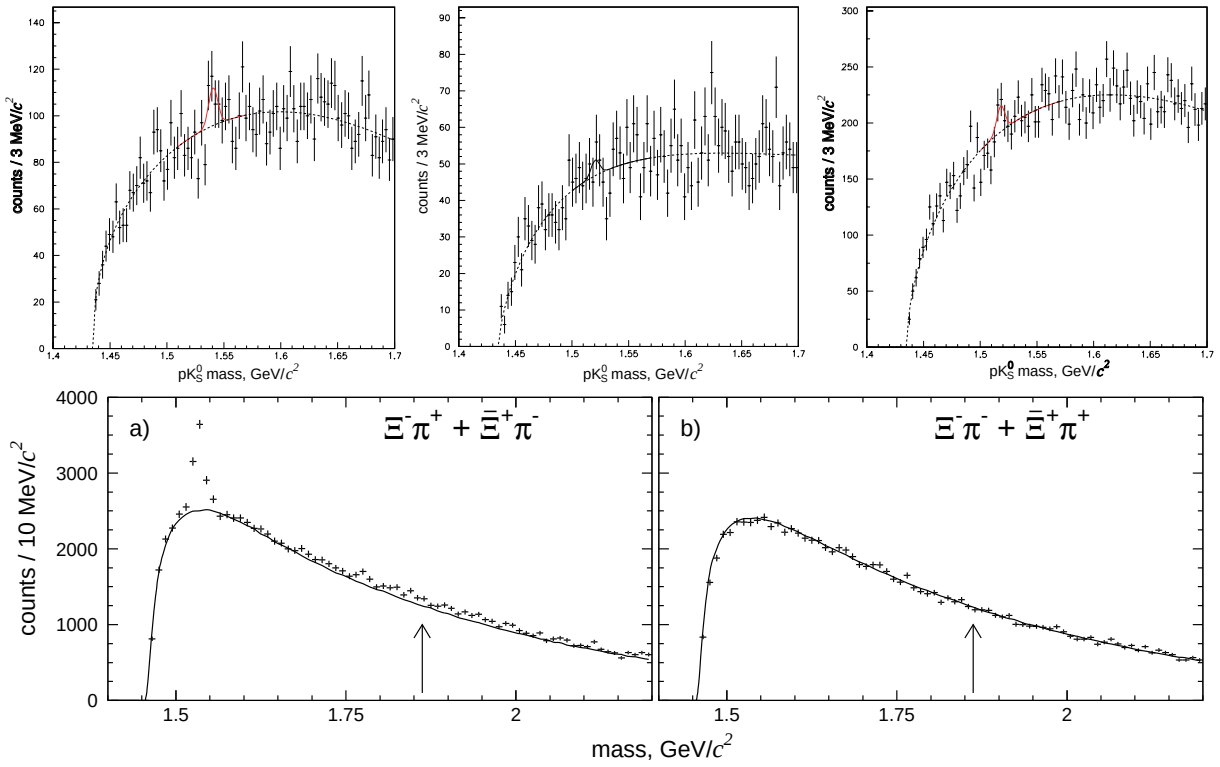

Figure 2.18: The search for Θ^+ and Ξ^{--} in pA reactions at the HERA-B experiment. For all three investigated target materials, carbon (left panel), titanium (middle panel), and tungsten (right panel), no statistically significant peak for the exotic baryon Θ^+ is invisible in the invariant mass distribution $M(pK^0_S)$. In the bottom panels the featureless distribution of the invariant masses $M(\Xi^-\pi^+)$ (left panel) and $M(\Xi^-\pi^-)$ (right panel) and charge conjugate modes are shown. Taken from references [50, 51].

Table 2.1: A large number of experiments is unable to confirm the existence of the exotic baryon Θ^+. These null results are listed here alongside the limits they impose on the branching ratio (B.R.) or relative yield of other resonances.

Group	Reaction	Limit
BES [52]	$e^+e^- \to J/\Psi \to \overline{\Theta}\Theta$	$< 1.1 \times 10^{-5}$ B.R.
BABAR [45, 53]	$e^+e^- \to \Upsilon(4S) \to pK^0X$	$< 1.0 \times 10^{-4}$ B.R.
Belle [44]	$e^+e^- \to B^0\overline{B}^0 \to p\overline{p}K^0X$	$< 2.3 \times 10^{-7}$ B.R.
LEP [54]	$e^+e^- \to Z \to pK^0X$	$< 6.2 \times 10^{-4}$ B.R.
HERA-B [55]	$pA \to K^0pX$	$< 0.02 \times \Lambda^*$
SPHINX [56]	$pC \to K^0\Theta^+X$	$< 0.1 \times \Lambda^*$
HyperCP [49]	$pCu \to K^0pX$	$< 0.3\%\ K^0p$
CDF [57]	$p\overline{p} \to K^0pX$	$< 0.03 \times \Lambda^*$
FOCUS [58]	$\gamma BeO \to K^0pX$	$< 0.02 \times \Sigma^*$
Belle [44]	$\pi + Si \to K^0pX$	$< 0.02 \times \Lambda^*$
PHENIX [59]	$Au + Au \to K^-\overline{n}X$	(not given)

baryon Ξ^{--} has not been confirmed by any experiment. For the exotic baryon Θ^+ a long list of experiments with null results, often associated with upper limits on the branching ratios or cross sections, is shown in table 2.1.

A small number of experiments is or will be collecting data in very similar conditions as for their earlier observation. With this new data they are expected to confirm or refute the earlier results. At the ZEUS experiment the original observation of the exotic baryon Θ^+ only involved data collected during the HERA I running period until the year 2000. Since the luminosity upgrade and the installation of an improved vertex detector in 2001, the ZEUS experiment has collected additional data in the HERA II running period until the year 2007. This data is still being analyzed. The CLAS experiment will collect new data on a proton target during the first half of 2008. This will allow for the refutation or confirmation of the observation of the exotic baryon Θ^+ in the original data set collected during the g6 run [34].

In table 2.2 several observations are listed alongside with a repetition of the measurement with higher statistical precision. This list is not intended to be complete, and it is certainly debatable whether some can be considered a repetition, but it indicates that several of the original experiments with only a small and unconvincing number of events have not stood up to the scruntiny of experiments with a very high statistical precision. In the few cases where the original observation was confirmed, the precision of the repeated result is still not convincing.

2.2 Theoretical models

In this section the theoretical models for hadrons and more specifically exotic baryons are discussed. Since a perturbative approach to QCD is impossible at the low energies of hadronic bound states, several phenomenological models have been proposed in the past. The concept of constituent quarks is important in all of these models. A quite different approach was taken by the chiral quark soliton model (χQSM), which provided the predictions of a narrow exotic baryons that lead to the recent experimental search for exotic baryons [17].

Several theoretical reviews on exotic baryons have been published before [60, 61, 62], but the most important theoretical approaches are summarized in this section.

2.2.1 The MIT bag model

A conceptually very simple model for hadrons is the MIT bag model [63, 64]. The massless (or very light) quarks and gluons are confined in a finite region with constant energy density, the 'bag'. Inside the bag the quarks do not interact with each other, leading to the property of asymptotic freedom. Outside the bag the masses of the quarks become infinitely large, and thus also the color confinement property of QCD is trivially satisfied. The content of the

Table 2.2: Comparison of observations of the exotic baryon Θ^+ with repeat experiment. The original positive results, claiming the observation of the exotic baryon $\Theta^+(1540)$, are compared to repeat experiments in very similar kinematic conditions but with higher statistical precision. Taken from reference [65].

Observation	Reaction	Repetition	Reaction	Increase	Result
LEPS [20]	$\gamma C \to K^+K^-(n)$	LEPS [22, 23]	$\gamma d \to K^+K^-(n)$	$\times 5$	Confirmed $5\,\sigma$
SVD-2 [43]	$pA \to pK^0_S X$	SVD-2 [66]	$pA \to pK^0_S X$	$\times$3–4	Confirmed 6–9 σ
DIANA [24]	K^+Xe $\to K^0 pX$	Belle [44]	K^+Si $\to K^0 pX$	$\times 10$	$\Gamma_\Theta < 1$ MeV
SAPHIR [27]	$\gamma p \to K^0K^+n$	CLAS (g11) [29]	$\gamma p \to K^0K^+n$	$\times 10$	$\sigma_{tot} < 1$ nb
CLAS (g2a) [32]	$\gamma d \to K^+K^-p(n)$	CLAS (g10) [33]	$\gamma d \to K^+K^-p(n)$	$\times 6$	$\sigma_{tot} < 3$ nb
HERMES [4]	$e^+d \to K^0pX$	BABAR [47]	e^+Be $\to K^0pX$	$\times 200$	No Θ^+ observed
COSY-TOF [40]	$pp \to \Sigma^-K^0p$	COSY-TOF [41]	$pp \to \Sigma^-K^0p$	$\times$4–8	$\sigma < 0.15\,\mu$b

bag can always be chosen as a color-singlet.

This simple model with a very limited number of parameters is surprisingly successful in the description of hadrons, reproducing not only the masses of the light baryons but also the proton radius and even quark distributions in the nucleon. The bag model can be readily extended to include five or more quarks. For the mass of the lightest exotic baryons values from 1700 to 2400 MeV were predicted [67].

2.2.2 Group theory of exotic baryons

To determine the configuration of exotic baryons states, we start from similar group theoretical arguments that were used to explain the regular meson and baryon multiplets in chapter I. In the expansion of $\mathbf{6} \otimes \mathbf{6} \otimes \mathbf{6} \otimes \mathbf{6} \otimes \overline{\mathbf{6}}$ the exotic baryons end up in antidecuplets, 27-plets, and 35-plets [68, 69, 70].

When we limit ourselves to states without angular momentum ($\ell = 0$), the exotic baryons with the lowest energy are organized in the antidecuplet ($\overline{\mathbf{10}}$) with spin and parity $J^\pi = \frac{1}{2}^+$. It is nearly degenerate with an octet ($\overline{\mathbf{8}}$) of states with negative parity, but in the octet no manifestly exotic states are present. The antidecuplet $\overline{\mathbf{10}}$ is shown in figure 2.19, where the masses are predictions of the chiral quark soliton model. To determine numerical values for the masses and widths of the exotic baryons, specific models have to be used.

2.2.3 The chiral structure of QCD

At low energies the chiral structure of QCD defines the dynamic behaviour of quarks, mesons and baryons [71, 72]. Because the u and d quarks are almost massless compared to the nucleon, the theory of QCD with only two flavors is invariant under transformation in the chiral symmetry group $SU(2)_R \times SU(2)_L$.[10] Since we do not observe pairs of hadrons with opposite parity, this chiral symmetry must be spontaneously broken down to the symmetry group $SU(2)_V$, where V refers to the invariant vector charge of the QCD ground state or vacuum. The three Goldstone bosons associated with the symmetry breaking are the pions π^-, π^0 and π^+. They are light but not massless due to the small but non-zero masses of the u and d quarks. When we consider the s quark in addition to the u and d quarks, the same mechanism of spontaneous chiral symmetry breaking occurs, but now eight massive Goldstone bosons are formed (π^-, π^0, π^+, K^-, K^0, $\overline{K}^0$, K^+, η). The η' is substantially heavier than the η because it is associated with the broken $U(1)$ axial symmetry.

The spontaneous symmetry breaking is accompanied by the formation of the gluon condensate $G_{\mu\nu}G^{\mu\nu}$ and the chiral quark condensate $\langle q\overline{q}\rangle$, which fills the vacuum with quark-antiquark pairs. The light 'bare' quarks and antiquarks that compose the mesons and baryons are 'dressed' in these fields and receive a momentum-dependent dynamical mass ($m_{u,d} \approx 350$ MeV, $m_s \approx 470$ MeV). These so-called constituent quarks have now masses approximately one half of the mass of the ρ meson or one third of the mass of the nucleon.

Baryons can now be described as three constituent quarks surrounded by a cloud of massless mesons. The interactions between the constituent quarks and the meson cloud determine the properties of the baryon.

2.2.4 The chiral quark soliton model

In the 1960s a different approach was proposed by Skyrme to study the nucleon [73, 74] and, by extension to $SU(3)_f$, baryons with strangeness [75, 76]. At low energies the baryons are regarded as spherically symmetric soliton solutions of the pion field or chiral field that forms due to the spontaneous breaking of the chiral symmetry of QCD.

This suggests a classification of the light baryons as rotational states. The minimal generalization of spherical symmetry in a system with three isospin components (*i.e.* the three pions) is

$$\pi^\alpha(x) = \frac{x^\alpha}{r} P(r),$$

where $P(r)$ is the spherically symmetric profile of the soliton. This implies that a space rotation of the field is equivalent to a rotation in isospace. From the analogy of this situation with the classical spherical top, one sees that

[10] For massless particles the helicity h, defined as the projection of the spin σ on the direction of the momentum $\sigma \cdot \frac{\vec{p}}{|\vec{p}|}$, is an invariant. It is then also referred to as the chirality or handedness. It can take the value $+1$ for right-handed or -1 for left-handed particles.

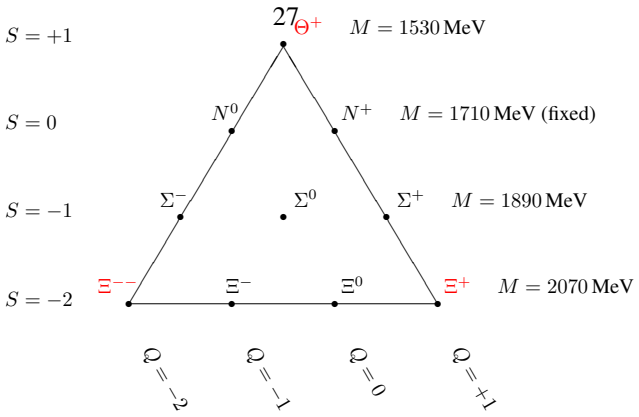

Figure 2.19: The ground state antidecuplet of the exotic $J = \frac{1}{2}$ baryon states, with the masses predicted by the chiral quark soliton model.

the rotational states are $(2J + 1)^2$-fold degenerate in spin and isospin. Applying this for $J = \frac{1}{2}$ we find the four nucleon states. For $J = \frac{3}{2}$ we find the sixteen Δ resonance states. The relations between the characteristics of the states are generally within about 30% of the experimental values [77].

If extended to three quark flavors, the rotations are performed in ordinary space and in $SU(3)$ space. Quantization shows that the lowest baryon state is the octet of regular baryons with spin $J = \frac{1}{2}$ and the second excitation is the decuplet of regular baryons with spin $J = \frac{3}{2}$. The relations between the mass, width and branching ratio of the members of the octet and decuplet are satisfied to an accuracy of up to one percent [17].

Already in 1987 the existence of the lightest exotic baryon with strangeness $S = +1$ at a mass of approximately 1530 MeV was predicted [78, 79].

The third rotational excitation in the $SU(3)$ case is an antidecuplet with spin $J = \frac{1}{2}$ (see figure 2.19). This exotic antidecuplet can be alternatively considered in a primitive way as states made of three quarks plus a quark-antiquark pair. The lightest member Θ^+ can then be considered a K^+n or K^0p bound state. The advantage of the chiral soliton model is that all concrete numbers follow from symmetry considerations and do not rely on a specific dynamical realization. If one number is extracted from experiment, one can completely fix all the other members of the antidecuplet, together with their widths and branching ratios.

By using the mass of the established neutron resonance N at 1710 MeV as the 'anchor' for the antidecuplet, the mass of the Θ^+ was predicted to be 1530 MeV and the width less than 15 MeV.[11] These predictions partially motivated the experimental searches for Θ^+ and are in agreement with the results of the different experiments.

However, in this model the predicted width of $N_{\overline{10}}$ and $\Sigma_{\overline{10}}$ are both below the experimental values listed by the Particle Data Group. 'Anchoring' the antidecuplet to these states increases the width of the Θ^+ to exceed the bounds set by experimental data [80].

2.2.5 The Jaffe-Wilczek diquark model

In an alternative positive-parity interpretation the exotic baryon Θ^+ is a bound state of two highly correlated ud diquarks and an $\overline{s}$ antiquark [81]. The quarks in the ud diquarks are necessarily in an antisymmetric color configuration $\overline{\mathbf{3}}_c$, otherwise no color singlet would be formed with the remaining antiquark. When the quarks have opposite spins, then they are simultaneously in an antisymmetric color, flavor, isospin, and spin configuration. A strong correlation between the quarks in the diquarks is then expected.

[11] After the first observations of the exotic baryon Θ^+ a numerical mistake in the calculation of the width was discovered. The correct value of the width following from the chiral quark soliton model is therefore closer to 30 MeV. Refer to references [82, 83, 84] in that order for a discussion of this issue.

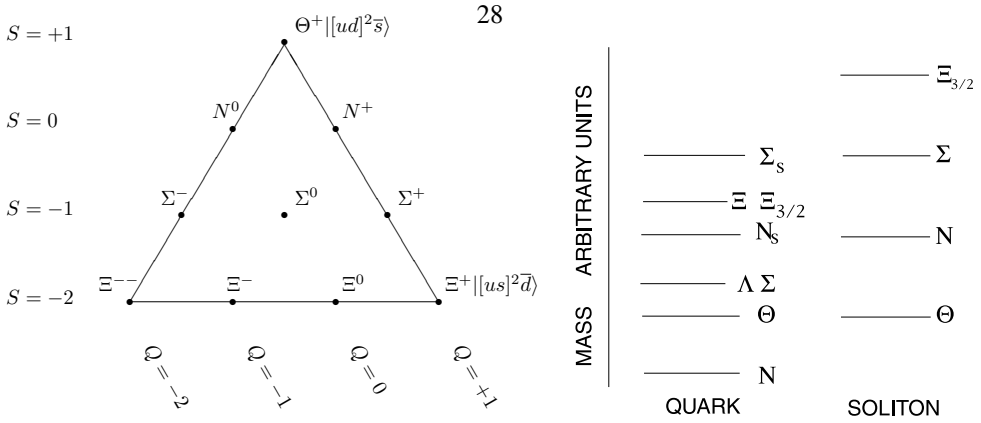

Figure 2.20: In the diquark model exotic baryons consist of two highly correlated diquarks and an antiquark. In the left panel the predicted $J = \frac{1}{2}$ antidecuplet and $J = \frac{3}{2}$ are shown. When the mass of the Θ^+ baryon is fixed to the value in the χQSM, the relative mass spectrum with the label "quark" in the right panel is obtained. Taken from reference [81].

While this models predicts the same exotic antidecuplet of states as the chiral quark soliton model in addition to a crypto-exotic octet, there are distinct differences in the masses of the states. The exotic antidecuplet and crypto-exotic octet of baryons is shown in the left panel, and the relative mass spectrum in the right panel of figure 2.20. Due to the mixing of the antidecuplet and the octet, one crypto-exotic state with a mass below that of the Θ^+ is formed. This state was identified as the Roper resonance $N(1440)$ in this model.

The diquark model predicts that the exotic baryon Ξ^{--} has a mass of 1750 MeV, when the mass of the Θ^+ is fixed at the observed value of 1540 MeV. Although no strong explanations for the narrow width are given, it may be possible to explain the narrowness by the weak coupling of the Θ^+ to the KN mode. However, the large width of the Roper resonance in the same multiplet makes this highly non-trivial.

2.2.6 The Karliner-Lipkin diquark triquark model

A challenge for any exotic baryon model is to explain the positive parity predicted by the Skyrme model for the Θ^+ state, while the 'standard' pentaquark involves five quarks in an S-wave and therefore has negative parity. If Θ^+ has indeed positive parity, then there is clearly one unit of angular momentum, which makes the calculations difficult.

In the diquark-triquark model two color nonsinglet clusters (a ud diquark and a $us\overline{s}$ triquark) are in a relative P-wave and kept together by the color-electric force [85, 10]. The P-wave configuration ensures that the parity is positive. The clusters are separated by a distance larger than the range of the color-magnetic force. The repulsive hyperfine interaction between two quarks of the same flavor is then not felt between the clusters.

CHAPTER III

The HERMES Experiment

The HERMES experiment[1] was designed to study the quark-gluon spin structure of the nucleon. This is accomplished by studying asymmetries in the cross section for deep-inelastic scattering (DIS) of longitudinally polarized leptons on light nuclear targets. Several other experiments have provided accurate data for the *inclusive* cross section asymmetry, *i.e.* when only the scattered lepton is detected. At the HERMES experiment, *semi-inclusive* deep-inelastic scattering (SIDIS) processes are studied, *i.e.* some of the hadrons created in the fragmentation of the target nucleon or the hadronization of the struck quark are detected as well. These data offer a way to determine the flavor of the struck quark, and thus access the flavor-dependent spin structure functions. Along with the accurate determination of the particle track and momentum, good particle identification (PID) is crucial for the HERMES experiment. It can identify pions, kaons, protons, and leptons with high efficiency and low contamination.

The HERMES experiment is located in one of the four experimental halls of the lepton-proton collider HERA[2] at the research institute DESY[3] in Hamburg, Germany. It only uses the lepton beam of the HERA collider. The lepton storage ring can be filled with either electrons or positrons,[4] which are accelerated to an energy of 27.6 GeV.

One of the characteristic properties of the HERA lepton storage ring is the large transverse self-polarization of the lepton beam built up in the arcs of the accelerator. Before the leptons reach the HERMES experiment, a spin rotator aligns the spin longitudinally, parallel or antiparallel to the beam direction. Behind the HERMES experiment the polarization of the leptons is measured with the longitudinal polarimeter (LPOL). Finally, before the leptons continue their way through the arcs of the HERA collider, their spin is rotated back transverse to the beam direction.

In the following sections the HERA lepton-proton collider, the HERMES target, and the HERMES spectrometer are described in more detail. A section on Monte Carlo simulations of reactions at the HERMES experiment follows. Finally, the operation of the longitudinal polarimeter (LPOL) of the lepton beam is discussed in light of high-precision lepton beam polarimetry measurements at future collider experiments (in particular the electron-ion collider EIC).

3.1 The HERA lepton-proton collider

Until the end of operations in 2007, the HERA lepton-proton collider at the research institute DESY was one of the world's highest-resolution probes into the quark structure of the proton. At the HERA collider electrons or positrons were accelerated to an energy of 27.6 GeV, and protons to an energy of 920 GeV. A schematic overview of the different accelerator systems, including the pre-accelerator PETRA, at the research institute DESY is shown in figure 3.1.

At two interactions points the lepton and proton beams collided at a center-of-mass energy of approximately 300 GeV. At these two interaction points, located in the North and South Hall, the experiments H1 and ZEUS studied deep-inelastic scattering reactions in the low-x region.[5] The other two experimental halls of the HERA collider were

[1] HERA Measurement of Spin

[2] Hadron-Elektron Ringanlage, hadron-electron ring facility

[3] Named after the Deutsches Elektron Synchrotron, the first synchrotron built at the research institute, which accelerated its first electrons to 7.4 GeV on January 1, 1960.

[4] Since the analysis presented in this work is independent of the charge of the colliding leptons, positrons are included when the text refers only to electrons, unless explicitly mentioned otherwise.

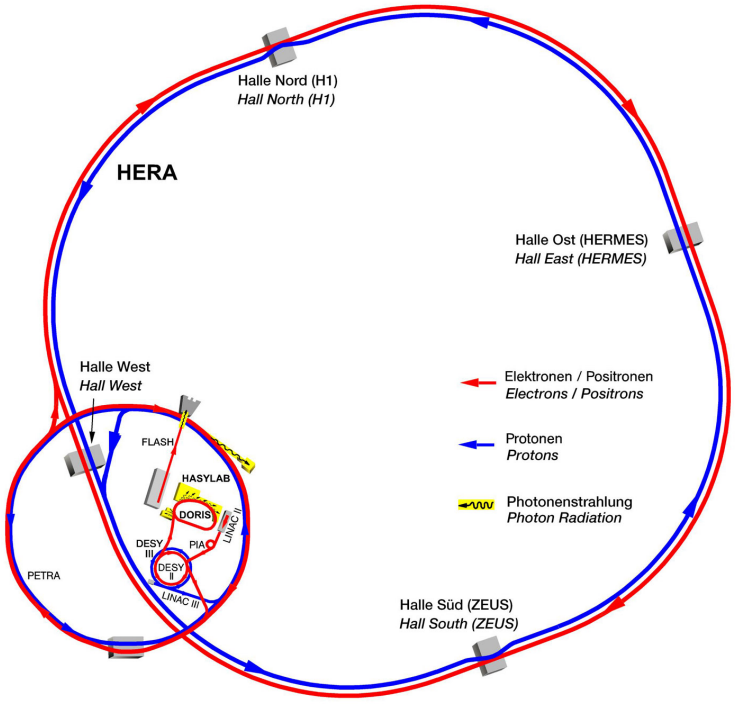

Figure 3.1: The research institute DESY consists of several accelerator systems. After generation of a low-energetic proton and lepton beam in the LINAC and DESY accelerators, the synchrotron PETRA was used as pre-accelerator for the approximately 6.3 km long HERA storage rings. The electrons or positrons (red) were accelerated to 27.6 GeV, the protons (blue) were accelerated to 920 GeV. At two interaction points (North and South) the leptons and protons were brought in collision for the H1 and ZEUS experiments. The HERA-B experiment in the West hall used only the proton beam. The HERMES experiment was located in the East hall and only used the electron or positron beam. Taken from reference [86].

occupied by fixed target experiments. The HERA-B experiment searched for CP-symmetry breaking in the decay of B-mesons generated in the interactions of protons in the proton beam halo with movable metal wires. The HERA-B experiment was terminated in 2003 and the HERA-B spectrometer was removed from the West Hall. The second fixed target experiment at the HERA collider was, of course, the HERMES experiment. The HERMES experiment used only the lepton beam of the HERA collider.

In the HERA lepton storage ring, electrons or positrons circulate in bunches with a length of 37 ps and separated by 96 ns. At most 220 bunches can be filled simultaneously, although in practice rarely more than 185 bunches are filled.[6] The lepton bunches with an energy of 12 GeV are injected in several steps from the PETRA pre-accelerator into the HERA lepton storage ring, until a current of approximately 45 mA is reached. They are then accelerated to the full energy of 27.6 GeV. During data collection with polarized target gases, the lepton beam current decreases exponentially with a life time of over 10 hours until it reaches approximately 15 mA. By injecting unpolarized gases with higher density in the HERMES target the life time is then further reduced and one hour later the remaining leptons are usually dumped. A new lepton beam is injected and data taking resumes. In a very similar fashion the HERA proton storage ring is operated. Because the proton beam current decreases more slowly, up to three regular lepton fills can be obtained for every proton fill.

Only very few leptons in the lepton beam interact in the HERMES target. Essentially, there is no influence of the HERMES target on the lepton beam at the usual low densities. To remove the synchrotron radiation travelling with the beam, two collimators are positioned upstream of the HERMES spectrometer.

A small asymmetry in the spin-flip amplitudes for leptons when emitting synchrotron radiation in a magnetic dipole field is amplified by the repeated revolutions in the HERA lepton storage ring and enhances the population of the spin state parallel (antiparallel) to the magnetic field for positrons (electrons), resulting in the transverse polarization of the lepton beam, in particular vertically upwards for both electrons and positrons. This effect, known as the Sokolov-Ternov effect [87], allows for a theoretical asymptotic self-polarization of the lepton beam up to 92.4% with a rise time of 37 minutes [88]. Due to the interaction with the proton beam and various other depolarizing effects, the lepton polarization obtained in the HERA storage ring was almost two times lower.

To perform physics experiments with longitudinally polarized lepton beams, the spin direction is rotated by 90°, before the leptons reach the HERMES experiment, to the direction parallel to the lepton beam. This is achieved in a spin rotator, which consists of three consecutive pairs of dipole magnets [89]. The now longitudinally polarized leptons interact with the target gas in the HERMES experiment, or with the proton beam in the collider experiments. The spin direction is rotated back to the transverse direction in a second spin rotator, before the leptons leave the straight section and enter the bending section again. During ther HERA I period until 2001, only one pair of spin rotators was installed, positioned around the HERMES experiment. During this period the asymptotic lepton polarization was typically around 55% with a risetime of 23 minutes [90]. In 2001 spin rotator pairs were installed around the two collider experiments, as part of the HERA II upgrade. After this upgrade, which resulted mainly in an increase of the collider luminosity, the lepton polarization was typically only around 50%, due to the increased beam-beam interactions.

At two locations on the HERA lepton storage ring, the beam polarization is measured continuously. Both polarimeter systems are based on asymmetries in the Compton back-scattering cross section of polarized laser photons from the lepton beam. Downstream from the HERMES experiment, but before the spin rotator, the longitudinal polarization of the leptons is measured. The energy-asymmetry in the Compton cross section is used in the longitudinal polarimeter (LPOL), which will be described in section 3.5. In a straight section without spin rotators, the transverse polarimeter (TPOL) measures the spatial asymmetry of the back-scattered Compton photons. Both polarimeters provide polarization measurements with a statistical precision of approximately 1% and a systematic uncertainty of 1.6% (LPOL) and 3.0% (TPOL).

[5] In DIS reactions the variable x can be interpreted as the fraction of the total momentum of the nucleon that is carried by the struck quark or gluon.

[6] Empty lepton bunches, not necessarily combined with a corresponding empty proton bunch, provide a convenient way of studying background events. However, the real reason for the empty bunches is purely technical: A long bunch-free region is needed for the ramp-up kicker magnets of the proton beam abort system.

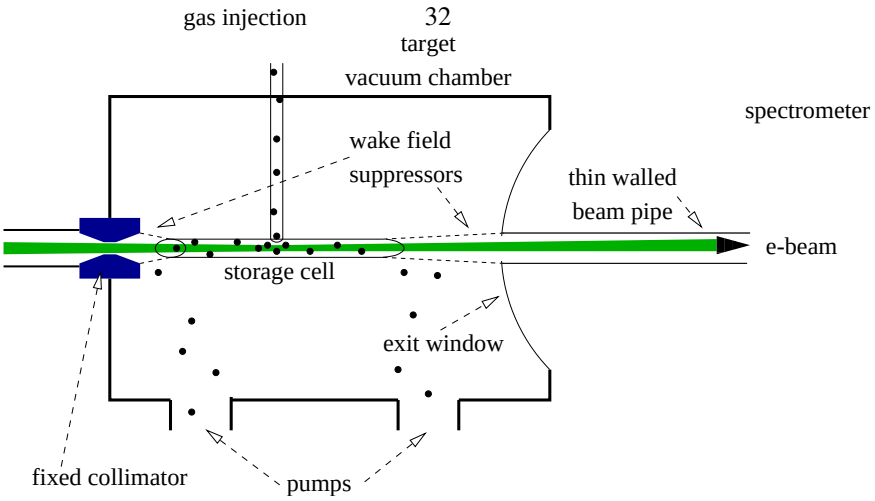

Figure 3.2: Schematic view of the HERMES target system. Taken from reference [91].

3.2 The HERMES target region

The HERMES target consists of a polarized or unpolarized gas in a storage cell internal to the HERA lepton storage ring [92]. A schematic view of the target region is shown in figure 3.2. The target cell is constructed as a 40 cm long, open-ended T-shaped tube that confines the gas atoms in a region around the lepton beam. The gas atoms leak out the ends and are pumped away by a high speed pumping system. The requirement of data collection without significant reduction of the lepton beam lifetime[7] limits the target density. At the end of lepton fills unpolarized high density data are collected with H_2, D_2, ^{3}He, N_2, Xe, or Kr gases, providing a substantial data sample for the study of unpolarized reactions and nuclear effects.

Since the initial commissioning of the HERMES experiment in 1995, several target gases and target polarization states have been used. In 1995, the gas in the storage cell was supplied by an optically pumped, longitudinally polarized $^3\overrightarrow{\text{He}}$ cell. In the period 1996–1997, an atomic beam source (ABS) was used to produce a longitudinally polarized $\overrightarrow{\text{H}}$ target, and in 1998–2000 the ABS was modified for operation with longitudinally polarized $\overrightarrow{\text{D}}$.

In 2001, the target region was modified substantially for the operation with the transversely polarized target gases $\uparrow$H and $\uparrow$D [93]. A magnet providing the transversely oriented holding field for the target gases was installed.[8] The synchrotron radiation generated by the deflection of the lepton beam limited the strength of the magnetic field to approximately 297 mT. The variations in the volume of the storage cell were smaller than $\Delta B_x = 0.60$ mT, $\Delta B_y = 0.15$ mT, and $\Delta B_z = 0.05$ mT. The variations outside of the storage cell volume were larger. The shift of the beam position in the transverse holding field amounts to approximately 2 mm, an effect that can be observed easily in the collected data.

At the end of 2005, the transversely polarized target system was removed. For the recoil data taking period 2006–2007 only unpolarized target gases were needed. To accomodate the recoil detector, the length of the storage cell was reduced to 15 cm. The elliptical cross section of $21 \times 9\,\text{mm}^2$ was unchanged.

3.3 The HERMES spectrometer

The HERMES spectrometer is a forward spectrometer, a design typically used for fixed-target experiments. It consists of several detector components to track and identify scattered and produced particles. The spectrometer is

[7] This is quantified by the requirement of a lepton beam lifetime larger than 45 hours if all other contributions to the lifetime are zero.

[8] A superconducting magnet, with longitudinal field direction, was installed during the years 1998–2000, but the effects of the transverse magnetic field on the tracking of scattered particles are more important.

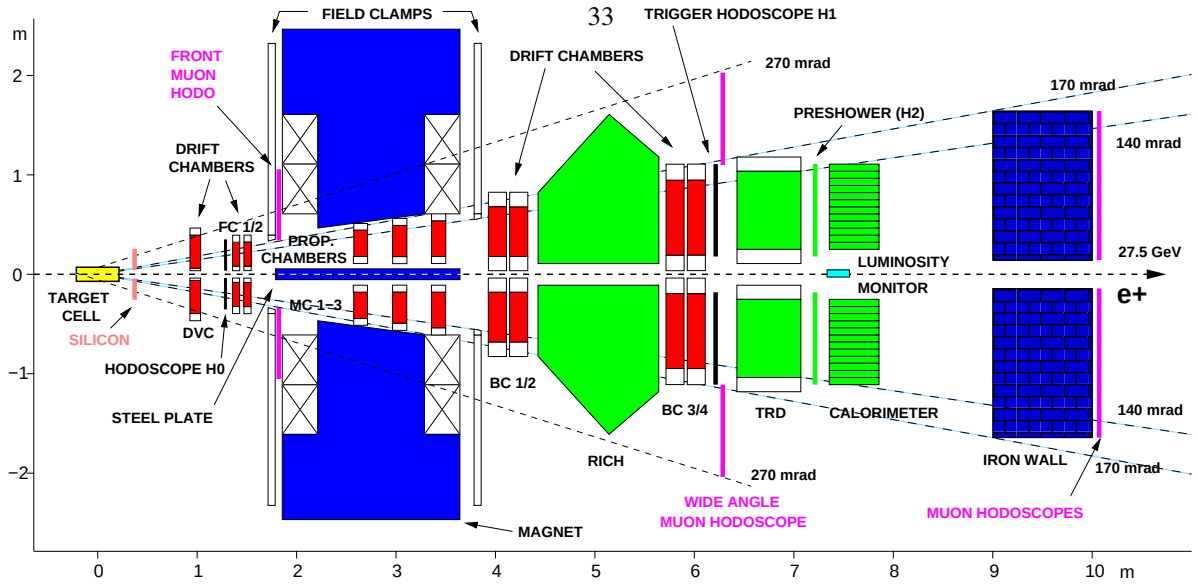

Figure 3.3: Schematic view of the HERMES spectrometer during the years 2002–2005. The target is shown in yellow, the spectrometer magnet in blue, the tracking detectors in red, and the particle identification detectors in green. Taken from reference [91].

described in great detail in reference [91]. In this section, only the detector components most relevant for the analysis of exotic baryons are described in detail.

The central component of the HERMES spectrometer is the H-shaped dipole magnet with an integrated field strength of $1.3\,\mathrm{T}\cdot\mathrm{m}$. In the symmetry plane of the spectrometer, a massive steel plate shields the lepton and proton beams as they pass through the spectrometer magnet, separated by a distance of 72 cm. Inside the shielding of the positron beam pipe, a correction coil corrects for fringe fields and the imperfections of the magnet shielding. The coil also serves to compensate the magnetic holding field of the target system when operating with transversely polarized target gases.

The horizontal symmetry plane defined by the shielding plate inside the spectrometer magnet separates the spectrometer in two identical *top* and *bottom* halves. The steel plate limits the acceptance at small angles in the vertical direction. A schematic side-view of the HERMES spectrometer during the years 2002–2005 is shown in figure 3.3.

The initial trajectory of the scattered particles is determined by the front tracking system, which consists of the front drift chambers (DVC and FC). Behind the spectrometer magnet, the momentum measurement is completed by the back drift chambers (BC). Inside the magnet, proportional chambers (MC) help match the front and back tracks, and allow track reconstruction for low-momentum particles that do not reach the back region.

In the front region, the acceptance for the decay of $\Lambda(1115)$ hyperons was increased in 2001 by the installation of two silicon detectors just downstream of the target region [94, 95]. In the beginning of 2006 a recoil detector was installed, adding acceptance for the recoiling target proton in DVCS events [96]. In the present analysis, these detectors have not been used.

Particle identification (PID) is provided by scintillator hodoscopes (H1 and H2), a transition radiation detector (TRD), a lead-glass calorimeter (CALO), and a ring imaging Čerenkov detector (RICH). The RICH detector identifies pions, kaons, and protons. Combination of the signals in the particle identification detectors allow for a hadron rejection factor of higher than 10^4. Until 1997, before the installation of the RICH detector, a single-gas radiator threshold Čerenkov detector (CER) was installed. The threshold Čerenkov detector allowed only for limited separation of pions from heavier hadrons.

3.3.1 The particle tracking detectors

The particle tracking system is used to determine the event vertex in the target cell and to measure the momentum and the angles of the scattered particles. The momentum resolution is better than 1.3%, and is limited by bremsstrahlung in the walls of the target cell, the vacuum window, and the front tracking detectors. The resolution in the scattering angle is better than 0.6 mrad and limited by multiple scattering in these materials.

The drift vertex chambers (DVC) and the front drift chambers (FC) provide the vertex reconstruction in the target cell and the definition of the scattering angles. The back drift chambers (BC) measure the magnetic deflection and hence the momentum of the detected particles. Proportional chambers inside the magnet (MC) are used for the momentum analysis of low energy decay products that are deflected too strongly to reach the back chambers.

The horizontal length of the drift chambers precluded the use of long horizontal wires. All planes use one of three wire orientations, either vertically (X) or tilted 30° right or left from the vertical axis (U and V).

The drift chambers

The drift chambers DVC, FC, MC, and BC are of the conventional horizontal-drift type. Each layer of drift cells consists of a plane of alternating anode and cathode wires between a pair of cathode foils. The charged particles passing through the detector generate an ionization avalanche, which is detected by the wires spun across the chambers. The chambers are assembled as modules consisting of six layers in three coordinate doublets (UU', XX' and VV'). The X', U' and V' planes are staggered by half the cell size in order to help resolve tracking ambiguities.

To ensure redundancy in the front tracking system and to provide a larger acceptance for muon detection, the drift vertex chamber DVC was constructed and installed after one year of HERMES operation. They are followed by the front chambers FC1 and FC2, providing good spatial resolution immediately in front of the spectrometer magnet.

The three magnet chambers MC are located in the gap of the spectrometer magnet and were originally intended to help resolve multiple tracks in case of high-multiplicity events. Since low backgrounds have made this unnecessary, their primary function is now the momentum analysis of particles with energies below 2 GeV, for example from the decay of the Λ hyperon. With the MCs particle tracks with a momentum as low as 0.5 GeV can be reconstructed.

Finally, the four back chambers BC are located behind the spectrometer magnet.

Track reconstruction

The HERMES track reconstruction program uses a tree-search algorithm for fast track finding and a look-up table for fast momentum determination of the tracks. Except for small curvatures caused by the magnetic fringe fields, the track projections are approximately straight lines outside of the magnetic field region. The basic idea of pattern recognition using the tree-search algorithm is to look at the whole hit pattern of the detectors with increasing resolution. In each step of the iteration, the algorithm checks if the pattern (at a given resolution) contains a sub-pattern that is consistent with an allowed track.

All allowed patterns are generated at the initialisation of the program. They are stored in a database. Because a given pattern at one resolution constrains the number of allowed patterns at a lower resolution, it is possible to reduce the CPU time involved. Symmetry is used to reduce the number of patterns that have to be stored.

To avoid the CPU intensive task of tracking a particle in a magnetic field, a large look-up table is generated during the initialization of the tracking program using the measured magnetic field map. It contains the momentum of a given track as a function of the track parameters in front and behind the magnet.

Transverse magnet correction After the installation of the transversely polarized target in 2001, the existing tracking algorithm was updated to take into account the slight deflection of the scattered particles in the transverse target magnetic field. Two algorithms were developed to perform this correction [97]. The first method (TMC1) is based on a transfer-matrix approach, the second method (TMC2) uses reference tracks. Both algorithms return the corrected, reconstructed interaction point of the track with the lepton beam. For secondary vertices, which are displaced from the lepton beam, these methods are not applicable.

3.3.2 The particle identification detectors

The HERMES particle identification (PID) system discriminates between positrons, pions, kaons, and protons. The PID system consists of four subsystems: two plastic scintillator hodoscopes, a transition radiation detector, a lead-glass calorimeter, and a dual radiator ring imaging Čerenkov detector. The scintillator hodoscopes and the electromagnetic calorimeter are also used in the first level trigger to select which events to consider for further processing.

Forward trigger scintillator (H0)

While technically not a PID detector, the forward trigger scintillator (H0) is located directly upstream of the front drift chamber to eliminate triggers from particle from the proton beam. A backward-going particle produces a pulse that is displaced by 36 ns from the normal trigger condition.

Scintillator hodoscopes (H1 and H2)

A scintillator hodoscope (H1) and a preshower scintillator counter (H2) provide fast trigger signals and information for particle identification. Both hodoscopes are composed of vertical, fast scintillator paddles of 1 cm thick and 9 cm wide with 2–3 mm overlap between each paddle. The scintillation light is detected by photomultiplier tubes coupled with light guides to the outer end of each scintillator paddle. In the passive radiator of the preshower scintillator counter H2, consisting of two radiation lengths of lead, electromagnetic showers are generated. The energy deposit in the scintillator paddles facilitates the discrimination between leptons and hadrons. Positrons typically deposit at least ten times more energy than hadrons, allowing for a pion rejection of 10 for lepton detection.

The scintillator hodoscopes can also be used as a time-of-flight (TOF) particle identification detector for low momentum hadrons [98]. This complements the hadron identification capabilities of the RICH detector (see below). The timing of the output signals in the PMTs of H1 and H2 are measured with respect to the bunch crossing time in the center of the target cell. The path length of each track is calculated from the straight partial tracks in the front region and the back region.[9] To account for differences in cable length, the time-of-flight timings are calibrated with cleanly identified electrons which move essentially at the speed of light. The (squared) mass of hadrons is then extracted from the relativistic momentum

$$p = m\frac{\beta}{\sqrt{1-\beta^2}}, \tag{3.1}$$

where β is the relativistic speed v/c. The squared particle mass obtained from the timing in H1 is shown in figure 3.4 for hadrons with a momentum in the range 0.6–1.1 GeV (left) and 1.5–2.0 GeV (right). Kaon identification is limited to momenta below 1.5 GeV, but pions and protons can be distinguished up to 2.9 GeV with efficiencies (contamination) above 98% and 85% (below 4% and 6%).

Electromagnetic calorimeter (CALO)

The calorimeter provides a first level trigger and measures the energy of electrons, positrons, and photons, but suppresses pions by a factor of more than 1000. It is composed of two times 420 lead-glass blocks of transverse dimensions $9 \times 9\,\mathrm{cm}^2$ and 18 radiation lengths long, viewed from the rear by a photomultiplier tube. Monitoring of aging effect in the glass-blocks is achieved using a dye laser, which sends light through glass fibers to every photomultiplier and a reference photodiode. Combining the preshower hodoscope (H2) with the electromagnetic calorimeter, the pion rejection factor integrated over all energies is approximately $2.5 \cdot 10^3$.

Transition radiation detector (TRD)

The purpose of the transition radiation detector (TRD) is to provide a pion rejection factor of at least 100 at positron energies higher than 5 GeV. At these energies, only electrons and positrons produce transition radiation in the form of X-rays in the 6 cm thick two-dimensional matrix of dielectric fibers. The generated X-rays are detected in proportional

[9] This approximation is adequate because the deflection angle in the spectrometer magnet is only $\pi/20$.

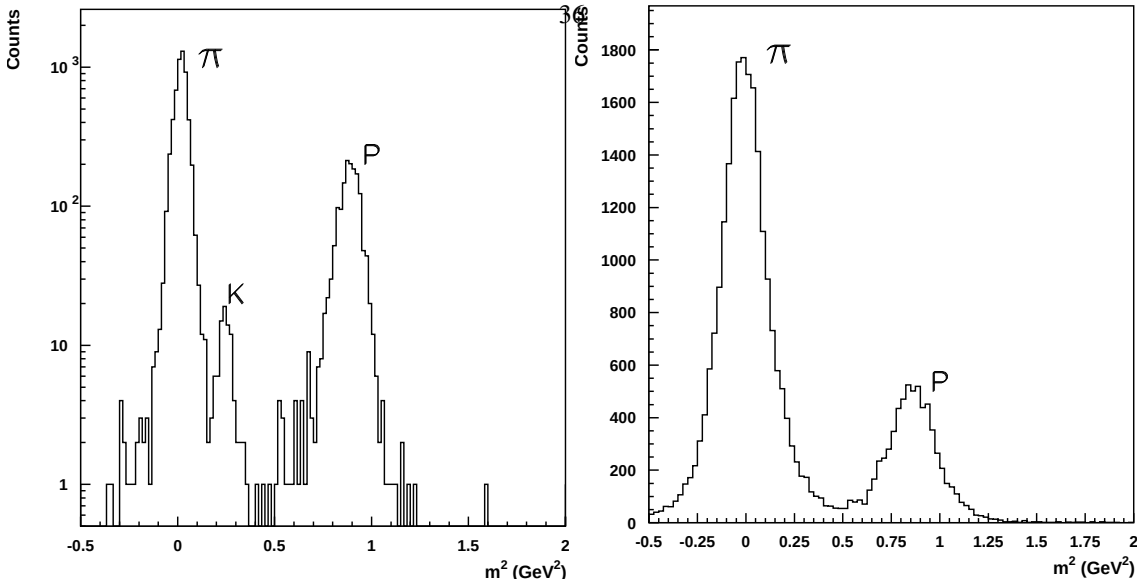

Figure 3.4: Time-of-flight hadron identification with the scintillater hodoscopes H1. Pions, kaons, and protons can be separated in the distribution of the squared mass m^2 for the momentum range 0.6–1.1 GeV (left). For the momentum range 1.5–2.0 GeV pions and protons can be distinguished. Taken from reference [98].

wire chambers. Pions deposit energy directly in the chambers due to ionisation of the chamber gas, but leptons deposit on average twice as much energy in addition to the energy in the X-rays. The average deposited energy of hadrons and leptons is shown in figure 3.5. The pion rejection factor satisfies the design goals, and reaches a value of 80 even below an energy of 5 GeV.

Single gas-radiator threshold Čerenkov counters (CER)

In the original setup of the HERMES spectrometer, used until 1997, pion identification was provided by a pair (top and bottom) of single gas-radiator threshold Čerenkov counters (CER). The Čerenkov counters were located between the back drift chambers, where the RICH was later installed. They were filled with freon, C_4H_{10}, and the produced Čerenkov radiation were detected by an array of 20 spherical mirrors that focus the light on 12.7 cm wide photomultiplier tubes. The momentum threshold was 3.8 GeV for pions, 13.6 GeV for kaons, and 25.8 GeV for protons. The number of detected photoelectrons for a track allows to distinguish between pions and heavier hadrons, but not between kaons and protons.

Lepton-hadron separation

The lepton-hadron separation of the separate detectors can be improved by combining the responses of the transition radiation detector (TRD), the Čerenkov counters (CER), the preshower hodoscope (PRE), and the electromagnetic calorimeter (CALO) using a Bayesian probabilistic approach. For each detector the so-called parent distributions specify the probability $\mathcal{L}^i$ to obtain a specific detector response for a given particle type i. They are determined from the measured responses in each detector using stringent selection requirements on the other detectors. The probability P^i that a given detector response originates in a particle of type i is then defined as

$$P^i = \frac{\phi^i \mathcal{L}^i}{\sum_j \phi^j \mathcal{L}^j}, \tag{3.2}$$

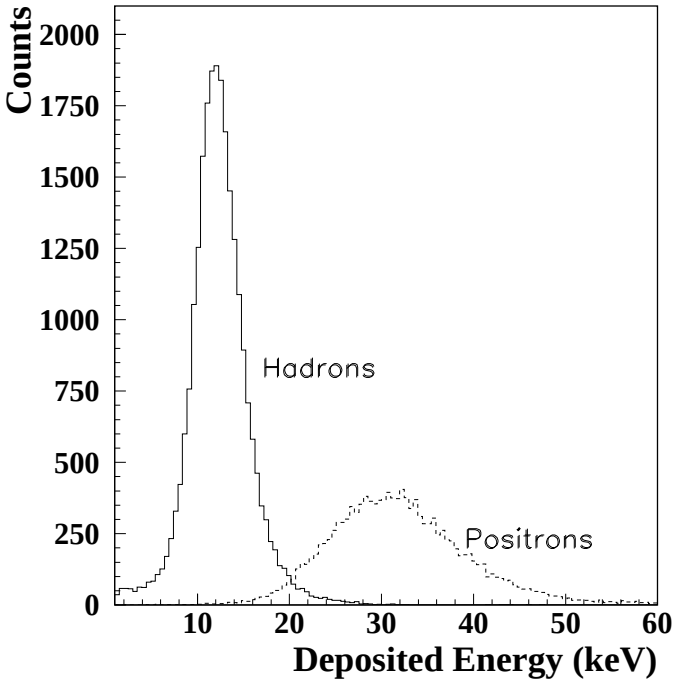

Figure 3.5: The average energy deposited in the transition radiation detector (TRD) by hadrons and leptons, averaged over all momenta. Taken from reference [91].

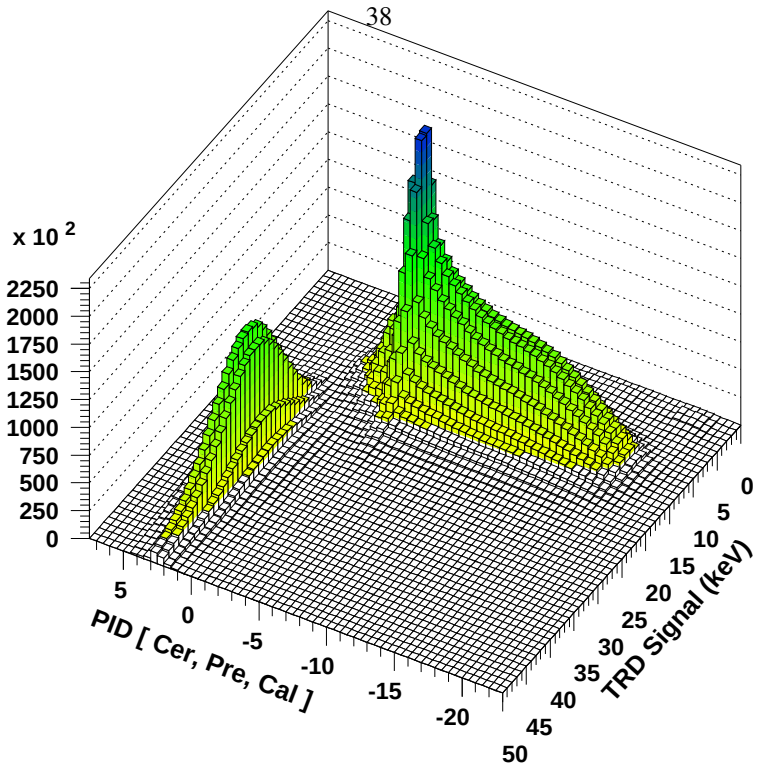

Figure 3.6: The combination of the signals in the Čerenkov counters, preshower-hodoscopes, and electromagnetic calorimeter (left axis) and the deposited energy in the TRD detector (right axis) allows for separation of leptons (left) and hadrons (right) with high efficiency and low contamination. Taken from reference [91].

where the sum runs over all particle types. The flux factor ϕ^i is the *a priori* probability that a track with given track parameters originates from a particle of type i. These flux factors are determined from the collected data with an iterative procedure starting from equal flux factors for all particle types.

The logarithm of the ratio of the probabilities P^h and P^e is calculated for each detector,

$$PID = \log_{10} \frac{P^e}{P^h}. \tag{3.3}$$

The following sums of the particle identification detectors are defined:

$$PID_3 = PID_{CALO} + PID_{PRE} + PID_{CER}, \tag{3.4}$$

$$PID_5 = PID_{TRD}. \tag{3.5}$$

In figure 3.6 the variables PID_3 and PID_5 are shown for events collected by the spectrometer. The separation between leptons (left) and hadrons (right) is clearly visible.

Usually, the sum $PID_3 + PID_5$ is required to be smaller than zero for hadrons and larger than zero for leptons. In hadron samples obtained by requiring $PID_3 + PID_5 < -1$, the probability that a track originated from a hadron is at least 10 times larger than the probability that it originated from a lepton.

Dual radiator ring imaging Čerenkov detector (RICH)

The dual radiator ring imaging Čerenkov detector (RICH) was designed to provide hadron identification for pions, kaons and protons in the momentum range from 2 to 15 GeV. The RICH detector is described in detail in reference [99].

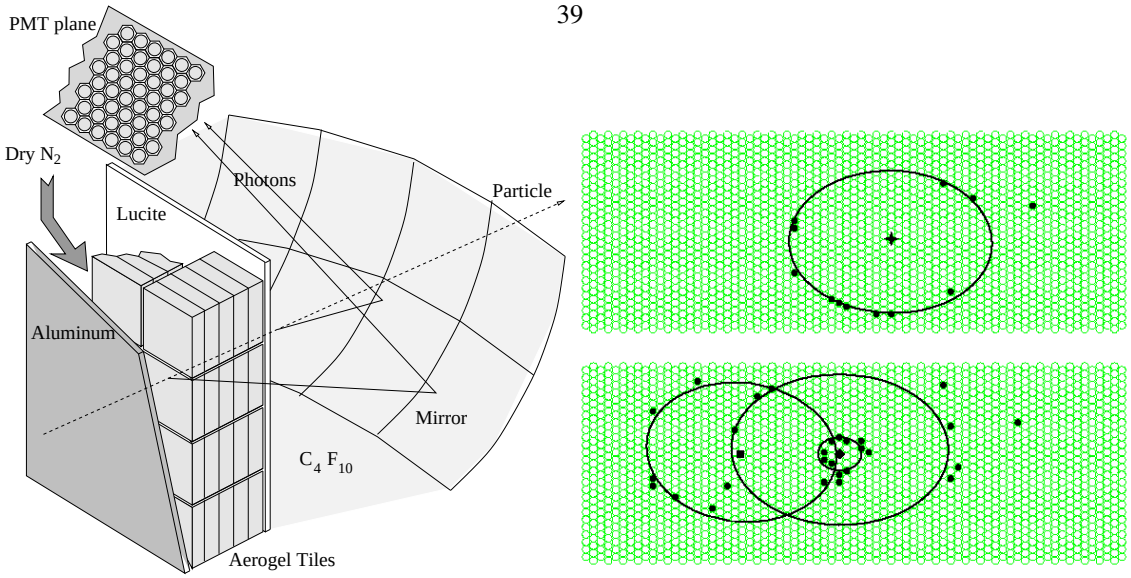

Figure 3.7: The dual radiator ring imaging Čerenkov detector (RICH). A schematic view of the detector setup and radiator configuration is shown in the left panel. The observed hit pattern for a typical three-track event is shown in the right panel. Taken from reference [99].

A schematic view of the detector setup is shown in the left panel of figure 3.7. It uses a wall of silica aerogel radiator tiles and a gas radiator volume with freon, C_4H_{10}, and the whole detector is located in the same location of the previous Čerenkov counter. The charged particles transversing the radiator materials emit Čerenkov radiation in a cone with an opening angle depending on the momentum and the particle type.

A light-weight mirror array was constructed using aluminized epoxy-coated carbon-fiber segments. The light substrate and support structure guarantees that the mirrors contribute negligibly to secondary scattering in the material of the detector. Compared to the freon gas (5% of X_0), the aluminum entrance windows (3.0% of X_0), and the aerogel tiles (2.8% of X_0), the mirrors contribute only 1% of a radiation length X_0. The alignment of the mirror array was determined from the data using a large sample of pions with well-defined gas rings. The additional volume of the RICH detector leads to a worse momentum resolution, reflected in an increase of the reconstructed K_S^0 resonance width from 5.7 MeV to 6.2 MeV [91, 4].

The reflected Čerenkov light, which is emitted mostly at visible wavelengths with a component from the gas radiator in the UV part of the spectrum, is detected in an array of 1934 photomultiplier tubes (PMT) that match the Čerenkov spectrum. The 0.75 inch photomultipliers were arranged in a hexagonal closed packed matrix with a final resolution of $\Delta\theta \approx 7.2$ mrad. To increase the coverage of the photon detector surface from 38% to 91%, the dead space between the photomultipliers was minimized by insterting small aluminized funnels in the entrance cones of the PMTs.

The data of the RICH detector consist of a hit pattern for the top and bottom detector half. An example of a typical three-track event is shown in the right panel of figure 3.7. Only a few photomultiplier tubes generate a signal for every Čerenkov ring. When two or more rings are tangent, this can lead to ambiguities.

From the radius of the ring the opening angle θ_c of the Čerenkov cone is determined. Together with the particle momentum p this allows particle identification. In the left panel of figure 3.8 the opening angles θ_c for pions, kaons, and protons for radiation generated in either of the radiators are shown as a function of the momentum. Due to their low mass the electrons or positrons always generate a Čerenkov cone with the asymptotic opening angle.

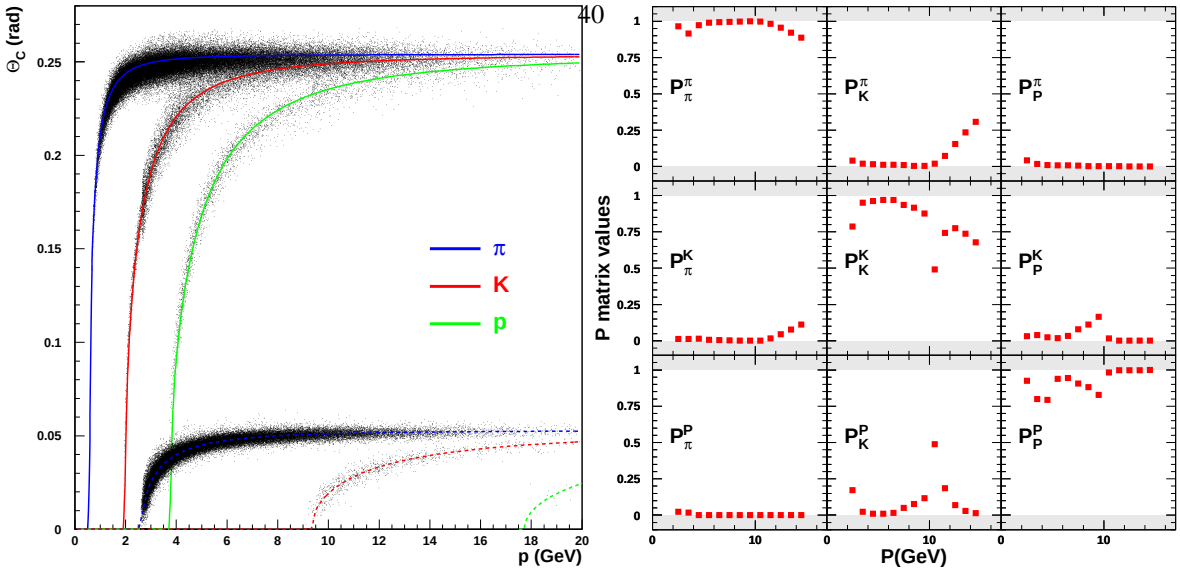

Figure 3.8: The dependences of the Čerenkov angle θ_c on the hadron momentum p (left) for the aerogel tiles (top curves) and C_4F_{10} gas radiators (bottom curves) are used to identify the hadrons. The identification efficiencies P_i^j for the identification of a hadron i as type j are shown in the right panel as a function of the hadron momentum. Taken from reference [99].

Hadron identification

After the separation of hadrons and leptons, the hadrons are identification by the opening angle of the Čerenkov cone in the RICH detector. As in the algorithm for the hadron-lepton separation, a likelihood is assigned for every particle type given the detector response. The particle is identified as the type with the largest likelihood. The logarithmic ratio between the largest likelihood P^1 and second largest likelihood P^2,

$$Qp = \log_{10} \frac{P_1}{P_2}, \tag{3.6}$$

is defined as a quality parameter for the type assignment.

A recent addition to the RICH particle identification algorithm is the determination of event-level likelihoods. All the combinations of particle assignments for all tracks in one detector half are considered in this approach, instead of handling each track separately. The ambiguities occurring when multiple Čerenkov cones overlap at the edges can be reduced in this approach. This improvement of the particle identification capabilities of the HERMES spectrometer is in particular relevant to processes with multiple hadrons in one detector half.

3.3.3 The trigger and readout system

The HERMES spectrometer is equipped with a single level event trigger system. The full readout of the spectrometer can be initiated by one of several trigger signals. Apart from physics triggers for the detection of physical processes, several trigger signals are generated for calibration and monitoring of the detectors. An example is the gain monitoring system (GMS) trigger which generates signals at a rate of approximately 3 Hz, synchronized with a laser pulse to the scintillator paddles and calorimeter blocks of the spectrometer. This trigger is generated during a (lepton) bunch-free period to avoid any effects from the lepton beam on the calibrations. Redundancy of the physics triggers allows for the calculation of the detector efficiencies.

After a trigger signal has been generated, the detector is read out and unable to record new events until the readout process is finished. This period of time is called the dead-time. A balance has to be found between high trigger

rates and acceptable dead-times. Before the installation of the Lambda Wheels and the recoil detector, the HERMES spectrometer was usually operated at trigger rates of 500 Hz with a dead-time of 10%. Due to the increase in event size associated with the large number of channels, the trigger rate was more than two times lower in the period 2002–2007.

The most important physics trigger for the HERMES experiment is the DIS trigger, which indicates coincident signals in the three scintillator hodoscopes and an energy deposit in two adjacent columns of the electromagnetic calorimeter exceeding an adjustable threshold. During normal low-density data taking the calorimeter energy threshold is set to 1.4 GeV, but to reduce the dead-time the threshold is increased to 3.5 GeV during high-density data taking. For DIS events, which always have a high energetic lepton, this change is irrelevant, but for the detection of hadrons with low energies it reduces the efficiency during high-density data taking.

The photoproduction trigger, which is relevant for the analysis of exotic baryons, is formed by a coincidence of the three scintillator hodoscopes with two tracking planes, requiring that at least one track appeared in each of the spectrometer halves. At the end of 2003, an additional 'pentaquark' trigger was implemented formed by two independent coincidences in the three scintillator hodoscopes of one spectrometer half and one coincidence in the scintillator hodoscopes of the other spectrometer half, combined with hits in the tracking planes of both halves. The efficiency of this last trigger was unfortunately rather low, due to the requirement of three tracks in the spectrometer. Monte Carlo studies showed that the width of the tracking detector segments reduced the efficiency for more than one hit in the tracking detectors by an additional 25%.

3.4 Monte Carlo simulations at the HERMES experiment

The HERMES spectrometer is a forward detector and does not cover the full 4π geometrical acceptance (in the center of mass frame of the decaying resonance) in which resonance cross sections are usually specified. Also the selection criteria necessary to resolve resonances reduce the number of observed decay events. To determine the combined effects of the detector acceptance and selection efficiency we use Monte Carlo simulations. Two different Monte Carlo generators are used in this work.

3.4.1 The gmc_dcay Monte Carlo generator

The toy Monte Carlo generator gmc_dcay, developed at the HERMES experiment, is used to simulate pure samples of decay events for one resonance only. With the gmc_dcay generator, single resonance decay events are generated with an invariant mass distributed according to a Breit-Wigner function with intrinsic width Γ around the resonance mass M. The simulation takes into account the distributions of initial transverse and longitudinal momentum P_t and P_z of the resonance. The initial momentum distributions, which are determined by the production mechanisms of the resonance, can be specified using the parameters of an internal model, or they can be generated according to distributions obtained from other sources.

The internal model of the gmc_dcay generator is based on hyperon production in the fragmentation region and consists of a Gaussian distribution for the transverse momentum P_t, and a monotonically falling distribution for the longitudinal momentum P_z. The transverse and longitudinal momentum distributions are in agreement with what is observed for the $\Lambda(1115)$ hyperon at the HERMES experiment.

3.4.2 The PYTHIA Monte Carlo generator

The PYTHIA Monte Carlo generator [100], tuned to describe the results observed at HERMES kinematics [101, 102, 103], can also be used to simulate hyperon decays (though not all hyperons are implemented in the PYTHIA generator). The PYTHIA generator simulates a wide range of processes, but only a small fraction of the simulated events are relevant for the determination of the efficiency. Most of the simulated events are outside the detector acceptance, or are discarded by the selection criteria.

The computational load to obtain a large sample of simulated events satisfying the selection criteria is much higher with the PYTHIA generator than with the gmc_dcay generator. The advantage of using the PYTHIA generator is that the production mechanism of the generated resonances, and thus the momentum distributions of the resonances before their decay, is simulated in detail. The PYTHIA generator is often used to generate realistic inital momentum

distributions (in 4π acceptance) for the simulated resonance, which is then used as input for gmc_dcay simulations. PYTHIA simulations are also used to cross-check the order of magnitude of the efficiency determined in the gmc_dcay simulations.

After the generation of the resonance decay events, the decay products are tracked through a full GEANT model of the HERMES spectrometer. The interactions of the particles with all materials of the detector are simulated, as well as the responses in the detector components. The resulting Monte Carlo events are written to files that have the same format as regular data files, and can be treated with exactly the same analysis code as the collected data.

3.5 The Longitudinal Polarimeter

As mentioned before, one of the characteristic properties of the HERA lepton storage ring is the large transverse self-polarization of the lepton beam. The demonstration that this large transverse polarization could be achieved and accurately measured was part of the requirements for the approval of the HERMES experiment in 1992. The transverse polarimeter (TPOL) was commissioned in the West straight section in 1991. After the installation of a pair of spin rotators around the HERMES experiment, the longitudinal polarimeter (LPOL) was commissioned in the East straight section in 1996, at a location before the spin orientation of the leptons is rotated back from the longitudinal to the transverse direction, and has since then provided an independent measurement of the polarization of the leptons until the end of HERA operation in June 2007.

Both polarimeter systems make use of asymmetries present in the cross section for Compton back-scattering of photons from an intense circularly polarized laser beam. The TPOL measures the small transverse spatial asymmetry ($\approx 60\,\mu$m) between the Compton photons from left and right circularly polarized laser photons to determine the transverse polarization. The TPOL system is described in detail in reference [104]. In the main mode of operation the LPOL measures the integrated energy asymmetry between Compton photons from left or right circularly polarized laser photons. In this section the LPOL system is described (although a detailed description of the longitudinal polarimeter can be found in reference [90]), and the experience in the operation of this system is used to suggest a possible setup for the lepton polarization measurement at the proposed electron-ion collider (EIC).

3.5.1 Polarization build-up

Due to the Sokolov-Ternov mechanism [87], based on the small asymmetry in the spin-flip amplitudes of leptons when emitting synchrotron radiation, the transverse polarization $P(t)$ builds up in time according to the expression

$$P(t) = P_\infty \left(1 - e^{-t/\tau}\right). \tag{3.7}$$

The asymptotic polarization P_∞ is approached with an exponential rise-time τ, determined by the characteristics of the storage ring. In the absence of any depolarizing effects the maximum achievable polarization, obtained in a planar storage ring, is $P_{\infty,th} = 92.4\%$, with a rise-time of $\tau_{th} = 37$ min for the HERA lepton storage ring with an energy of $E_e = 27.5$ GeV [88]. The inherent non-flatness of a storage ring with spin rotators, and other depolarizing effects can reduce the asymptotic polarization significantly. At the HERA storage ring the asymptotic polarization was typically only 55%.[10] Associated is a decrease of the rise-time, given by the expression

$$\tau = \tau_{th} \frac{P_\infty}{P_{\infty,th}}, \tag{3.8}$$

to approximately 23 min.

A small number of filled lepton bunches are synchronized with an empty proton bunch at the interaction points of the collider experiments. Consequently, the polarization of these non-colliding bunches is not affected by the depolarizing beam-beam interaction, usually resulting in a higher polarization. Normally less than ten non-colliding lepton bunches are present, compared to almost 180 colliding bunches. Since the depolarizing effects are different

[10] The average polarization during the HERA I running period until the luminosity upgrade in 2001 was approximately 55%, but due to the increased beam-beam interaction during the HERA II running period the polarization was approximately 5% lower.

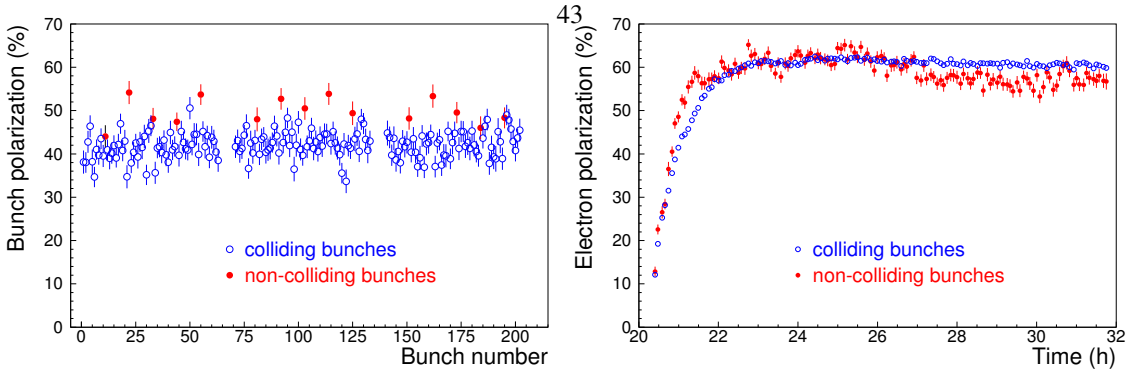

Figure 3.9: Individual and averaged polarization for colliding and non-colliding bunches. In the left panel the measured polarization for the individual lepton bunches is shown. In the right panel the bunch polarization is averaged and shown as a function of time. The two panels were obtained during different fills. Taken from reference [90].

for colliding and non-colliding bunches, the polarization build-up behavior is different for both subsets. For a typical lepton fill the polarization for colliding and non-colliding bunches is shown in figure 3.9. In the left panel the measured polarization for the individual bunches is shown; in the right panel the polarization during a different fill is averaged separately over all colliding and non-colliding bunches and shown as a function of time.

Measurements of the rise-time and the asymptotic polarization can be used to determine the absolute scale of the polarimeters, when the theoretical values for $P_{\infty,th}$ and τ_{th} are known [104]. This is usually done with non-colliding bunches only to avoid the depolarizing effects from the proton beam. The theoretical uncertainties associated with the value of $\frac{\tau_{th}}{P_{\infty,th}}$ in a non-flat storage ring are only understood to a few percent, and have to be determined from computational models and simulations. This method of calibration of the absolute scale also requires an unperturbed machine during the polarization build-up, a situation which in practice requires the use of depolarizing resonance or of an accelerator tune shift after the normal injection procedure. Accurate timing and non-zero initial polarization levels can both complicate the calibration procedure. Nevertheless this procedure was successful in estimating the absolute scale of the TPOL with one pair of spin rotators [104].

3.5.2 Polarized Compton scattering and Compton polarimetry

Compton scattering is the physical process of scattering a photon from a charged particle. For our purposes the charged particle is a lepton in the HERA storage ring, which collides nearly head-on with a laser photon and scatters it back in the direction of the high-energetic lepton. The following kinematic variables are useful in the discussion of Compton scattering [105]. The incident photon with momentum k is scattered off the incoming lepton with energy E_e. The outgoing photon has a momentum $k' \gg k$, and the energy of the outgoing lepton is now E'_e. Due to the large Lorentz factor, $E_e/m_e = 5.4 \cdot 10^4$ for the HERA lepton energy, the scattered photon and lepton are boosted forward to very small angles in the laboratory reference frame, and leave the interaction point practically parallel to the lepton beam. The maximum achievable Compton photon energy k'_{max} is referred to as the Compton edge.

The differential cross section for the Compton scattering of circularly polarized photons from longitudinally polarized leptons is given by

$$\frac{d\sigma}{dk'} = \frac{d\sigma_0}{dk'} \left[1 - P_\lambda P_e A_z(k')\right]. \tag{3.9}$$

In this expression $\frac{d\sigma_0}{dk'}$ is the unpolarized Compton cross section, P_λ the circular polarization of the incident photons, P_e the longitudinal polarization of the lepton beam, and $A_z(k')$ the longitudinal asymmetry function of the cross sections for left and right circularly polarized photons as a function of the energy k' of the back-scattered Compton photon.[11] In the LPOL system the circular polarization of the incident laser light is to very good approximation $P_\lambda \approx 100\% \cdot \lambda$, with alternating helicity $\lambda = +1$ for right and $\lambda = -1$ for left circularly polarized laser light. This corresponds to

$S_3 = \pm 1$ when expressed with the Stokes vector. Together with the helicity $\pm\frac{1}{2}$ for the leptons, the total spin for antiparallel and parallel helicities is then $\frac{1}{2}$ or $\frac{3}{2}$, respectively.

In the LPOL system the crossing angle of the laser beam and the lepton beam is 8.7 mrad, or almost head-on. The laser photons with an energy $k = 2.33\,\text{eV}$ collide with the leptons in the HERA storage ring with an energy $E_e = 27.5\,\text{GeV}$. For these kinematic conditions the Compton edge is $k'_{max} = 13.6\,\text{GeV}$. The future electron-ion collider will likely operate at lower lepton energies $E_e \approx 10\,\text{GeV}$, corresponding to lower values of the Compton edge, which scales as $k'_{max} \sim k \cdot E_e^2$.

For perfect head-on collisions the differential Compton cross section is shown in the top panels of figure 3.10. In the left panels the incident laser photons have an energy $k = 2.33\,\text{eV}$ and the lepton energy E_e is varied. The right panels were obtained for different values of the incident laser photon energy k but with a fixed lepton energy $E_e = 27.5\,\text{GeV}$. The bottom panels of figure 3.10 present the asymmetries of the cross sections shown in the top panels. The maximum asymmetry is reached at the Compton edge k'_{max}. For lower lepton beam energies E_e the asymmetry decreases as $A_{max} \sim k \cdot E_e$, but higher photon energies can be used to compensate for this effect.[12]

In the LPOL system, two alternative methods for the measurement of the polarization can be used exclusively. In a *differential polarization measurement* (or single-photon mode) the energy of every scattered Compton photon is measured, event by event. For each photon energy bin the asymmetry in the number of Compton photons $d\sigma$ is exploited to determine the polarization

$$A_s(k') = \frac{d\sigma_{\frac{1}{2}} - d\sigma_{\frac{3}{2}}}{d\sigma_{\frac{1}{2}} + d\sigma_{\frac{3}{2}}} = P_e P_\lambda A(k'). \tag{3.10}$$

The lepton polarization is then determined as the weighted mean over all photon energy bins k'. An advantage of this method is that the large asymmetry at the Compton edge can be exploited. Together with the asymmetry zero-crossing point, the Compton edge is one of the two characteristic locations with a well determined energy that can be measured in the energy spectrum. This allows for a calibration of the energy scale of the detector. However, in addition to the Compton photons, synchrotron and bremsstrahlung photons will be detected, dominating the energy spectrum at lower energies. A major disadvantage of this method in the LPOL system is the low counting rate. Since the laser is pulsed at only 100 Hz and the intensity has to be reduced to ensure that only one interaction occurs per bunch crossing, it takes an impractically long time to accumulate the required number of events for a precise polarization measurement.

In an *energy-weighted integrated polarization measurement* (or multi-photon mode) the polarization is determined from the integrated asymmetry of the Compton cross section, weighted with the scattered photon energy k'. At high laser intensity a large number of Compton reactions take place during one bunch crossing. More than 1000 Compton photons are produced for every bunch crossing in the LPOL interaction region. Their energy k' is distributed according to $\frac{d\sigma}{dk'}$, as shown in the top panels of figure 3.10. The energy deposition in the detector is distributed according to the weighted cross section $k'\frac{d\sigma}{dk'}$, as shown in the left panel of figure 3.11,[13] and increases the asymmetry at higher scattering energies k' relative to low scattering energies. When the response I of the detector is proportional to the sum of the scattered photon energies, *i.e.* it integrates the Compton spectrum weighted with the energy, then the experimental energy asymmetry

$$A_m = \frac{I_{\frac{1}{2}} - I_{\frac{3}{2}}}{I_{\frac{1}{2}} + I_{\frac{3}{2}}} = P_e P_\lambda A_P \tag{3.11}$$

can be used to determine the lepton polarization P_e. The analyzing power A_P of the process is determined analytically by integrating the distribution of the scattered photon energy for left and right circularly polarized incident photons, under the assumptions that the Compton photon detector is linear over the full operating range and that $P_e P_\lambda = 1$. In the right panel of figure 3.11 the analyzing power A_P is shown as a function of the lepton beam energy and for three different incident photon energies. The intersection of the dashed vertical line at the HERA energy of 27.5 GeV with the curve for green incident laser light corresponds to the working point of the LPOL system.

[11] The sign of the longitudinal asymmetry function $A_z(k')$ differs from the convention used in reference [105].

[12] This ignores the problems that exist with operating a high-power UV laser optical system and the reduced differential cross section.

[13] For antiparallel lepton and photon helicities (spin $\frac{1}{2}$) the energy-weighted differential cross section $k'\frac{d\sigma}{dk'}$ is independent of the lepton energy E_e and the incident photon energy k.

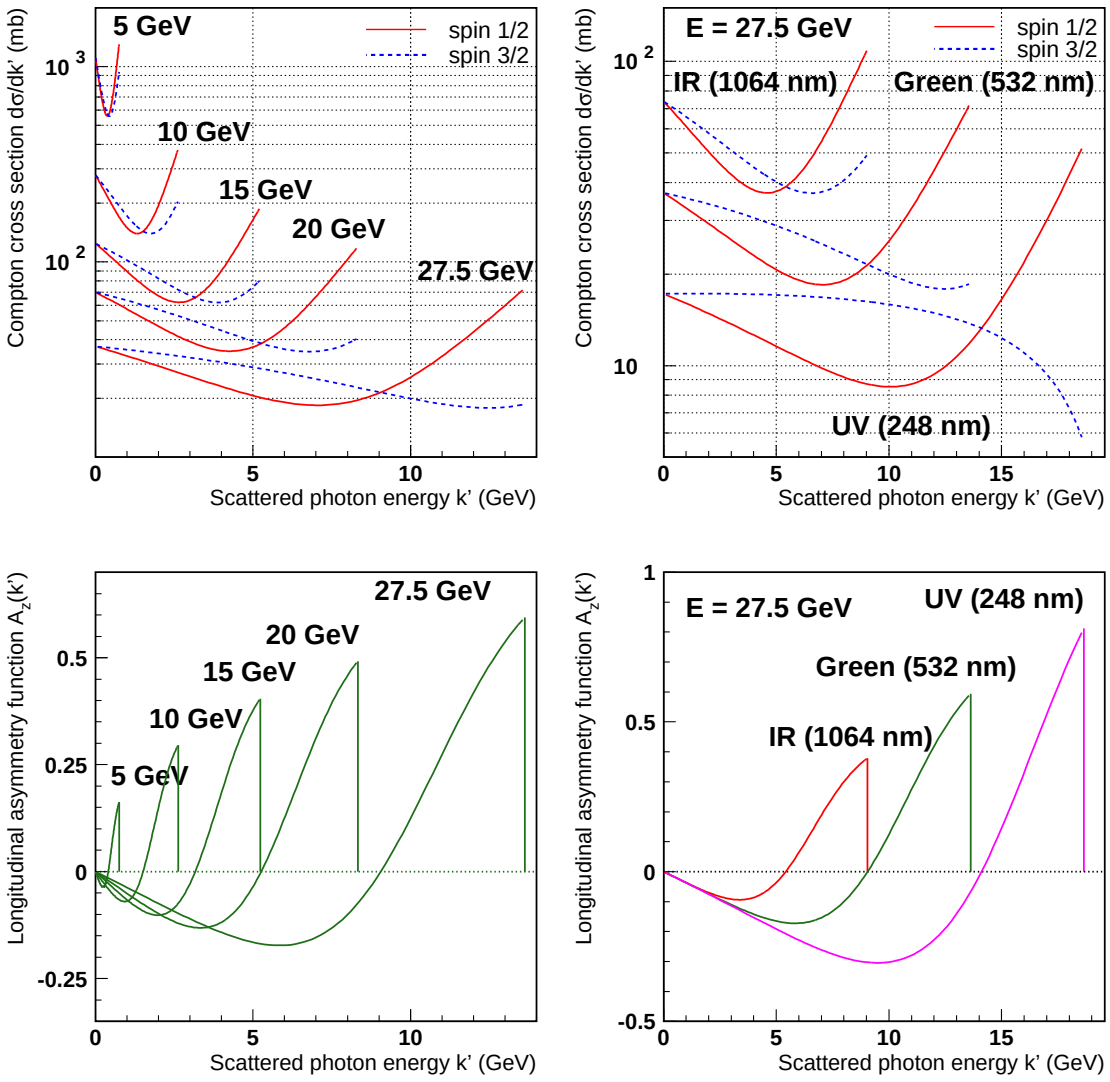

Figure 3.10: The differential Compton cross section $\frac{d\sigma}{dk'}$ (in the top panels) and longitudinal asymmetry function $A_z(k')$ (in the bottom panels) for antiparallel (spin $\frac{1}{2}$) and parallel (spin $\frac{3}{2}$) lepton and photon helicities. In the left panels the photon energy is fixed at 2.33 eV or 532 nm and different lepton beam energies are shown. In the right panels the laser photon energy is varied and the lepton beam energy fixed at 27.5 GeV.

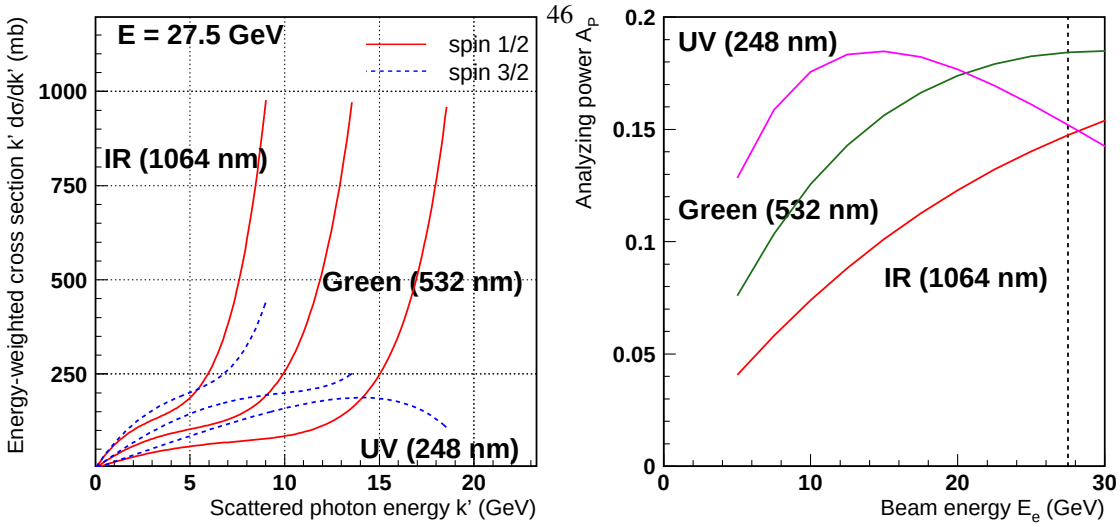

Figure 3.11: The energy-weighted differential Compton cross section $k' \frac{d\sigma}{dk'}$ and the integrated energy-weighted Compton asymmetry A_P. When the energy-weighted differential Compton cross sections for antiparallel (spin $\frac{1}{2}$) and parallel (spin $\frac{3}{2}$) lepton and photon helicities at the HERA energy $E_e = 27.5\,\text{GeV}$ in the left panel are integrated over the scattered photon energy k', the analyzing power A_P is obtained. The working point for the LPOL system is at the intersection of the dashed vertical line with the curve corresponding to green laser light in the right panel.

The number of synchrotron or bremsstrahlung photons from a single bunch is small compared to the large number of Compton photons, and their effect can be neglected. The drawback of an energy-weighted integrated polarization measurement is the importance of the linearity of the detector; deviations from linearity change the weighting and a different value of A_P would have to be determined.

Until 2006 the LPOL system was routinely operated in the multi-photon mode, with the single-photon mode reserved for tests and energy scale calibrations. With the installation of a laser cavity around the lepton beam line and the commissioning of this LPOL-Cavity project, the sampling calorimeter (see below) was often operated in the single-photon mode. Due to the continuous wave mode of the cavity laser system, the event rate was much higher than with the regular LPOL system. Unfortunately the goal of routine data taking with the LPOL-Cavity system was never reached.[14]

3.5.3 The LPOL system

The main components of the LPOL system are a high-power pulsed laser system with associated optics shown in figure 3.12, a laser transport system to guide the laser beam to the interaction region shown in figure 3.13, and two interchangeable calorimeters for the measurement of the Compton photon energy.

The laser and optical system

In figure 3.11 it was shown that, at a lepton beam energy of $E_e = 27.5\,\text{GeV}$, the green laser photons (with an incident energy of $k = 2.33\,\text{eV}$) have a maximum analyzing power $A_P = 0.1838$, which motivates the choice for this type of laser in the LPOL system. The pulsed, frequency-doubled Nd:YAG laser with a wavelength of 532 nm (corresponding to a photon energy of $k = 2.33\,\text{eV}$) is located in the laser hut, six floors above the lepton storage ring.

[14] The LPOL-Cavity project was designed and commissioned completely independent of the regular LPOL system, without involvement of members of the LPOL group.

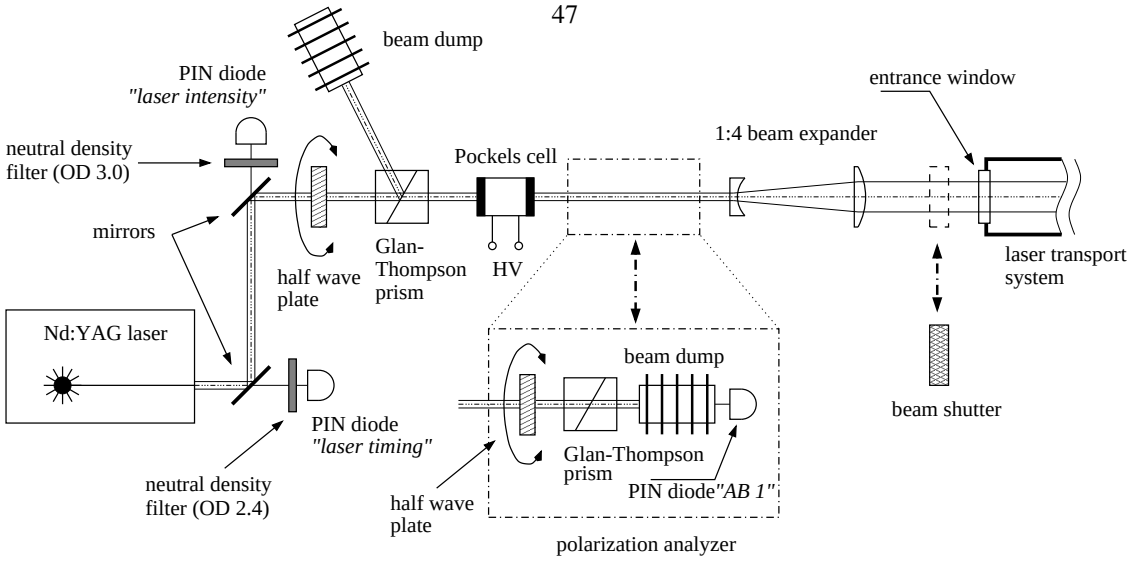

Figure 3.12: Schematic view of the LPOL laser optics in the laser hut. Taken from reference [90].

This choice of location was made to allow for easy maintenance of the laser system.[15] The laser pulses with a length of approximately 3 ns are fired at a rate of 100 Hz with a pulse energy of 200 mJ. The linearly polarized laser light is transformed in circularly polarized laser light in a Pockels cell (PC). The PC is a crystal cell whose birefringence can be changed by applying a voltage (of approximately 1700 V for our system). The voltage on the PC is reversed for every pulse, generating alternating pulses of left and right circularly polarized laser light. The circular polarization is maximized by scanning over the voltage range, but care is taken to have equal laser polarizations for left and right helicity states. A misalignment of the PC can lead to spatially displaced left and right circularly polarized laser beams, which can affect the location of the interaction point, or to large voltage differences for left and right polarization, which leads to early degradation of the PC. Therefore a careful aligment procedure is applied.

To traverse the distance of 80 m between the laser system and the interaction point in the HERA tunnel, the laser is guided in a vacuum system.[16] Before the beam enters the transport system, the beam is expanded to decrease the energy density on the optical elements and to reduce the effects of any irregularities on the optical surfaces. In the laser transport system remotely controlled phase-compensated mirrors with CCD-cameras mounted behind them are used to monitor and align the laser beam position.

Any depolarizing effects of the transport system are detected by a remotely-controlled polarization analyzer located after the interaction point with the lepton beam in the HERA tunnel (see figure 3.13). This analyzer system consists of a rotatable half wave plate and a Glan-Thompson prism. The reflected and transmitted laser beams are detected in photodiodes. Comparing the measured polarization in the analyzer in the tunnel with a similar analyzer located directly behind the Pockels cell (see figure 3.12) allows to determine any depolarizing effect. Problems with the alignment of the optics in the analyzer box in the tunnel rendered the system useless for absolute measurements, but it allowed to monitor changes in the polarization between manual measurements during exclusive accesses to the tunnel.

At the interaction point the laser pulses are focused to a transverse size of approximately 0.5 mm by guiding the laser beam parallel to the vacuum pipe in exclusive access mode. With an accuracy of approximately 1 m the focusing point is placed at the expected interaction region where lepton beam position monitors are located.

[15] The laser has operated reliably during the many years it was in operation. The monthly replacement of the laser flash lamp, responsible for building up the population inversion in the Nd:YAG-doped crystals, was greatly facilitated by the easy access to the laser system.

[16] The vacuum system has several uses. It provides a closed path to the interaction point, necessary for the safe transportation of a high-power laser beam, with detection of intrusion based on the air pressure inside. Moreover, it ensures a clean environment for the optical elements in the laser path. Lastly, air flows between the laser system and the interaction point, caused by unequal heating, could influence the laser alignment.

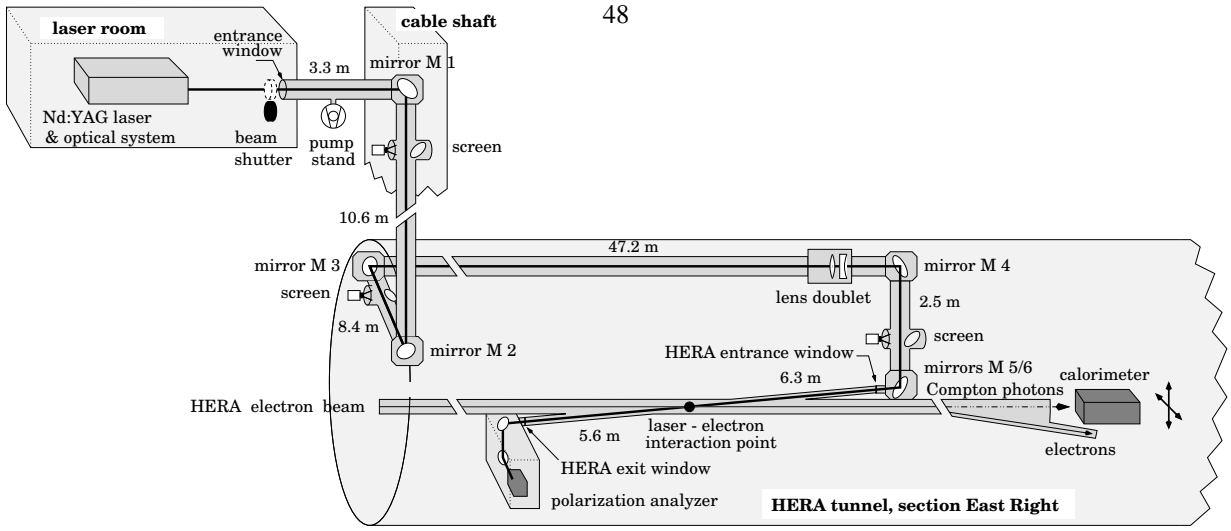

Figure 3.13: Schematic view of the LPOL laser transport system. Taken from reference [90].

For every laser pulse the intensity and the timing are measured with photodiodes in the laser hut. The timing jitter between the laser trigger signal, generated in the electronics trailer on the ground floor of the East Hall, and the actual laser pulse is approximately ± 1.5 ns. Because the the 3 ns long laser pulse is much longer than the lepton bunch, the leptons sample the different regions of the laser pulse. The laser intensity is not constant for the duration of the laser pulse. The timing information from the photodiode and the corresponding response from the PMTs are used to determine the laser pulse profile, as shown in figure 3.14. The signals are then normalized for the actual laser intensity at the moment of the interaction.

Compton photon detection

Two different calorimeters were routinely used to measure the energy of the Compton photons. The original crystal calorimeter is based on the generation of Čerenkov light in crystals; a newer sampling calorimeter was constructed using alternating plates of radiator and scintillator material. The two calorimeters are positioned on a remotely controlled table that allows for horizontal and vertical alignment with respect to the Compton photon cone. By moving the table up and down, an operation that takes only minutes, either of the two calorimeters can be selected for the measurements.

The theoretical value for the analyzing power A_P with a perfectly linear photon detector is 0.1838, but non-linearities in the detector can change this value. Due to shower leakage to the rear end of the calorimeter, the analyzing power of the crystal calorimeter is 0.1929. This value was determined from measurements in a test beam at CERN, and later confirmed by Monte Carlo simulations [106].

The crystal calorimeter The crystal calorimeter (CR) consists of a 2×2 array of $22\,\text{mm} \times 22\,\text{mm}$ radiation-hard $NaBi(WO_4)_2$ crystals with a length of 20 cm (19 radiation lengths), which are optically separated and each read out by a photomultiplier tube (PMT). When a Compton photon exits the HERA beam vacuum, it enters the crystal calorimeter through a set of two lead plates (each with a thickness of 1.1 radiation length). An additional tungsten plate was added before the lead plates after synchrotron radiation emerging from the transversely polarized HERMES target destroyed the crystals in 2004. The charged particles in the electromagnetic shower generated in the lead plates and the crystals emit Čerenkov radiation which is detected in the PMTs. After normalization for the different PMT gains the distribution of the deposited energy is used to automatically center the Compton photon beam with sub-millimeter precision on the calorimeter.

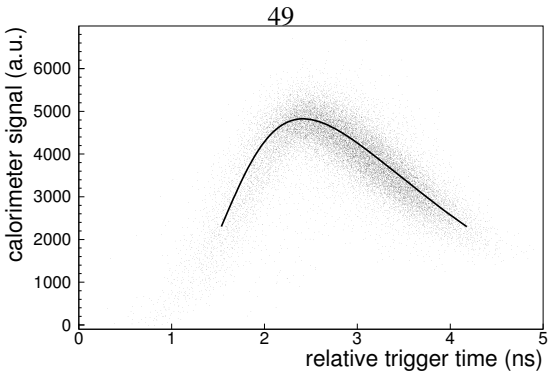

Figure 3.14: The laser pulse profile sampled by the lepton bunches. Due to the jitter in the laser triggering, the much shorter lepton bunches sample different time slices of the laser pulse, resulting in different average intensities in the photomultiplier tubes. The reconstructed laser pulse profile is used to normalize the laser intensity at the moment of the interaction. Taken from reference [90].

The sampling calorimeter The sampling or sandwich calorimeter (SW) is composed of 24 layers of 2.6 mm thick 20 mm $\times$ 20 mm plastic scintillator material, alternated between 3 mm thick layers of tungsten. On the four sides wavelength shifters and light guides transport the generated light to one photomultiplier tube (PMT) behind the stack of plates. The sampling calorimeter is not position-sensitive, but is independent of the energy within 5% for Compton cone positions up to 12 mm removed from the center. The custom-made PMT was designed to be linear over a very wide dynamic range, allowing the same detector to be used in single-photon mode at high gain and in multi-photon mode at low gain. Except for the years 2006 and 2007, the sampling calorimeter was used only occasionally, as an independent test of the crystal calorimeter. To avoid radiation damage by synchrotron and bremsstrahlung photons it was usually kept out of the cone of Compton photons. In 2006 and 2007 the sampling calorimeter was used in the single-photon mode in conjunction with optical cavity around the lepton beam as part of the LPOL-Cavity project.

Both calorimeters experienced small problems with radiation damage. In 2004 an accidental beam loss in the neighborhood of the crystal calorimeter destroyed the four crystals. The scintillator plates of the sampling calorimeter were replaced approximately once per year, even though usually only some plates exhibited slight signs of radiation damage.[17]

Data acquisition

The data acquisition cycle of the LPOL is limited to 200 Hz, twice the rate at which the laser can be fired. For the measurement of the polarization of one lepton bunch, four events are considered. During the first two events the Pockels cell is set for one helicity; the next two events are collected with the opposite helicity. For one of the two events at a particular helicity the laser is fired, during the other event the laser stays off and no Compton photons are expected. For the next lepton bunch this procedure is repeated. The helicity selection of the Pockels cell thus alternates between left and right at a frequency of 100 Hz, and a signal is digitized alternatingly for laser on and laser off at 200 Hz.

The response of the PMTs propagates to the electronics trailer in the East Hall and is read out by an analog-to-digital convertor (ADC) with an integration window of 96 ns, which is set to contain the full energy deposition peak. To remove baseline shifts and low-frequency noise components that are picked up in the 130 m of cable between the calorimeters and the electronics trailer, the signal is split into two copies when it reaches the electronics trailer. Both signals lines are digitized in an ADC channel, but in one of the lines a delay of 96 ns is introduced before it is digitized.

[17] Due to the electromagnetic shower profile in the sampling calorimeter the first scintillator plates never showed any signs of radiation damage. The damage occurred mostly in the plates 4 until 10.

The digitized signal in the delayed line will thus correspond to the 96 ns window *before* the energy deposition signal arrived, and is an accurate estimate of the baseline contribution inside the signal window.

The trigger electronics of the laser system induces noise in the signal lines coming from the PMTs. This is corrected for by comparing trigger events when the laser was on and when the laser was off, in the absence of lepton beam events (*i.e.* for empty bunches). The shift in the integrated signal window was usually smaller than ten ADC channels.

To account for differences in the gain of the four PMTs of the crystal calorimeter, a gain matching procedure is used. By moving the Compton cone off-center until the Čerenkov light is mostly confined to one of the crystals, the gain correction factors are determined approximately twice per year. Spatial information about the horizontal and vertical location of the Compton cone on the front face of the crystal calorimeter is calculated from the asymmetry in the energy deposition in the left and right, and top and bottom crystals. By moving the calorimeter table, the Compton cone is kept centered on the calorimeter within a few millimeter.

Optical fibers connected to the HERMES gain monitoring system (GMS) are used to monitor degradations in the gain of the crystals and scintillator plates. Due to variable light losses in the bends of the optical fibers when entering the calorimeter, the response from a GMS laser pulse could not be used for the gain matching of the crystal calorimeter. The changes in the response from each PMT separately provided relative gain information. A decrease of approximately 10% in the response during each fill lead to the conclusion that the crystal or PMT temperature influences the gain or fiber transmissivity. This does not influence the polarization measurement, because the PMTs keep their linear behavior.

3.5.4 Evaluation of the systematic uncertainty

A full discussion of the systematic uncertainty of the polarization measurements of the LPOL is available in reference [90].[18] Although this treatment is still expected to be valid and complete, the systematic uncertainty of 1.6% was inflated to 2% for the HERA II running period to account for changes in the running conditions (higher beam currents, increase in synchroton radiation from the transversely polarized target) that were not foreseen in the original calculations [107]. Since the crystal calorimeter was rebuilt with different crystals in 2004, the current calorimeter was not used to perform the original test beam studies of the systematic uncertainty. The specifications of the new crystals are identical to the original crystals.

The presence of two completely independent polarimeters for the HERA lepton storage ring not only increases the availability of a polarization measurement when technical problems affect one of the polarimeters. A comparison of the two polarimeters can give us also indications about unknown contributions to the systematic uncertainty. In figure 3.15 the ratio of the LPOL and TPOL polarization measurements (averaged in 5 minute intervals) is shown for the five six-month periods since the beginning of 2005.

In 2005 a dependence of the TPOL polarization measurement on the beam waist size at the interaction point was discovered, which resulted in a 10% disagreement between the LPOL and TPOL measurements for all data collected in the HERA II running period since the year 2002. The data in figure 3.15 is corrected for this effect.

In August 2005 a new period of disagreement at the 10% level started, visible in the second panel of figure 3.15. After the startup in July 2005 the polarization measured by the LPOL was approximately 10% lower than the polarization measured by the TPOL. After the flip of the lepton helicity in September 2005 the disagreement disappeared after some initial problems with the TPOL visible in the figure. Even though the disagreement at first seemed to be concentrated in only one month, the problem returned in October 2005 with a smaller disagreement in the opposite direction and has since then plagued the polarimeter groups until the end of HERA operations in 2007. It sparked a lot of hardware investigations and systematic studies, but although smaller effects were found the main source of the disagreement has not been found until now.

During an extensive inspection of the hardware of the LPOL in the Winter shutdown in the beginning of 2006, the laser transport system was vented and all optical components inspected. The mirrors M3 and M4 showed minor signs of damage by the laser beam, in both cases one spot smaller than 1 mm in diameter, and they were replaced.

[18] When expressing the uncertainty on the polarization as a percentage, the fractional uncertainty dP/P is meant. A fractional uncertainty of 1% on a measured polarization of 50% corresponds to an absolute uncertainty of 0.5%. In this work the values of systematic uncertainties will sometimes be given as fractional numbers to avoid confusion, *i.e.* 0.01.

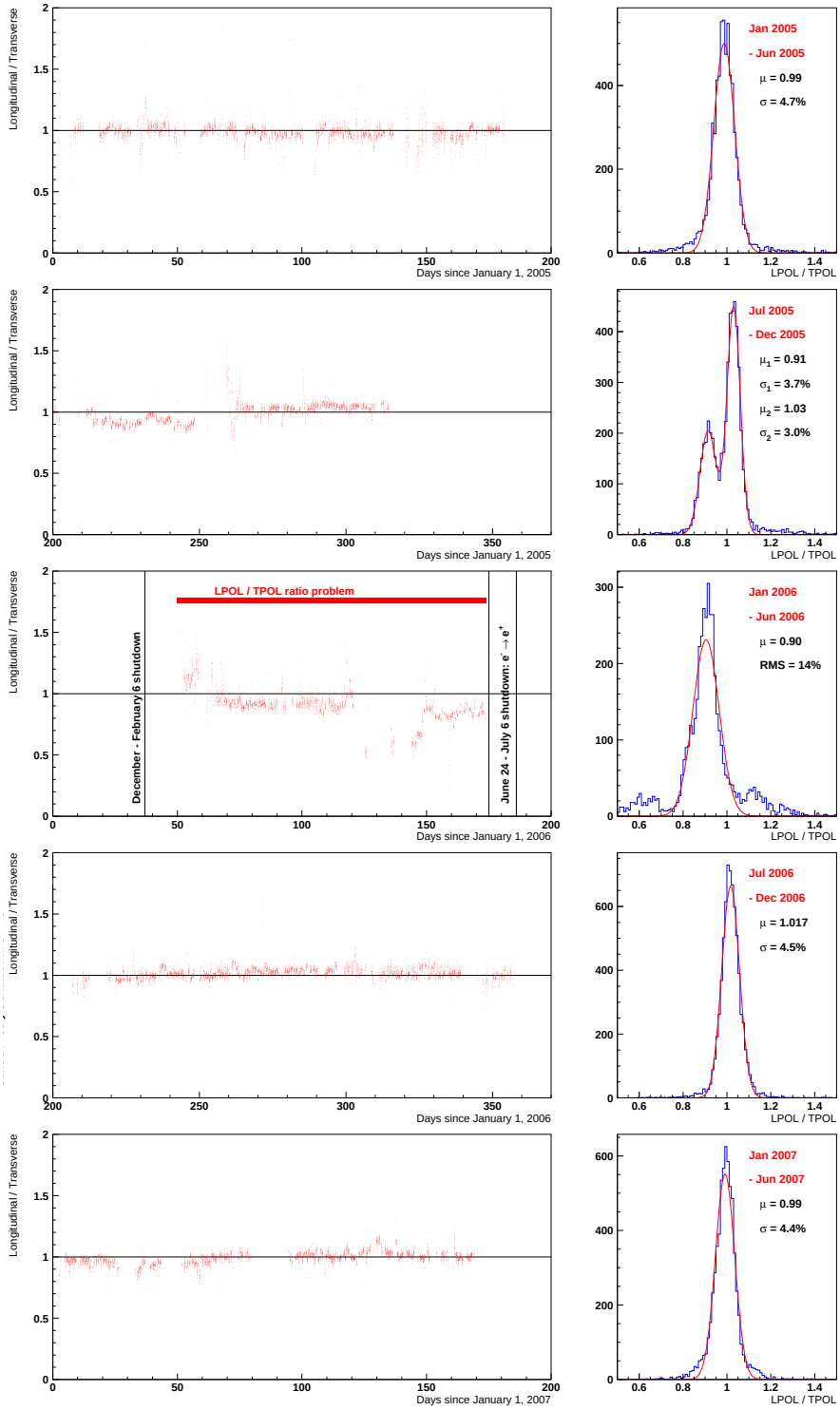

Figure 3.15: Comparison of the LPOL and TPOL polarization measurements from 2005 to 2007.

Because the laser beam travels through the transport system with an expanded beam size the small spots would not have affected the circular polarization or laser intensity, but due to the increased heat accumulation at these spots they could grow and become a major nuisance at a less convenient time.

Due to a mistake mirror M3 was inserted with the coating backwards after the inspection of the laser transport system. This introduced an unknown phase shift between the S and P waves, which strongly affected the circular polarization. The problem with the mirror M3 rendered the LPOL measurements during the first half of 2006 highly questionable. The HERA running schedule made access difficult, so the problem was only found and corrected after half a year. The disagreement between the LPOL and TPOL polarimeters inspired an ever growing number of investigations into the LPOL system and different approaches to the analysis of the collected data.

After the problem with mirror M3 was solved in the shutdown at the end of June 2006, excursions in the ratio of the LPOL and TPOL measurements exceeding 5% still occured in the second half of 2006 and the final period of data taking in 2007. Often the disagreement would vary slowly during one lepton fill, hinting to an unknown systematic influence on either the LPOL or TPOL, or both.

To search for the causes of this time-dependent disagreement between the LPOL and TPOL inspired a series of systematic studies to explain differences of more than 2%, the order or magnitude of the total systematic uncertainty of the polarimeters.

Compton cone centering

When the Compton cone is not centered correctly on the calorimeter, it is possible that part of the electromagnetic shower leaks out sideways. Because the shower profile depends on the energy of the Compton photon, this would induce a non-linearity in the detector. To investigate whether this effect has large influences on the polarization measurement, spatial scans of the Compton cone were performed regularly.

During a spatial scan the position of the calorimeter is manually adjusted such that the Compton cone is intentionally offset from the center. The automatic calorimeter centering is turned off. The polarization measurements of the TPOL are used as a reference during the scan. This measurement is only performed during periods of stable polarization to avoid sudden changes in the value of the polarization. In left panels of figure 3.16 the results of a spatial scan in the horizontal and the vertical direction are shown. Each data point corresponds to an average of approximately 20 minutes. In the horizontal direction the movement of the calorimeter is limited by the lepton beam pipe. The horizontal and vertical scan were not done simultaneously. During the vertical scan a constant disagreement between the LPOL and the TPOL was presen during the entire measurement.

In the right panel of figure 3.16 the results of a measurement are shown for a period with large disagreement between the LPOL and TPOL measurements. In the top right panels the polarization and the ratio LPOL and TPOL indeed disagree by approximately 10% during the entire duration of the spatial scan. The middle right panels show the evolution of the horizontal and vertical position of the Compton cone on the calorimeter. In the bottom right panels the ratio of the LPOL and TPOL measurements is plotted versus the distance of the Compton cone from the center of the calorimeter. No systematic correlation between the ratio and the position of the Compton cone on the calorimeter can explain the disagreement of 10% that is observed.

Laser delay timing

Through the jitter in the laser triggering the laser pulse profile is determined, as shown in figure 3.14. The optimal timing for firing the laser pulses is determined every minute by fitting the expected laser pulse profile to the collected events. Using a variable delay inside the laser electronics a delay of up to 24 ns can be set to obtain the correct timing. After one minute of data taking the chosen value can be compared to the optimal value for that minute. To avoid setting the variable laser delay too frequently, the laser delay is only changed when the determined optimal value is more than 2 ns lower or more than 1 ns higher. This difference is somewhat confusingly called the laser trigger delay. The asymmetric boundaries are motivated by the asymmetric pulse profile in which shifts to lower timing result sooner in a significant loss in interaction between photons and leptons.

During some fills it was observed that the optimal value would change erratically in the allowed range, or consistently move upwards or downwards. The effect of this behavior on the polarization measurement was determined

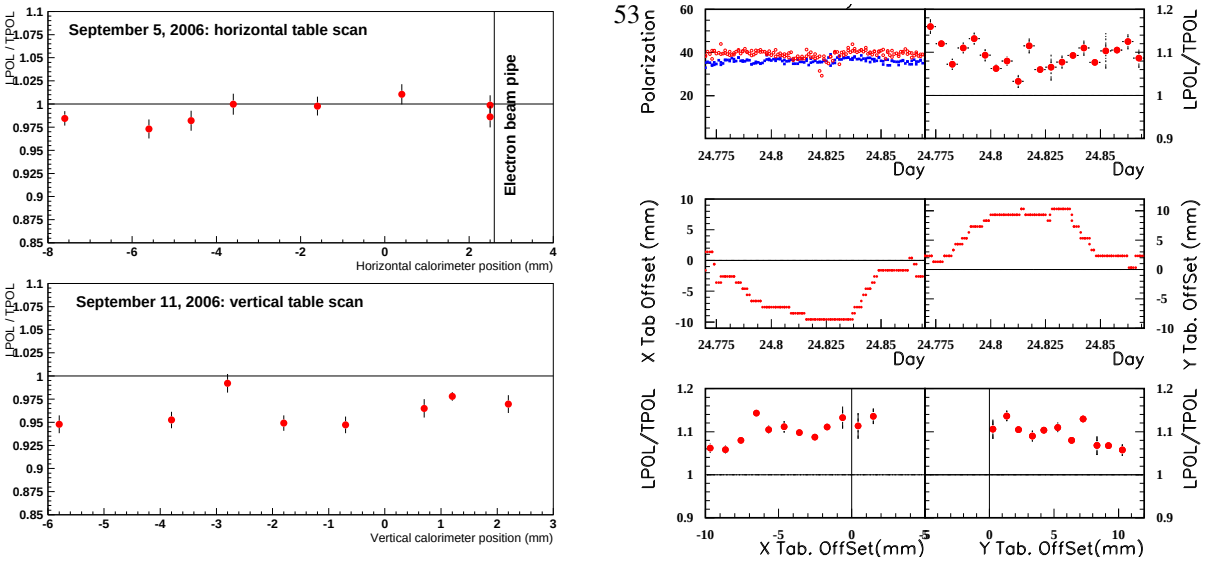

Figure 3.16: Results of a spatial calorimeter scan. In the top left panels the calorimeter was moved horizontally, in the bottom left panel vertically. The horizontal movement was limited by the electron beam pipe at the indicated position. In the right panel a similar measurement was performed during a period with a strong disagreement between the LPOL and TPOL measurements.

by laser timing measurements. By comparing the measurements (or rather the ratio of the LPOL and TPOL measurements) during minutes with a high laser trigger delay to minutes with a low laser trigger delay, a systematic effect of this delay on the measured polarization can be determined. In figure 3.17 the result of one of these measurements is shown. In the bottom panel the maximum deviation is only 1.3%. During other laser timing measurements the deviation was small, or in the other direction. This indicates that this is not a systematic effect, but related to variations in the beam polarization that are unrelated to the laser trigger delay.

Luminosity dependence

The disagreements between the two polarimeters LPOL and TPOL often varied slightly during a lepton fill, though not consistently going up or down. A dependence on the beam current could explain this behavior. For the measurements of the LPOL this translates to a luminosity dependence. To artificially create a different luminosity in the LPOL, the laser intensity can be changed. When this is done during stable lepton beam conditions, any luminosity dependence should immediately result in changes to the measured beam polarization.

Several times these luminosity scans were performed. One example of a measurement during the first period of disagreement in August 2005 is shown in figure 3.18. By changing the intensity of the laser over almost one order of magnitude, no systematic change of more than 1% in the measured polarization can be observed.

Comparison of LPOL polarization with crystal and sampling calorimeters

The presence of two calorimeters in the LPOL system allows for cross comparisons. In the left panel of figure 3.19 an example of such a comparison between the measurements of the crystal and sampling calorimeter is shown. In the first panel the polarization value measured by the LPOL is shown. The data points collected with the crystal calorimeter (the first and the last hatched intervals) are indicated in black, the data points collected with the sampling calorimeter (the two hatched intervals in between) are indicated in blue. The ratio between the polarization values measured with the LPOL (in the first panel) and the TPOL (in the second panel) is shown in third panel, averaged over five-minute intervals. When the ratio of LPOL and TPOL is averaged for the hatched periods, the values in the

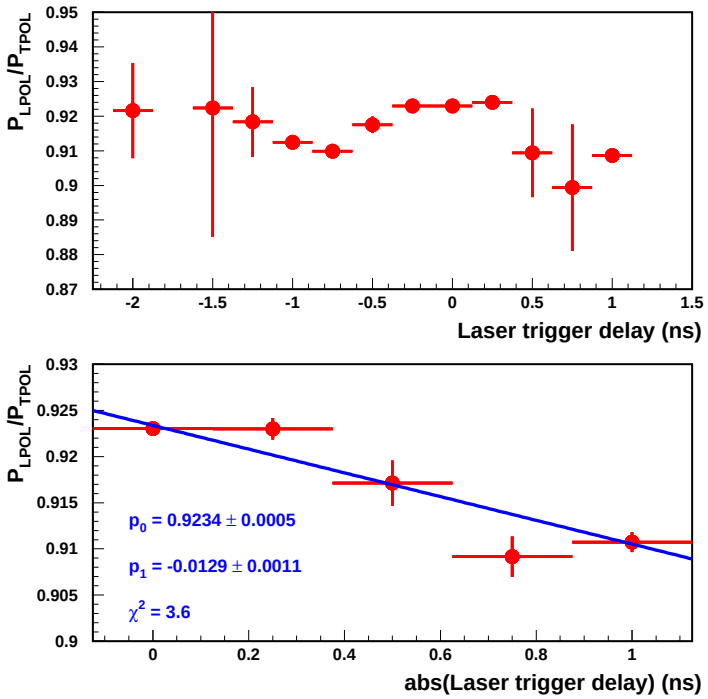

Figure 3.17: Results of a timing delay scan. In the top panel the averaged ratio of the two polarimeters for different values of the laser trigger delay is shown. In the bottom panel the results are shown versus the absolute value of the laser trigger delay. A laser trigger delay of 1 ns corresponds with a difference of 1.3% in the ratio of the polarimeters.

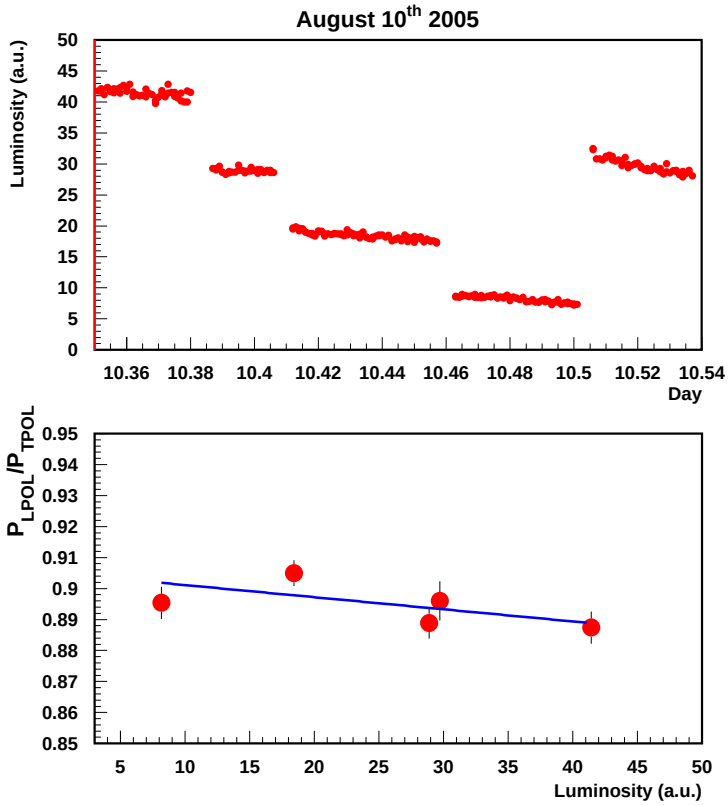

Figure 3.18: Results of a luminosity scan. The incident laser power was varied between 50 mJ and 200 mJ. The corresponding change in the measured luminosity (signal strength in the calorimeter) is shown in the top panel. In the bottom panel the influence on the ratio of the two polarimeters is shown. No systematic change larger than 1% is observed.

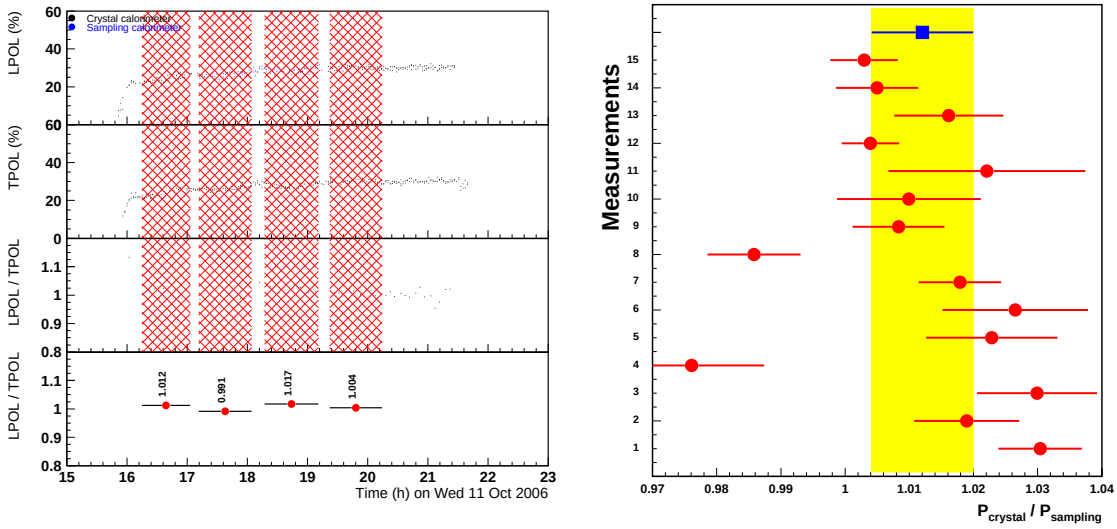

Figure 3.19: Comparison of polarization measurements taken with the crystal and sampling calorimeters. A typical example of a study by alternating the crystal and sandwich calorimeters is shown in the left panels. The black points in the first panel on the left are obtained with the crystal calorimeter, the blue points with the sampling calorimeter. The second panel shows the polarization measurements of the transverse polarimeter, taken as a reference for this study. In the third panel the ratio per minute is shown, and after averaging over the red hatched intervals the fourth panel is obtained. In the right panel, the results of fifteen similar studies are summarized.

fourth panel are obtained. The difference in each transition from crystal to sampling calorimeter is used to estimate the systematic difference between the polarization measurements with the two calorimeters.

In the right panel of figure 3.19 several crystal/sampling calorimeter cross comparison measurements, collected during approximately one year, are summarized. The average ratio of the polarization measurements with the crystal and sampling calorimeter is 1.012 ± 0.008.

Linearity measurement of the sampling calorimeter

The linearity of the calorimeter over the entire Compton energy range is an important requirement for the polarimeter. To quantify any changes in the linearity, possibly introduced by the exchange of the crystals in 2004 or by radiation damage in the scintillator plates, measurements in the test beam DESY T22 were repeated in 2005. The maximum energy the test beam could provide was 6 GeV, but both calorimeters proved to be linear within 1% in this range, as shown in figure 3.20.[19]

Other methods were used to confirm the linearity of the calorimeter and electronics. A rotatable quarter-wave plate and Glan-Thompson prism before the Pockels cell were used to change the laser beam power over one order of magnitude. The measured deposited Compton energy in the calorimeter was linear within 1%. This is related to the luminosity scans described earlier.

3.5.5 Precision polarimetry at the Electron-Ion Collider

Since the end of operations at the HERA collider in 2007 there are no high energy electron-proton colliders left in the world. The study of the spin-dependent properties of QCD with polarized electromagnetic probes continues at

[19] Due to the energy-weighted integration in multi-photon mode, linearity in the low energy part of the Compton spectrum is less important than in the high energy part. Unfortunately no new measurements at the CERN test beam could be taken after the end of HERA operations.

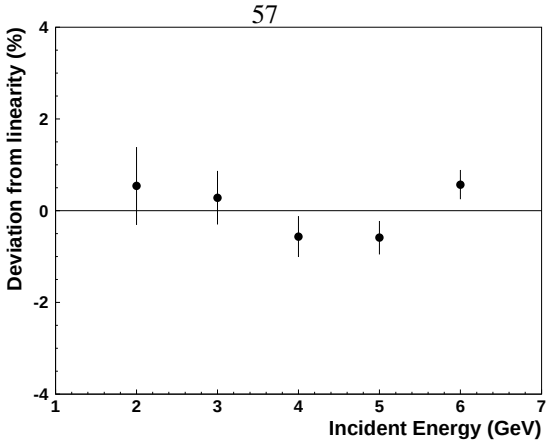

Figure 3.20: Demonstration of the linearity of the sampling calorimeter, as measured in the test beam at DESY in 2005.

the Jefferson Laboratory (JLab) by scattering polarized electrons of energies up to 6 GeV (and up to 12 GeV after an upgrade planned for 2009) on the hadrons in (polarized) gas targets. In the RHIC collider at the Brookhaven National Laboratory polarized proton beams are accelerated to energies of 250 GeV before they collide with each other in the PHENIX and STAR experiments. Proton collisions are inherently less 'clean' because the energy of the colliding parton (quark or gluon) is not exactly known but distributed according to the parton distribution functions.

At both the JLab and RHIC facilities the design of a new electron-hadron collider is in progress, extending the hadronic component to light and heavy ions as already successfully applied at the RHIC facility. The current design of this electron-ion collider (EIC) foresees collisions of 3–20 GeV longitudinally polarized electrons or positrons on 30–250 GeV protons or 50–100 GeV/u heavy ions (such as gold) at center of mass energies of 20–100 GeV. Bunch separations of 3–35 ns are discussed to achieve machine luminosities in electon-proton collisions of approximately 10^{33}–$10^{34}\,\mathrm{cm}^{-2}\,\mathrm{s}^{-1}$. The EIC would not only operate with polarized electron and positron beams, but also with polarized proton and light ion beams. The anticipated electron polarization is above 70% and needs to be measured with a systematic uncertainty better than 0.01.

Several methods for the polarization measurement of the electron beams have been proposed. They all involve the measurement of asymmetries in the cross section for the scattering of polarized electron beam from other particles. In Mott polarimeters the spatial dependence of electrons back-scattered from nuclei is measured. This destructive measurement is mainly used to measure the electron beam polarization at low energies between 30 keV and 5 MeV. In Møller or Bhabha scattering the electrons or positrons collide on the electrons in an externally magnetized metal foil. This polarimetry technique is applicable to beam energies between 100 MeV to many GeV, but is unfortunately also destructive. For a continuous polarization measurement a non-destructive polarimeter concept is preferable or even necessary. In a new idea Møller scattering would be measured non-destructively on polarized atomic hydrogen in an ultra-cold magnetic trap, or with a hydrogen jet target.

Compton scattering of electrons or positrons and photons is not destructive and suitable for energies above 1 GeV and ideal for energies above 10 GeV. It is the only non-destructive polarimetry technique that has been successfully applied in high energy storage rings, and therfore a main contender in the design of a polarimeter for the EIC.

The main differences between the HERA storage ring and the proposed EIC collider are the lower energy which translates in a smaller asymmetry (see figure 3.10). By using a laser with a higher photon energy this can be avoided, but unfortunately this is difficult to achieve with the current UV laser technology. Progress in the new technology of fiber lasers allows to reach a duty factor of almost 100% by only emitting laser light when electrons are passing by. The use of a cavity around the interaction point also allows to increase the intensity of the laser photons, resulting in a higher counting rate in the photon detector and thus higher statistical precision.

One of the problems in operating the HERA longitudinal polarimeter in single-photon mode was the background

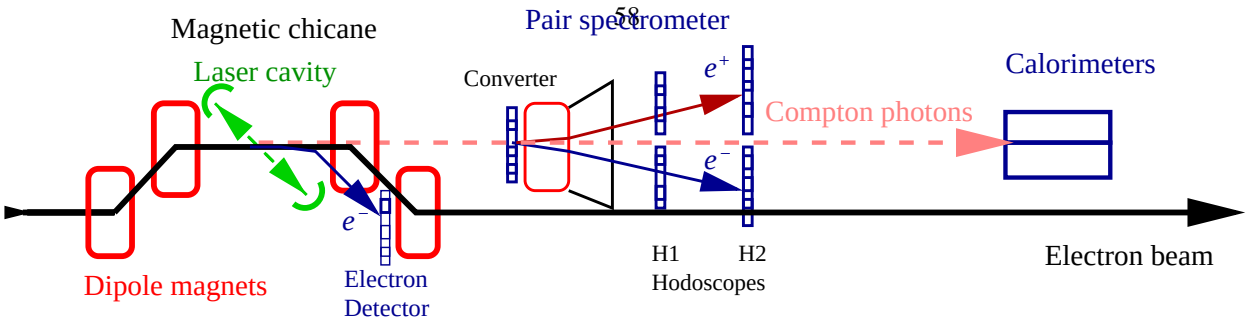

Figure 3.21: Schematic design for a hybrid Compton polarimeter at the EIC. Taken from reference [108].

rates from bremsstrahlung of remaining gas atoms in the beam vacuum. Another problem was posed by the constraints on the movement of the calorimeter imposed by the beam pipe. Both these problems can be avoided when polarimetry is incorporated in the design of the collider, by including a chicane with soft bends to minimize the synchrotron radiation. In figure 3.21 a possible design of a hybrid Compton polarimeter is shown. By including a chicane the bremsstrahlung would be reduced because the section of beam pipe from which bremsstrahlung enters the photon detector is much shorter. The distance between the electron beam and the Compton photon cone can be increased, which allows for much more freedom in the design of the calorimeter and could allow for the inclusion of a pair spectrometer.

The use of multiple independent devices for the measurement of the polarization has definitely been an advantage of the HERA storage ring. Disagreements between the LPOL and the TPOL led to the discovery of systematic effects that would otherwise have remained unknown. For the design of an EIC polarimeter with chicane there are several possibilities for the parallel measurement of the polarization. The scatter Compton electron can be detected in an electron detector (a Si strip detector). The Compton photons can be detected in a position sensitive calorimeter similar to the sampling calorimeter at the LPOL, with a wide dynamic range to allow for operation in the single- and multi-photon modes. With the inclusion of a converter with a dipole pair spectrometer the energy of the photons is measured using the coincident electron-positron pairs.

We are still in the early stages of the design of the EIC and many numerical simulations will have to be completed before a decision can be made on a final design. At this point the qualitative experiences from working with the LPOL can only provide some guidance and suggestions as to what should not be overseen.

CHAPTER IV

The Analysis of Exotic Baryons at the HERMES Experiment

In this chapter the search for the exotic baryons Θ^+ and Ξ^{--} is presented using their decays to a proton p and a neutral kaon K^0_S, respectively a negative pion π^- and a hyperon Ξ^-. The neutral kaons and hyperons decay weakly inside the HERMES spectrometer and the tracks of the daughter particles allow us to reconstruct their properties. After separating for the different running conditions several data taking periods are considered, each characterized by the target gas and the trigger setup, and influenced by improvements in the particle identification capabilities and the introduction of the transverse target magnet. Since it is not *a priori* clear whether the independent data sets can be added together, they are presented separately.

First we give a short overview of all the data sets that were used, with details about their characteristics. This includes information about the triggers and target gases. Next the event selection criteria are introduced, as they are very similar for the analyses that follow. Then we present the search for the exotic baryon Ξ^{--} using the same data set in which the exotic baryon Θ^+ was observed. In the next section we describe the analysis of the exotic baryon Θ^+ using low-momentum protons identified with the time-of-flight technique. The absence of a corresponding exotic antibaryon Θ^- is addressed using the cross section ratio of the $\Lambda(1520)$ hyperon and antihyperon. A correction method for hadrons decaying in the magnetic field of the transverse target is developed and used in the search for the exotic baryon Θ^+. The next section focuses on the mixed event method for the estimation of background distributions. Finally all obtained results about the exotic baryon Θ^+ are combined and discussed.

4.1 Overview of the analyzed data sets

For the analysis of the exotic baryon Θ^+ all data sets collected since the start of the HERMES experiment in 1996 until its completion in 2007 were investigated. The search for the exotic baryon Ξ^{--} was performed on a subset of this data. Due to differences in the target gases, the trigger system, and the setup of the experiment in the data sets, it is difficult to combine all data sets. In this section the different data sets are presented separately with their characteristics.

4.1.1 Low density and high density target gas

During regular operation of the HERA collider and the HERMES experiment, the first 10 to 12 hours of a lepton fill were used for reactions on polarized gas targets. The low areal densities of the polarized gases have a small effect on the beam lifetime. If the influence of the target gas could be isolated, the lepton beam lifetime would have been typically 45 hours, far above the usual lifetime of 15 hours dominated by other factors. The last hour of every fill was typically used for high density data taking with unpolarized gas targets. The lepton beam current was then usually below 15 mA, but the high density of the target gas and the higher polarization of the leptons make these end-of-fill runs very effective.

As already described in section 3.3.3, the main physics trigger requires an energy deposit in the electromagnetic calorimeter above an adjustable threshold. During low density data taking that lasted through most of the lepton fill

the threshold was usually set to 1.4 GeV. However, during high density unpolarized data taking this energy threshold would overwhelm the data acquisition system and thus lead to an unacceptably large dead time. To reduce the number of events to acceptable levels the threshold was therefore increased to 3.5 GeV during the high density periods.

In most deep-inelastic scattering events the scattered lepton has an energy high enough to generate a trigger, even with the increased threshold during high density data taking. In photoproduction events at the HERMES experiment the momentum transfer from the colliding lepton to the target is too low for the deflected lepton to be detected by the spectrometer. The deposited energy in the calorimeter has to come from one of the hadronic reaction products. Because they have a much lower average energy,[1] usually between 1 and 4 GeV, the increase in the required energy deposit is detrimental to the collection of photoproduction events.

Due to the unfavorable trigger conditions during high density data taking the analysis presented in this work uses exclusively the data collected during polarized data taking. In the overview section 4.8 the high density data sets are included, but are expected to be featureless due to the suppression of photoproduction events. They can be used as an estimate for the amount of non-photoproduction and background events.

4.1.2 Target gases

The HERMES experiment can operate with a variety of target gases (see section 3.2). For the analysis of exotic baryons the focus has been on photoproduction reactions on hydrogen and deuterium nuclei. These target gases make up the bulk of the available data. Reactions on the heavy nuclei such as Kr and Xe were collected exclusively during high density data taking and suffer from unfavorable trigger conditions. Due to the absence of low density data and limited number of collected events on these heavy nuclei they are ignored here.

4.1.3 The pre-RICH period (1996–1997)

During the first years after commissioning the HERMES experiment the RICH particle identification detector (described in section 3.3.2) had not been installed yet. Instead, the threshold Čerenkov counters were available for the separation of pions and protons. The reduced particle identification capabilities are mostly relevant in analyses which depend on the presence of a kaon. In this work an identified proton track is required, which is possible with the threshold Čerenkov counters.

4.1.4 The polarized deuterium period (1998–2000)

After the installation of the RICH detector the particle identification capabilities of the HERMES experiment improved substantially.

During the years 1998, 1999 and 2000 the HERMES experiment operated with a longitudinally polarized deuterium target during low density data taking, and collected an integrated luminosity of approximately $209.2\,\mathrm{pb}^{-1}$. In the periods of high density data taking at the end of every fill several unpolarized target gases were alternated. This longitudinally polarized low density data combined with the high density data collected on a deuterium target was used for the published observation of the exotic baryon $\Theta^+(1540)$ [4]. During the same period a high density data set was collected on an unpolarized hydrogen target.

4.1.5 The transverse magnet period (2002–2005)

In the long shutdown in the year 2001 that marked the transition of the HERA I period to the HERA II period with increased luminosity at the collider experiments H1 and ZEUS, a transversely polarized hydrogen target was installed at the HERMES experiment. The bending effect of the magnetic holding field with a strength of 0.3 T on the charged particle tracks leads to a significantly worse resolution of the spectrometer when no corrections are applied.

During the shutdown a silicon strip detector array for the study of the Λ^0 hyperon polarization was installed just downstream of the target region. These so-called Lambda Wheels are not integrated in the track reconstruction

[1] In figures 4.31 and 4.32 the distribution of the longitudinal momentum P_z for the Σ^- hyperon is representative for the energies considered here.

algorithms. The wider acceptance of the Lambda Wheels overlaps partially with the acceptance of the forward spectrometer, depending significantly on the longitudinal position of the interactions in the target cell. The effects of the Lambda Wheels on the resolution are small, but lead to a slight degradation of the momentum resolution for events in the region of overlapping acceptance.

During the running period from 2002 until 2005, data were collected on transversely polarized hydrogen during low density periods and on several unpolarized target gases during high density periods. For the analysis of the exotic baryons in the data collected on the polarized target it is necessary to apply a transverse magnet correction. The development of this correction will be described in section 4.6.

4.1.6 The recoil period (2006–2007)

For the last two years of the HERMES experiment, three new detectors were installed to detect and identify the recoiling target proton in deeply-virtual Compton scattering events. Collectively called the recoil detector, they consist of a silicon strip detector for vertex tracking, a scintillating fiber barrel tracker for momentum determination in a solenoidal field, and a photon detector for particle identification. Consistent with to the goal of detecting the recoiling protons, there is no overlap between the recoil detector and the main spectrometer [96].

As part of the recoil upgrade the length of the target cell was reduced from 40 cm to 15 cm and the entire cell was moved 25 cm forward into the detector. This changed the geometrical acceptance for $\Theta^+(1540)$ events by approximately 15%, a value that was determined with Monte Carlo simulations.

The recoil detector uses a completely independent tracking algorithm. Events that are detected by any of the recoil subdetectors are not included in the presented analyses. Because of the kinematic regime that is covered by the recoil detector, which requires detected particles to be produced with momentum pointing backwards, it is very unlikely that it can be used for the analysis of photoproduction events. The tracks detected by the forward spectrometer can still be analyzed independently.

At the time of writing the data set collected during this period is in the final stages of calibration. The calibration process, involving input from all subdetectors, influences the momentum resolution and the particle identification efficiency. The data set that was available for the analysis presented in this thesis was calibrated with the calibration data of the year before. It is therefore safe to assume that the conclusions are valid, although small changes in the selected events will occur when the calibrated data becomes available.

The resolution of several resonances in data collected during the recoil period seems to be worse than is expected even for uncalibrated tracks. A detailed map of the small solenoidal magnetic field of recoil detector was measured, including the fringe fields in the front region of the forward spectrometer. For the analysis of the exotic baryons no correction for these fringe field has been applied. It is not clear yet whether the degradation of the resolution is mainly attributable to the fringe field.

The installation of the recoil detector required the removal of the polarized target gas system. The separation between low density and high density data taking was still maintained. The target gas was varied between hydrogen and deuterium, with a preference for hydrogen that resulted in a five times large data set on the hydrogen target. The recoil data set collected on the deuterium target is expected to be the most similar to the polarized deuterium data set of the period 1998–2000. The only differences are the installation of the Lambda Wheels in the front region, partially overlapping with the forward spectrometer, and the shift of the target cell which reduces the acceptance for very forward events.

4.1.7 Overview

In table 4.1 the number of collected DIS events and the total integrated luminosity for each data set is summarized. For the observation of the exotic baryon Θ^+ in the data collected on a deuterium target between the years 1998 and 2000 an integrated luminosity of $209.2\,\mathrm{pb}^{-1}$ was used, corresponding to 9.4 million DIS events. The only other data set with a comparable number of events on a deuterium target was taken during the years 2006 and 2007, and which is expected to contain approximately twice as many events. An even larger number of events was collected on a hydrogen target during that period.

Table 4.1: Comparison of the number of deep-inelastics scattering (DIS) events and integrated luminosity $\mathcal{L}$ for all data sets. For the years 2006 and 2007 the integrated luminosity is not available yet, and the number of DIS events is only available for the year 2006, and for hydrogen not separated in low and high density periods. These values are therefore given in parentheses.

Data period	Gas type	DIS (M)	$\mathcal{L}$ (pb^{-1})
1996–1997	H (pol)	2.382	49.9
1996–1997	H (unpol)	2.797	56.6
1996–1997	D (unpol)	4.511	104.5
1997	N (unpol)	1.919	51.4
2000	H (unpol, hd)	6.850	132.5
1998–2000	D (pol, ld)	9.407	209.2
2002–2005	H (pol, ld)	7.439	150.2
2002–2005	D (unpol, hd)	10.29	158.1
2006–2007	H (unpol, ld)	(30.58)	n.a.
2006–2007	H (unpol, hd)	(30.58)	n.a.
2006–2007	D (unpol, ld)	(7.07)	n.a.

4.2 Event selection criteria

The HERMES experiment was designed as a multi-purpose experiment. The collision events are collected and stored on tape or disk for a wide range of different analysis topics, ranging from deep-inelastic scattering (where only the detection of the scattered lepton is required) to hadron photoproduction (which requires several hadrons in the final state but where the lepton is not detected). The hardware event triggers described in section 3.3.3 are purposely kept general and additional selection criteria have to be applied to remove events that are not relevant to the analysis. A balanced set of selection criteria reduces the number of background events while maintaining an unbiased and sufficiently large sample of signal events.

Because the analyses presented in the following sections are all rather similar with respect to the selection criteria, this section describes them in detail. The selection criteria can be divided in two groups: *track selection criteria* involve only information from a single track, and *event selection criteria* combine multiple tracks in order to restrict the event topology.

4.2.1 Track selection criteria

We first consider the track selection criteria. Before discussing the different resctrictions that are placed on the kinematic parameters of the tracks used in this work, it is helpful to divide the detected tracks in two categories depending roughly on the momentum of the particle that created them.

Often, low momentum particles are bent outside the geometrical acceptance of the back tracking region by the field of the spectrometer magnet. The magnet chambers located inside the spectrometer magnet were designed to reconstruct the momentum of these so-called *magnet* or *short tracks*. Because the particle identification detectors are in the back region, it is impossible to identify these tracks or even separate them in hadrons and leptons. Commonly, short tracks are assumed to be created by pions (and thus hadrons), since they are by far the most frequent particle type at this low momentum. Only in the search for the exotic baryon Ξ^{--} will these short tracks be used.

The higher-momentum *long tracks* leave a signal in the back tracking detectors and, if they reach the particle identification detectors, lepton-hadron separation and hadron identification are possible.

Fiducial volume

To ensure that each track is sufficiently inside the active volume of the tracking detectors and, for long tracks, particle identification detectors, and to reduce secondary scattering events on the spectrometer magnet field clamps

and structural parts of the detectors, only tracks in the *fiducial volume* are selected. The acceptable track parameter are delimited by several components of the spectrometer:

- the front field clamp: $|x_{off} + 172.0\ \tan\theta\cos\phi| < 31.0\,\text{cm}$,
- the shielding plate: $|y_{off} + 181.0\ \tan\theta\sin\phi| > 7.0\,\text{cm}$,
- the rear field clamp, determined using the front partial track and neglecting the small vertical bend by the spectrometer magnet: $|y_{off} + 383.0\ \tan\theta\sin\phi| < 54.0\,\text{cm}$,
- the rear field clamp, determined using the back partial track: $|x_{pos} + 108.0\ x_{slope}| < 100.0\,\text{cm}$ and $|y_{pos} + 108.0\ y_{slope}| < 54.0\,\text{cm}$,
- the volume of the electromagnetic calorimeter: $|x_{pos} + 463.0\ x_{slope}| < 175.0\,\text{cm}$ and $30.0\,\text{cm} < |y_{pos} + 463.0\ y_{slope}| < 108.0\,\text{cm}$.

In these expressions the coordinates x_{off} and y_{off} refer to the intersections with the plane $z = 0$, while the angles θ and ϕ are the polar angles of the front partial track. For the back partial track the intersection with the plane $z = 0$ is given by the coordinates x_{pos} and y_{pos}, and the horizontal and vertical slopes by x_{slope} and y_{slope}. Since short tracks do not reach the back region, they only have to satisfy the first three expressions.

For short tracks there are no other track selection criteria that can be applied. There is no particle identification possible; the short tracks are all assumed to be pions. For long tracks we need to ensure that the tracks are hadrons and have the correct hadron type (pion, kaon, or proton) required for the analysis.

Hadron separation and identification

Hadron tracks are separated from lepton tracks by combining the signals of the preshower detector, the transition radiation detector, the electromagnetic calorimeter, and the Čerenkov counters or the RICH detector using the probabilistic procedure discussed in section 3.3.2. In this work tracks are considered hadrons when the probability that the track was generated by a hadron is larger than the probability for a lepton, using the detector responses generated by the event. In other words, the parameter $PID_3 + PID_5$ is required to be negative for hadron tracks.

Before the installation of the RICH detector only the Čerenkov detector was available for the separation of pions and protons. In the events collected during that period, we identify the hadrons with a momentum above 4 GeV and with a Čerenkov response below a threshold value as protons; the remaining hadrons are identified as pions. The momentum of the protons will therefore always be larger than 4 GeV.

After the installation of the RICH detector, hadron identification improved due to the ability to separate kaons from pions and protons. The hadron (mis-)identification efficiencies for the identification of a hadron i as type j were shown in the form of the P-matrices P_i^j in the right panel of figure 3.8. For pions the identification efficiency P_π^π is above 90% for the full momentum range up to 15 GeV. No momentum restrictions need to be imposed on the pion tracks, although tracks below 1 GeV and above 15 GeV are excluded to avoid outliers.

For kaons and protons the identification efficiencies P_K^K and P_p^p are not smooth or consistently high over the full momentum range. For both kaons and protons a cusp is visible in the efficiencies at 10 GeV, caused by the Čerenkov threshold for kaons in the gas radiator. This affects the misidentification of kaons as protons adversely. At 10 GeV half of the kaons are misidentified as protons, indicated by the value $P_K^p \approx 50\%$. To avoid contamination of the proton tracks with misidentified kaons, the momentum of the proton tracks is limited to values below 9 GeV. A substantial contribution of misidentified kaons could introduce reflections of resonance decays in other hadronic decay channels. As P_π^K and P_p^K are both below 20%, there is no large misidentification of pions or protons as kaons and no risk of a high contamination of the kaon tracks above 10 GeV. For kaons the momentum is thus allowed to be as large as 15 GeV.

The Čerenkov threshold in the aerogel tiles determines the minimum momentum at which a particle can be identified. For kaons this threshold is 2 GeV, for protons 4 GeV. Below the momentum threshold the particle will not generate any Čerenkov light and cannot be identified by measuring the opening angle of the Čerenkov cones. Between 2 and 4 GeV the absence of any Čerenkov light is used as an identifying factor to provide proton identification, but at

a lower efficiency. Due of these physical considerations the momentum for kaons is required to be larger than 2 GeV and for protons larger than 4 GeV to obtain optimal hadron identification. Only in the search for the exotic baryon Ξ^{--} was the minimum momentum of protons lowered to 2 GeV to access the low momentum protons required for this final state.

For every identified particle the particle identification algorithm of the RICH returns a quality parameter, as already discussed in section 3.3.2. This is defined as the logarithm to base 10 of the probability ratio for the most likely and next-most likely particle type assignment. To reduce misidentification effects for protons this parameter is required to be larger than 1.5. In other words, the proton tracks are over 30 times more likely created by a proton than by anything else. The calculation of the RICH quality parameter is not included in the Monte Carlo simulations. When the data was compared to Monte Carlo simulations or when the event selection efficiency was determined using Monte Carlo simulations, this requirement on the RICH quality parameter had to be relaxed.

For pions no requirement is placed on the RICH quality parameter. The discussion above is also only applicable to the hadron identification with the RICH detector, and not to events collected with the threshold Čerenkov counter. No quality parameter is calculated for tracks collected during that period.

Summarizing these track selection criteria, the momentum selection for hadron requires the momenta $1 < P_\pi < 15\,\text{GeV}$, $2 < P_K < 15\,\text{GeV}$, and $4 < P_p < 9\,\text{GeV}$. With the threshold Čerenkov counters no kaons can be identified, but the momentum requirements for pions and protons are maintained. To further reduce misidentification of (mostly) kaons as protons, the RICH quality parameter for protons was required to be larger than 1.5.

Combinatorics

For the exotic baryon analyses presented in this thesis a fixed number of tracks was required in every event: two hadrons for the $\Lambda(1520)$ hyperon, three for the Θ^+ analysis, and four for the Ξ^{--} search. Many events consist of more tracks than the necessary configuration. In these cases all possible combinations with the necessary number of tracks are considered. For example, when an event contains two protons (p_1 and p_2) and three pions (π_1, π_2, and π_3) but only one proton and two pions are required, the following six combinations of tracks are considered: $p_1\pi_1\pi_2$, $p_1\pi_1\pi_3$, $p_1\pi_2\pi_3$, $p_2\pi_1\pi_2$, $p_2\pi_1\pi_3$, $p_2\pi_2\pi_3$.

4.2.2 Event reconstruction

To select candidate events that contain a decaying resonance, for example, a K^0_S meson decaying to two pions, we need to combine information from the two pion tracks. Since the two decay particles are created at the same position, their tracks have to intersect within the resolution of the track reconstruction. Adding the four-momenta of the decay tracks, we can determine the four-momentum, and thus the invariant mass of the resonance. The decay vertex and the reconstructed invariant mass allow us to impose event selection criteria.

Topological selection

To determine whether two tracks originate at the same position, we determine the distance of closest approach between the two tracks. The midpoint of the segment connecting the two points of closest approach on the tracks is then defined as the decay vertex. For straight tracks the distance of closest approach can be calculated analytically, but in the case of helically curved tracks in a (quasi-)homogenous magnetic field an approximation has to be used, or a numerical solution calculated with an iterative method. The development of this algorithm will be the topic of section 4.6.

Several weakly decaying resonances considered in this work (K^0_S, Λ, Ξ^-) are relatively long-lived. This means that the vertex where they are created and their decay vertex can be resolved as separate points by the spectrometer. The distance between these two vertices is called the vertex separation or decay length. The decay length can be used as a (rather ineffective) selection parameter. Requiring a decay length larger than the resolution of the spectrometer will remove a large number of background events, but select many resonance events. Unfortunately also a substantial number of these long-lived resonance events will decay within the tracking resolution of the spectrometer.

If we want to go up in the decay chain, in order to determine the vertex of the proton and K^0_S tracks, we need to require that the track of the K^0_S meson reconstructed from the two pions has indeed a invariant mass that is consistent

Table 4.2: Average horizontal and vertical positions of the production vertex pK^0_S for all data sets.

Data period	Gas type	x_0 (cm)	$\sigma(x)$ (cm)	y_0 (cm)	$\sigma(y)$ (cm)
1996–1997	D (unpol)	-0.090 ± 0.002	0.125 ± 0.002	0.062 ± 0.002	0.152 ± 0.003
1996–1997	H (pol)	-0.082 ± 0.002	0.136 ± 0.002	0.040 ± 0.002	0.174 ± 0.003
1996–1997	H (unpol)	-0.067 ± 0.002	0.135 ± 0.002	0.051 ± 0.002	0.164 ± 0.002
1997	N (unpol)	-0.060 ± 0.002	0.136 ± 0.002	0.037 ± 0.002	0.165 ± 0.002
1998–2000	D (pol, ld)	-0.129 ± 0.003	0.222 ± 0.003	0.054 ± 0.004	0.253 ± 0.004
2000	H (unpol, hd)	-0.119 ± 0.007	0.217 ± 0.007	0.040 ± 0.009	0.233 ± 0.008
2002–2005	H (pol, ld)	e^+: 0.046 ± 0.008	0.232 ± 0.009	0.06 ± 0.02	0.197 ± 0.02
		e^-: 0.359 ± 0.005	0.233 ± 0.007		
2002–2005	D (unpol, hd)	0.236 ± 0.003	0.216 ± 0.005	0.057 ± 0.004	0.247 ± 0.005
2006–2007	D (unpol, ld)	0.191 ± 0.003	0.214 ± 0.004	-0.031 ± 0.003	0.237 ± 0.003
2006–2007	H (unpol, hd)	0.198 ± 0.003	0.209 ± 0.003	-0.033 ± 0.003	0.248 ± 0.004
2006–2007	H (unpol, ld)	0.189 ± 0.002	0.206 ± 0.002	-0.031 ± 0.002	0.244 ± 0.002

with the mass of the K^0_S meson. To account for the effects of the spectrometer resolution σ or the width of the resonance Γ, we select events with an invariant mass inside a sufficiently broad window around the resonance mass. A window with a width of $3\,\sigma$ will select almost all resonance events, but if the resonance is distributed among a large amount of background events, the proportional increase of the number of selected events when going from a $2\,\sigma$ to a $3\,\sigma$ invariant mass window is small. In the case of the K^0_S resonance the number of background events can be reduced sufficiently by requiring a small distance of closest approach between the two pion tracks.

Production vertex

When we have reached the hypothetical event production vertex after stepping up the decay chain, we require that this event production vertex is inside the target cell in the longitudinal direction. In the transverse direction the tracking resolution would allow us to put strict requirements on the production vertex because the lepton beam is approximately 10 times narrower than the target cell. Unfortunately small, unknown changes in the beam position force us to take a more ad-hoc approach. For every data set the average transverse coordinates of the production vertex are determined. The deviations from this average beam position are then required to be comparable to the width of the distributions, in much the same way as with the invariant mass window around intermediate resonances.

The average beam positions of the different data taking periods and conditions are compiled in table 4.2. The average production vertex positions and distribution widths for events collected on the polarized hydrogen target during the years 2002–2005 are separated for positron beam (2002–2004) and electron beam (2005). The transverse target magnetic field shifted the positron and electron beam in opposite directions. The difference between the average vertex position for electrons and for positrons was approximately 3 mm.

In the search for the exotic baryon Θ^+, decaying to a proton and K^0_S meson, the selection requirements were extensively studied during the analysis of the events collected on the deuterium target in the period 1998–2000. The distance of closest approach between the two pions was required to be smaller than 1.0 cm. The decay length of the reconstructed K^0_S meson was required to be larger than 7.0 cm. Based on the width of the observed K^0_S resonance peak in the distribution of the invariant mass $M(\pi^+\pi^-)$, a window between 485 and 509 MeV was chosen. When combining the reconstructed K^0_S track with the proton track, a distance of closest approach smaller than 0.6 cm was required. This vertex was required to be inside the target region and within 0.4 cm of the lepton beam.

The selection criteria determined during the original analysis of the exotic baryon Θ^+ were verified to be valid in the other data sets. Differences in the experimental conditions of other data sets did not influence the distribution of the selection parameters. Only the tracking algorithm developed for the treatment of resonances decaying in the transverse magnetic field was plagued by a worse longitudinal resolution, which affected the decay length requirement of the K^0_S meson.

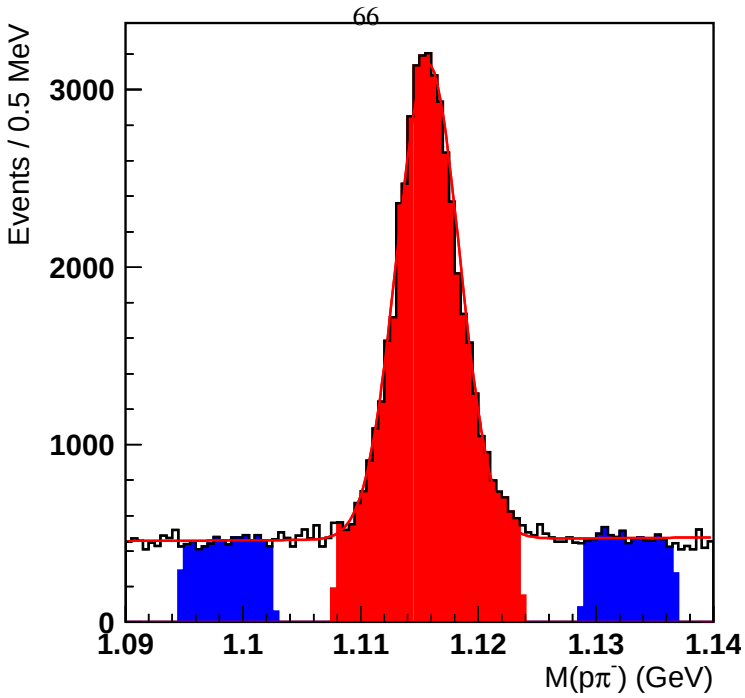

Figure 4.1: The peak region (red shaded region) and the sideband region (blue shaded region) for the Λ hyperon.

The selection criteria used in the search for the exotic baryon Ξ^{--} were based on the previous selection criteria. They were verified using events in the peak and the sidebands of resonance events, using a method presented in section 4.2.3.

4.2.3 Optimization of event selection criteria

To determine the optimal values for the hard cut-off parameters in selection criteria, the distributions of the selection variables are compared for events in the peak and sideband regions of well established resonance peaks. In figure 4.1 this is demonstrated for the Λ hyperon. The peak region is usually defined as the $\pm 3\,\sigma$ interval around the mean position of the Gaussian peak. Smaller intervals are appropriate when there are many background events inside the peak region. The sideband region is defined outside of an approximately $\pm 5\,\sigma$ interval around the central value of the Gaussian peak but not further away than $8\,\sigma$. This region is chosen to remove all resonance events, but at the same time keep the kinematic differences between events in the sideband region and background events in the peak region small. The background events in the peak region are assumed have the same kinematic characteristics as events in the sideband region.

When the distribution $dist_{\text{sidebands}}$ of the selection variable for events in the sideband region is normalized to unity, it is written as $pdf_{\text{background}}$ and can be interpreted as the probability distribution for background events to have a specific value of the selection variable. After correcting the distribution $dist_{\text{peak}}$ for events in the peak region for background events under the peak by subtracting a fraction of the sideband region from the peak region, and after normalization, a similar probability distribution pdf_{signal} for signal events is constructed. The probability distributions

of the selection parameter are then compared for both types of events. Mathematically, this can we summarized as

$$pdf_{\text{signal}} = \frac{1}{n_{\text{signal}}}(dist_{\text{peak}} - n_{\text{background}}\frac{dist_{\text{sidebands}}}{n_{\text{sidebands}}}), \tag{4.1}$$

$$pdf_{\text{background}} = \frac{dist_{\text{sidebands}}}{n_{\text{sidebands}}}. \tag{4.2}$$

The region where values of the selection variable are more likely to occur for signal events than for sideband events, is selected. Events outside of this region are discarded.

When the number of events in the signal and sideband region are of similar magnitude, this method gives a realistic estimate for the optimal value. Changes in the optimal value will lead to addition of events that are more likely background, or removal of events that are more likely signal. For situations where a small number of signal events has to be selected from a sample with many background events, a stronger suppression of background events is beneficial.

4.3 Search for the exotic baryon $\Xi(1860)$

In October 2003 the experiment NA49 at CERN presented evidence for an exotic baryon $\Xi(1860)$.[2] At a mass of 1862 MeV a narrow resonance was observed in the particle and antiparticle final states corresponding to the decay of the $\Xi^{--}(1860)$ resonance to a $\Xi^{-}(1320)$ hyperon and a negative pion, and the decay of the $\Xi^{0}(1860)$ resonance to a $\Xi^{-}(1320)$ hyperon and a positive pion [39]. The observed resonance was interpreted as the exotic baryon multiplet $\Xi(1860)$ with strangeness $S = -2$, predicted by the Chiral Quark Soliton Model [17], with a crypto-exotic quark configuration $ssud\overline{d}$ for the $\Xi^{0}(1860)$ and a manifestly exotic quark configuration $ssdd\overline{u}$ for the $\Xi^{--}(1860)$. This result has never been confirmed by other experiments.

In this section the search for the exotic baryon resonance $\Xi(1860)$ at the HERMES experiment is presented. We consider the decay of the neutral and of the doubly charged members of the $\Xi(1860)$ multiplet, *i.e.* $\Xi^{--}(1860) \to \Xi^{-}(1320)\,\pi^{-}$ and $\Xi^{0}(1860) \to \Xi^{-}(1320)\,\pi^{+}$. The results are compared to the $\Xi^{0*}(1530)$ hyperon, which has the same decay channel as the $\Xi^{0}(1860)$ resonance.

First the data set and trigger configuration used for this analysis are discussed, and basic event selection criteria are described. Ghost tracks could influence the results of this analysis and have to be discarded. In addition, event selection is performed using topological information about the different tracks in the event. After determining the efficiency of event detection at the HERMES experiment in simulations, the results for the cross section are presented.

4.3.1 Data sets and event reconstruction

Trigger configuration

In the original $\Theta(1540)$ and $\Xi(1860)$ analyses at the HERMES experiment [4, 5], both polarized and unpolarized deuterium data collected during the years 1998, 1999 and 2000 were included. Later it was realized that the trigger configuration for unpolarized high density data taking during these years suppressed photoproduction events, as described in section 4.1.1. During high density data taking a minimum energy deposit in the electromagnetic calorimeter of 3.5 GeV was required, compared to 1.5 GeV for low density polarized data taking. The effect of the unpolarized high density data in the original analysis is limited to an increase of the number of background events, and the inclusion does not change the number of events in the $\Xi^{0*}(1530)$ resonance peak.

In this section the original $\Xi(1860)$ analysis, described in detail in the release report [109] and published as reference [5], is repeated using only the polarized deuterium data[3] collected during the years 1998, 1999, and 2000 (corresponding more specifically to the latest offline data productions `98d0`, `99c0`, and `00d0`). The data sample contains a total integrated luminosity of $\mathcal{L} = 209.2\,\text{pb}^{-1}$, or approximately 9.4 M DIS events collected by the HERMES detector.

[2] In its 2004 version of the Review of Particle Physics [110], the Particle Data Group has included this state under the name $\Phi(1860)$. We will continue to use the name $\Xi(1860)$ in this work, as it is commonly referenced as such in the literature.

[3] This includes both longitudinally and tensor-polarized deuterium data.

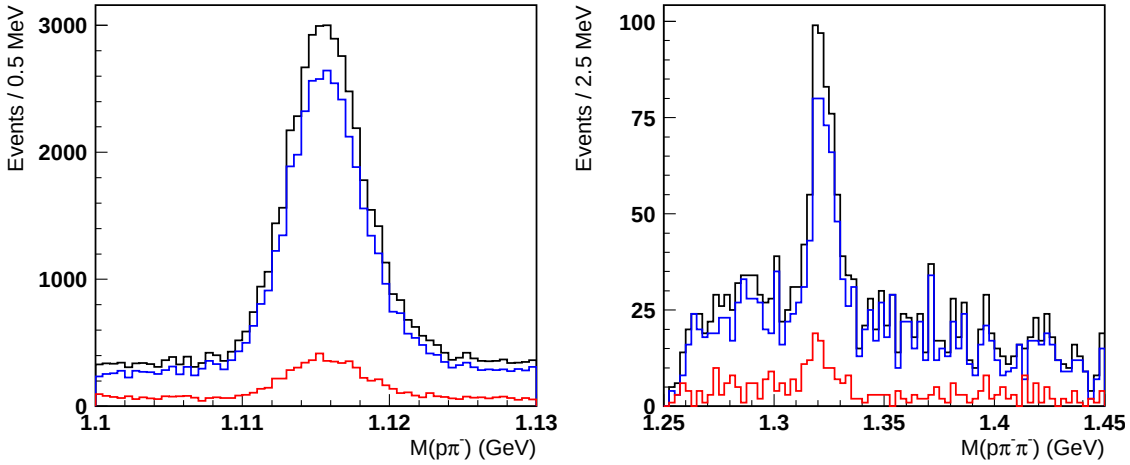

Figure 4.2: The distributions of the invariant mass $M(p\pi^-)$ (left panel) and $M(p\pi^-\pi^-)$ (right panel) for the particle (blue) and antiparticle decay chains (red), and for the combination of both (black).

Reaction channels

In the search for the exotic baryons $\Xi^{--}(1860)$ and $\Xi^0(1860)$ and the simultaneous analysis of the hyperon $\Xi^{0*}(1530)$, we considered the same decay chains as the NA49 experiment. The $\Xi^{--}(1860)$ baryon decays to a $\Xi^-(1320)$ hyperon and a negative pion π^-. The $\Xi^{0*}(1530)$ and $\Xi^0(1860)$ baryons both decay to a $\Xi^-(1320)$ hyperon and a positive pion π^+. The $\Xi^-(1320)$ hyperon in turn decays to a $\Lambda(1115)$ hyperon and a negative pion π^-. Finally, the $\Lambda(1115)$ hyperon decays to a proton p and a negative pion π^-.

In the notation for the invariant mass and other variables, the required charges of the pions are indicated consistently. The first pion always indicates the charge required for the decay pion from the $\Lambda(1115)$ hyperon, the second pion the charge required for the decay pion from the $\Xi^-(1320)$ hyperon, and the third pion the charge required for the decay pion from the $\Xi(1530)$ or $\Xi(1860)$ hyperons. Using this notation, the event candidates from a $\Xi^{0*}(1530)$ decay are denoted as $p\pi^-\pi^-\pi^+$ and the candidates from a $\Xi^{--}(1860)$ decay as $p\pi^-\pi^-\pi^-$.

Naturally, the decay chains of the antiparticles consist of the corresponding antiparticles. Whenever the charge of the proton is not explicitely indicated, antiparticle events are considered together with the corresponding particle events in all kinematic distributions. For example, when the invariant mass $M(p\pi^-\pi^-\pi^+)$ for $\Xi^{0*}(1530)$ candidate events is shown, also $\overline{\Xi}^{0*}(1530)$ candidates decaying to $\overline{p}\pi^+\pi^+\pi^-$ are included. When the charge of the proton p is indicated explicitely, only events with this proton charge are included. Anti-particle decay events contribute for approximately 20% to the total number of collected events. In figure 4.2 the distributions of the invariant mass $M(p\pi^-)$ and $M(p\pi^-\pi^-)$ are shown for particle (blue) and antiparticle (red) decay chains separately.

Magnet tracks or short tracks

Due to the high track multiplicity required for this analysis, a significant fraction of the pions in the candidate $\Xi(1860)$ decay events have a momentum low enough to be bent outside of the geometrical acceptance of the spectrometer. These *magnet tracks* or *short tracks* still generate signals in the magnet chambers (MC), located inside the spectrometer magnet, which allows their momentum to be reconstructed. They are not required to be outside of the rear field clamp or inside the electromagnetic calorimeter, as is required for regular (or long) tracks.

Because the magnet tracks do no reach the particle identification detectors, we have to make assumptions as to

the type of particle that generated the track. Since the majority of the low momentum particles at HERMES are pions, magnet tracks are usually considered to be pions. Approximately 70% of the events selected for this analysis contain at least one short pion track.

Track selection

For every event we require four or more hadron tracks in the spectrometer. Every event has to contain at least one proton p or antiproton $\overline{p}$, as identified by the RICH detector, and at least three charged pions π (either as identified by the RICH detector, or as a magnet track). The charges of the proton and pion tracks determine in which reaction channel the event will be counted.

In events with more than three charged pion tracks, all combinations with three pion tracks ($p\pi_1\pi_3\pi_4$, $p\pi_2\pi_3\pi_4$,...) are considered as separate events. Different permutations of the three pion tracks are considered, assigning each pion the roles of decay product from the $\Lambda(1115)$, $\Xi(1320)$, or $\Xi(1860)$. In the rare event that multiple permutations pass the selection criteria only one permutation is accepted in the distributions for the invariant mass $M(p\pi^-\pi^-\pi^\pm)$ to avoid double counting. All permutations correspond to the same invariant mass $M(p\pi^-\pi^-\pi^\pm)$.

No explicit momentum requirements are imposed, but the minimal momentum for pions is 0.5 GeV for magnet tracks due to the bending in the spectrometer magnet, and 1.0 GeV for identification in the RICH detector. Tracks with a momentum below 2 GeV are never identified as protons by the RICH detector. Therefore, all protons will have a momentum greater than 2 GeV.

Event reconstruction

To select only those events that can accomodate the full $\Xi(1530)$ or $\Xi(1860)$ decay chain, the invariant mass of the proton and the first pion $M(p\pi^-)$ is required to be in the $\pm 3\,\sigma$ window around the mass of the $\Lambda(1115)$ hyperon. This ensures that a $\Lambda(1115)$ candidate was present in the event. Similarly, the invariant mass $M(p\pi^-\pi^-)$ should be in the $\pm 2.5\,\sigma$ window around the mass of the $\Xi(1320)$ hyperon. Because the distribution of the invariant mass $M(p\pi^-\pi^-)$ has a significant contribution of background events under the $\Xi(1320)$ hyperon peak, the invariant mass window is chosen smaller. The numerical invariant mass ranges are determined in section 4.3.3.

The combination of the previous particle identification requirements and the invariant mass windows will be referred to as *basic selection criteria*. In figure 4.3 the distributions of the invariant masses $M(p\pi^-)$, $M(p\pi^-\pi^-)$, $M(p\pi^-\pi^-\pi^+)$ and $M(p\pi^-\pi^-\pi^-)$ are shown in black for events that satisfy the basic selection criteria.

The distributions of the invariant masses $M(p\pi^-\pi^-\pi^\pm)$ are expected to be similar in shape, due to the parallels between the decay chains $\Xi^0(1860) \rightarrow p\pi^-\pi^-\pi^+$ and $\Xi^{--}(1860) \rightarrow p\pi^-\pi^-\pi^-$. From naive combinatorics we expect the distribution of background events in the $p\pi^-\pi^-\pi^+$ spectrum to be three times larger than the background in the $p\pi^-\pi^-\pi^-$ spectrum. There are only two possibilities to have three equally charged pions, but six possibilities when one pion has a different charge. In the lower panels of figure 4.3 we observe that the $M(p\pi^-\pi^-\pi^-)$ distribution is indeed lower than the $M(p\pi^-\pi^-\pi^+)$ distribution, but by less than a factor three. However, this naive calculation does not take into account other non-combinatoric contributions to the distribution of background events.

4.3.2 Ghost tracks

In the distribution of the invariant mass $M(p\pi^-\pi^-)$ for events with a $\Lambda(1115)$ candidate, shown in the upper right panel of figure 4.3 and reproduced in the right panel of figure 4.4, the $\Xi(1320)$ hyperon is clearly visible at the expected mass, but also a strong unphysical peak is present at approximately 1280 MeV.

When the invariant mass $M(p\pi^-)$ is plotted versus the invariant mass $M(p\pi^-\pi^-)$, as shown in the left panel of figure 4.4, the $\Lambda(1115)$ hyperon is visible as a horizontal band with an accumulation of events corresponding to the $\Xi(1320)$ hyperon. In addition, an unphysical correlation between the two invariant masses shows up (between the diagonal red lines). When only the events with an invariant mass $M(p\pi^-)$ in the horizontal band are selected, the $\Xi(1320)$ hyperon is again clearly visible at the expected position in the distribution of the invariant mass $M(p\pi^-\pi^-)$. When we select only the correlated events between the diagonal red lines, the distribution shown in red is obtained, with an excess of events responsible for the unphysical peak.

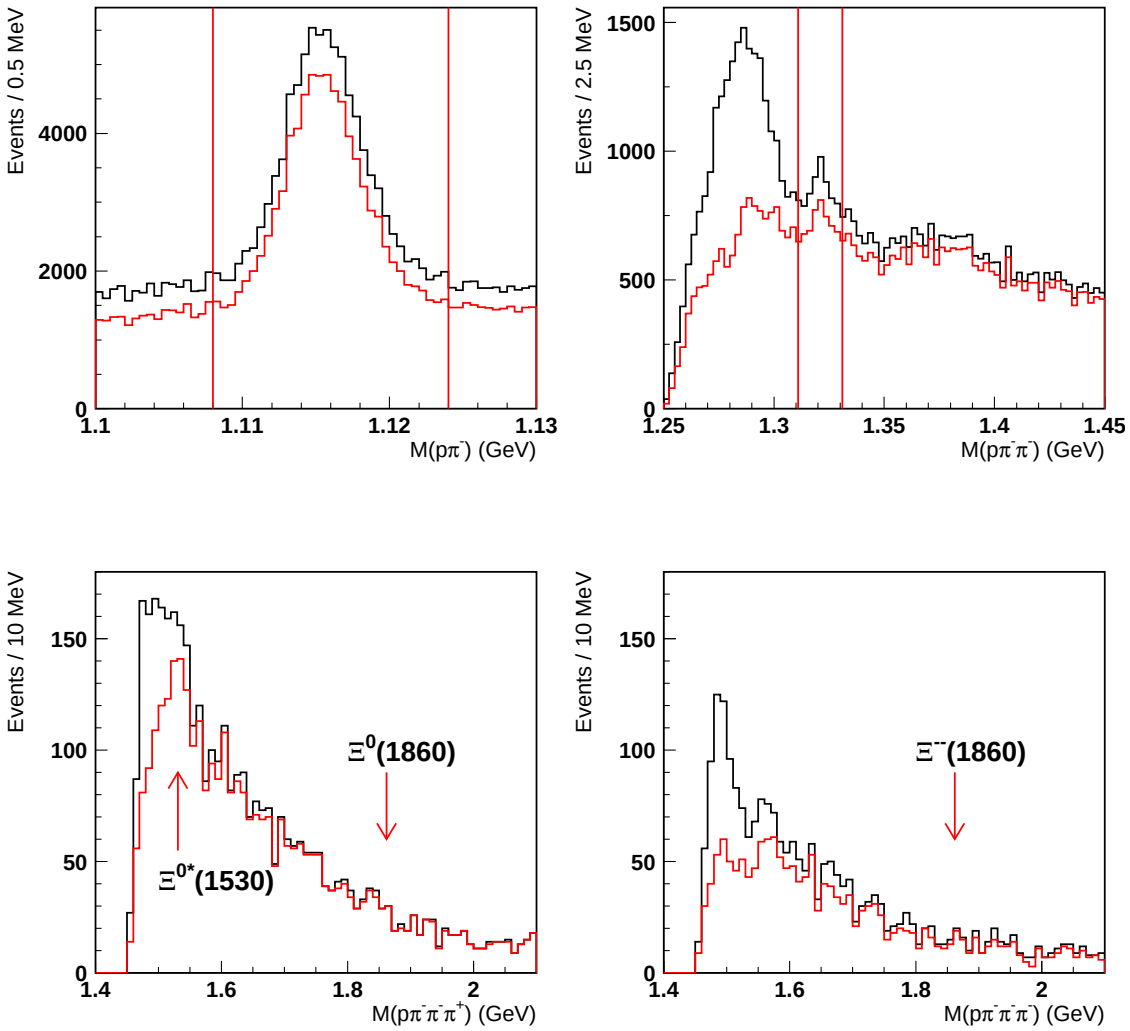

Figure 4.3: The distributions of the invariant mass $M(p\pi^-)$ (upper left panel), $M(p\pi^-\pi^-)$ (upper right panel), $M(p\pi^-\pi^-\pi^+)$ (lower left panel) and $M(p\pi^-\pi^-\pi^-)$ (lower right panel), before (black) and after (red) ghost tracks are removed (see section 4.3.2) and when the invariant mass windows between the vertical red lines are used for event selection (corresponding to the basic selection criteria). The expected position of the $\Xi(1530)$ hyperon and the $\Xi(1860)$ resonance are indicated.

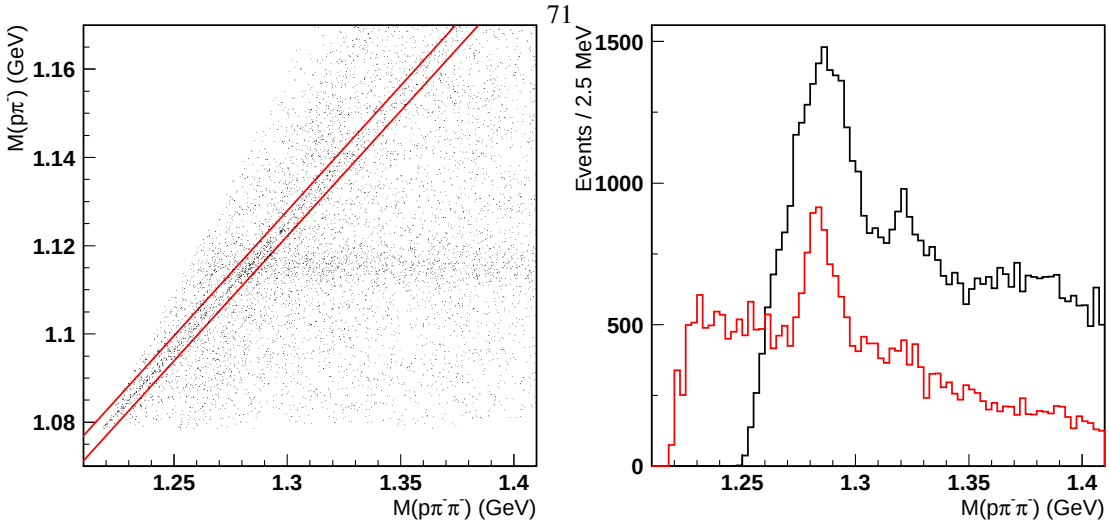

Figure 4.4: The effect of ghost tracks on the distributions of the invariant masses $M(p\pi^-)$ and $M(p\pi^-\pi^-)$. When the invariant mass $M(p\pi^-)$ is plotted versus the invariant mass $M(p\pi^-\pi^-)$ (left panel), an unphysical correlation between the two invariant masses shows up (between the diagonal red lines). When only the events with an invariant mass in the horizontal band corresponding to the $\Lambda(1115)$ candidate are selected, the $\Xi(1320)$ hyperon is clearly visible in the distribution of the invariant mass $M(p\pi^-\pi^-)$ (right panel), but a strong unphysical peak at approximately 1280 MeV forms. The distribution shown in red includes only the correlated events between the red lines.

In order to understand the correlation in figure 4.4, we selected events on the diagonal correlation line and discovered that these events are indeed responsible for the unphysical peak in the distribution of the invariant mass $M(p\pi^-\pi^-)$ (right panel of figure 4.4).

The two negative pions in the events responsible for the correlation are both magnet tracks, and they have almost the same momentum P and track angles θ and ϕ. This can be observed without any event selection criteria, as shown in figure 4.5. Magnet tracks are sometimes reconstructed twice in the same event with only slightly different track parameters. We will refer to these spurious tracks as *ghost tracks*, a term also used in the literature [49].

In this analysis, the lower limit on the decay length of the $\Lambda(1115)$ candidate indirectly removes most ghost tracks from the selected events. When very similar pion track parameters are used to reconstruct the decay vertices of the $\Lambda(1115)$ and $\Xi(1320)$ candidates, the vertices will be close together. Even though these decay length criteria will remove most of the ghost track events from the sample of selected events, we constructed a dedicated test for ghost track suppression based on the differences between the momenta ΔP, and the angles $\Delta\theta$ and $\Delta\phi$ for two like sign pions in the event. Events are rejected when the differences ΔP, $\Delta\theta$, and $\Delta\phi$ are in one of the two rectangular regions delimited by

$$|\Delta P| < 0.1\,\text{GeV}, \quad (4.3)$$
$$|\Delta\phi| < 0.3\,\text{rad}, \quad (4.4)$$
$$|\Delta\theta| < 0.03\,\text{rad}, \quad (4.5)$$

$$|\Delta P| < 0.75\,\text{GeV}, \quad (4.6)$$
$$|\Delta\phi| < 0.03\,\text{rad}, \quad (4.7)$$
$$|\Delta\theta| < 0.005\,\text{rad}. \quad (4.8)$$

Additionally, two pions in an event are required to have intersection points with the $z = 0$ plane separated by a distance larger than 0.0001 cm. This value, much smaller than the resolution of the track reconstruction, was chosen such that no legitimate events have a smaller track separation, but ghost track have a separation of exactly zero. The intersection of a track with the $z = 0$ plane his used as a track parameter in the HERMES data, and comes directly from the track reconstruction algorithm.

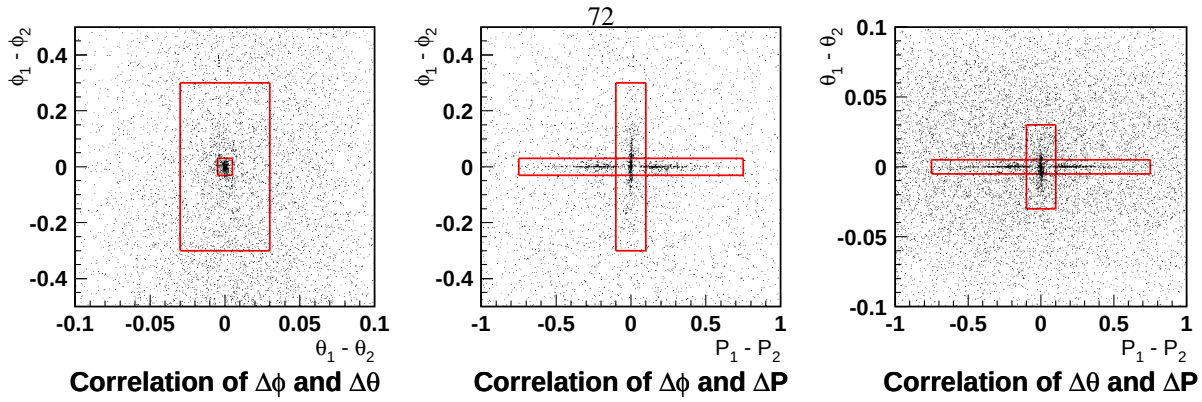

Figure 4.5: The difference of the track angles θ and ϕ, and the momentum P for two like sign pion tracks in the same event indicates that the track reconstruction code introduces ghost tracks. The structure in the correlation of the angles θ or ϕ, and the momentum difference for the two pions is not understood. The ghost track suppression regions (see text) are indicated in red. To prevent overpopulation only a fraction of the events is drawn.

The effect of the ghost track suppression on the distribution of the invariant mass $M(p\pi^-\pi^-)$, before applying the decay length and DCA selection criteria, is shown in figure 4.6. Not every trace of the fake peak has disappeared, but since we select only events inside the $\Xi(1320)$ peak, the possible effect of ghost tracks on this analysis will be negligible.

With a similar layout as figure 4.3 before event selection, figure 4.15 presents the distributions of the invariant mass $M(p\pi^-)$, $M(p\pi^-\pi^-)$, $M(p\pi^-\pi^-\pi^+)$, and $M(p\pi^-\pi^-\pi^-)$ after event selection and ghost track suppression. In the first figure the black distributions include ghost track events, and the red distributions were obtained after ghost track suppression. The large effect in the upper right panel of figure 4.3 is drastically reduced when the selection criteria (in particular the lower limit on the decay length) are introduced. The influence of ghost tracks on this analysis is assumed to be removed.

In principle this ghost track problem should be resolved at the track reconstruction level, which is outside the scope of this thesis. A remaining correlation seems to be present in the left panel of figure 4.6, but no particular anomaly for events in that region could be determined.

4.3.3 Event selection

In addition to the basic selection criteria discussed in section 4.3.1, the topology of each event is used to select candidate $\Xi(1530)$ and $\Xi(1860)$ decay events. Since the $\Xi(1530)$ and $\Xi(1860)$ resonances both have decay modes to the $\Xi(1320)$ hyperons, which in turn decays to $\Lambda(1115)$ hyperons, these hyperons have to be reconstructed from the detected final state. To select events which can accomodate the full decay chain, we used selection criteria based on the distance of closest approach between two tracks, the decaylength of a resonance candidate (defined as the distance between the production and the decay vertex), and the invariant mass of the intermediate resonances.

Method for determination of optimal selection parameters

In order to determine the optimal selection criteria, we studied each selection variable individually, while keeping the other selection criteria unchanged. In the distributions of selection variables in the following subsection, events are included that satisfy all but the criteria under study.

We used the optimization method described in section 4.2.3. The criteria were optimized using the well established $\Lambda(1115)$ and $\Xi(1320)$ hyperons. For example, the distance of closest approach between the proton and pion tracks at the $\Lambda(1115)$ decay vertex was optimized using events in the $\Lambda(1115)$ peak and sideband regions in the distribution of

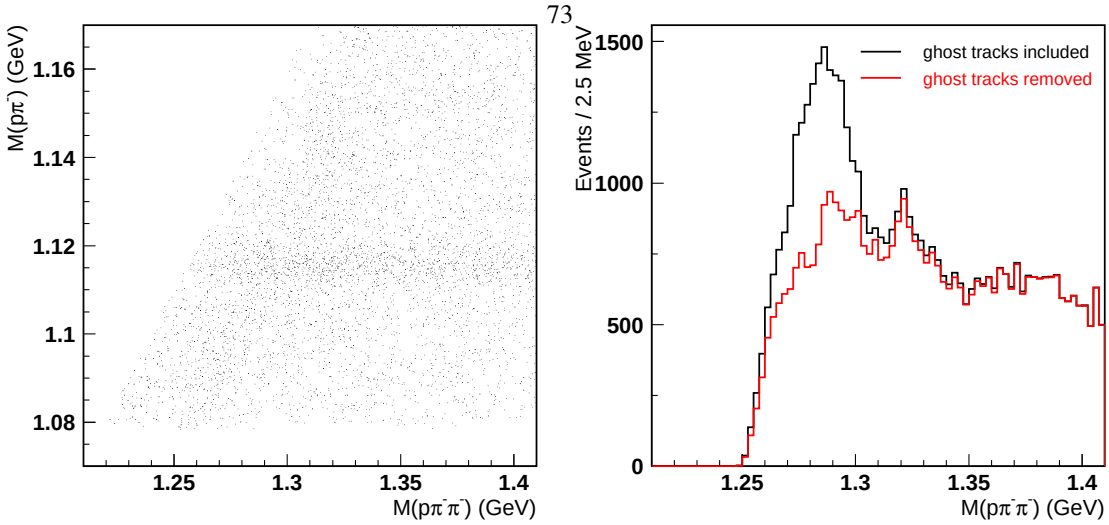

Figure 4.6: The suppresion of ghost tracks in the distributions of the invariant masses $M(p\pi^-)$ and $M(p\pi^-\pi^-)$. In the correlations between the invariant mass $M(p\pi^-)$ and $M(p\pi^-\pi^-)$ (left panel), the unphysical correlation is removed. In the distribution of the invariant mass $M(p\pi^-\pi^-)$ (right panel), the unphysical peak at 1280 MeV is strongly reduced after ghost track suppression (red).

the invariant mass $M(p\pi^-)$. Similarly, the distance of closest approach between the $\Lambda(1115)$ and pion tracks at the $\Xi(1320)$ decay vertex was optimized using events in the $\Xi(1320)$ peak and sideband regions.

Since the peak of the $\Xi^{0*}(1530)$ hyperon in the distribution of the invariant mass $M(p\pi^-\pi^-\pi^+)$ is not very prominent (see figure 4.3), we used the same optimization technique but intentionally extend the allowed ranges to values that are assumed to be safe. This avoids narrow kinematic selection when the motivation is not convincing. Also, it allows the extrapolation of the selection criteria to the $\Xi^{--}(1860)$ decay chain.

$\Lambda(1115)$ selection

To select events containing a $\Lambda(1115)$ candidate, we use the distance of closest approach $DCA(p,\pi)$ between the proton track and the pion track. The midpoint of the segment of closest approach defines the decay vertex of the $\Lambda(1115)$ candidate. Due to the long lifetime of the $\Lambda(1115)$ hyperon, the longitudinal decay length $\Delta Z(\Lambda)$, defined as the difference between the z-coordinates of the production and decay vertex, is required to be large. Finally, the invariant mass $M(p\pi^-)$ has to be inside a $\pm 3\,\sigma$ window around the determined $\Lambda(1115)$ mass.

Distance of closest approach between the proton and pion tracks In the left panel of figure 4.7 the normalized distributions of the distance of closest approach $DCA(p,\pi)$ between the proton and pion tracks for signal and background events are shown. The signal events (red) have a narrow distribution compared to the distribution for the background events (blue). The difference between the two distributions is shown in the right panel, and is used to determine the value of the distance of closest approach below which an event is more likely a signal event than from background. The upper limit for the distance of closest approach is chosen at 1.5 cm.

Longitudinal decay length of the $\Lambda(1115)$ candidate In the left panel of figure 4.8 the normalized distributions of the longitudinal decay length $\Delta Z(\Lambda)$ of the $\Lambda(1115)$ candidate for signal and background events are shown. The signal events (red) have longer decay lengths than background events (blue). Above 7.0 cm signal events are more

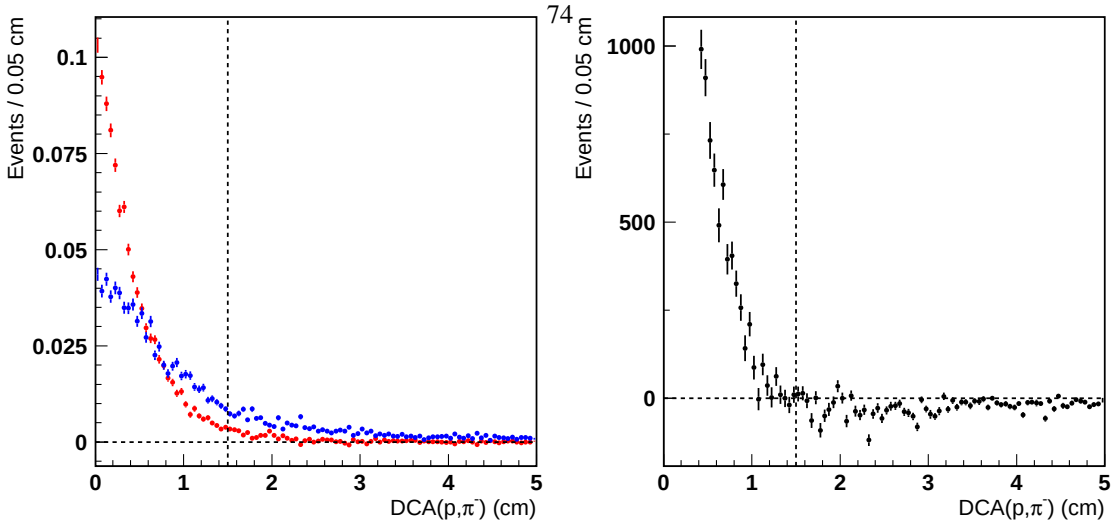

Figure 4.7: The normalized distributions of the distance of closest approach $DCA(p, \pi)$ between the proton and pion tracks from the decay of the Λ candidate (left panel), for signal (red) and the background events (blue), and the difference between signal and background distributions (right panel). The vertical lines indicate the maximum distance of closest approach allowed by the selection criteria.

likely to be accepted than background events, so that value is used as the lower limit for the decay length of the $\Lambda(1115)$ candidate.

Distribution of the invariant mass $M(p\pi^-)$ In figure 4.9 the distribution of the invariant mass $M(p\pi^-)$ is shown. When we fit the distribution with a Gaussian function on top of a second order polynomial background shape, the mean value of the peak is 1115.79 ± 0.012 MeV and the width is 2.58 ± 0.018 MeV. The $\pm 3\,\sigma$ interval around the central value corresponds with the range $1.108 < M(p\pi^-) < 1.124$ GeV.

$\Xi(1320)$ selection

We proceed one step up the decay chain with the requirements for the $\Xi(1320)$ candidate. The distance of closest approach $DCA(\Lambda, \pi)$ between the reconstructed $\Lambda(1115)$ track and the pion track is used to select $\Xi(1320)$ candidates. The midpoint of the segment of closest approach defines the decay vertex of the $\Xi(1320)$ candidate and the production vertex of the $\Lambda(1115)$ candidate. The longitudinal decay length $\Delta Z(\Lambda)$ of the $\Xi(1320)$ candidate is required to be large, again motivated by the long lifetime of the $\Xi(1320)$ hyperon. The invariant mass $M(p\pi\pi)$ has to be inside a $\pm 2.5\,\sigma$ window around the determined $\Xi(1320)$ mass.

Distance of closest approach between the $\Lambda(1115)$ and pion tracks In the left panel of figure 4.10 the normalized distributions of the distance of closest approach $DCA(\Lambda, \pi)$ between the reconstructed $\Lambda(1115)$ track and the pion track for signal and background events are shown. The signal events (red) have a narrower distribution than the background events (blue), although the difference is not as pronounced as for the $\Lambda(1115)$ vertex. The difference between the two distributions is shown in the right panel. The upper limit for the distance of closest approach is chosen at 1.0 cm.

Longitudinal decay length of the $\Xi^-(1320)$ candidate In the left panel of figure 4.11 the normalized distributions of the longitudinal decay length $\Delta Z(\Xi)$ of the $\Xi(1320)$ candidate for signal and background events are shown. The

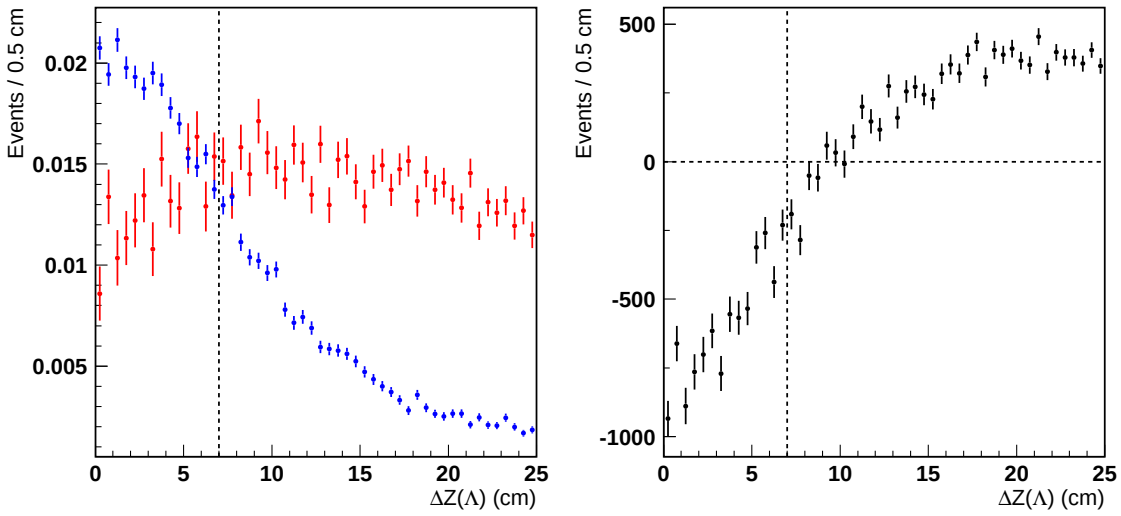

Figure 4.8: The normalized distributions of the longitudinal decay length $\Delta Z(\Lambda)$ of the $\Lambda(1115)$ candidate (left panel), for signal (red) and the background events (blue), and the difference between signal and background distributions (right panel). The vertical lines indicate the minimum decay length required by the selection criteria.

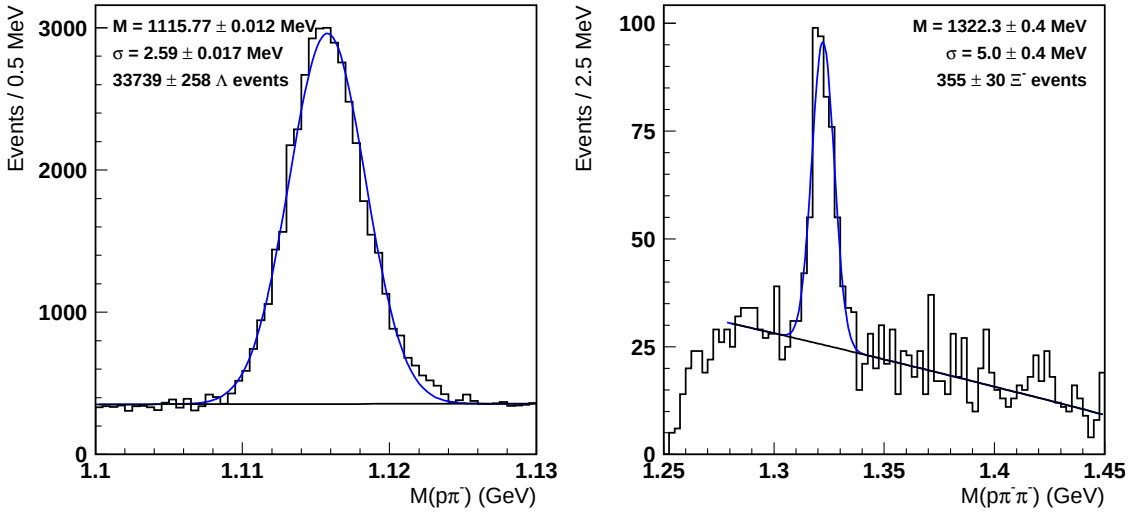

Figure 4.9: The distributions of the invariant masses $M(p\pi^-)$ (left panel) and $M(p\pi^-\pi^-)$ (right panel) after applying event selection criteria, fitted with a Gaussian function on top of a second order polynomial background shape.

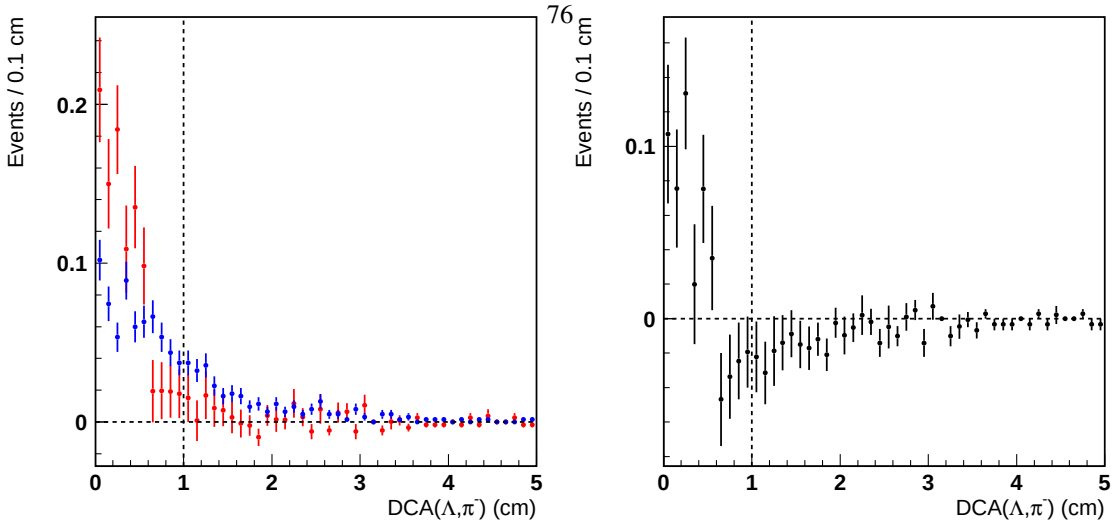

Figure 4.10: The normalized distributions of the distance of closest approach $DCA(\Lambda, \pi)$ between the $\Lambda(1115)$ candidate and the pion track (left panel), for signal (red) and the background events (blue), and the difference between signal and background distributions (right panel). The vertical lines indicate the maximum distance of closest approach allowed by the selection criteria.

signal events (red) have longer decay lengths than background events (blue). Above 10.0 cm signal events are more likely to be accepted than background events, so that value is used as the lower limit for the decay length of the $\Lambda(1115)$ candidate.

Distribution of the invariant mass $M(p\pi^-\pi^-)$ In figure 4.9 the distribution of the invariant mass $M(p\pi^-\pi^-)$ is shown for events. When we fit the distribution with a Gaussian function on top of a second order polynomial background shape, the mean value of the peak is 1322.3 ± 0.4 MeV and the width is 5.0 ± 0.3 MeV. The $\pm 2.5\,\sigma$ interval around the central value corresponds with the range $1.309 < M(p\pi^-\pi^-) < 1.335$ GeV.

$\Xi(1530)$ and $\Xi(1860)$ selection

Finally, to select $\Xi(1530)$ and $\Xi(1860)$ candidate events, the distance of closest approach $DCA(\Xi, \pi)$ between the reconstructed $\Xi(1320)$ track and the pion track at the $\Xi(1530)$ or $\Xi(1860)$ decay vertex can be used as a selection variable. The midpoint of the segment of closest approach defines the production vertex of the $\Xi(1320)$ candidate.

Distance of closest approach between the $\Xi(1320)$ **and pion tracks** Due to the low number of events with a $\Xi(1320)$ candidate track, it is difficult to find an optimal value for the distance of closest approach $DCA(\Xi, \pi)$ between the $\Xi(1320)$ and pion tracks. In figure 4.12 the normalized distribution of this variable is shown for signal and background events. To avoid any bias, but at the same time remove unphysical events, we decide to select all events with a distance of closest approach smaller than 2.5 cm. This removes only outliers in the distribution.

Event production vertex

The event production vertex is defined as the midpoint of the segment of closest approach between the lepton beam and the reconstructed $\Xi(1530)$ or $\Xi(1860)$ track. In figure 4.13 the transverse and longitudinal coordinates of the production vertex are shown for signal and background events in the $\Xi^{0*}(1530)$ peak. The number of events

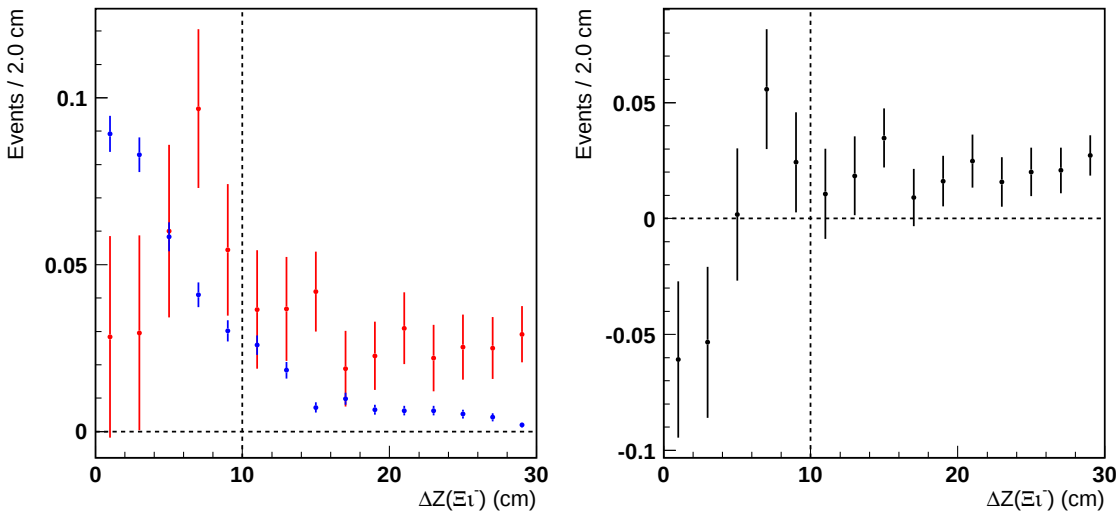

Figure 4.11: The normalized distributions of the longitudinal decay length $\Delta Z(\Xi)$ of the $\Xi(1320)$ candidate (left panel), for signal (red) and the background events (blue), and the difference between signal and background distributions (right panel). The vertical lines indicate the minimum decay length required by the selection criteria.

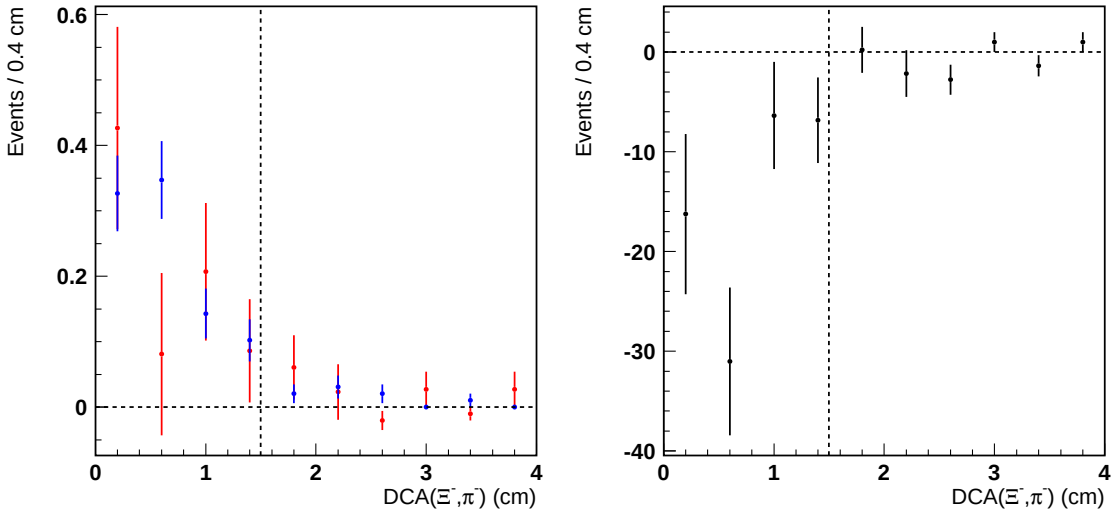

Figure 4.12: The normalized distributions of the distance of closest approach $DCA(\Xi, \pi)$ between the Ξ^- candidate and the pion track from the decay of the Ξ^{0*} candidate (left panel), for signal (red) and background events (blue), and the difference between signal and background distributions (right panel). The vertical lines indicate the maximum distance of closest approach allowed by the selection criteria.

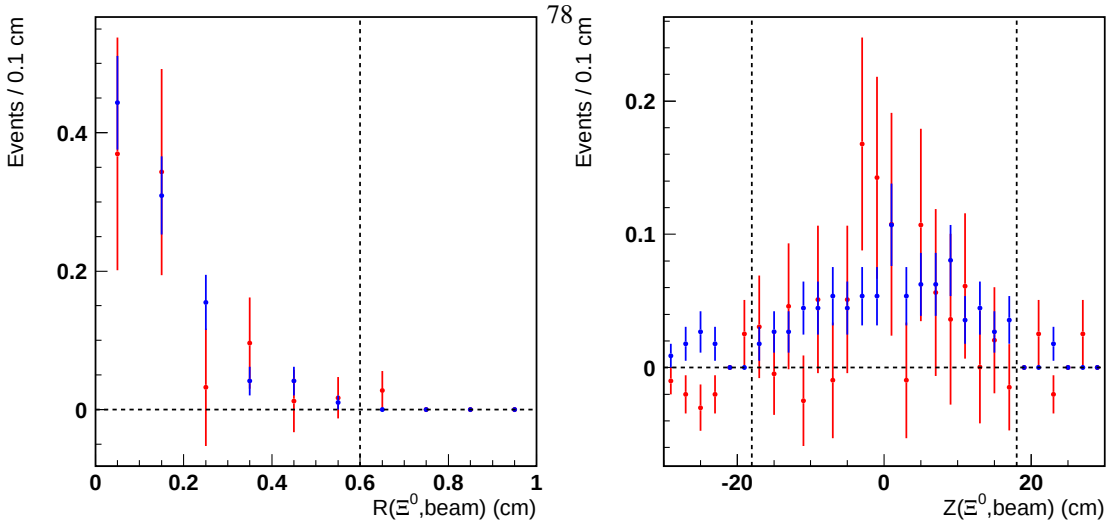

Figure 4.13: The normalized distributions of the transverse (left panel) and longitudinal (right panel) coordinates of the production vertex of the Ξ^{0*} candidate, for signal (red) and background events (blue).

in these distributions is very low and the low statistical precision makes it difficult to conclude on any meaningful limits. We therefore decide to use the following commonly accepted selection criteria. By imposing a maximum allowed transverse distance between the production vertex and the lepton beam of 0.6 cm, we ensure that the selected events originate from beam-target interactions. We ensure that the production vertex is located inside the target cell by requiring longitudinal coordinates between -18.0 cm and 18.0 cm.

Contamination from K^0_S events

In figure 4.14 the distribution of the invariant mass of the oppositely charged pions $M(\pi^+\pi^-)$ is shown for the $\Xi^{0*}(1530)$ candidate events. There is no peak visible at the mass of the K^0_S resonance, indicating that there is negligible contamination from this resonance. We decided not to discard events in an invariant mass windows around the K^0_S peak.

Summary of the event selection criteria

In figure 4.15 the invariant mass distributions of $M(p\pi^-)$, $M(p\pi^-\pi^-)$, $M(p\pi^-\pi^-\pi^+)$, and $M(p\pi^-\pi^-\pi^-)$ are shown for events satisfying the event selection criteria and ghost track suppression outlined in the previous sections.

4.3.4 Detector acceptance and selection efficiency

As described in section 3.4, the HERMES spectrometer is a forward detector and does not cover the full 4π geometrical acceptance in which resonance cross sections are usually specified. In order to calculate the cross section (or an upper limit) for the photoproduction of the baryons $\Xi(1530)$ and $\Xi(1860)$ from the observed events in the HERMES spectrometer, we need to determine the fraction of the produced events that are first detected in the spectrometer, and also satisfy the selection criteria listed in section 4.3.3. The combined effect of the detector acceptance and the selection efficiency will be referred to as the *efficiency*.

Since the production mechanism of $\Xi(1860)$ baryons is unknown, we used the Monte Carlo generator gmc_dcay, described in section 3.4, and varied the parameters of the internal model. For the $\Xi(1530)$ hyperon the initial momen-

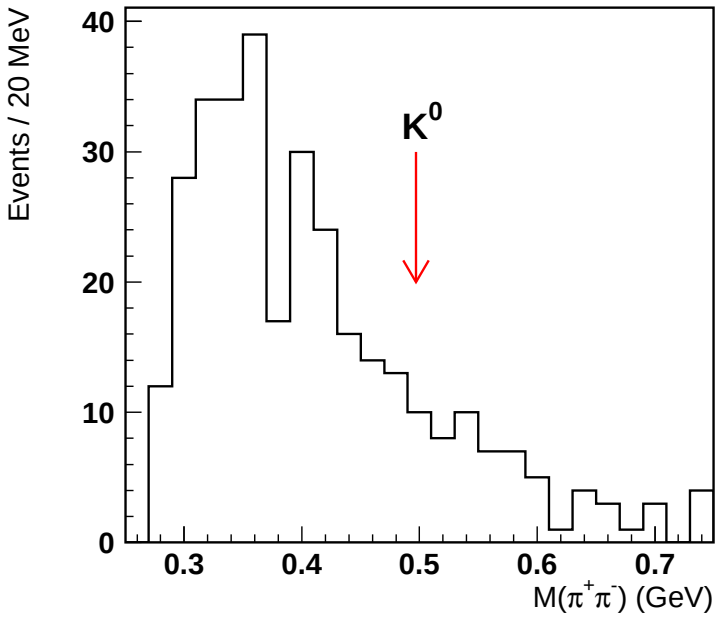

Figure 4.14: The distributions of the invariant mass $M(\pi^+\pi^-)$ for the two oppositely charged pions in $\Xi^{0*}(1530)$ candidate events. No K^0_S peak can be observed at the expected mass, indicated by the arrow.

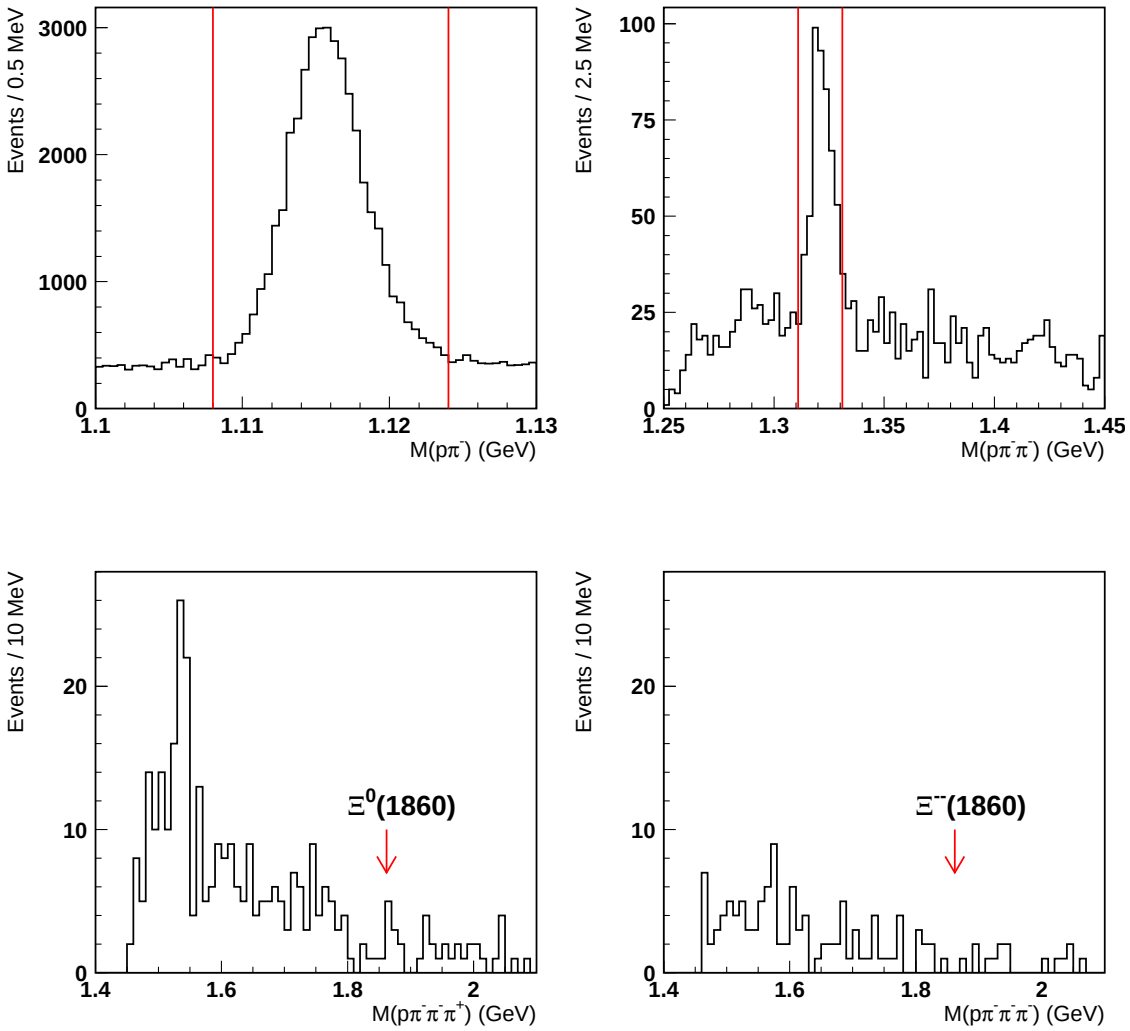

Figure 4.15: The distributions of the invariant mass $M(p\pi^-)$ (upper left panel), $M(p\pi^-\pi^-)$ (upper right panel), $M(p\pi^-\pi^-\pi^+)$ (lower left panel) and $M(p\pi^-\pi^-\pi^-)$ (lower right panel), after ghost tracks are removed. The expected position of the $\Xi^{0*}(1530)$ hyperon and the $\Xi(1860)$ resonance are indicated.

Table 4.3: The efficiency for $\Xi^{--}(1860)$ events from gmc_dcay Monte Carlo simulations with different values of the width $\sigma(P_t)$ of the transverse momentum distribution and the mean $\langle P_z \rangle$ of the longitudinal momentum distribution.

$\sigma(P_t)$ (GeV)	0.2	0.3	0.4	0.4	0.4	0.4
$\langle P_z \rangle$ (GeV)	3.95	3.95	3.95	3.67	3.95	4.22
efficiency (%)	0.022	0.027	0.031	0.028	0.031	0.027

tum distributions P_t and P_z from a PYTHIA Monte Carlo simulation were used as input for the gmc_dcay Monte Carlo generator.

Efficiency for $\Xi^{--}(1860)$ events

With the gmc_dcay Monte Carlo generator, $\Xi^{--}(1860)$ events were generated with an invariant mass distribution with mean $M = 1862$ MeV and finite but small intrinsic width $\Gamma = 2$ MeV. The unknown initial momentum distribution of the $\Xi(1860)$ baryon was modeled as a Gaussian distribution with width $\sigma(P_t)$ for the transverse momentum P_t, and a monotonically falling distribution with mean $\langle P_z \rangle$ for the longitudinal momentum P_z. The Gaussian width σ of the reconstructed mass peak is 10.2 MeV, defining the experimental resolution in the invariant mass $M(p\pi^-\pi^-\pi^-)$.

We varied the parameters of the initial momentum distributions P_t and P_z to determine the effects on the efficiency. Changing the width of the transverse momentum distribution $\sigma(P_t)$ from 0.4 GeV to 0.2 GeV corresponds to a decrease of 30% in the efficiency (a wider transverse momentum distributions P_t will lead to more events in the detector acceptance). The average longitudinal momentum $\langle P_z \rangle$ was changed from the default value 3.9 GeV by 0.3 GeV in both directions without a significant effect on the efficiency.

The efficiency for $\Xi^{--}(1860)$ decay events with these momentum distributions is summarized in table 4.3. We conclude that the final acceptance is quite insensitive to variations in the longitudinal momentum distribution P_z, but varies mildly with the width of the transverse momentum distribution P_t. No simulations were performed for the $\Xi^0(1860)$ baryon, and the efficiency is assumed to be equal as for $\Xi^{--}(1860)$ decay events.

Efficiency for $\Xi^{0*}(1530)$ events

For the $\Xi^{0*}(1530)$ hyperon we repeated the same procedure as for the $\Xi^{--}(1860)$ baryon. Since the $\Xi^{0*}(1530)$ is a P_{13} resonance with non-zero spin, and at the time of writing it was not possible to generate these states with the gmc_dcay Monte Carlo generator, we simulated only isotropic decays. $\Xi^{0*}(1530)$ events were generated with the gmc_dcay Monte Carlo generator using a Gaussian mass distribution with width $\Gamma = 2$ MeV around the central value 1530 MeV. The Gaussian width σ of the reconstructed mass peak is 7.3 MeV, defining the experimental resolution in the invariant mass $M(p\pi^-\pi^-\pi^+)$.

The parameters of the initial momentum distributions P_t and P_z were varied. In table 4.4 the efficiency for $\Xi^{0*}(1530)$ baryons is summarized for the different parameters for the initial momentum distributions that were simulated. The variation of the efficiency with the average longitudinal momentum $\langle P_z \rangle$ is small, but for the $\Xi^{0*}(1530)$ hyperon the width of the transverse momentum distribution has more influence.

The $\Xi^{0*}(1530)$ hyperon can also be simulated with the PYTHIA Monte Carlo generator. The generation of events with the PYTHIA Monte Carlo generator is many times slower than with the gmc_dcay Monte Carlo generator, and only a small number of events in the detector acceptance could be obtained. A sufficiently large number of $\Xi^{0*}(1530)$ events could be simulated in the full 4π acceptance, but the small detector acceptance reduced this number enormously, resulting in only a few candidate events after event selection. In figure 4.16 (left panel) the full simulated sample is presented before and after event selection. The result for the efficiency for the $\Xi^{0*}(1530)$ hyperon is summarized in table 4.5, but this should only be considered as an order of magnitude, not as a precise value.

From the PYTHIA Monte Carlo simulation in the full 4π acceptance (with a sufficiently large number of events) we extracted the initial momentum distributions of the $\Xi^{0*}(1530)$ hyperon. These distributions were then used as input for the gmc_dcay Monte Carlo generator and the efficiency was extracted using a large number of simulated events.

Table 4.4: The efficiency for $\Xi^{0*}(1530)$ events from gmc_dcay Monte Carlo simulations with different values of the width $\sigma(P_t)$ of the transverse momentum distribution and the mean $\langle P_z \rangle$ of the longitudinal momentum distribution.

$\sigma(P_t)$ (GeV)	0.3	0.4	0.4	0.4	0.4
$\langle P_z \rangle$ (GeV)	3.95	3.95	3.67	3.95	4.22
efficiency (%)	0.026	0.036	0.032	0.036	0.035

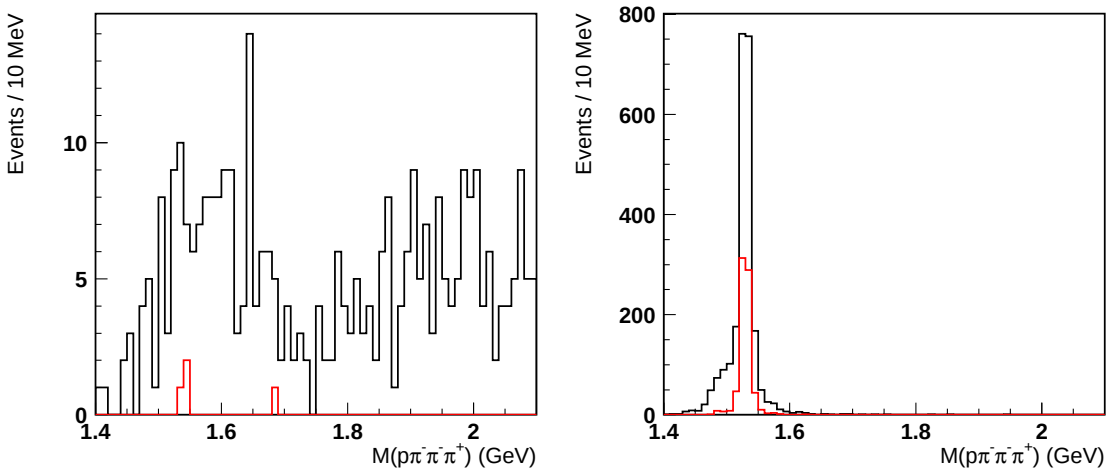

Figure 4.16: The reconstructed $\Xi^{0*}(1530)$ peak obtained with the PYTHIA Monte Carlo generator (left panel) and with the gmc_dcay Monte Carlo generator using the decay angular distribution obtained from the PYTHIA simulation (right panel). The distributions in black are obtained with all simulated events, in red after event selection. In table 4.5 the number of generated and accepted events are summarized.

The determined efficiency for the $\Xi^{0*}(1530)$ hyperon is given in table 4.5. In figure 4.16 the simulated $\Xi^{0*}(1530)$ peak is shown before and after event selection. The event selection criteria reduce the number of events by a factor three.

4.3.5 Determining the number of $\Xi(1530)$ and $\Xi(1860)$ events

The distributions of the invariant masses $M(p\pi^-\pi^-\pi^+)$ and $M(p\pi^-\pi^-\pi^-)$ are shown as figure 4.17 for events satisfying the selection criteria determined in section 4.3.3. A peak corresponding to the $\Xi^{0*}(1530)$ hyperon is visible, but in the region around 1860 MeV no structure is observed.

To determine the central value of the $\Xi^{0*}(1530)$ peak and the upper limits on the number of $\Xi^0(1860)$ and $\Xi^{--}(1860)$ events in the region around 1860 MeV, we needed to estimate the number of background events. We used the event mixing method to obtain a description of the background shape. Several precautions had to be taken before a reliable estimate was obtain. A discussion of the event mixing method will be given in section 4.7. By combining a $\Xi(1320)$ candidate from one event with pions from other events, we obtain a statistically uncorrelated sample of mixed events in which we do not expect to see any narrow resonances. We can use the distributions of the invariant mass $M(p\pi^-\pi^-\pi^+)$ and $M(p\pi^-\pi^-\pi^-)$ for mixed events as estimates for the distributions of background events. Because we can take a large number of mixing combinations, the statistical precision of the mixed event distributions

Table 4.5: The results of the Monte Carlo simulation of the $\Xi^{0*}(1530)$ with PYTHIA and with gmc_dcay using the decay angular distribution obtained from the PYTHIA simulation. The value obtained directly from the PYTHIA simulation is based on only a handful of events for which all decay products were inside the acceptance of the spectrometer. Due to the large statistical uncertainty it is therefore given in parentheses and only indicative of the order of magnitude.

Generator P_t, P_z	PYTHIA simulated	gmc_dcay from PYTHIA
efficiency (%)	(0.15)	0.10

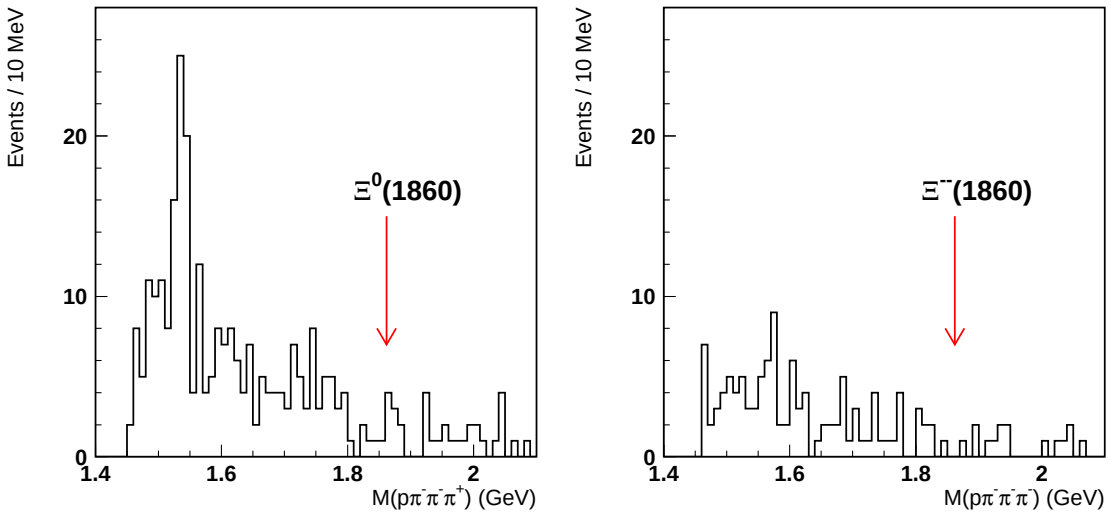

Figure 4.17: The distributions of the invariant masses $M(p\pi^-\pi^-\pi^+)$ (left panel) and $M(p\pi^-\pi^-\pi^-)$ (right panel) after event selection.

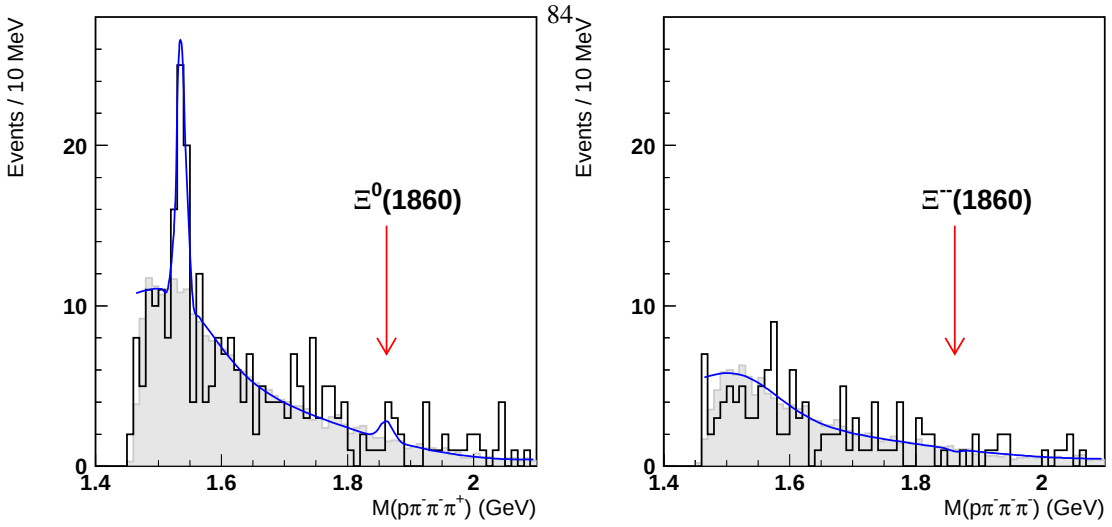

Figure 4.18: The distributions of the invariant mass $M(p\pi^-\pi^-\pi^+)$ and $M(p\pi^-\pi^-\pi^-)$ after removing ghost tracks and applying all selection criteria. The fit to the mixed event background (green) describes the distribution well in the relevant region above 1.48 GeV. The fit was allowed to accommodate a Gaussian peak at 1862 MeV in both channels, but the number of events is consistent with zero.

is considerable better than for the original distributions. The invariant mass distributions for mixed events was fitted with the sum of a fourth order polynomial and a Gaussian with large width, which describes the shape sufficiently well above 1.48 GeV.

To determine the number of $\Xi^{0*}(1530)$ events, the shape of the mixed event distribution was fixed but the normalization allowed to vary. Additionally, two Gaussian functions were added to describe the $\Xi^{0*}(1530)$ hyperon and the $\Xi^0(1860)$ resonance. For the $\Xi^0(1860)$ resonance we fixed the mass to 1862 MeV and the width to the resolution of 10.2 MeV, determined with Monte Carlo simulations (section 4.3.4). After fitting we find for the $\Xi^{0*}(1530)$ a mass $M = 1536.5 \pm 2.5$ MeV and a width $\sigma = 6.9 \pm 1.6$ MeV, consistent with the resolution determined with Monte Carlo simulations (section 4.3.4). The number of events in the $\Xi^{0*}(1530)$ peak equals 29 ± 8. For the $\Xi^{0*}(1860)$ resonance the number of events is 3 ± 3, consistent with zero.

Similarly, one Gaussian function with fixed mass and width was added to describe the $\Xi^{--}(1860)$ resonance. For the $\Xi^{--}(1860)$ resonance the number of events in the peak is 0 ± 5, consistent with zero.

The uncertainty on the number of events is calculated from the fit results assuming a Gaussian uncertainty distribution. For a small number of events, however, a Poisson distribution is more appropriate. With a 90% confidence level, the actual number of events is less than 7.4 for the $\Xi^0(1860)$ resonance, and less than 2.4 for the $\Xi^{--}(1860)$ resonance [1].

4.3.6 $\Xi(1530)$ and $\Xi(1860)$ cross sections

The cross section $\sigma_{\gamma N \to \Xi X}$ for photoproduction of a the resonance Ξ on a deuterium target is given by

$$\sigma_{\gamma D \to \Xi X} = \frac{\sigma_{eD \to \Xi X}}{\Phi}, \tag{4.9}$$

$$= \frac{N^{\Xi \to p\pi\pi\pi}_{produced}}{\Phi \cdot Br \cdot L}, \tag{4.10}$$

$$= \frac{N^{\Xi \to p\pi\pi\pi}_{observed}}{\Phi \cdot Br \cdot L \cdot \epsilon}. \tag{4.11}$$

The photoproduction cross section is related to the electro-production $\sigma_{\gamma N \to \Xi X}$ by the photon flux factor Φ. At the HERMES experiment the flux factor is $\Phi = 0.02\,\mathrm{GeV}^{-3}$. The electro-production cross section is calculated using the integrated luminosity $\mathcal{L} = 209.2\,\mathrm{pb}^{-1}$, the branching ratio Br of the decay channel $\Xi \to p\pi\pi\pi$, and the number of produced decay events $N_{produced}^{\Xi \to p\pi\pi\pi}$. To determine the number of produced events from the number of observed events $N_{observed}^{\Xi \to p\pi\pi\pi}$, the efficiency ϵ determined in section 4.3.4 is used.

For the decay of the $\Xi^{0*}(1530)$ hyperon, the efficiency varies between 0.036% and 0.10%, depending on the model for the production mechanism. The larger value was obtained from gmc_dcay Monte Carlo simulations with initial momentum distributions from PYTHIA Monte Carlo simulations, whereas for the smaller value the internal model of gmc_dcay was used. For the $\Xi^0(1860)$ and $\Xi^{--}(1860)$ resonances, the efficiency is between 0.022% and 0.031% depending on the parameters P_t and P_z of the initial momentum distributions.

For the decay of the $\Xi^0(1860)$ and $\Xi^{--}(1860)$ resonances the branching ratio Br is equal to 1. The 90% confidence level upper limit on the photoproduction cross section $\sigma_{\gamma D \to \Xi^{--}(1860)X}$ is between 1.9 nb and 2.7 nb. For the cross section $\sigma_{\gamma D \to \Xi^0(1860)X}$ we find an upper limit between 5.7 nb and 8.1 nb, depending on the kinematic model used in determining the efficiency.

The decay of the $\Xi^{0*}(1530)$ hyperon to $Xi^-\pi^+$ has a branching ratio $Br = \frac{2}{3}$. The photoproduction cross section $\sigma_{\gamma N \to \Xi^{0*}(1530)X}$ is then between 10.4 ± 2.9 nb and 28.8 ± 8.0 nb.

The main source of systematic uncertainty on the determined cross section and upper limits is the unknown production mechanism for the $\Xi^{0*}(1530)$, $\Xi^0(1860)$ and $\Xi^{--}(1860)$ resonances. Although the $\Xi^{0*}(1530)$ resonance is simulated in the PYTHIA Monte Carlo generator, it is not clear whether a realistic model for its production mechanism is used. The gmc_dcay Monte Carlo generator makes assumptions on the momentum distributions P_t and P_z, which are based on the extrapolation of the production mechanism of known hyperons.

4.3.7 Summary and conclusion

We have shown that at the HERMES experiment the neutral and doubly-charged members of the exotic baryon multiplet $\Xi(1860)$ could not be detected in the expected invariant mass region in a total integrated luminosity of $209.2\,\mathrm{pb}^{-1}$. The hyperon $\Xi^{0*}(1530)$ is observed at an invariant mass of 1536.5 ± 2.5 MeV, compared to the the world average value $M = 1531.8 \pm 0.3$ MeV [1]. This difference between the determined mass and the world average is very similar to the observed difference for $\Lambda(1520)$ hyperons due to the effect of a variable acceptance in the mass region around the peak.

After Monte Carlo simulations of the $\Xi^{--}(1860)$ baryon, performed with the gmc_dcay Monte Carlo generator, we determined that the detector acceptance and selection efficiency for $\Xi^{--}(1860)$ decay events is between 0.022% and 0.031%. The yield of $\Xi^{--}(1860)$ decay events is less than one event, corresponding to an upper limit (at 90% confidence level) on the photoproduction cross section of 2.7 nb for the doubly-charged member, and 8.1 nb for the neutral member of the $\Xi(1860)$ multiplet, assuming equal detector acceptance and selection efficiency.

The cross section for photoproduction of the $\Xi^{0*}(1530)$ hyperon was determined to be between 10.4 nb and 28.8 nb. The large systematic uncertainty is due to the unknown production mechanism of the $\Xi^{0*}(1530)$ hyperon.

4.4 Search for the exotic baryon Θ^+ using time-of-flight identification

In this section we present the search for the exotic baryon Θ^+ in the same data set used for the original analysis at the HERMES experiment [4] but using events with a different kinematic behavior. The observation of the exotic baryon Θ^+ in these events could be considered a confirmation of the original observation. A null result would not contradict the original analysis but provide important information on the production mechanism of the exotic baryon Θ^+ if its existence is confirmed by other experiments.

The proton identification capabilities of the RICH detector are significantly reduced at momenta below 4 GeV. This can be observed in the identification efficiencies P_i^j in figure 3.8. For low momenta no Čerenkov rings are generated in the radiator gas volume. The identification is completely determined by the rings generated in the aerogel tiles, which are absent entirely for proton momenta below 3.6 GeV. In the published searches for exotic baryons at the HERMES experiment proton tracks with a momentum below 4 GeV were excluded to avoid these inefficiencies [4, 5].

The tracks of low momentum particles can be identified using the time-of-flight technique described in section 3.3.2. This technique does not allow a full separation of pions, kaons, and protons at all momenta below 3 GeV, but pions and protons can be distinguished. Due to the low number of kaons produced at the HERMES experiment, this is not a limiting condition when no kaons are required in the final state.

The analysis presented in this section only includes the data set collected on the polarized deuterium target between 1998 and 2000. In the data taking period between the years 2002 and 2007, problems with double pulsing of the scintillator hodoscope readout electronics prevented the identification of hadron tracks with the time-of-flight technique.

4.4.1 Time-of-flight identification

As described in section 3.3.2, particle tracks are identified by the reconstructed mass calculated from the timing difference between the bunch crossing and the detector signal in the scintillator hodoscopes H1 and H2. For each hodoscope detector a squared mass m_i^2 is reconstructed, if the particle generated a response in the detector. For some events only one of the two detectors generated a response. These events are not included in this analysis, but they only represent a small fraction of the events.

To identify protons and pions, a rectangular region was defined in the space (m_1^2, m_2^2). The boundaries of the region were left to vary and their position was optimized on the number of reconstructed $\Lambda(1115) \rightarrow p\pi^-$ decays. Only for tracks with a momentum below 2.7 GeV the time-of-flight identification is performed. Proton and pion tracks with a higher momentum are very difficult to separate with this method.

The optimal identification was reached for the region shown in the left panel of figure 4.19. The boundaries are defined by $1.3 < m_1^2 + m_2^2 < 2.5$ and $|m_1^2 - m_2^2| < 0.7$. In figure 4.20 the distributions of the difference $m_1^2 - m_2^2$ and the sum $m_1^2 + m_2^2$ are shown, with vertical lines indication these boundaries. The corresponding distribution of the invariant mass $M(p\pi^-)$ is shown in the right panel of figure 4.19. We experimented with different selection criteria, for example a circular region in (m_1^2, m_2^2) space, but they did not significantly improve the identification efficiency. The misidentification of pions and kaons as protons using the time-of-flight method can be estimated from the right panel of figure 4.20. It is large, but unfortunately unavoidable when using this method where only a limited amount of information about each track is available.

4.4.2 Reconstruction of the K_S^0 meson and exotic Θ^+ baryon

For the reconstruction of the K_S^0 meson and the exotic Θ^+ baryons, events are selected with three hadrons, one of which is required to be identified as a proton by the time-of-flight technique, but without particle identification requirements on the other two hadrons. Due to the requirement that the proton is identified by the time-of-flight technique, its momentum is restricted to be below 2.7 GeV. This selects a completely independent set of events as compared to the original analysis.

The usual event selection criteria for the search for exotic Θ^+ decays were used. They were discussed in sections 4.2.1 and 4.2.2.

The distribution of the invariant mass $M(\pi^+\pi^-)$ for the reconstructed K_S^0 candidates is shown in the left panel of figure 4.21. The K_S^0 resonance peak contains approximately 1500 events. We point out that many of these events are three pion events where one pion is misidentified as a proton by the time-of-flight technique.

In the right panel the distribution of the invariant mass $M(p\pi^+\pi^-)$ is shown. By selecting events that have different average kinematic variables, the shape of the distribution has changed substantially. Unfortunately the number of events in the relevant invariant mass region is reduced. The arrow indicates the position of the observed resonance in the original analysis. In the inset the distribution is shown with error bars to indicate that the small excess of events is completely consistent with a statistical fluctuation.

4.4.3 Monte Carlo simulation

The expected acceptance for decay events of an exotic Θ^+ resonance with a mass of 1540 MeV with a low momentum proton was studied with the gmc_dcay Monte Carlo generator described in section 3.4. In figure 4.22 the momentum distribution of the proton is shown after generation, simulation and reconstruction of the detected tracks,

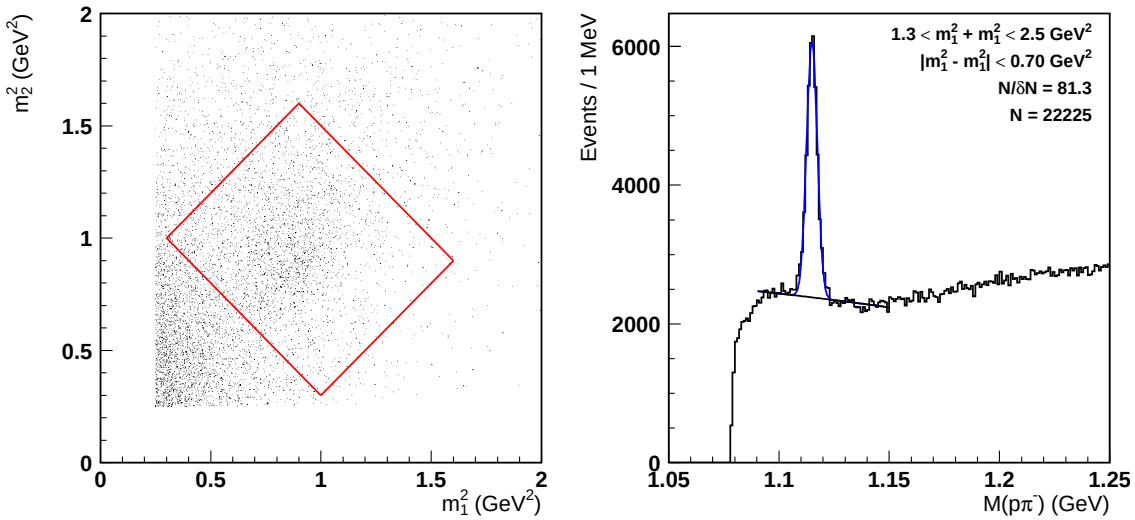

Figure 4.19: Separation of pions and protons at low momentum with the time-of-flight technique. Tracks with reconstructed squared mass m_1^2 and m_2^2 in the region indicated in the left panel are treated as protons. This region was determined by optimizing the number of $\Lambda(1115)$ decay events. The corresponding distribution of the invariant mass $M(p\pi^-)$ is shown in the right panel.

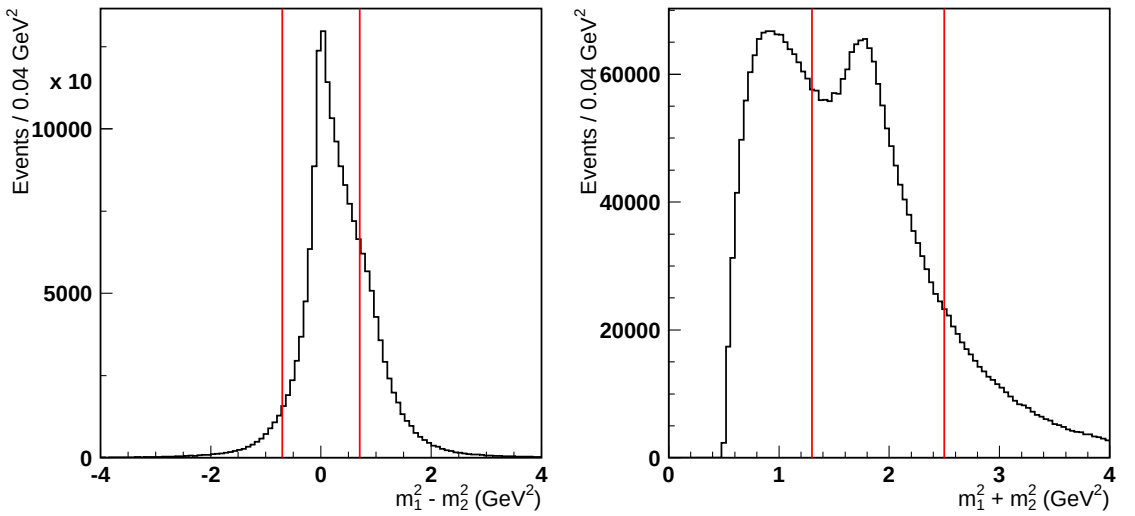

Figure 4.20: Separation of pions and protons at low momentum with the time-of-flight technique. The difference (left panel) and sum (right panel) of the reconstructed squared masses m_1^2 and m_2^2 allows for the identification of protons. All tracks for which the difference $m_1^2 - m_2^2$ and the sum $m_1^2 + m_2^2$ are in the region indicated by the vertical red lines are identified as protons.

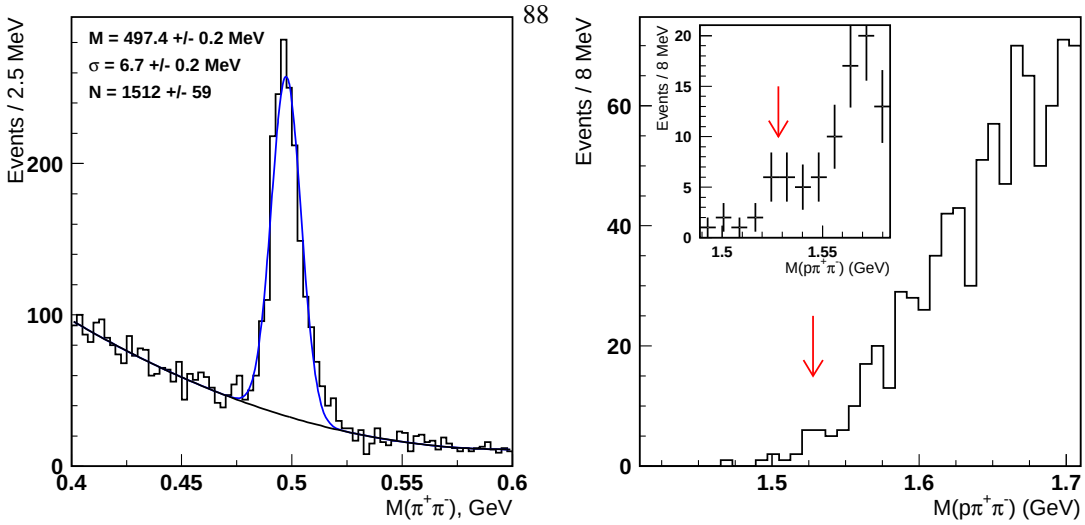

Figure 4.21: The distributions of the invariant mass $M(\pi^+\pi^-)$ (left) and $M(p\pi^+\pi^-)$ (right) when the proton is identified using the time-of-flight technique for data collected during the years 1998–2000. No resonance is observed in the region around 1.54 GeV (inset shows region between 1.50 and 1.58), or at the position of the previously reported mass 1.528 GeV indicated by the arrow.

and after event selection. The number of events with a proton momentum below 2.7 GeV is small when compared to the number of events with a proton momentum above 4 GeV.

The distribution of the proton momentum depends on the unknown production mechanism of the Θ^+ baryon. For this simulation the momentum distribution of the $\Xi^{0*}(1530)$ hyperon obtained from a simulation with the PYTHIA Monte Carlo generator was used as input for the momentum distribution of the $\Theta^+(1540)$ baryon in the gmc_dcay Monte Carlo generator. The acceptance for $\Theta^+(1540)$ decay events is not expected to change significantly for other assumed production mechanisms.

4.4.4 Summary and conclusion

In this section the identification of low momentum proton tracks was presented using the time-of-flight technique. By reconstructing the mass of the particles from the timing information in the scintillator hodoscopes, protons with a low momentum can be identified. The method was demonstrated and optimized on the Λ hyperon. In the distribution of the invariant mass $M(p\pi^+\pi^-)$ for events where the proton was identified using the time-of-flight technique no resonance peak was observed, although the number of events is very small. Monte Carlo simulations confirm that the acceptance for events originating in the decay of an exotic baryon Θ^+ to a proton and K^0_S meson is small.

4.5 Determination of the cross section of the hyperon $\Lambda(1520)$

Since the first publications in the recent wave of evidence for the exotic baryon Θ^+ the interest in baryon spectroscopy has revived. Not only were there numerous theoretical and experimental studies on the properties of the members of the predicted exotic baryon multiplet, but also non-exotic baryons have regained interest because they might give us information on the exotic production mechanisms necessary to explain the experimental disagreement. In particular hyperons with a mass close to the observed mass $M = 1540\,\text{MeV}$ of the exotic baryon Θ^+, such as the hyperon $\Lambda(1520)$, have been the subject of several theoretical publications [66, 111, 112]. The values of the production cross sections for hyperons and antihyperons, and their ratio, could help in determining the production

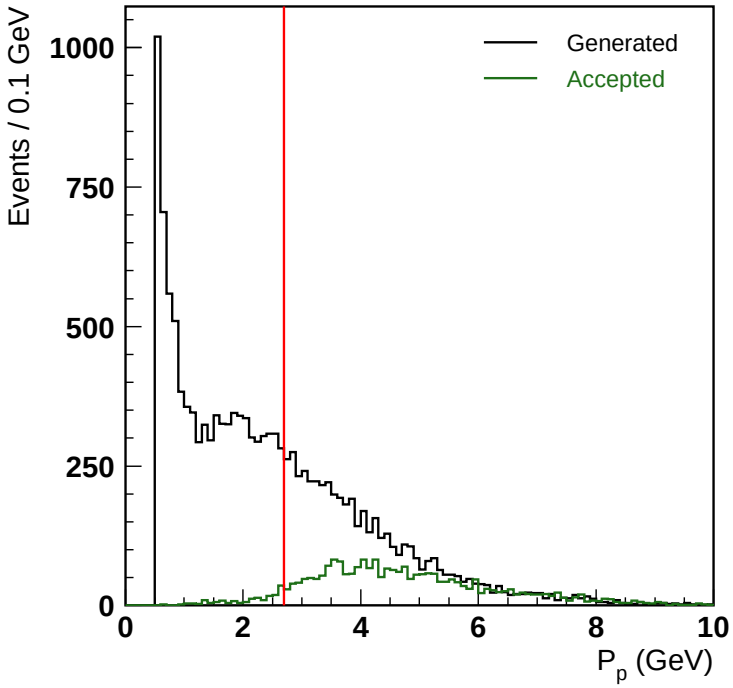

Figure 4.22: The acceptance and efficiency for the detection of Θ^+ decays using a the time-of-flight method was determined using a Monte Carlo simulation. In black the generated momentum distribution of all proton is shown, marked by a sharp increase at low momentum due to secondary particles. In green the momentum is shown for the protons that are accepted by the detector acceptance and particle tracking algorithms. The vertical red line limits the low momentum region where the TOF method is available for proton identification.

mechanisms relevant in the observed exotic processes. Recent results presented by the LEPS experiment even point to the simultaneous production of the exotic baryon Θ^+ and the non-exotic baryons $\Lambda(1520)$ [22].

The neutral hyperon $\Lambda(1520)$, decaying into a proton p and a negative kaon K^- with a branching ratio of 22.5%, is a well established resonance with a mass $M = 1519.5 \pm 1.0\,\text{MeV}$ and intrinsic width $\Gamma = 15.6 \pm 1.0\,\text{MeV}$ [1]. It has the isospin I, spin J, and parity P given by the configuration $I(J^P) = 0(\frac{3}{2}^-)$. At the HERMES experiment the $\Lambda(1520)$ hyperon is clearly visible in the collected data. Its antiparticle $\overline{\Lambda}(1520)$, with the corresponding decay channel to an antiproton $\overline{p}$ and a positive kaon K^+, is more difficult to distinguish due to the lower number of detected events with antiprotons. Additional event selection criteria are necessary to suppress background events.

In this section the photoproduction cross section of the $\Lambda(1520)$ and $\overline{\Lambda}(1520)$ hyperons are determined. With the ratio of the cross sections for particle and antiparticle the expected number of observed Θ^- at the HERMES experiment is calculcated, assuming similar production mechanisms.

4.5.1 Data sets and event selection

In the published analyses of the exotic baryons Θ^+ and Ξ^{--} at the HERMES experiment [4, 5], both polarized and unpolarized deuterium data collected during the years 1998, 1999, and 2000 were included. As described in section 4.3.1, it was later realized that the trigger configuration for unpolarized high-density data taking suppressed photoproduction events. In this analysis only low-density polarized deuterium data collected during the years 1998, 1999, and 2000 are included. The data sample, identical to the sample used in section 4.3, contains a total integrated luminosity $\mathcal{L} = 209.2\,\text{pb}^{-1}$ equivalent to approximately 9.4 M DIS events collected by the HERMES spectrometer.

Due to the general nature of the events collected with the HERMES spectrometer, we need to apply additional selection criteria for the analysis of this data set. In the following paragraphs the selection criteria are summarized. It is understood that the antiparticle decay channels are treated similarly as the corresponding particle decay channels, except where explicitely mentioned otherwise. Details on the implementation of the following track and event selection criteria can be found in section 4.2.

Basic selection criteria

For every event we require two or more long hadron tracks in the main spectrometer.[4] When more than two long hadron tracks are present, all combinations of two tracks are considered. For the selection of $\Lambda(1520)$ events ($\overline{\Lambda}(1520)$ events), every event has to contain one proton (antiproton), as identified by the RICH detector, with a momentum between 4 and 9 GeV, and one oppositely charged kaon, also identified by the RICH detector, with a momentum between 2 and 15 GeV. The momentum ranges are chosen such that the identification efficiencies are high and do not change abruptly with varying momentum. Together, these criteria are referred to as the *basic selection criteria* in what follows.

The efficiency of the particle identification algorithms was studied by the RICH group for the original analysis of the exotic baryon Θ^+ (see the discussion in section 4.2.1). The P-matrices were not determined explicitely for the topology and kinematics of the $\Lambda(1520)$ resonance decay to a two-hadron final state, but were assumed to be equal in the relevant momentum region (4–9 GeV for p, and 2–15 GeV for K). The difference in track multiplicity (three tracks for the decay of the exotic baryon Θ^+, compared to two tracks in the decay of the $\Lambda(1520)$ hyperon) will lead to a higher probability for correct hadron identification in this analysis, since the number of possibly overlapping rings in the RICH detector is smaller.

In this analysis no requirements are imposed on the value of the RICH quality parameter for the proton or kaon tracks. As explained in section 3.3 the RICH quality parameter is defined as the logarithm to base 10 of the ratio of the likelihoods for the particle type assignments that are most likely and next most likely to have produced the hit pattern in the RICH detector. The effect of different quality parameter requirements was studied. Minimum values between 0 and 4 were investigated, corresponding to at least equal and to at least 10^4 times higher probabilities for the mostly

[4] Long tracks reach the particle identification detectors in the back region of the HERMES spectrometer. Short tracks or magnet tracks, on the other hand, are bent outside of the spectrometer acceptance by the spectrometer magnet. These tracks, usually with low momentum, cannot be identified in the spectrometer. More details about magnet tracks can be found in section 4.3.1.

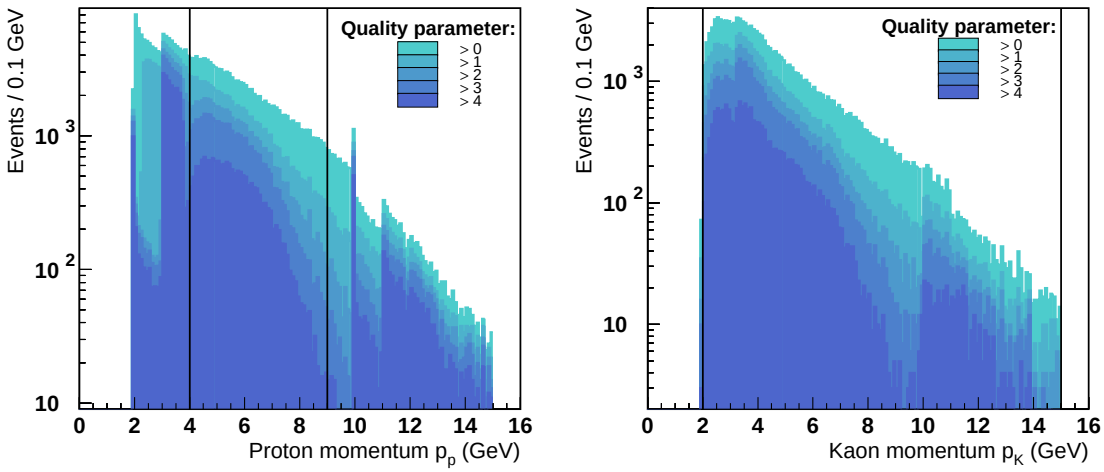

Figure 4.23: The momentum distribution of the protons p (left panel) and kaons K (right panel) for different minimum values of the RICH quality parameter. From light to dark the quality parameter is required to be larger than 0, 1, 2, 3, and 4. Inside the selected momentum range indicated by the vertical lines, there is a distortion of the shape of the distributions. Consequently, no lower limit on the value of the quality parameter was imposed for the selection of candidate $\Lambda(1520)$ events.

likely particle type assignment compared to the other possible particle types.[5] Higher values of the quality parameter correspond to more reliably identified particle tracks, and thus cleaner data samples.

Only a small improvement in the resolution of the invariant mass $M(pK)$ was observed for higher values of the quality parameter. For a quality parameter value larger than 4 the resolution was 3.95 MeV, compared to 4.05 MeV without any requirement on the quality parameter. The number of selected events was approximately three times lower when requiring a quality parameter higher than 4, than without such a requirement.

By selecting events according to the quality parameter, an implicit momentum selection is introduced. Particles with a higher momentum are more difficult to distinguish and have correspondingly lower values for the quality parameter. As shown in figure 4.23, an increase of the required minimum quality parameter changes the momentum distribution in the relevant momentum range for both protons (left panel) and kaons (right panel). Neither this distortion nor the shape of the quality parameter distributions itself could be reproduced in Monte Carlo simulations.

The requirements on the quality parameter were abandoned due to the associated implicit but unknown distortion of the momentum distribution of the selected events. Since the determination of the detector acceptance and selection efficiency depends strongly on the correct description of the spectrometer in the Monte Carlo simulations (see section 4.5.2), the results presented here are obtained without a lower limit on the value of the quality parameter.

$\Lambda(1520)$ selection criteria

In addition to the basic selection criteria, which use only information from a single particle track, the topology of the event is used to select candidate $\Lambda(1520)$ decay events. The distance of closest approach $DCA(p, K)$ between the proton and kaon tracks is required to be less than 0.6 cm. The midpoint of the line segment of closest approach defines the decay vertex of the $\Lambda(1520)$ candidate. The production vertex of the $\Lambda(1520)$ is defined as the midpoint of the

[5] The quality parameter is a strictly positive number. When two particle type assignments have equal likelihood, a situation that occurs trivially for all short tracks, the track is considered not identified and is discarded in this analysis.

segment of closest approach between the reconstructed $\Lambda(1520)$ track and the lepton beam.[6]

Motivated by the longitudinal vertex resolution of the HERMES spectrometer of approximately 3 cm and the mean lifetime of the $\Lambda(1520)$ resonance $c\tau \approx 12.6\,\text{fm}$, the distance ΔR between the production vertex and the decay vertex of the $\Lambda(1520)$ candidate is required to be less than 5 cm (and for causality the decay vertex is required to be downstream of the production vertex). This means that, within the tracking precision of the spectrometer, the production and decay vertices of the $\Lambda(1520)$ hyperon are at the same position. It follows that the longitudinal coordinate of the decay vertex should be inside the target cell, within the range $-18.0 < z < 18.0\,\text{cm}$. The transverse distance $R(p, K)$ of the decay vertex to the average position of the lepton beam is required to be smaller than 4 mm.

A Monte Carlo simulation, discussed in section 4.5.2, was used to determine the parameters of these selection criteria, which will be referred to as the $\Lambda(1520)$ *selection criteria*.

Resonance suppression

Events from the resonance decays $\phi(1020) \rightarrow K^+K^-$ and $K^*/\overline{K}^*(892) \rightarrow K^\pm\pi^\mp$ are an important source of background events in this analysis. One of the decay products of the $\phi(1020)$ or $K^*(892)$ can be misidentified as the proton from a $\Lambda(1520)$ decay[7], or it can be identified correctly and act as a third track in the event[8].

The clearest contamination occurs when the two kaons from the $\phi(1020)$ resonance decay are selected as the two decay particles of the $\Lambda(1520)$ candidate, which means that one of the kaons is misidentified. In figure 4.24 the distributions of the invariant mass $M(K^+K^-)$ are shown for the charge combinations pK^- (left panel) and $\overline{p}K^+$ (right panel), when the proton p is assigned the kaon mass. A clear resonance peak corresponding to the $\phi(1020)$ meson indicates that kaon misidentification as protons is substantial.[9] These events are easily removed by requiring the invariant mass $M(K^+K^-)$ to be outside the interval 1.01–1.03 GeV (as indicated on the figure). This is referred to as the $\phi(1020)$ *veto*.

It is also possible that only one of the decay particles of the $\Lambda(1520)$ candidate originated in a $\phi(1020)$ or $K^*(892)$ resonance decay. The second decay particle of the $\phi(1020)$ or $K^*(892)$ escapes detection in the spectrometer, or is detected as an additional particle in the final state. In the latter case, combinations with all other tracks in the detector are considered and the invariant mass is required to be outside of a sufficiently broad window around the mass of the $\phi(1020)$ or $K^*(892)$. With this method we can reject all $\phi(1020)$ and $K^*(892)$ decay events where a kaon is misidentified as a proton and the other decay product identified correctly, and all $\phi(1020)$ and $K^*(892)$ decay events where both decay particles are correctly identified.[10]

In the left panel of figure 4.25 the effect of the simple $\phi(1020)$ veto and of the additional resonance suppression criteria involving a third track is visualized. Before any resonance suppression is applied, the black distribution is obtained. The entries in the filled blue distribution are removed by the $\phi(1020)$ veto and the open blue distribution is obtained. The other resonance suppression criteria remove only the entries included in the filled red distribution. The effect of the additional resonance suppression criteria is small compared to the simple $\phi(1020)$ veto. The number of entries not removed by the $\phi(1020)$ veto is low and no structure is visible for these events in the invariant mass region relevant for this analysis. Since the number of collected events decreases by approximately one order of magnitude for every additional hadron in the acceptance of the HERMES spectrometer, this is in line with expectations. For this analysis only the $\phi(1020)$ veto resonance suppression is used.

When looking at the Dalitz plot for the kaon track and proton/misidentified kaon track in the right panel of figure 4.25, it is clear that $\phi(1020)$ resonance events (corresponding to the vertical band) can not be completely removed without sacrificing some $\Lambda(1520)$ events (corresponding to the horizontal band). However, the effect is negligible

[6] The mean values of the transverse horizontal and vertical coordinates of the $\Lambda(1520)$ decay vertex are $x_0 = -0.141\,\text{cm}$ and $y_0 = 0.056\,\text{cm}$. For this analysis the lepton beam was assumed to have transverse coordinates $(0, 0)$. The selection criteria influenced by this transverse deviation impose a limit that is more than three times the average deviation from zero. The results presented here are unlikely to be changed significantly when the average beam position would be taken into account.

[7] Very few events are assumed to have two or more misidentified tracks.

[8] A third possibility, namely when one of the two decay particles escapes detection, cannot be removed by an event-based selection criterium.

[9] Due to the low probability for misidentification of pions as protons, as can be seen in the P_π^p panel of the P-matrix in figure 3.8, the corresponding contamination from $K^*(892)$ resonance decays is negligible.

[10] The rejection of $K^*(892)$ decay events also takes into account the distance of closest approach and the decay vertex position. These additional requirements prevent that too many legitimate events are removed.

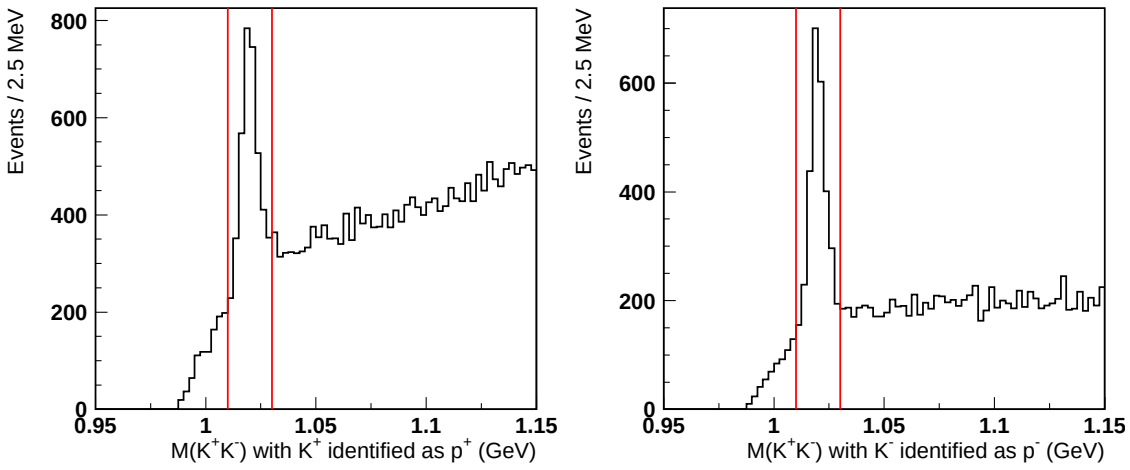

Figure 4.24: The distributions of the invariant mass $M(K^+K^-)$ for events in the pK^- (left panel) and $\overline{p}K^+$ (right panel) samples, when the proton is assumed to be a misidentified kaon. All event selection criteria are applied, except for the $\phi(1020)$ veto. A clear $\phi(1020)$ peak indicates that there is a substantial contamination of the protons. The vertical red lines indicate the invariant mass region where events are suppressed by the $\phi(1020)$ veto.

because the bulk of the bands of the $\phi(1020)$ and $\Lambda(1520)$ hyperons are well separated, and no peak is visible in the filled blue distribution.

The effect of ghost track events was investigated here as well. No ghost tracks were observed among the selected events (*i.e.* the number of events with momenta and angles close together was not larger than expected for physical tracks). This is due to the different identification requirements for the two tracks. Thus, no ghost track suppression was applied. The list of selected events was also checked for event double counting.

The lists of selected events for the $\Lambda(1520)$ and $\overline{\Lambda}(1520)$ decay channels were cross-checked between two analyzers, using different analysis platforms, with a nearly perfect agreement of 99.9%. All different events were manually inspected and could be explained as numerical precision errors (for example, a decay length of 5.0001 cm versus 4.9999 cm).

4.5.2 Monte Carlo simulations

As described in section 3.4, the HERMES spectrometer is a forward spectrometer and does not cover the full 4π geometrical acceptance (in the resonance center of mass frame) in which resonance cross section are usually specified. The event selection criteria necessary to resolve the $\Lambda(1520)$ resonance peak reduce even further the number of observed $\Lambda(1520)$ decay events used in the determination of the cross section. We have to determine the combined effects of the detector acceptance and the selection efficiency using Monte Carlo simulations. Additionally, the Monte Carlo simulations help us to determine the detector resolution and the optimal selection parameters.

Because the $\Lambda(1520)$ hyperon is not included in the PYTHIA Monte Carlo generator, the samples of $\Lambda(1520)$ and $\overline{\Lambda}(1520)$ decay events were generated with the gmc_dcay Monte Carlo generator. Unless mentioned otherwise, the simulations were performed around a central mass $M = 1520\,\text{MeV}$ with an intrinsic width $\Gamma = 16\,\text{MeV}$, corresponding to the world average value [1]. The initial momentum distributions P_t and P_z were obtained from PYTHIA simulations, except when the details of the production mechanism were not expected to influence the results. Specifically, for the determination of the resolution and the study of the selection criteria, the internal model of the gmc_dcay Monte Carlo generator was used.

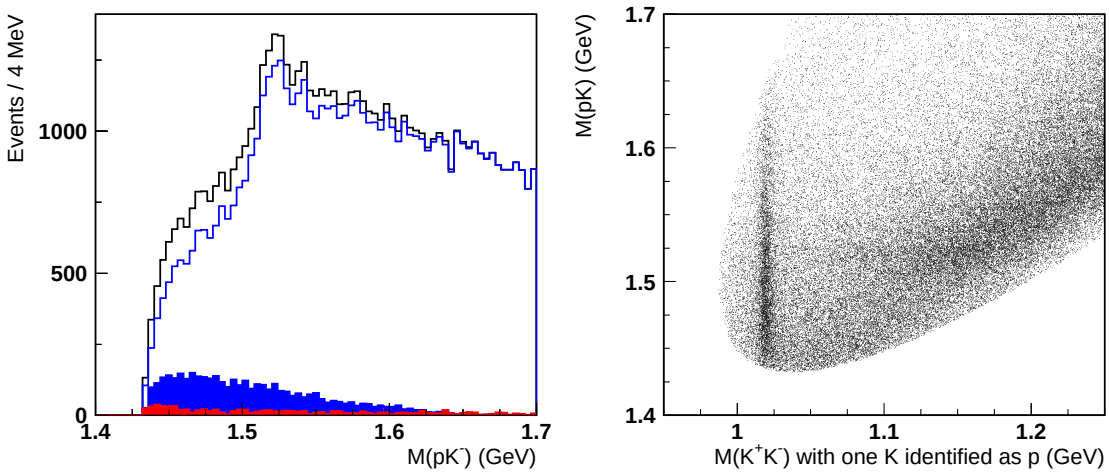

Figure 4.25: The effect of the additional resonance suppression criteria on the distribution of the invariant mass $M(pK^-)$ is investigated in the left panel. The distribution in black is obtained without suppression of events from $\phi(1020)$ or $K^*(892)$ resonance decays. The distribution in blue is obtained after applying only the $\phi(1020)$ veto. The events removed by the $\phi(1020)$ veto are shown as the filled blue distribution. The filled red distribution consists of the events that are only removed by all additional resonance suppression criteria. In the right panel the Dalitz plot is shown for the kaon track and proton/misidentified kaon track.

Experimental resolution in the invariant mass $M(pK)$

To determine the experimental resolution in the invariant mass $M(pK)$ of the HERMES spectrometer, $\Lambda(1520)$ and $\overline{\Lambda}(1520)$ decay events were generated with zero intrinsic width $\Gamma = 0$ MeV. In other words, all decay events were generated with the same resonance mass $M = 1520$ MeV. In this simulated sample the resolution of the spectrometer is responsible for any smearing of the reconstructed invariant mass. In the invariant mass region around 1520 MeV, and after applying all selection criteria, the resolution is 4.05 MeV for the $\Lambda(1520)$ events and 4.29 MeV for the $\overline{\Lambda}(1520)$ events. Consequently, the binning for the invariant mass distributions is chosen as 4 MeV. The values for the resolution will later be used to fit the invariant mass distributions of the selected data events with the convolution of a Breit-Wigner function to describe the resonance and a Gaussian function for the spectrometer resolution.

Verification of the selection criteria

Using the Monte Carlo samples we investigated the validity of the selection criteria. Since the gmc_dcay Monte Carlo generator does not produce background events, we are not able to optimize the selection criteria by comparing the background events with the signal events. However, the simulated $\Lambda(1520)$ decay events allow us to determine how many legitimate events would be removed by the selection criteria. Since the distributions in the recorded data are wider due to the presence of events which are not described by our required event topology, we remove as many background events as possible without removing a substantial fraction of the events from $\Lambda(1520)$ decays.

The upper limit on the distance of closest approach $DCA(p, K)$ between the proton and the kaon tracks was varied from 0.1 cm to 1.0 cm, gradually weakening the requirement on the events. For each value the selection efficiency was determined. The results are shown in the left panel of figure 4.26 for the $\Lambda(1520)$ and $\overline{\Lambda}(1520)$ events. The upper limit of 0.6 cm provides a good trade-off between selecting most of the $\Lambda(1520)$ events and reducing the amount of background events from unrelated events. The distribution of the distance of closest approach after all other selection

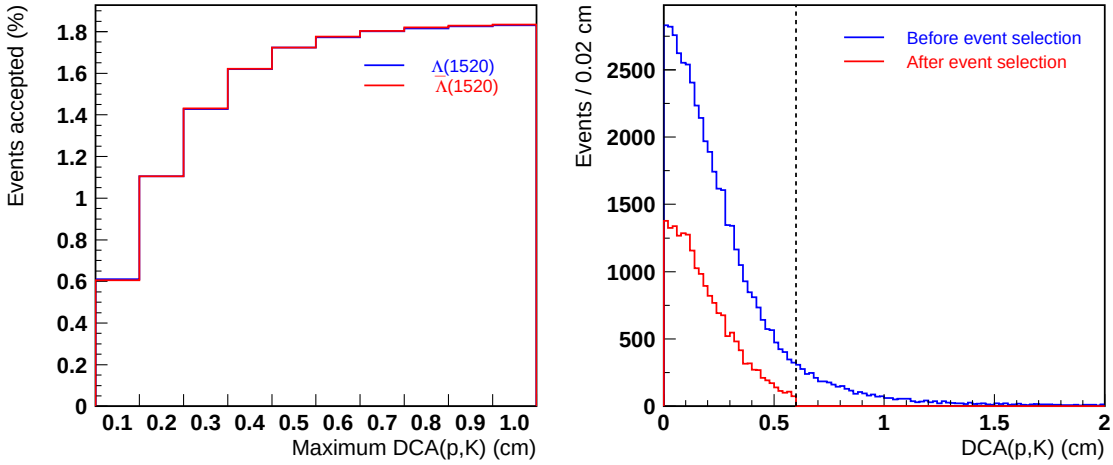

Figure 4.26: The maximum distance of closest approach $DCA(p, K)$ between the proton and the kaon track was varied between 0.1 cm and 1.0 cm for events generated with the Monte Carlo generator gmc_dcay. For every value of the upper limit the percentage of selected events is shown in the left panel. In the right panel, the distribution of the distance of closest approach between the proton and the kaon track is shown, before (blue) and after (red) applying all selection criteria. An upper limit of 0.6 cm on the distance of closest approach with the upper limit (indicated by the vertical line) selects most events.

criteria in the right panel of figure 4.26 also indicates that this upper limit selects the majority of the $\Lambda(1520)$ events, and removes only the small fraction of outliers.

Similarly, the optimal value for the decay length ΔR of the $\Lambda(1520)$ candidate can be determined. The upper limit on the decay length was varied from 1.0 cm to 10.0 cm and for every value of the upper limit the selection efficiency was determined. In the left panel of figure 4.27 the results are shown for $\Lambda(1520)$ and $\overline{\Lambda}(1520)$ events. The upper limit of 5.0 cm removes some legitimate events (as can be seen on the right panel), but this stricter limit is motivated by the distribution of the decay length in the data. The width of the fitted Gaussian with mean fixed at zero is $\sigma = 2.7$ cm, which corresponds to the longitudinal distance resolution.

Finally, the optimal value for the distance $R(p, K)$ of the $\Lambda(1520)$ decay vertex to the lepton beam was determined. Also here the maximum distance was varied between 0.1 cm and 1.0 cm, and the efficiency was determined for every value. The left panel of figure 4.28 shows the results for $\Lambda(1520)$ and $\overline{\Lambda}(1520)$ events. The upper limit of 0.4 cm removes very few legitimate events (as visible on the right panel), but reduces the number of background events substantially.

Detector acceptance and selection efficiency for $\Lambda(1520)$ events

To obtain the cross section for photoproduction of the $\Lambda(1520)$ and $\overline{\Lambda}(1520)$ hyperons, we need to determine the fraction of the produced $\Lambda(1520)$ and $\overline{\Lambda}(1520)$ hyperons that decay inside the limited acceptance of the spectrometer and, after track reconstruction, satisfy the selection criteria listed in section 4.5.1. The combined effects of the detector acceptance and the selection efficiency, from now on for brevity referred to as the *efficiency*, are determined with Monte Carlo simulations.

Because the $\Lambda(1520)$ hyperon is not included in the PYTHIA Monte Carlo generator, we cannot determine the efficiency for $\Lambda(1520)$ and $\overline{\Lambda}(1520)$ events using a realistic model for the production of the $\Lambda(1520)$ hyperon. Instead, we used the gmc_dcay Monte Carlo generator to simulate $\Lambda(1520)$ and $\overline{\Lambda}(1520)$ decay events. The efficiency for

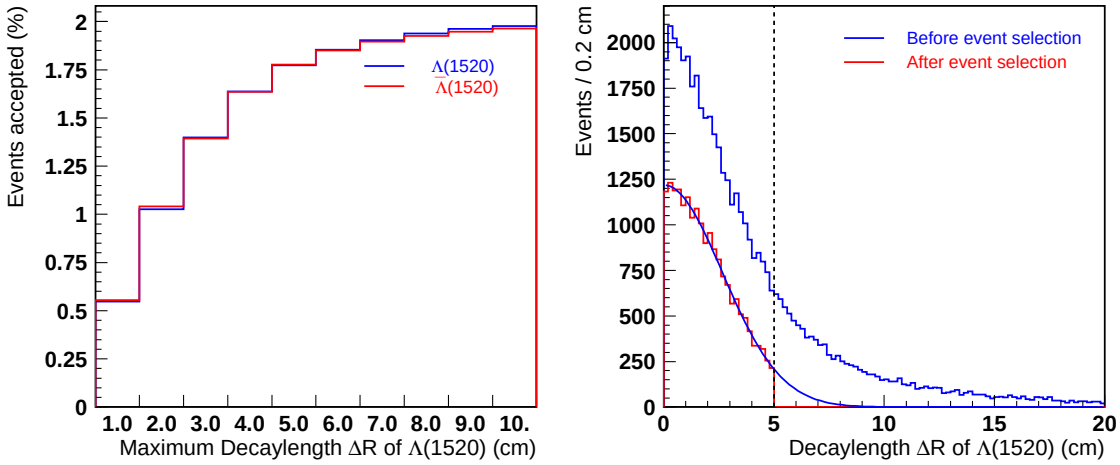

Figure 4.27: The maximum decay length ΔR of the $\Lambda(1520)$ candidate was varied between 1.0 cm and 10.0 cm for events generated with the Monte Carlo generator gmc_dcay. For every value of the upper limit, the percentage of selected events is shown in the left panel. In the right panel, the distribution of the decay length of the $\Lambda(1520)$ candidate is shown, before (blue) and after (red) applying all selection criteria. An upper limit of 5.0 cm on the decay length (indicated by the vertical line) discards a moderate number of events. The fit with a Gaussian function is used to determine the resolution in the z direction as approximately $\sigma = 2.7$ cm.

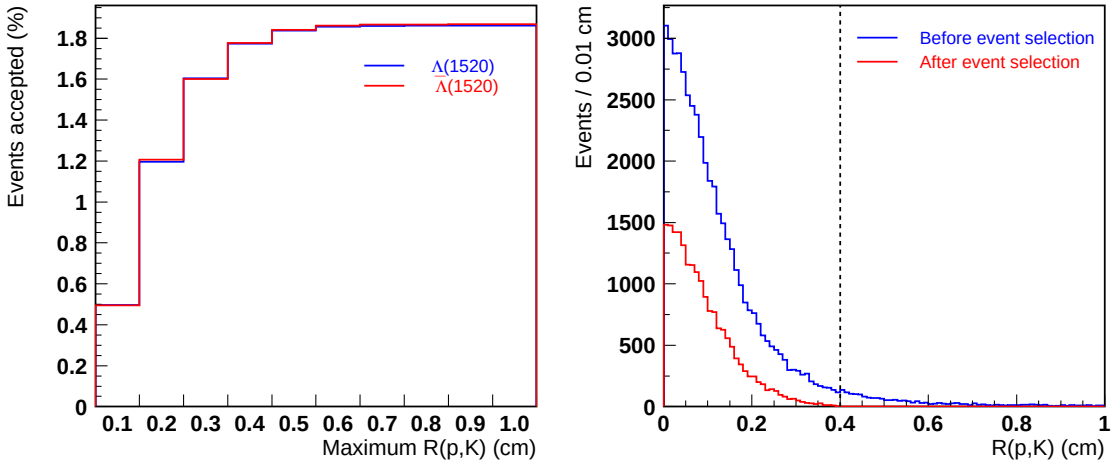

Figure 4.28: The maximum distance $R(p, K)$ of the $\Lambda(1520)$ decay vertex to the lepton beam was varied between 0.1 cm and 1.0 cm for events generated with the Monte Carlo generator gmc_dcay. For every value of the upper limit, the percentage of selected events is shown in the left panel. In the right panel, the distribution of the distance of the $\Lambda(1520)$ decay vertex to the lepton beam is shown, before (blue) and after (red) applying all selection criteria. An upper limit of 0.4 cm on the distance (indicated by the vertical line) selects nearly all events.

$\Lambda(1520)$ and $\overline{\Lambda}(1520)$ events determined from the Monte Carlo simulations is assumed to be the same as for the data events collected by the spectrometer.[11]

The unknown initial momentum distributions of the $\Lambda(1520)$ resonances are needed to generate decay events with the gmc_dcay Monte Carlo generator. We used the momentum distributions P_t and P_z of several other hyperons obtained from PYTHIA Monte Carlo simulations in the full 4π acceptance (the momentum distributions of the antihyperons were used for the simulations of the $\overline{\Lambda}(1520)$ hyperon). In table 4.6 the used hyperons are listed together with their quark configuration and mass. It is assumed that the production mechanism of the $\Lambda(1520)$ resonance is similar to the production mechanisms of the other hyperons, and thus that the initial momentum distributions are indeed comparable. After determining the initial momentum distributions for the hyperons, we used the gmc_dcay Monte Carlo generator to determine the efficiency for $\Lambda(1520)$ and $\overline{\Lambda}(1520)$ events.

To determine any systematic differences between proton and neutron targets, three different PYTHIA Monte Carlo simulations in the full 4π acceptance were used. The first two samples were generated on a proton target (*proton sample*) and on a neutron target (*neutron sample*), without any restrictions on the generated events. Due to their low cross section, the heavier hyperons Σ^* and Ξ^* have a very low yield in the proton and neutron samples. When nuclear effects are ignored, the deuterium target used in this analysis can be described by the average of the proton and neutron samples.

In a third simulation, available only on a proton target, all generated events were required to contain at least one $\Lambda(1115)$ in the final state before simulation of the detector responses and track reconstruction.[12] Since the simulation of the particle tracks in the detector is the most computationally intensive step, this speeds up the simulation process significantly and more events could be generated. All hyperons used in this analysis, except the Σ^+ and Σ^- resonances, have dominant decay modes to $\Lambda(1115)$, so in most cases the $\Lambda(1115)$ requirement does not restrict the simulated sample. This sample will be referred to as the *selector sample*.

Efficiency for the detection of $\Lambda(1520)$ events In figure 4.29 the efficiencies for the detection of a produced $\Lambda(1520)$ or $\overline{\Lambda}(1520)$ hyperon are shown, when using the simulated momentum distributions of the indicated hyperons on a proton sample (left panel) and the neutron sample (right panel) as input for the gmc_dcay Monte Carlo generator. In figure 4.30 the efficiencies obtained with the momentum distributions from the selector sample are shown.

The efficiencies for $\overline{\Lambda}(1520)$ events are equal on the proton and neutron targets, and rise slowly with the mass of the antihyperon used as model for the initial momentum distribution. In the simulations, the average transverse momentum P_t of the produced hyperons is higher for heavier hyperons, associated with more hyperon decay products in the detector acceptance.

For the efficiency of the $\Lambda(1520)$ resonance a similar general behavior is visible, although largely obscured by outliers due to the specific quark configuration of the hyperons.[13] The detector acceptance depends strongly on the transverse momentum of the produced hyperon, which is determined by the specific production mechanism. Lower efficiencies are observed when the initial momentum distributions are modeled after the $\Lambda(1115)$, $\Sigma(1190)$ and $\Sigma^*(1385)$ resonances. This can be explained by the lower transverse momentum of hyperons which are produced as decay product of a higher resonance, or where a diquark from the target is reused in the produced hyperon.

Effects of the resonance momentum distributions after production In figures 4.31 (proton sample) and figure 4.32 (neutron sample) the reason for the differences in efficiency for $\Lambda(1520)$ and $\overline{\Lambda}(1520)$ events is illustrated in the case of an initial momentum distribution from the Σ^- hyperon. For the proton sample the momentum distributions for the Σ^- and Σ^+ hyperons exhibit a similar behavior and the efficiencies for $\Lambda(1520)$ and $\overline{\Lambda}(1520)$ events are of similar magnitude. For the neutron sample the momentum distributions are very different, which is reflected in the very different efficiencies for $\Lambda(1520)$ and $\overline{\Lambda}(1520)$ events.

[11] Hardware trigger inefficiencies (in the order of a few percent) are not included in the Monte Carlo simulations, but the resulting differences in efficiency between data events and simulated Monte Carlo events are negligible compared to the uncertainty caused by other effects.

[12] This Monte Carlo sample was generated for $\Lambda(1115)$ polarization studies on the transversely polarized hydrogen target. A similar sample on a neutron target was not available.

[13] Because the HERMES experiment uses a particle target, large differences between physical observables for particle or antiparticle final states are common.

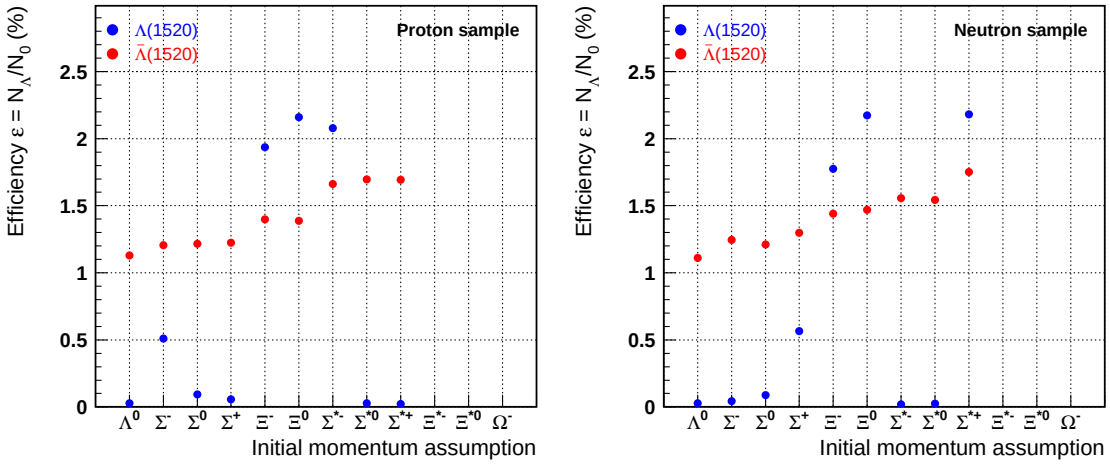

Figure 4.29: The efficiency for $\Lambda(1520)$ and $\overline{\Lambda}(1520)$ events, determined using initial momentum distributions taken from the production of the indicated hyperons on a proton target (left panel) and a neutron target (right panel). For the heavier hyperons (Ξ^*, Ω) not enough simulated events were available to determine the initial momentum distributions and thus the efficiency.

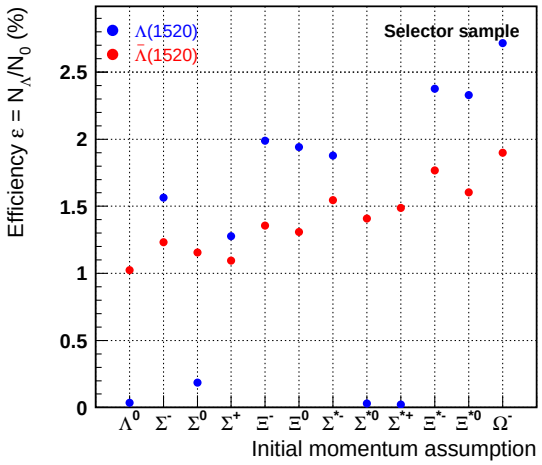

Figure 4.30: The efficiency for $\Lambda(1520)$ and $\overline{\Lambda}(1520)$ events, determined using initial momentum distributions taken from the production of the indicated hyperons on a proton target with at least one $\Lambda(1115)$ hyperon involved in the reaction process.

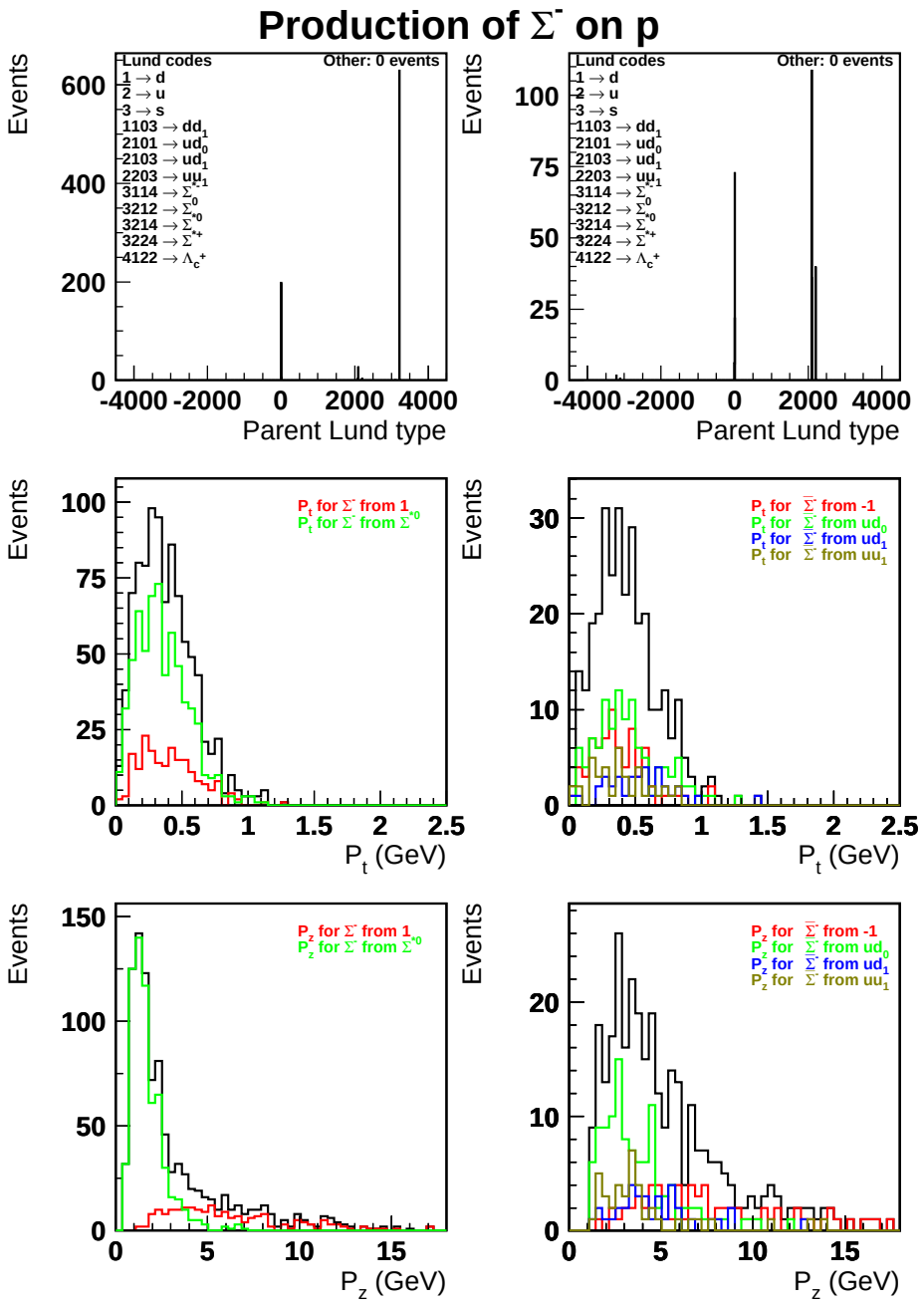

Figure 4.31: The initial momentum distributions for the Σ^- baryons produced on a proton target (proton sample) determined in a PYTHIA Monte Carlo simulation. From top to bottom the parent Lund type, the P_t distributions, and the P_z distributions are shown, for particles (left panel) and antiparticles (right panel). The total initial momentum distributions is shown in black, the different production mechanisms are shown in colors.

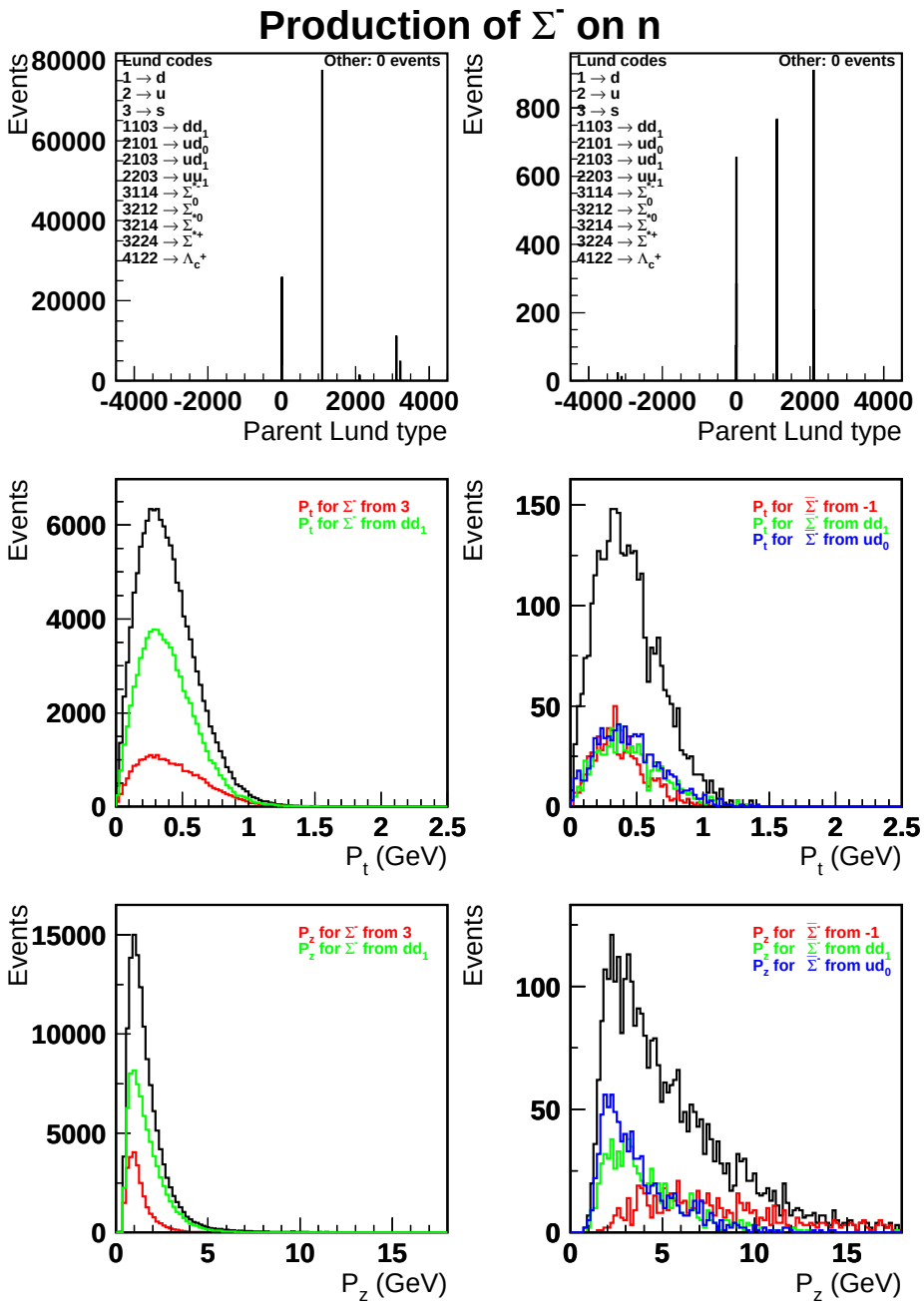

Figure 4.32: The initial momentum distributions for the Σ^- baryons produced on a neutron target (neutron sample) determined in a PYTHIA Monte Carlo simulation. From top to bottom the parent Lund type, the P_t distributions, and the P_z distributions are shown, for particles (left panel) and antiparticles (right panel). The total initial momentum distributions is shown in black, the different production mechanisms are shown in colors.

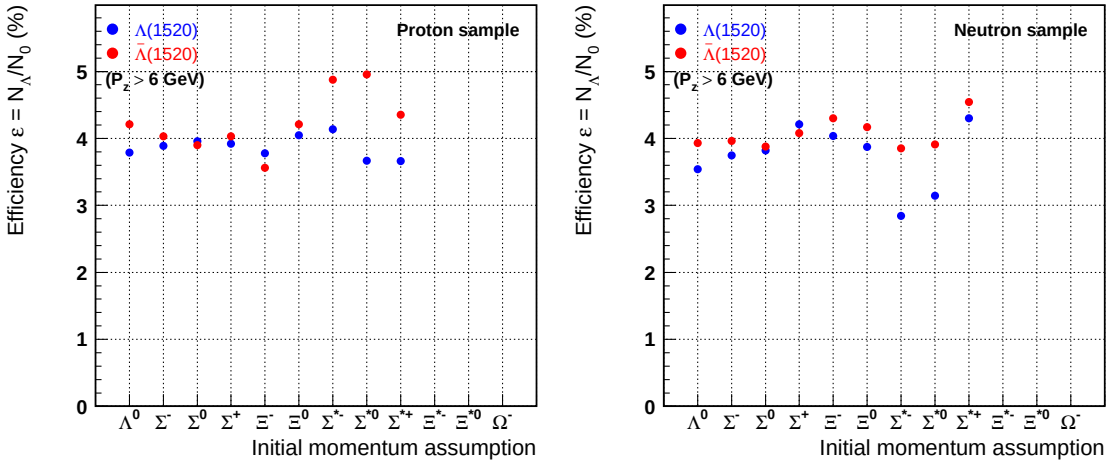

Figure 4.33: The efficiency for $\Lambda(1520)$ and $\overline{\Lambda}(1520)$ events, determined using initial momentum distributions taken from the production of the indicated hyperons on a proton target (left panel) and a neutron target (right panel), when a longitudinal momentum P_z larger than 6 GeV is required.

When the momentum distributions of the $\Sigma^{\pm}$ and $\Sigma^{*\pm}$ resonances are ignored, the efficiencies for the $\Lambda(1520)$ on the proton and neutron targets are in agreement. The disagreement between proton and neutron targets is again caused by the specific quark structure; one of the two d quarks of the Σ^- state is not available in the proton. The creation of a $d\overline{d}$ quark-antiquark pair leads to a higher transverse momentum P_t, corresponding to a higher detector acceptance. Due to isospin symmetry, the detection of the produced Σ^+ resonances on a neutron target is similarly suppressed.

When comparing the initial momentum distributions between the proton sample and the selector sample, almost all agree very well. Only the P_z distribution of the Σ^- and Σ^+ resonances is very different (the Σ^{*-} and Σ^{*+} resonances agree though). The reason for this is that the $\Sigma^{\pm}$ decays only weakly to $\Lambda(1115)$, with a branching fraction of 10^{-5}. What we might be seeing here instead are the initial momentum distributions for associated production of $\Lambda(1115)$ and $\Sigma^{\pm}$ hyperons, rather than the averaged distributions for all $\Sigma^{\pm}$ produced at the HERMES experiment.

Efficiency for the detection of $\Lambda(1520)$ events with P_z greater than 6 GeV Due to the momentum requirements for the proton (larger than 4 GeV) and for the kaon (larger than 2 GeV), the momentum of the reconstructed $\Lambda(1520)$ and $\overline{\Lambda}(1520)$ candidates will usually be larger than 6 GeV. Since the differences between the hyperon momentum distributions resulting in large differences of the determined $\Lambda(1520)$ efficiency are the largest in the low momentum region, they are not relevant for the $\Lambda(1520)$ resonance decays in this analysis. Therefore we limited the longitudinal momentum P_z of the $\Lambda(1520)$ resonance to values larger than 6 GeV, corresponding to the events collected by the spectrometer, and determined the efficiency. The results are shown in figure 4.33 and figure 4.34.

The variations between the efficiencies obtained with different initial momentum distribution assumptions, are reduced when only the longitudinal momentum region $P_z > 6$ GeV is considered. The hyperon mass dependence is also less pronounced. We conclude that the detector acceptance and selection efficiency for $\Lambda(1520)$ events is $3.8 \pm 0.4\%$ and for $\overline{\Lambda}(1520)$ events $4.2 \pm 0.4\%$.

Influence of a possible $\Lambda(1520)$ polarization

The $\Lambda(1520)$ resonance is a hyperon with spin $J = \frac{3}{2}$. The detector acceptance for $\Lambda(1520)$ and $\overline{\Lambda}(1520)$ hyperon decays could be influenced by a possible polarization of the produced resonance. For every produced $\Lambda(1520)$ two

Table 4.6: Efficiency for initial momentum distributions taken from the indicated hyperons using a PYTHIA Monte Carlo simulation in 4π acceptance. The hyperons above the line were obtained with the selector sample, below the line with the proton sample (see text).

Hyperon	Quarks	Mass	$\epsilon_{\Lambda(1520)}$	$\epsilon_{\overline{\Lambda}(1520)}$	$\epsilon_{\Lambda(1520),P_z>6\,\mathrm{GeV}}$	$\epsilon_{\overline{\Lambda}(1520),P_z>6\,\mathrm{GeV}}$
Λ^0	uds	1115 MeV	0.0354 ± 0.0008	1.02 ± 0.010	3.66 ± 0.015	4.07 ± 0.016
Σ^-	dds	1190 MeV	1.56 ± 0.013	1.23 ± 0.011	3.82 ± 0.015	4.00 ± 0.016
Σ^0	uds	1190 MeV	0.186 ± 0.002	1.16 ± 0.010	3.89 ± 0.016	3.89 ± 0.015
Σ^+	uus	1190 MeV	1.28 ± 0.011	1.10 ± 0.010	4.07 ± 0.016	4.05 ± 0.016
Ξ^-	dss	1321 MeV	1.99 ± 0.015	1.36 ± 0.012	3.91 ± 0.015	3.93 ± 0.016
Ξ^0	uss	1315 MeV	1.94 ± 0.015	1.31 ± 0.012	3.96 ± 0.015	4.19 ± 0.017
Σ^{*-}	dds	1385 MeV	1.88 ± 0.015	1.55 ± 0.013	3.49 ± 0.015	4.36 ± 0.017
Σ^{*0}	uds	1385 MeV	0.0289 ± 0.0008	1.41 ± 0.013	3.41 ± 0.015	4.43 ± 0.018
Σ^{*+}	uus	1385 MeV	0.0232 ± 0.0007	1.49 ± 0.013	3.98 ± 0.016	4.45 ± 0.017
Ξ^{*-}	dss	1535 MeV	2.38 ± 0.017	1.77 ± 0.015	3.74 ± 0.020	4.24 ± 0.024
Ξ^{*0}	uss	1535 MeV	2.33 ± 0.017	1.60 ± 0.014	3.81 ± 0.021	3.99 ± 0.023
Ω^-	sss	1670 MeV	2.71 ± 0.018	1.90 ± 0.015	3.81 ± 0.020	4.09 ± 0.022
Σ^-	dds	1190 MeV	0.495 ± 0.005	1.11 ± 0.010		
Σ^+	uus	1190 MeV	0.0507 ± 0.0010	1.40 ± 0.012		

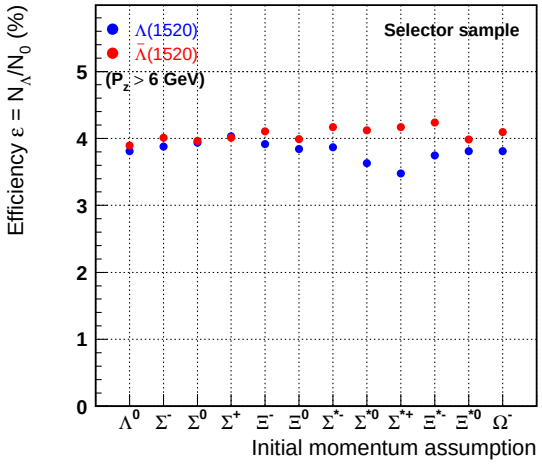

Figure 4.34: The efficiency for $\Lambda(1520)$ and $\overline{\Lambda}(1520)$ events, determined using initial momentum distributions taken from the production of the indicated hyperons on a proton target with at least one $\Lambda(1115)$ hyperon involved in the reaction process, and when a longitudinal momentum P_z larger than 6 GeV is required.

Table 4.7: Efficiency for different $\Lambda(1520)$ and $\overline{\Lambda}(1520)$ polarization scenarios.

Polarization	$\epsilon_{\Lambda(1520)}$	$\epsilon_{\overline{\Lambda}(1520)}$
Unpolarized	1.80 ± 0.013	1.81 ± 0.013
$\sin^2\theta$	2.15 ± 0.015	2.11 ± 0.014
$1 + 3\cos^2\theta$	1.22 ± 0.012	1.18 ± 0.011

physically distinguishable spin orientations are possible. The projection of the spin on the quantization axis is either equal to $\pm\frac{1}{2}$, or equal to $\pm\frac{3}{2}$. The corresponding distributions of the angle θ between the proton momentum and the quantization axis in the $\Lambda(1520)$ center-of-mass frame are given by $1 + 3\cos^2\theta$ and $\sin^2\theta$.

The degree of polarization is determined by the fraction of $\Lambda(1520)$ states that are produced in each of the two spin sub-states. If the $\Lambda(1520)$ states are mostly produced in one spin sub-state, the production is polarized and one of the angular decay distributions will dominate. If both spin sub-states are equally likely to be produced, the production of the $\Lambda(1520)$ hyperon is said to be unpolarized. The angular decay distributions will then contribute equally and result in an isotropic angular distribution $1 + \cos^2\theta$.

Results of the LAMP2 experiment indicate the $\Lambda(1520)$ is mostly produced in the spin sub-states $\pm\frac{3}{2}$ [113], but there is no reason to assume that at the HERMES experiment this is also the case. Moreover, the degrees of polarization can be different for particle and antiparticle, due to possibly different production mechanisms for the $\Lambda(1520)$ and $\overline{\Lambda}(1520)$ hyperons.

To estimate the effect of the different sub-states on the acceptance, the gmc_dcay Monte Carlo generator was modified to include the angular distributions corresponding to the spin sub-states $\pm\frac{1}{2}$ $(1 + 3\cos^2\theta)$ and $\pm\frac{3}{2}$ $(\sin^2\theta)$. The initial momentum distributions P_t and P_z from the Ξ^{*0} obtained with the PYTHIA Monte Carlo generator were used for both the $\Lambda(1520)$ and $\overline{\Lambda}(1520)$ hyperons. The results of the three simulations, two for fully polarized production in each of the polarization states and one for unpolarized production followed by isotropic decay, are summarized in table 4.7.

The effect of a possible polarization of the $\Lambda(1520)$ hyperon in the spin sub-states $\pm\frac{3}{2}$ is an increase in acceptance

of almost 20% compared to an unpolarized $\Lambda(1520)$. If the $\Lambda(1520)$ hyperons are produced predominantly in spin substates $\pm\frac{1}{2}$, the acceptance decreases by 30%. For equal initial momentum distributions, and assuming equal polarization after production, the effect on the detector acceptance is equal for particle and antiparticle. The degree of polarization can still be different for the $\Lambda(1520)$ and $\overline{\Lambda}(1520)$ hyperons.

Due to the large uncertainty on the detector acceptance and selection efficiency associated with the possible polarization of the $\Lambda(1520)$ and $\overline{\Lambda}(1520)$ hyperons, we do not include this effect in the quoted systematic uncertainty. It is assumed that the degree of polarization is equal for particles and antiparticles, and small enough that this effect can be ignored. In what follows we only consider isotropic $\Lambda(1520)$ and $\overline{\Lambda}(1520)$ production.

4.5.3 Determination of the observed $\Lambda(1520)$ and $\overline{\Lambda}(1520)$ events

To determine the number of events in the $\Lambda(1520)$ and $\overline{\Lambda}(1520)$ peaks, we need to have an accurate description of the distribution of background events. Unfortunately a full Monte Carlo simulation of the expected background distribution was impossible because the $\Lambda(1520)$ resonance and more importantly several excited Λ^* resonances at higher invariant mass are not included in the PYTHIA Monte Carlo generator. For this analysis we decided to use the traditional method of describing the background distribution with a polynomial function, when simultaneously fitting only the resonance.

First, the $\Lambda(1520) \rightarrow pK^-$ invariant mass spectrum was fitted with the sum of a third order polynomial function and a Breit-Wigner resonance shape convolved with the Gaussian detector resolution of 4 MeV. Since the reconstructed mass and intrinsic width of a particle and its antiparticle are expected to be equal, but not the shape of the background, the third order polynomial function was left to vary freely. The determined width and mean of the Breit-Wigner resonance shape for the $\Lambda(1520)$ resonance were fixed and inserted in the fit of the $\overline{\Lambda}(1520) \rightarrow \overline{p}K^+$ invariant mass distribution. Ambiguities in the fit results introduced by different binning are avoided by using unbinned maximum likelihood fits, as implemented in the software package RooFit [114].

The results of the fit procedure are shown in figure 4.35. The mass for the $\Lambda(1520)$ is determined as $M_{\Lambda(1520)} = 1522.5 \pm 0.8\,\text{MeV}$ and the intrinsic width as $\Gamma_{\Lambda(1520)} = 16.7 \pm 3.4\,\text{MeV}$. The number of events in the $\Lambda(1520)$ peak is 2337 ± 316. In the $\overline{\Lambda}(1520)$ peak there are 388 ± 104 events.

Additional structures at 1470 MeV and 1540 MeV

In figure 4.35 additional structures can be noticed at invariant masses below and above 1520 MeV. There is a shoulder in the distribution of the invariant mass $M(pK^-)$ at approximately 1470 MeV, and an excess of events at 1540 MeV for the distributions of both the invariant mass $M(pK^-)$ and $M(\overline{p}K^+)$.

When trying to fit the excess of events at 1540 MeV as an additional resonance with a Breit-Wigner shape convolved with the Gaussian resolution, the intrinsic width obtained for the $\Lambda(1520)$ resonance $\Gamma_{\Lambda(1520)} = 11.8 \pm 2.5\,\text{MeV}$ is significantly smaller than the world average value $\Gamma = 15.6 \pm 1.0\,\text{MeV}$. The excess at 1540 MeV has a width compatible with the experimental resolution of 4 MeV, indicated by a zero intrinsic width for the Breit-Wigner function. This conclusion holds true when looking at the $\overline{\Lambda}(1520)$ channel. When requiring better particle identification by choosing higher values for the RICH quality parameter, the structure at 1540 MeV disappears. This leads us to the conclusion that the excess of events at 1540 MeV is caused by particle misidentifications.

When the distribution for mixed events is constructed, the shoulder at 1470 MeV is reproduced. In section 4.7, which is entirely devoted to the method of event mixing to determine distributions of background events, the distribution of the invariant mass $M(pK)$ is reproduced as figure 4.56. At higher invariant mass the description is however unsatisfactory. Since the shoulder at 1470 MeV is reproduced in the mixed events distribution, we decide to simply place the lower limit of the fitting region above 1476 MeV.

Order of background polynomial

When using a polynomial to describe the background, the appropriate order has to be found. Too low orders do not describe the background sufficiently well, but too high degrees can mimic peaks and bias the results. The distributions of the invariant mass $M(pK^-)$ and $M(\overline{p}K^+)$ were therefore fitted with second order and fourth order polynomial

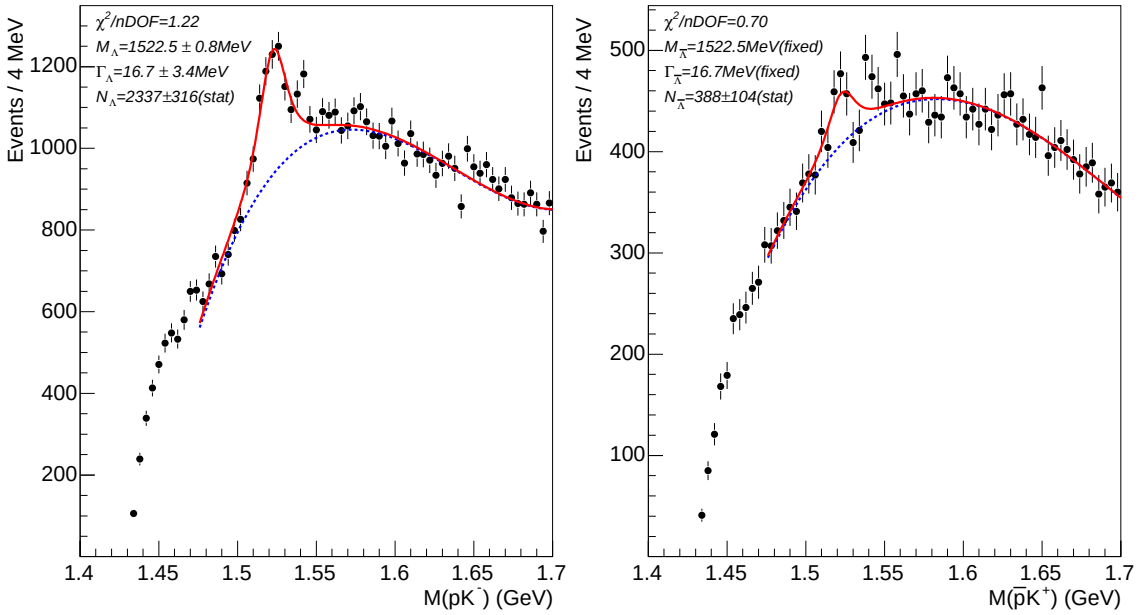

Figure 4.35: The distribution of the invariant mass $M(pK)$ for the $\Lambda(1520) \to pK^-$ (left panel) and $\overline{\Lambda}(1520) \to \overline{p}K^+$ (right panel) decay channels for the selected events in the collected data. The results of an unbinned fit with a Breit-Wigner resonance shape convolved with the Gaussian detector resolution of 4 MeV to describe the resonance peak (solid red line) and a third order polynomial for the background (dashed blue line) are superimposed. For the fit of the $\overline{\Lambda}(1520)$ invariant mass distribution, the parameters $M_{\overline{\Lambda}(1520)}$ and $\Gamma_{\overline{\Lambda}(1520)}$ were fixed to the values obtained in the $\Lambda(1520)$ fit.

Table 4.8: Additional Λ resonances contributing at higher invariant mass.

Resonance	Mass range	Intrinsic width range
$\Lambda(1600)$	$1560 < M < 1700\,\text{MeV}$	$50 < \Gamma < 250\,\text{MeV}$
$\Lambda(1670)$	$1660 < M < 1680\,\text{MeV}$	$25 < \Gamma < 50\,\text{MeV}$
$\Lambda(1690)$	$1685 < M < 1690\,\text{MeV}$	$50 < \Gamma < 70\,\text{MeV}$

functions. The goodness of fit $\chi^2/ndof$ with the second order polynomial function was 1.9, indicating the need for a higher order. For the fit with the fourth order polynomial function, the $\chi^2/ndof$ is comparable to the value with a third order polynomial function, and the number of events is equal within the statistical uncertainty. Thus, we decided to use a third order polynomial function for the background.

Fixed intrinsic width

To check whether the previous results are consistent with the existing knowledge on the $\Lambda(1520)$ resonance, we decided to keep the intrinsic width of the $\Lambda(1520)$ and $\overline{\Lambda}(1520)$ fixed at the world average value $\Gamma = 15.6\,\text{MeV}$. The determined number of resonance events $N_{\Lambda(1520)}$ and $N_{\overline{\Lambda}(152)}$ are consistent with the values obtained previously when the Breit-Wigner width was left unconstrained.

Inclusion of additional Λ^* resonances

There are several known Λ^* resonances with NK decay channels in the invariant mass region $1.4 < M(pK) < 1.7\,\text{GeV}$. They are summarized in table 4.8 [1]. The $\overline{p}K^+$ system has resonances at the same invariant mass and with the same intrinsic width as for the pK^- system.

We tried to fit the invariant mass distributions using the additional Λ^* resonances. On top of the mixed event background the Breit-Wigner resonances are superposed with mass and width varying in the mentioned ranges (corresponding to one standard deviation). The full results can be found in reference [115]. When comparing the results with the polynomial background model, there is an increase in $\chi^2/ndof$. Several fit parameters are at the boundaries of their allowed domain. We decided not to include the additional Λ resonances.

Effect of the acceptance on the reconstructed $\Lambda(1520)$ mass

In the fit of the $M(pK)$ invariant mass distribution, after selection of events corresponding to the decay $\Lambda(1520) \rightarrow pK^-$, the position of the $\Lambda(1520)$ peak is determined as $1522.5 \pm 0.8\,\text{MeV}$. However, the world average value is $1519.5 \pm 1.0\,\text{MeV}$. This difference of 3.6 standard deviations can be explained by the mass dependence of the detector acceptance in the invariant mass region around the $\Lambda(1520)$ peak.

Using the internal model for the initial momentum distributions P_t and P_z in the Monte Carlo generator gmc_dcay, several samples were generated with events distributed according to a Breit-Wigner function with different central masses. For these samples the detector acceptance and selection efficiency were determined (defined as the ratio of the number of selected events over the number of generated events). The results are shown in the left panel of figure 4.36. More events with an invariant mass above 1520 MeV are accepted than events with an invariant mass below 1520 MeV. Due to the large width of the $\Lambda(1520)$ hyperon this has a visible effect on the reconstructed spectrum, the acceptance effect skews the Breit-Wigner distribution. The difference between the reconstructed and the set $\Lambda(1520)$ mass is shown in the left panel of figure 4.37.

The product of the linear fit to the acceptance and a Breit-Wigner distribution was used to naively correct for this acceptance effect. Indeed, the acceptance becomes flat (see right panel of figure 4.36) and the mass differences disappear (see right panel of figure 4.37). Additionally, the fits to the distributions of the invariant mass $M(pK)$ improve. In figure 4.38 the distribution of the invariant mass for a set mass of 1520 MeV is shown. Before the acceptance correction the fit with the Breit-Wigner resonance shape has a $\chi^2/ndof$ larger than 3, and is offset by 1.4 MeV. When correcting for the dependence of the acceptance on the mass, the $\chi^2/ndof$ becomes 1. The shift in the position of the peak is reduced to within the statistical uncertainty.

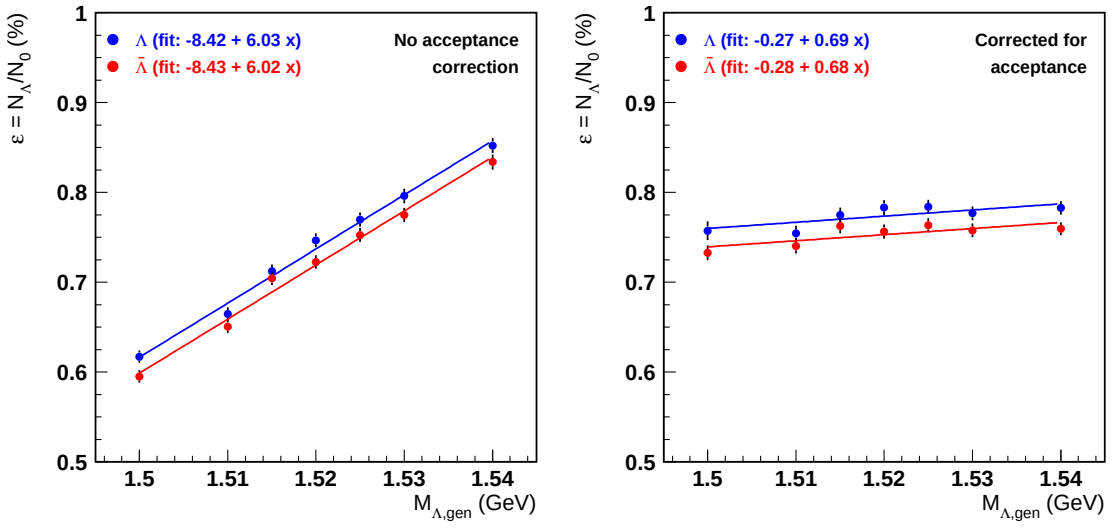

Figure 4.36: The detector acceptance and selection efficiency for the $\Lambda(1520)$, determined from different Monte Carlo simulations with varying set mass for the $\Lambda(1520)$. The slope in the left panel is used to correct for this acceptance effect, a procedure that indeed flattens out the acceptance in the right panel.

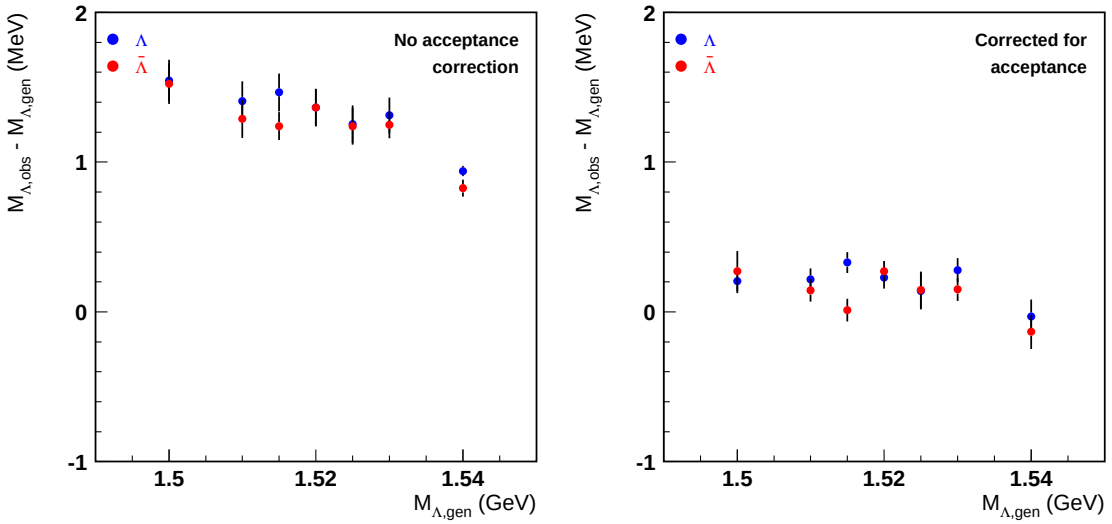

Figure 4.37: The deviation of the reconstructed $\Lambda(1520)$ mass from the set mass for different Monte Carlo simulations. Without acceptance correction, the mass of the $\Lambda(1520)$ is consistently overestimated by approximately 1.5 MeV (left panel). After correcting for this effect, the mass difference between the reconstructed and set mass is consistent with the statistical uncertainty (right panel).

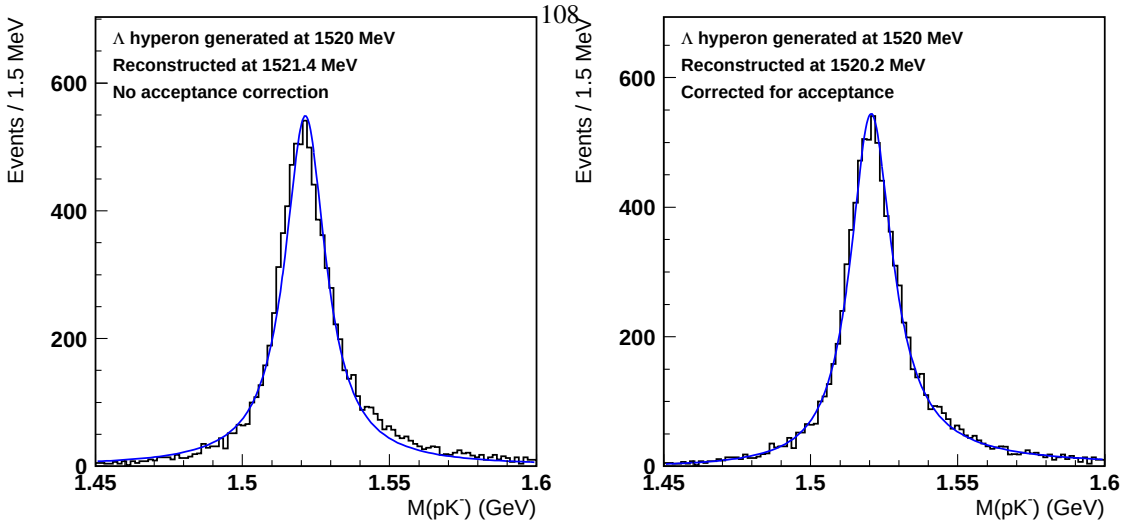

Figure 4.38: The $M(pK)$ invariant mass spectrum for Monte Carlo events, before (left panel) and after (right panel) a correction for the variable acceptance.

We do not intend to develop an acceptance correction to be used when fitting the data. We would need to know the initial momentum distributions accurately, as differences can change the acceptance correction.[14] Also, at the edges of the mass region studied here, the acceptance starts to deviate from a straight line. Rather, we want to show that the difference between the determined $\Lambda(1520)$ mass and the reference value is well understood. We estimate that due to this acceptance effect a systematic uncertainty of 1.5 MeV on the reconstructed and corrected $\Lambda(1520)$ mass is introduced.

4.5.4 Photo-production cross section of the $\Lambda(1520)$ and $\overline{\Lambda}(1520)$ hyperons

After determining the detector acceptance and selection efficiency in section 4.5.2 and the number of observed $\Lambda(1520)$ and $\overline{\Lambda}(1520)$ hyperon decays in section 4.5.3, we can now determine the cross sections for photoproduction of the $\Lambda(1520)$ and $\overline{\Lambda}(1520)$ hyperons. We use the formula

$$\sigma_{\gamma^* D\to\Lambda(1520)X} = \frac{N^{eD\to\Lambda(1520)X}_{observed}}{\Phi \cdot Br \cdot \mathcal{L} \cdot \epsilon}, \tag{4.12}$$

where $Br = 22.5\%$ is the branching ratio, $\Phi = 0.02\,\mathrm{GeV}^{-3}$ is the photon flux factor for the HERMES experiment, and ϵ is the combined detector acceptance and selection efficiency determined from the Monte Carlo simulations discussed in section 4.5.2.

Using the values for $N^{eD\to\Lambda(1520)X}_{observed}$ determined above, we obtain a cross section for photoproduction of $\Lambda(1520)$ hyperons of $\sigma_{\gamma^* D\to\Lambda(1520)X} = 65.3 \pm 8.8(\mathrm{stat}) \pm 6.9(\mathrm{sys})\,\mathrm{nb}$, and for photoproduction of $\overline{\Lambda}(1520)$ hyperons of $\sigma_{\gamma^* D\to\overline{\Lambda}(1520)X} = 9.8 \pm 2.6(\mathrm{stat}) \pm 0.9(\mathrm{sys})\,\mathrm{nb}$. The systematic uncertainty is due to the uncertainty on the determined efficiency, stemming from the unknown production mechanisms of the $\Lambda(1520)$ and $\overline{\Lambda}(1520)$ hyperons. The ratio of the two cross sections is given by

$$R_{\overline{\Lambda}/\Lambda} = 0.15 \pm 0.05(\mathrm{stat}) \pm 0.02(\mathrm{sys}). \tag{4.13}$$

[14] The acceptance differences introduced by a polarization of the $\Lambda(1520)$ hyperon discussed in section 4.5.2 are accompanied by different acceptance corrections.

4.5.5 Summary and conclusion

The photoproduction cross section for the $\Lambda(1520)$ and $\overline{\Lambda}(1520)$ hyperons was determined as $\sigma_{\gamma^* D\to\Lambda(1520)X} = 65.3\pm8.8(\text{stat})\pm6.9(\text{sys})$ nb and $\sigma_{\gamma^* D\to\overline{\Lambda}(1520)X} = 9.8\pm2.6(\text{stat})\pm0.9(\text{sys})$ nb. The systematic uncertainty is caused by the unknown production mechanism for these hyperons. The ratio of the $R_{\frac{\overline{\Lambda}}{\Lambda}} = 0.15\pm0.05(\text{stat})\pm0.02(\text{stat})$ can be used to estimate the number of Θ^- baryons that are expected to be observed with the HERMES experiment, assuming an equal particle to antiparticle ratio for exotic baryons.

4.6 Analysis of exotic baryons $\Theta(1540)$ decaying in the transverse target magnetic field

From the year 2002 until the end of 2005, the largest part of the HERMES data was collected with a transversely polarized hydrogen target. The holding field for the polarized nuclei with a strength of approximately 0.3 T was provided by a transverse magnet around the target cell. When the small deflection of charged particles in this field is ignored, the resolution in both the decay vertex position and the invariant mass of mesons and baryons decaying inside the field region is considerably worse. Without a decay vertex reconstruction method that takes the transverse magnetic field into account, the analysis of this set of polarized data is impossible.

In this section, the effects of the transverse target magnet when using standard tracking (see section 4.2) are described, highlighting the need for a different vertexing algorithm. A reconstruction method for particles decaying in the transverse target magnetic field was developed by M. Demey for the $\Lambda^0 \to p\pi^-$ vertex [94]. For the $\Theta(1540)$ and $\Xi(1860)$ analyses, this method was expanded to allow for general decay chains, involving more than one consecutive decay and both charged and neutral tracks. The new method is explained and its accuracy is demonstrated. Finally, this is applied on the search for the exotic baryon Θ^+ in the data collected on the transversely polarized hydrogen target.

4.6.1 Effect of the target magnet on event reconstruction

In the transverse magnetic field of the target magnet (see section 3.2) charged particles are deflected before they enter the main spectrometer. The track parameters determined by the standard tracking algorithms (the polar angles θ and ϕ of the tracks, and their intersections with the $z = 0$ plane or *offsets*) are only valid for the straight track segments in the front region, between the transverse target magnet region and the spectrometer magnet, where the front tracking detectors are located.

In the target region the particle follows a trajectory that cannot be described as a linear track.[15] At every point of the trajectory, the track can still be described with the usual track parameters, but they are only valid at that point.[16] For decay vertices in the magnetic field region, the angles and offsets of the decay particle tracks at the decay vertex (tangent to the real trajectory) will be different from the angles and offsets given by the spectrometer. This has two effects on the physical parameters used for event selection. First, the decay vertex will be reconstructed at an incorrect position. Depending on the actual topology of the tracks, bending towards each other or bending away from each other, the decay vertex will be reconstructed with a z coordinate that is too small, or too large respectively. Also, due to the incorrect angle between the tracks of the decay products, the invariant mass will be over- or underestimated. This leads to a degradation of the resolution of the invariant mass.

To understand the second effect, it suffices to take a look at the definition of the invariant mass M of a particle with momentum p and energy E, decaying to two particles with masses $m_{1,2}$, momenta $\vec{p}_{1,2}$, and energies $E_{1,2}$, with

$$\begin{aligned} M^2 &= E^2 - |\vec{p}|^2 = (E_1+E_2)^2 - (\vec{p}_1+\vec{p}_2)^2, && (4.14)\\ &= m_1^2 + m_2^2 + 2E_1E_2 - 2\vec{p}_1\cdot\vec{p}_2, && (4.15)\\ &= m_1^2 + m_2^2 + 2\sqrt{m_1^2-|\vec{p}_1|^2}\sqrt{m_2^2-|\vec{p}_2|^2} - 2|\vec{p}_1||\vec{p}_2|\cos\alpha. && (4.16)\end{aligned}$$

[15] The distinction between the target region and the front region is not well defined, as the magnetic field changes from 0.3 T to zero over a distance of approximately 30 cm.

[16] Since the momentum is conserved in a magnetic field, this track parameter is a constant for the complete trajectory.

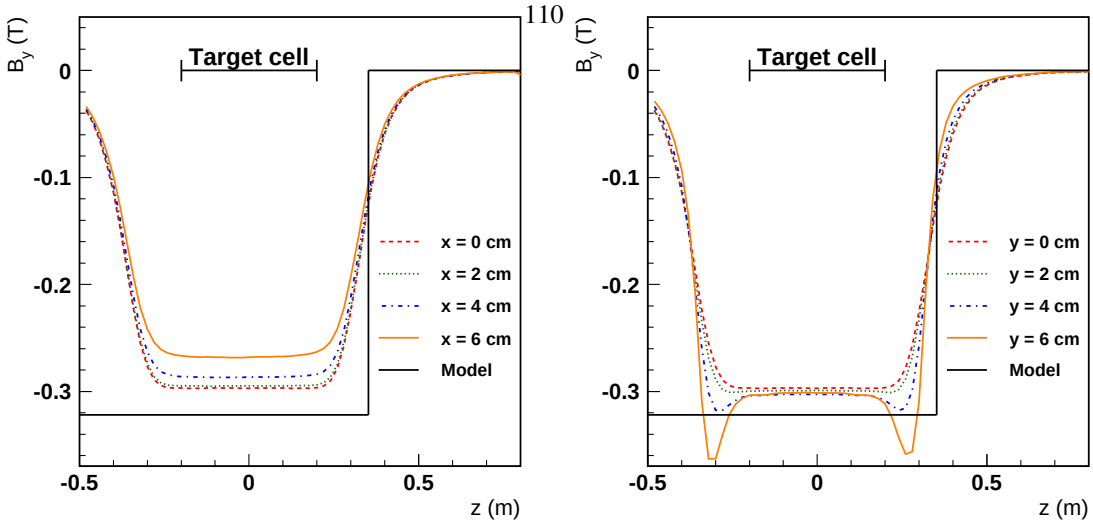

Figure 4.39: Vertical component of the transverse target magnetic field measured along the z axis for different x and y positions. In the left panel the y coordinate is kept at zero, and the x coordinate is varied. In the right panel, the y coordinate is varied keeping the x coordinate zero. The field is symmetric in x and y for the values shown. The solid black line indicates the model for the field, with the parameters determined in section 4.6.2.

Here α is the angle between the tracks of the decay particles at the vertex. It is clear that an incorrect value of α can lead to large errors on the invariant mass M, especially when the momenta $\vec{p}_{1,2}$ are large compared to M.

To correct the track of the scattered lepton, two different correction methods were already developed by the transversity group at Hermes [97]. These so-called `tmc` (transverse magnet correction) methods take into account the measured fieldmap in the target region. The first method uses a transfer matrix to determine the track parameters at the interaction point, given the track parameters after the magnetic field in the front region. For the second method a set of reference tracks was calculated, which are used to determine the track parameters. Since both correction methods inherently assume that the track is coming from the interaction point of the lepton beam with the target nucleon, the reconstruction of secondary vertices not in the immediate vicinity of the beam is impossible.

4.6.2 Correction method

In the almost homogenous section of the transverse target magnetic field (see figure 4.39), a charged particle describes in good approximation a helical track segment before it leaves the target region and is detected in the HERMES spectrometer. From the signals in the spectrometer, the (straight) track leaving the target region is reconstructed.

The ideal reconstruction method takes into account the best knowledge of the magnetic field, in the form of a measured field map, and uses a numerical integration method to determine the trajectory in the field region. Numerical minimization of the distance between two trajectories leads to the vertex position and associated distance of closest approach between the tracks. For every event, this involves a lot of calculations, which would make this method too slow for an interactive analysis.

The analytic method described in this section allows for faster vertex determination, at the cost of lower spatial accuracy. Since the magnetic field is approximately constant between the field boundaries (see figure 4.39 for the field along the lepton beam axis, larger deviations occur away from the beam axis), we can approximate the magnetic field as a one-dimensional 'box', *i.e.* a constant value below the field boundary and zero above.[17] This simplifies the tracking problem to the determination of a helical track segment inside the field box.

[17] Particles that leave the field region through the sides or the rear faces are outside of the acceptance of the main spectrometer, and thus not

An analytical solution for the point of closest approach of two helices could not be found, so an additional approximation is necessary. The radius of curvature for particles that have a momentum greater than 0.5 GeV (the minimum momentum of reconstructed tracks in the main spectrometer) is much larger than the field region (0.5 GeV corresponds to approximately 560 cm), so the deviation from a circular track will be small. In this method, the helical track with large radius of curvature is approximated by an ellipse in a tilted plane.

Mathematically, a helix around the y axis is described by

$$x = A\cos(t-\phi_0) \tag{4.17}$$
$$y = y_0 + \alpha \cdot A \cdot t \tag{4.18}$$
$$z = A\sin(t-\phi_0), \tag{4.19}$$

while our approximation is given by

$$x = A\cos(t-\phi_0) \tag{4.20}$$
$$y = y_0 + \alpha \cdot z \tag{4.21}$$
$$z = A\sin(t-\phi_0). \tag{4.22}$$

In both equations $t = \phi_0$ can be chosen to correspond to the vertex. Then $t - \phi_0$ is small and the approximation is good. For this report the z axis is in the direction of the lepton beam, the y axis in the direction of the magnetic field (but pointing upwards in the lab frame), and the x axis horizontal to the outside of the HERA ring.

Method

To calculate the vertex starting from two tracks, in a uniform magnetic field in the y direction, only the projection of the tracks in the xz plane is considered (this is the plane perpendicular to the magnetic field). This reduces the helical track segments to circle segments and neutral tracks to lines in the same plane.

In the xz plane the intersections of the (circular) projections are now determined. In this step the full circles are used, not just segments (this could lead to causality violation if subsequent decay vertex are wrongly ordered, so we have to be careful). When multiple (*i.e.* two) intersections occur, the difference in distance in the y direction for the two (unprojected) tracks is used to select one intersection over the other. This distance is also assigned as the distance of closest approach between the two tracks, and the midpoint is defined as the decay vertex. When the projections do not intersect, the distance of closest approach between the circles is determined. The points of closest approach are calculated on the track, and their midpoint is taken as the vertex, while their distance is the distance of closest approach. In the case of one neutral particle, the situation simplifies due to one straight track.

After determining the vertex, the momenta have to be rotated (the absolute value of the momentum stays the same in the conservative magnetic field). This is done by determining the tangent vector in the point of closest approach on the unprojected track. After adding the corrected momenta of the two decay products, the momentum of the mother particle is found, and the whole procedure can be repeated to find another decay vertex, if needed.

Magnetic field parameters

To determine the best values for the magnetic field boundary z_{field} and magnetic field strength B_{field}, a simultaneous scan of these two parameters was performed. Only a minimal set of event selection criteria, requiring only two oppositely charged pions and a proton or antiproton, was applied to improve the statistical precision and increase the sensitivity to differences between neighboring parameter values.

For every set of parameters the width of the K^0_S peak was determined (see figure 4.40, left panels). The set of parameters providing the narrowest peak, or in other words the lowest resolution, corresponds to the parameters of the magnetic field that provide the best reconstructing in this method.

A different, independent method for determining the best field parameters looks at the K^0_S decay tracks in two distinct topologies. The oppositely charged pion decay tracks can either bend away from each other, or bend towards

considered in this analysis.

each other. When the field parameters are chosen incorrectly, the effect on the invariant mass for these topologies will be opposite. An increase in the magnetic field causes increased bending of the tracks, and an opening angle of the decay tracks that is larger for tracks bending towards each other, or smaller for tracks bending away from each other. For every set of parameters, the difference between the K^0_S invariant mass for these two topologies is determined (see figure 4.40, right panels). Where the difference is zero, the parameters are optimal for the rconstruction method.

From figure 4.40, we conclude that optimal values for the field boundary and strength are $z_{field} = 35.2\,\text{cm}$ and $B_{field} = -0.305\,\text{T}$. The determined values correspond approximately to the physical values, as can be seen in figure 4.39. The correlation between B_{field} and z_{field} is strong, because the bending of the tracks is determined by the product of z_{field} and B_{field}.

Demonstration

In figure 4.41 a Θ decay candidate is shown. Red tracks and upward triangles (for the vertices) correspond to positive tracks, green tracks and circles to neutral tracks, and blue tracks and downward triangles to negative tracks. In the top panels the K^0_S vertex is shown, projected on the (xz) plane (left panel) and the (yz) plane (right panel). The bottom panels show the projections of the Θ vertex. The green circle corresponds to the K^0_S vertex. The dashed colored lines indicate the circular trajectory of the track and the continuation of the straight track in the field region. The dashed black lines indicate the border of the magnetic field region and the beam line.

4.6.3 Analysis of the $\Theta(1540)$

Data and event selection

All transversely polarized hydrogen data collected between the years 2002 and 2005 (corresponding to the offline data productions `02c0`, `03c0`, `04b0`, and `05b1`[18]) were used for this analysis. This corresponds to an integrated luminosity of $161.4\,\text{pb}^{-1}$, or a total of 7.413 M DIS events collected by the spectrometer. We need to apply additional selection criteria for the analysis of this data set. Details of the implementation of the following track and event selection criteria can be found in section 4.2.

In every event we require three or more long hadron tracks in the main spectrometer. When more than three hadron tracks are present, all combinations of three tracks are considered as separate events. Every event has to contain one (positively charged) proton, as identified by the RICH, with a momentum between 4 and 9 GeV, and two oppositely charged pions, as identified by the RICH, with a momentum between 1 and 15 GeV. Only events with a particle identification quality parameter for the proton track larger than 1.5 are selected. Together, these are referred to as *basic selection criteria* in what follows.

Since no reliable Monte Carlo simulations for production and decay of the $\Theta(1540)$ exist, and to allow for a comparison of previously published results on other data sets, the *standard selection criteria* were used at first. The effect of the different vertexing algorithm is accounted for in a set of *updated selection criteria*.

The distance of closest approach between the two corrected pion tracks is smaller than 1 cm. The midpoint of this line segment is defined as the K^0_S decay vertex. Similarly, the production vertex is defined as the midpoint of the distance of closest approach between the corrected p and reconstructed K^0_S track. The distance between the production vertex and the K^0_S decay vertex should be larger than 7 cm, and causality requires that the z coordinate of the K^0_S decay vertex is larger than the z coordinate of its production vertex. These selection criteria (including the *basic selection criteria*) will be referred to as *kshort selection criteria*.

For the $M(p\pi^+\pi^-)$ invariant mass spectra, additionally the following selection criteria were applied. To select only events that contain a K^0_S candidate track, the invariant mass $M(\pi^+\pi^-)$ is required to be between 0.485 and 0.509 GeV, corresponding to a $\pm 2\,\sigma$ window around the K^0_S peak in the deuterium data of 2000. The distance of closest approach between the reconstructed K^0_S track and the proton track should be smaller than 0.6 cm.

The production vertex is required to be inside the target cell (*i.e.* a z coordinate between $-18\,\text{cm}$ and $+18\,\text{cm}$[19]), and have a radial distance to the lepton beam smaller than 0.4 cm (determined by the transverse tracking resolution). The lepton beam position is corrected by a year-averaged offset (x, y) cm, to account for changes in the beam position.

[18] For the years 2004 and 2005 new offline data productions became available after this analysis was performed. However, only modifications to the lepton transverse magnet correction methods `tmc` were applied, which are not used in this analysis.

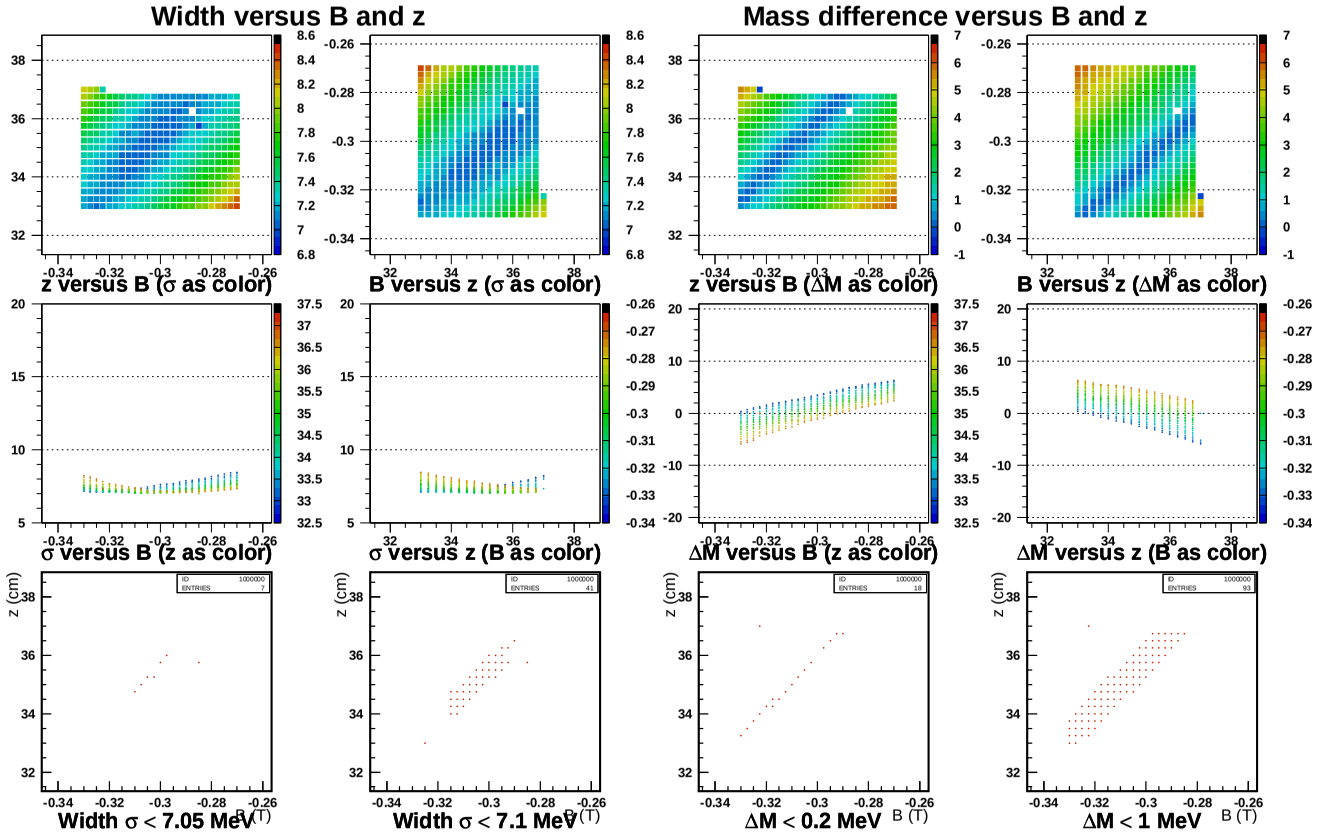

Figure 4.40: Scan of the field boundary and field strength in the reconstruction of the K^0_S from data. The width of the K^0_S peak is shown in the left panels, the difference between the K^0_S mass for two different topologies (see text) is shown in the right panels. The optimal field parameters are chosen as $z = 35.2\,\text{cm}$ and $B = -0.305\,\text{T}$. Axis labels are missing due to technical limitations in PAW.

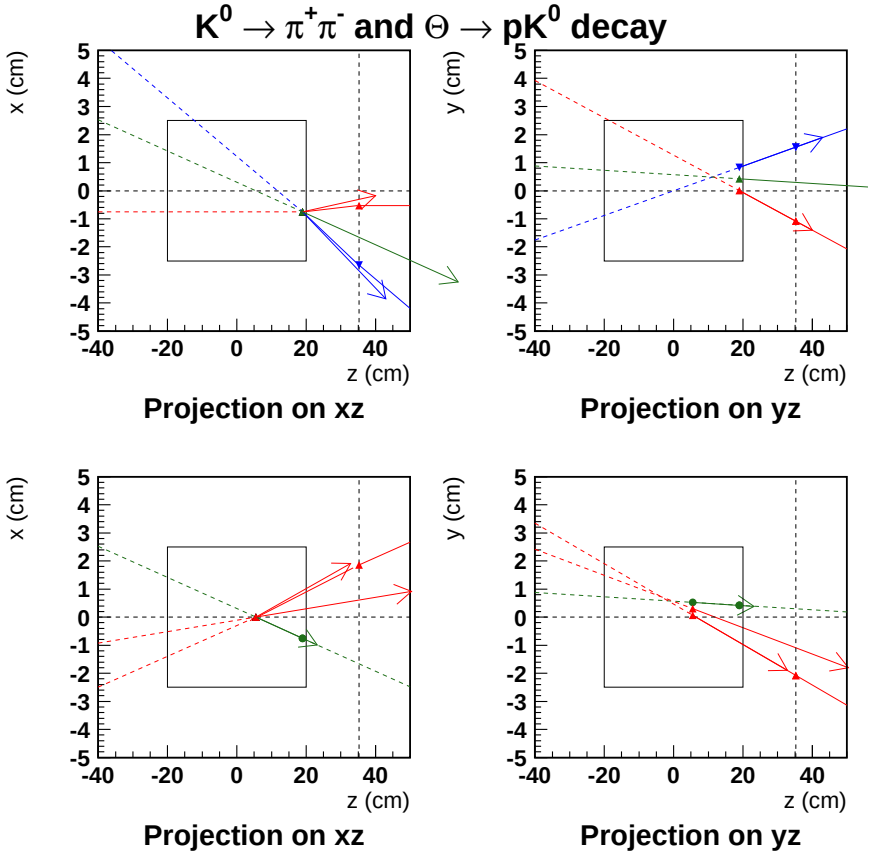

Figure 4.41: An event display of a Θ candidate event. The top panels correspond to the $K^0_S \rightarrow \pi^+\pi^-$ vertex, the bottom panels to the $\Theta \rightarrow pK^0_S$ vertex. The magnetic field was inflated to 1 T to show the effects on the vertexing. For more information, refer to the text.

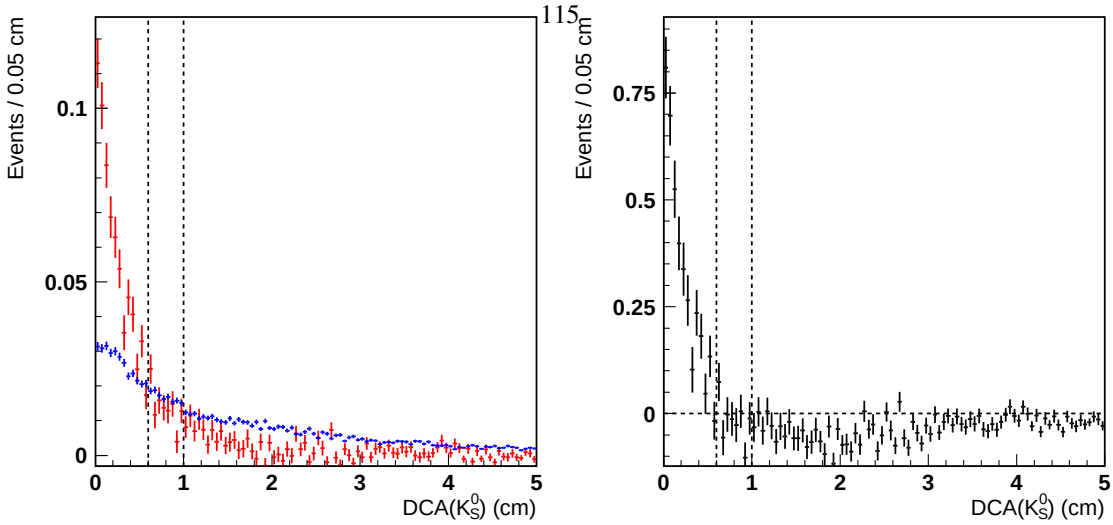

Figure 4.42: The normalized distributions of the distance of closest approach between the two pions from the decay of the K^0_S candidate (left panel), for signal (red histogram) and the background events (blue histogram), and the difference between signal and background distributions (right panel). The vertical lines indicate the maximum distance of closest approach allowed for the standard and the updated selection criteria.

In table 4.2 the offset parameters for the data sets can be found. These last set of selection criteria (including the *kshort selection criteria*), necessary to select candidate $\Theta(1540)$ events, are called *theta selection criteria*.

The contribution of ghost track events was investigated. Among the selected events, no ghost track events were found. No additional ghost track suppression was applied. The list of selected events was checked for event double counting.

Updated selection criteria

Since a different vertexing algorithm is used in this analysis, changes in the tracking and vertexing resolution are expected. The upper limit on the distance of closest approach between the two pions, the lower limit on the decay length of the K^0_S candidate, and the $M(\pi^+\pi^-)$ invariant mass window were re-evaluated for this analysis. To determine the optimal values for the cut-off parameters in selection criteria, the method discussed in 4.2.3 was used. The distributions of the selection variables for events in the peak region and the sideband regions of the K^0_S peak in the $M(\pi^+\pi^-)$ invariant mass distribution were compared. The peak region, defined here as the $\pm 2\,\sigma$ interval around the mean position of the Gaussian peak (*i.e.* between 0.485 and 0.509 GeV), contains also background events which are assumed have the same characteristics as events in the sideband region, defined outside of an approximately $\pm 5\,\sigma$ interval around the peak, *i.e.* not between 0.470 and 0.530 GeV, but between 0.4 and 0.6 GeV.

In the left panel of figure 4.42 the normalized distributions of the distance of closest approach between the two pions are shown for signal (red histogram) and background events (blue histogram). This corresponds to the probability distributions for signal and background events. Similarly, in figure 4.43 the normalized distributions of the decay length of the K^0_S candidate are shown for both types of events. In the right panel, the difference between the probability distributions is shown. The region with a positive difference between the probability distributions corresponds with events that are more likely signal events. These plots were obtained using the *kshort selection*, except for the criterium involving the plotted parameter.

[19] For the recoil data the target cell was moved closer to the spectrometer, and the limits were changed to -5 cm and $+25$ cm.

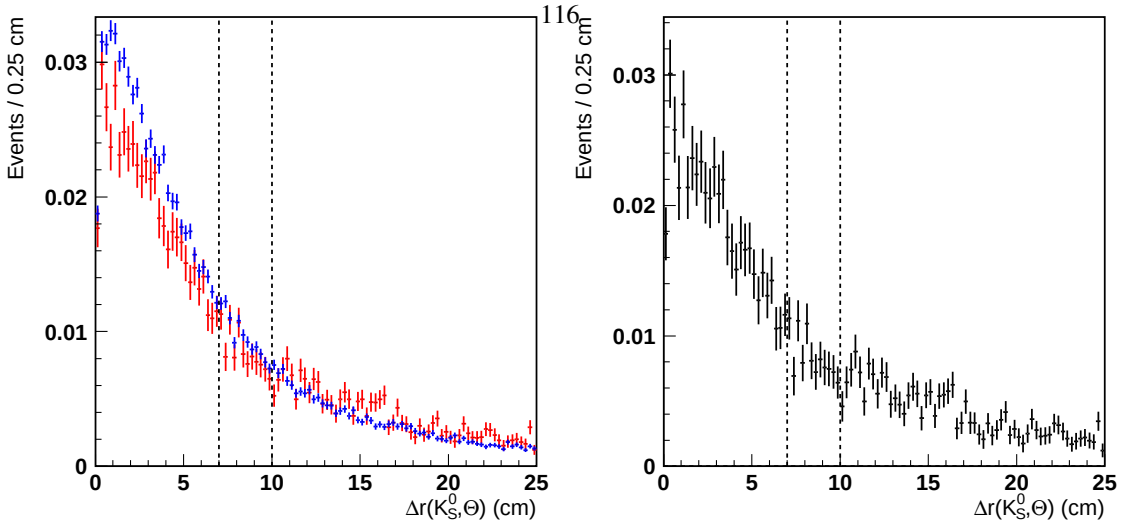

Figure 4.43: The normalized distributions of the decay length of the K^0_S candidate (left panel), for signal (red histogram) and the background events (blue histogram), and the difference between signal and background distributions (right panel). The vertical lines indicate the minimum decay length allowed for the standard and the updated selection criteria.

The limits on the distance of closest approach between the two pions and the decay length of the K^0_S candidate in the standard selection criteria are approximately correct, even with the transverse target magnet deflection and track correction. For this analysis we also consider an updated set of selection criteria, for which we choose the upper limit on the distance of closest approach between the two pions at 0.6 cm, and the lower limit on the decay length of the K^0_S candidate at 10.0 cm. The K^0_S invariant mass window is also updated after these two changes, now corresponding to a $2\,\sigma$ window, between 0.484 and 0.511 MeV.

K^0_S selection

We now determine the $M(\pi^+\pi^-)$ invariant mass distributions for all events that pass the selection criteria. In figure 4.44 only the *basic selection criteria* are applied. To show the effect of the transverse target magnet corrections, the distributions are shown for uncorrected events (left panel) and for corrected events (right panel). Since the transverse target magnet corrections to the tracks do not influence the selection criteria, the total number of events is equal before and after the correction is applied. In figure 4.45 the *kshort selection criteria* are required. Since now events are selected according to the distance of closest approach between the two pions and the decay length of the K^0_S candidate, the number of events in the corrected and uncorrected distributions are different.

When using the standard `tmc` methods intended for lepton track correction,[20] we obtain the $M(\pi^+\pi^-)$ invariant mass distribution in figure 4.46. Due to the distance of closest approach and decay length selection criteria, the number of selected events is more than a factor two lower when using the standard `tmc` methods compared to our correction method, reflected in the number of events per bin.

In the figures 4.44 and 4.45, the K^0_S peaks are fitted with a Gaussian function and a linear background. In both figures 4.44 and 4.45, the difference between the corrected and uncorrected distributions is clearly visible (even though a Gaussian function does not describe the data well for uncorrected tracks). The width of the Gaussian function fitted to the distributions is 12.5 MeV before any correction, and 6.9 MeV after our correction.[21] The width of the K^0_S peak when the standard `tmc` methods are applied, is 11.3 MeV. The smearing of the K^0_S peak due to the transverse target

[20] For each year the appropriate method was selected: `tmc1` for 2003 and 2004, `tmc2` for 2002 and 2005.

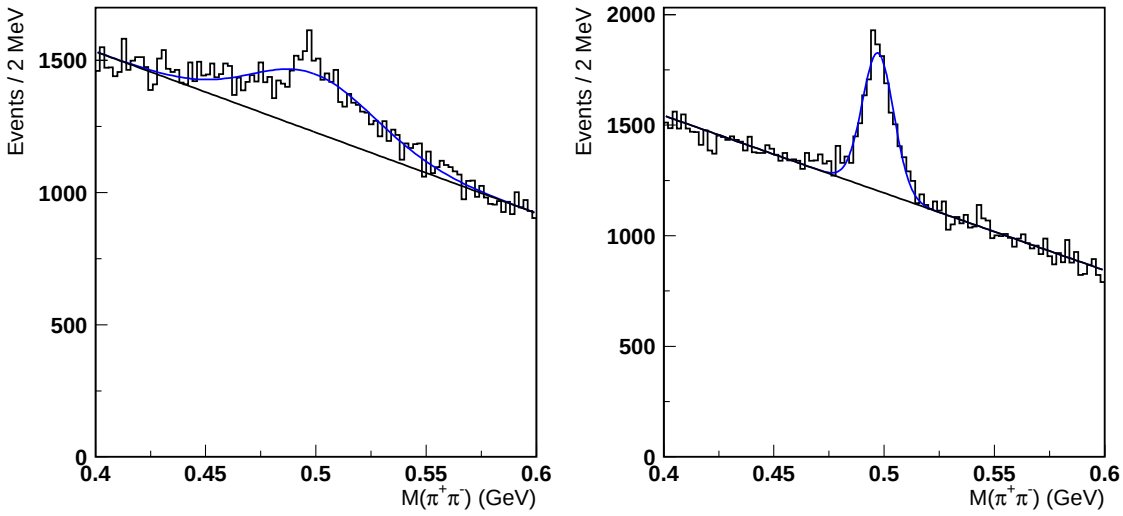

Figure 4.44: The $M(\pi^+\pi^-)$ invariant mass distribution after all *basic selection criteria*, before (left panel) and after our transverse target magnet correction (right panel).

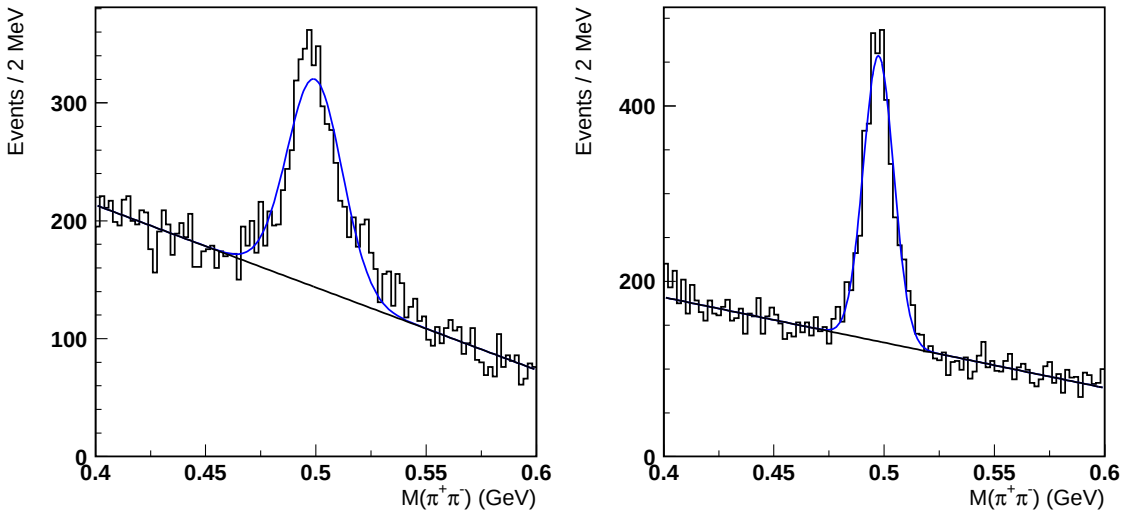

Figure 4.45: The $M(\pi^+\pi^-)$ invariant mass distribution after all *kshort selection criteria*, before (left panel) and after our transverse target magnet correction (right panel). The number of selected events is different due to the distance of closest approach and decay length selection criteria, which involve the corrected track parameters.

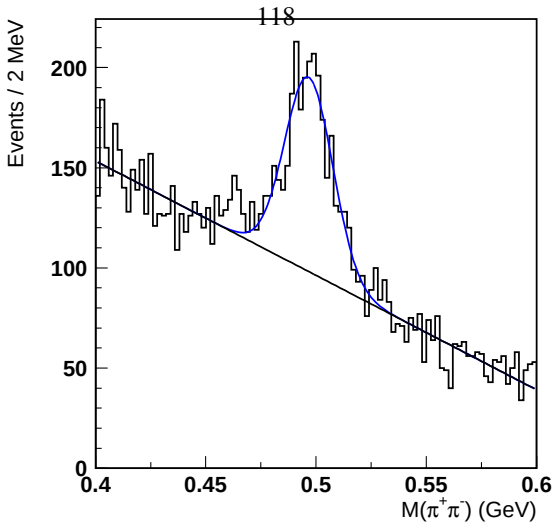

Figure 4.46: The $M(\pi^+\pi^-)$ invariant mass distribution after all *kshort selection criteria*, determined with the standard `tmc` correction methods. This figure should be compared to figure 4.45.

magnet is significantly reduced by our correction method. The standard `tmc` methods are not applicable for this analysis.

Using the *basic selection criteria* and our correction method, the K^0_S mass is determined as 497.4 ± 0.3 MeV, and the width of the peak is 7.4 ± 0.3 MeV. After applying the *kshort selection criteria*, the K^0_S mass is 497.6 ± 0.2 MeV, and the width of the peak becomes 6.9 ± 0.2 MeV. In figure 4.44 the total number of K^0_S events in the Gaussian peak is approximately 7700. After *kshort selection criteria*, the total number of K^0_S events in the Gaussian peak is 3297 ± 97, on a background of 3009 events. The visible suppression of the background events is not accompanied by a change in the K^0_S peak position and width.

When the *theta selection criteria* are applied, we obtain the $M(\pi^+\pi^-)$ invariant mass distribution in figure 4.47 (left panel). The K^0_S mass resulting from the fit with a Gaussian function is now 497.7 ± 0.4 MeV, and the width of the peak is 6.5 ± 0.4 MeV. The number of K^0_S events is 575 ± 37, on a background of 145 events. The additional selection criteria are not expected to influence the signal to background ratio, and are also not accompanied by a change in the K^0_S peak position and width.

Finally, the distribution of the $M(\pi^+\pi^-)$ invariant mass when events are selected according to the *updated selection criteria*, taking into account changes in the tracking resolution, is shown in figure 4.47 (right panel). The number of K^0_S events is reduced to 410 ± 33 events, while the K^0_S mass and width are now 496.9 ± 0.4 MeV and 6.4 ± 0.4 MeV.

Θ^+ selection

With the *theta selection criteria* the $M(p\pi^+\pi^-)$ invariant mass distribution is determined, shown in the left panel of figure 4.48. Expanding the invariant mass range, the $M(p\pi^+\pi^-)$ invariant mass distribution is shown in figure 4.48 (right panel). The bin size and starting point is equal in both figures, and choses to correspond to the binning in figure 2 of the first HERMES publication on this topic[4]. Similarly, using the *updated selection criteria* the distributions in 4.49 were obtained.

No prominent features are visible in the $M(p\pi^+\pi^-)$ invariant mass distributions, but the low number of events makes it difficult to determine a quantitative statement (in terms of an upper limit on the yield) for this data set.

[21] This number can be compared to the width of the K^0_S peak in a similar data sample, with identical selection criteria, obtained on unpolarized deuterium gas without transverse target magnet. In that case the width is 6.7 MeV.

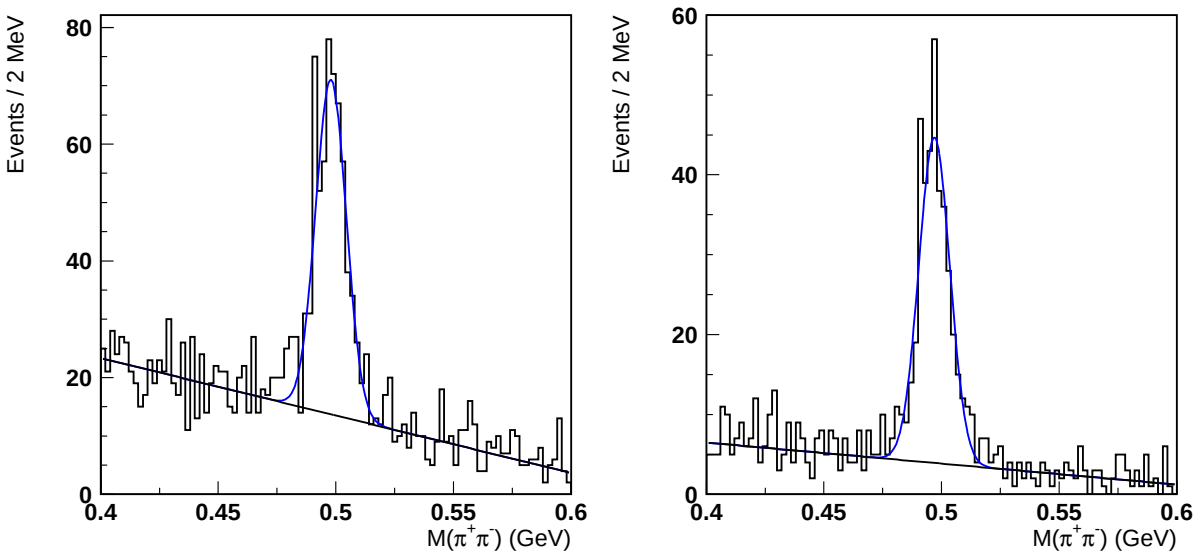

Figure 4.47: The $M(\pi^+\pi^-)$ invariant mass distribution after all *theta selection criteria* (left panel) and after the *updated selection criteria* (right panel). The *updated selection criteria* take into account the possible effects of our correction method on the tracking resolution.

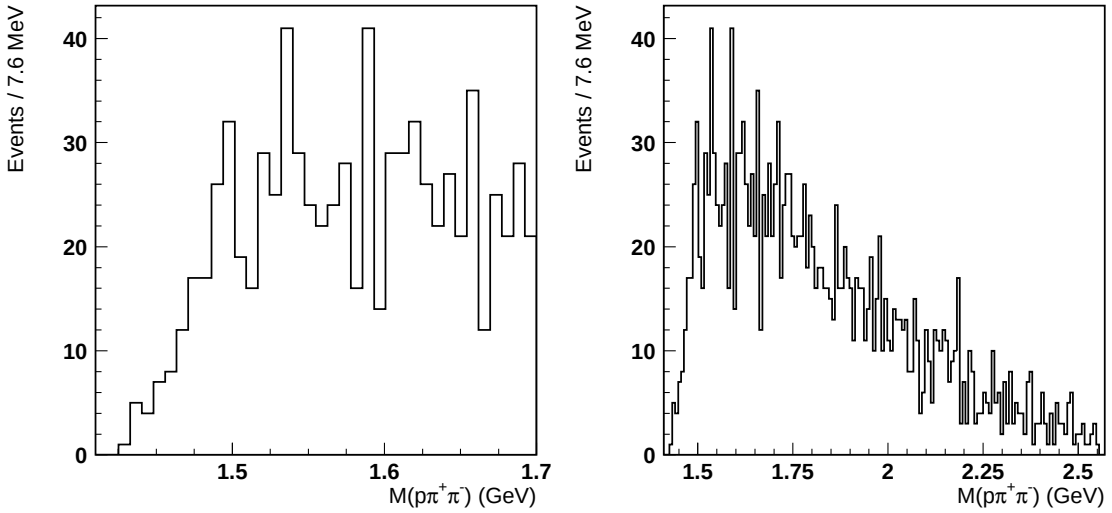

Figure 4.48: The $M(p\pi^+\pi^-)$ invariant mass distribution after the *theta selection criteria* (left panel) in a binning corresponding to [4]. In the right panel, the invariant mass range was expanded to 2.3 GeV without changing this binning.

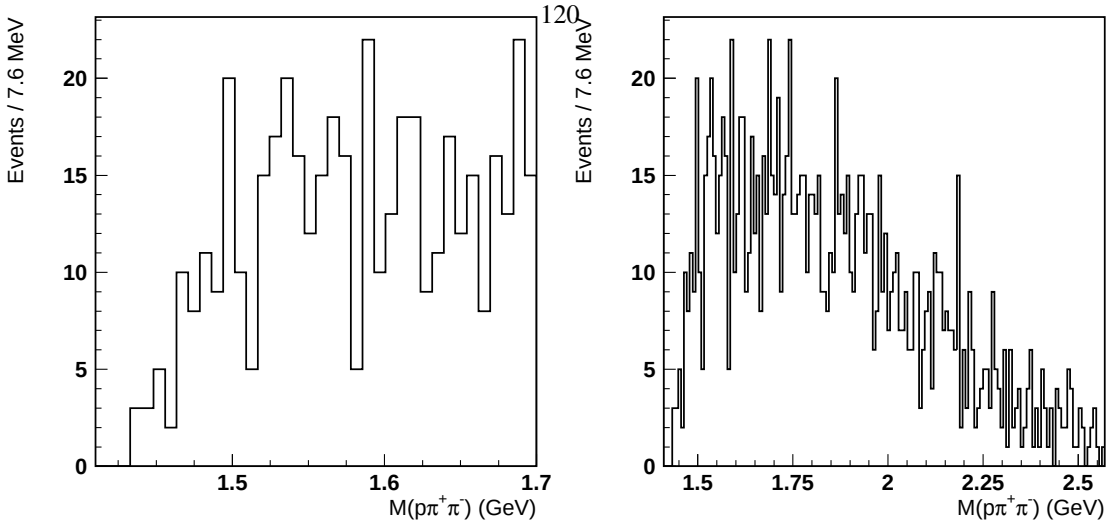

Figure 4.49: The $M(p\pi^+\pi^-)$ invariant mass distribution after *updated selection criteria* (left panel) in a binning corresponding to [4]. In the right panel, the invariant mass range was expanded to 2.3 GeV without changing this binning.

4.6.4 Summary and conclusion

We conclude that for the analysis of the transversely polarized hydrogen target data set a new correction method is necessary. The `tmc` correction methods developed for leptons from beam interactions are not sufficient. A different vertexing method, developed by M. Demey, was expanded in this thesis, and shown to work satisfactorily, reproducing resonances with a resolution consistent with the data taking period without transverse magnetic field.

The standard selection criteria of the $\Theta(1540)$ analysis were re-evaluated to account for changes in the tracking resolution associated with the new vertexing method. In the Θ invariant mass distributions with these standard or updated selection criteria, not enough events were available to either confirm the existence of the Θ, or to set an upper limit on its cross section or yield.

Weakening the requirements will increase the number of selected events, but proportionally also background events will be accepted. A careful study of this strategy could be pursued, but the collection and analysis of more data on an unpolarized deuterium target is a more straight forward way to significant results.

4.7 Event mixing as an estimator for the distribution of background events

To determine the number of resonance events in an invariant mass,[22] it is important to have an accurate description of the invariant mass distribution of background events, or in short the background distribution.[23] Statistical fluctuations of a poorly known background distribution can easily create an excess of events above the underestimated background distribution, which could be mistaken for a real resonance peak. Since the uncertainty on the number of events n in an invariant mass bin is proportional to $\sqrt{n}$, and even larger for small n where n does not follow a Gaussian distribution, this is in particular important when there are only few events in the distribution. An accurate estimation of the background distribution can influence the conclusions on the observation of a resonance.

[22] Although in this section only invariant mass distributions are used, this method is applicable to other distributions too.

[23] With background events we mean here all events that do not originate from the decay of the resonance under study. This could include events with misidentified tracks, decays of other resonances, or just combinatorial background events which are formed by the combination of tracks created in different processes during the same collision.

Several methods exist to estimate the background distribution. Ideally the background distribution can be simulated with Monte Carlo methods. At the HERMES experiment the PYTHIA Monte Carlo generator would be most suitable for the determination of the background distributions. Unfortunately, a number of broad resonances in the mass region relevant for the analysis of the exotic baryon $\Theta(1540)$ are not included in the PYTHIA Monte Carlo generator. Because the properties of these resonances are poorly known, it is difficult to implement them in a Monte Carlo generator without introducing large uncertainties. Different assumptions for the unknown spin of these resonances could result in a different acceptance and resonance shape in the final distributions. A more practical limitation is the time it takes to simulate enough collision events to retain a statistically relevant sample of final events in the acceptance of the spectrometer and after event selection criteria.

For some reaction channels the symmetry of the background events can be exploited to obtain a distribution which does not contain the resonance under study (after normalization to account for a potentially different yield). For example, by using the charge symmetry the background distribution of the Λ hyperon decaying to $p\pi^-$ can be estimated quite well with the final state $p\pi^+$, even without normalization. Because the number of events in the symmetric decay channel is usually of the same order as in the original distribution, the statistical precision of the background description that can be reached is limited. In the case of the exotic baryon $\Theta^+(1540)$ with the decay mode to pK^0_S the final state is already charge symmetric. The K^0_S meson is a mixture of both K^0 and $\overline{K}^0$ components, and exchanging the proton p for an antiproton $\overline{p}$ will just select $\Theta^-(1540)$ resonance decays in the final state. This renders the method unusable for the exotic baryon $\Theta^+(1540)$.[24]

Without knowledge of the origin and the physical production mechanisms of the background events, and without knowledge of a process with a similar background shape for symmetry reasons, a fit with a polynomial or other suitably chosen function is often used to determine the shape of the background distribution. By choosing a polynomial function of sufficiently high degree any distribution can be fitted.[25] The problem of over-fitting is not really relevant in the current discussion, but rather under-fitting. Deviations from the fitted polynomial function are sometimes mistakenly assumed to be physical events that are not part of the background. First, one has to motivate why a polynomial function with a particular degree can be considered a good estimate of the background.

In this section the method of event mixing is presented. It is another method for the determination of the background distribution. When the detected particle tracks of different events are combined as if they were from one event, resonances will not be reproduced. In fact, all statistical correlations will be removed from the sample. Because the number of possible combinations of two events increases as $\mathcal{O}(n^2)$ for n physical events, the statistical precision of the background distribution can be increased substantially. Usually the distribution of the mixed events has to be scaled down or normalized to the original distribution in a region without resonances, or by using a different kinematic variable which is expected to have a similar distribution for resonance and background events.

Even though the event mixing method seems conceptually very simple, several effects have to be taken into account. One immediately realizes that events with different track multiplicities should only be mixed with caution, because these events have different kinematic distributions.[26] The mixed events have to be kinematically similar to the original events, otherwise different distribution of the final invariant mass are obtained.

We discuss the subtle effects that make the method more difficult to use. The results of the method are demonstrated on several well-established resonances. In the section 4.8 the event mixing method is applied on the invariant mass distributions of the exotic baryon analysis.

4.7.1 Event mixing method

At the HERMES experiment knowledge about the event mixing method came only slowly. Although the method of event mixing was already applied in the original analysis of the $\Theta^+(1540)$ [4], several improvements were needed.

[24] The exchange of the proton and the antiproton also changes the shape of the background at the HERMES experiment, due to the different origins of protons and antiprotons when a particle target is used. The target gas contains only atoms, and no anti-atoms, which creates an asymmetry in favor of particles. Only one fifth of the proton tracks at the HERMES experiments is negatively charged. They correspond to production mechanisms where either a sea antiquark was struck by the DIS lepton, or where a quark/antiquark pair was produced in the fragmentation of the struck nucleon. Naturally, the kinematic parameters of the final state particles will be different, leading to different final invariant mass distributions.

[25] With enough parameters even elephants can be fitted! (John von Neumann)

[26] On average, the momentum of the tracks in four particle events will be lower than the momentum of the tracks in three particle events.

Effects of event selection

Originally the candidate events for $\Theta^+ \rightarrow pK^0_S \rightarrow p\pi^+\pi^-$ decay events were subjected to the selection criteria before the p and (reconstructed) K^0_S tracks were mixed. This meant that only the (approximately one thousand) events in the final invariant mass distribution were used for the event mixing. Because of the large number of combinations a statistically precise background distribution could still be obtained.

However, when the steps are applied in this order the mixed events will not satisfy the event selection criteria. It is possible, and even probable, that the distance of closest approach between the mixed p and K^0_S tracks is large, in contrast to the background events which compose the actual background distribution. The constructed mixed events have different characteristics compared to the background events we are trying to investigate. This means that generally the invariant mass distribution of these naively mixed events will be different from the invariant mass distribution of the background events.

If we want the mixed event to have an invariant mass distribution that represents the background distribution, also the distribution of the other kinematic and topological parameters have to be similar. Although we are not able to determine these distributions for the background events, we have constrained them by the event selection criteria. To constrain the mixed event distributions to the same ranges will improve the similarity between the mixed and unmixed background distributions. A better approach is therefore to mix the events before applying the event selection criteria.

One could argue that, even before the data are analyzed, several selection criteria are already applied. Tracks with a small transverse momentum are not detected, low-momentum tracks do not reach the particle identification detectors and are discarded, etc… However, these selection criteria are also 'applied' to the background events. All selection criteria which act on a single track can be applied before the event mixing, since they have no way of changing in the process of event mixing. Selection variables which combine the information of two tracks, such as the distance of closest approach, will change when one track is combined with a different track.

Some subtleties in the operation of the RICH particle identification detector in the HERMES spectrometer (see section 3.3.2) introduce implicit correlations between two tracks. Because the RICH detector is less efficient when the distance between the image of two tracks on the photomultiplier array is equal to the radius of the Čerenkov rings, there are less identified protons when a second track is in the same detector half. This could artificially increase the probability that the proton and the K^0_S meson are in opposite detector halves.[27] After event mixing the probability for tracks in opposite and equal detector halves is equal. Since the background distribution for events with p and K^0_S tracks in opposite halves is different from the background distribution for events with tracks in the same half, this could affect the mixed event distribution. This effect is assumed to be small, but is practically very difficult to estimate. Improvements to the identification algorithm of the RICH detector are expected to solve this problem.

If a resonance does not decay immediately to π, K or p tracks detected in the spectrometer, but instead decays to an intermediate resonance, the selection criteria for this intermediate resonance have to be applied before the event mixing. In the case of the exotic decay $\Theta^+(1540) \rightarrow pK^0_S \rightarrow p\pi^+\pi^-$ this means that the distance of closest approach between the two pion tracks can be restricted before the reconstructed K^0_S track and the proton track are mixed.

Effects of mixed resonance events

When events are mixed to determine the shape of the invariant mass distribution for background events, it is important to realize that not only background events are mixed but also resonance events [116, 117]. The underlying assumption of the method of event mixing is that the distribution of the uncorrelated background events does not change when the events are mixed. This is not necessarily true for resonance events when they are mixed among each other. Unfortunately they cannot easily be excluded from an analysis (the goal is to determine the number of these resonance events, after all). We do assume that the combinations of resonance tracks with a non-resonance tracks lead to the distribution of background events.

Monte Carlo simulations can be used to determine the shape of the invariant mass distribution of resonance events after event mixing. The invariant mass distribution of the Λ hyperon is a good example of a distribution with only one prominent resonance. With the PYTHIA Monte Carlo generator a large number of events were simulated, with the only

[27] The K^0_S meson is already more likely to decay in two pions in the same detector half, due to the acceptance gap between the detector halves. When an additional proton is required in the event, this effect would reduce the number of events with one pion in each detector half even more.

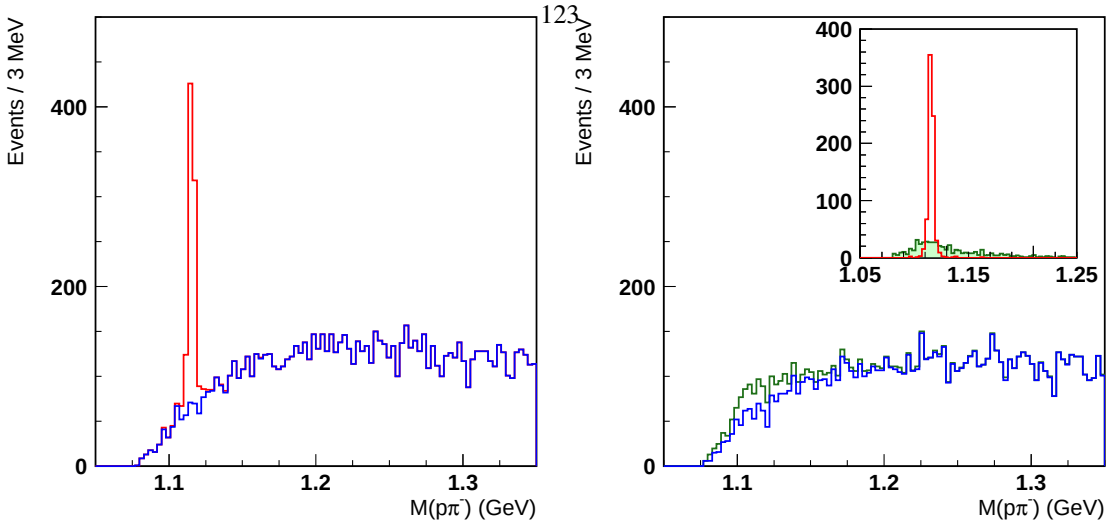

Figure 4.50: The effect of resonance events on the mixed event distribution is demonstrated with events simulated with the PYTHIA Monte Carlo generator. The distributions of the invariant mass $M(p\pi^-)$ without event mixing (left panel) and with event mixing (right panel) contain Λ hyperon decay events (indicated in red without event mixing and in green after event mixing) and uncorrelated combinatorial and string fragmentation events are shown in the blue histogram. After event mixing the Λ resonance is smeared out, as shown in the inset of the right panel (shaded green histogram) for only resonance events.

requirement that a high-momentum hadron ($P > 4\,\text{GeV}$) was detected by the spectrometer. The invariant mass distribution without event mixing for these simulated events is shown in the left panel of figure 4.50. The resonance peak of the Λ hyperon is clearly visible and the remaining components of the distribution are mostly combinatorial (*i.e.* the proton and the pion were created in different processes) or from string breaks in the Lund model for fragmentation.[28]

When we mix the events of this simulated sample, we obtain the distributions in the right panel of figure 4.50. The shape of the combinatorial event distribution is unchanged, but the narrow resonance peak is now smeared out and has become a relatively broad contribution to the total mixed event distribution. In the inset the narrow resonance peak and the smeared distribution with mixed events are compared.

When a Monte Carlo simulation of the resonance is available, the following procedure can be used to extract the background distribution. The mixed event distribution is constructed including all data events and the mixed resonance distribution is constructed using the simulated resonance events only. Using a variable normalization the mixed resonance distribution is subtracted from the mixed event distribution of the data events. The normalization of the mixed event distribution for data events is first determined in a region where the mixed resonance distribution is negligible. The normalization of the mixed resonance distribution is then determined just outside the resonance peak, but where it has a significant contribution.

Because of the low number of simulated events available compared to the number of collected events in the data sample, the mixed resonance distribution could not be determined with high statistical precision. In the left panel of figure 4.51 the distributions after event mixing with simulated events are compared to the distributions obtained with the collected data. The disagreement that is present after event mixing of the collected data can indeed be attributed to the mixed resonance distribution. In the inset the difference between the distribution for regular and mixed events is compared with the mixed resonance distribution obtained with the Monte Carlo simulation. The good agreement indicates that the disagreement between the original invariant mass distribution and the mixed event distribution can

[28] A very small number of events from decays of Δ^0 baryons is ignored.

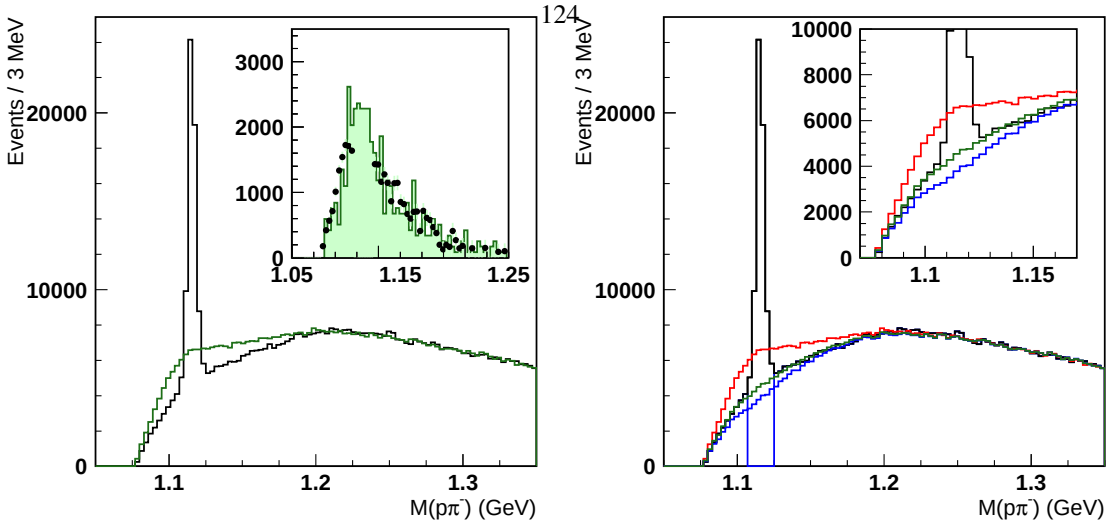

Figure 4.51: The mixed resonance events are modeled with Monte Carlo or discarded before mixing the events. In the left panel the disagreement between the mixed event distribution (green curve) and the normal distribution (black curve) for events collected by the spectrometer is shown. In the inset the mixed resonance distribution determined from a Monte Carlo simulation (shaded green curve) is compared with the difference between the normal and mixed event distributions (black dots). In the right panel the blue curve is obtained when all resonance events between the blue vertical lines are discarded before the events are mixed. A rough estimate of the number of discarded resonance and background events is used to combine the red and blue curves to determine the green curve.

be explained by this effect.

Another method to reduce the effect of resonance events is to exclude them before event mixing. While this brings us back to the problems with event selection before event mixing, the number of events that are discarded should be kept small by only removing a narrow window around the resonance peak. This approach is demonstrated in the right panel of figure 4.51. The distortion of the kinematic phase space due to the discarded events, which could influence the shape of the distribution of the mixed events, seems to be relatively small. Using an estimate of the number of resonance events and the number of background events in the discarded mass window, the appropriate combination of the mixed event distributions with and without resonance events is constructed. This method seems to describe the background distribution rather well. In the inset of figure 4.51 the relevant invariant mass region is blown up for more detail.

The advantage of discarding all events in an invariant mass window around the resonance peak is that no Monte Carlo simulation is needed anymore. When it is impossible to simulate the resonance, for example due to an unknown production mechanism, this is the only way to determine the background distribution.

Effects of kinematic mismatch

Event mixing is often criticized for the potential violation of momentum conservation. This formulation is somewhat exaggerated when only inclusive processes are concerned, but it points to an important problem with the method.[29] When we ignore the previously discussed problems with the event selection, the mixed event distribution in the original $\Theta^+(1540)$ analysis was constructed by replacing each K^0_S track with the K^0_S track of the next event. It is likely that the new track has very different kinematic variables. This kinematic mismatch distorts the mixed event distributions.

[29] It is immediately clear that for exclusive processes the method of event mixing needs to be applied very carefully.

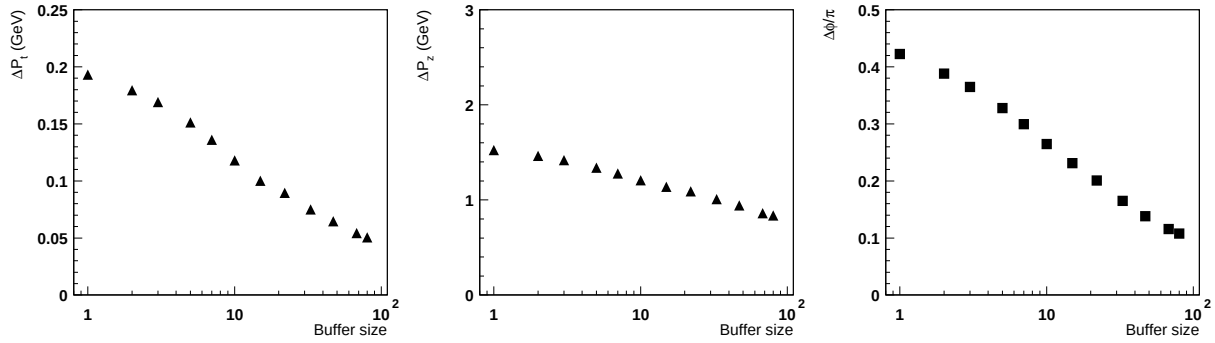

Figure 4.52: The average distances ΔP_t, ΔP_z and $\Delta\phi$ between the original and replacing track are shown versus the size of the event mixing buffer N.

Imagine that in a photoproduction interaction with low momentum transfer Q^2 only a single K^0_S meson is produced, and that the electron is not scattered into the acceptance of the spectrometer. We ignore what this means for strangeness conservation, and focus on the decay of the K^0_S meson in a positive and a negative pion, each in opposite halves of the spectrometer. When we apply event mixing to this particular event, which contains only the two pions π^+ and π^-, the probability to obtain an event with two pion tracks in the same half of the detector is approximately $\frac{1}{2}$, even though there is then a clear problem with missing transverse momentum. These mixed events are unphysical and will not be representative of the real background events. They have to be excluded to obtain the correct background shape.

The previous example was an extreme case of a more general problem. Can we just replace one track with a track that has a different momentum, with a different azimuthal angle ϕ, and was thus detected in a different part of the spectrometer? If we replace tracks with very different tracks, the shape of the mixed event background will not be representative of the real background shape. On the other hand, imposing too narrow requirements on how close a second track is before it is used to mix will just reproduce the resonance (which brings us back to the previous subsection about the inclusion of resonance events).

To solve this problem, we use a buffer in which we store the tracks of the last N processed events ($N = 80$ seemed a reasonable value).[30] For each event we choose from this buffer the track that has transverse and longitudinal momentum P_t and P_z and azimuthal angle ϕ that are closest to the original track. Using weight factors the relative importance of the three kinematic distances can be changed. By increasing the size of the event mixing buffer, the new track could be chosen closer to the original track.

The average distances ΔP_t, ΔP_z and $\Delta\phi$ between the original and the replacing track for different values of N are shown in figure 4.52. The difference in transverse momentum P_t and azimuthal angle ϕ can be reduced by a factor four when an event mixing buffer is introduced with size $N = 80$. The average distance ΔP_t, ΔP_z and $\Delta\phi$ can be reduced arbitrarily by choosing a large enough buffer size. There is therefore no natural choice of N, corresponding to a plateau. The decrease of the average distances ΔP_t, and $\Delta\phi$ is largest between 5 and 20.

For the decay of the K^0_S meson and the Λ hyperon the influence of this mixing buffer on the mixed event distribution is shown in figure 4.53. In the left panel the distribution of the invariant mass $M(\pi^+\pi^-)$ is shown with clear K^0_S and ρ^0 resonance peaks, in the right panel the distribution of the invariant mass $M(p\pi^-)$ is shown with a clear Λ resonance peak. In both panels the mixed event distributions are overlaid for buffer size $N = 1$ and $N = 80$. For both the $M(\pi^+\pi^-)$ and $M(p\pi^-)$ distributions there are significant differences between the mixed event distributions for $N = 1$ and for $N = 80$. In particular the background underneath the K^0_S resonance peak is poorly described for

[30] Some high-multiplicity events contain multiple combinations of tracks, which are handled as separate events. To avoid event mixing within the same events, a delay has to be introduced before an event becomes part of the buffer. For the same reason a delay is necessary before a track in the mixing buffer becomes available again for selection.

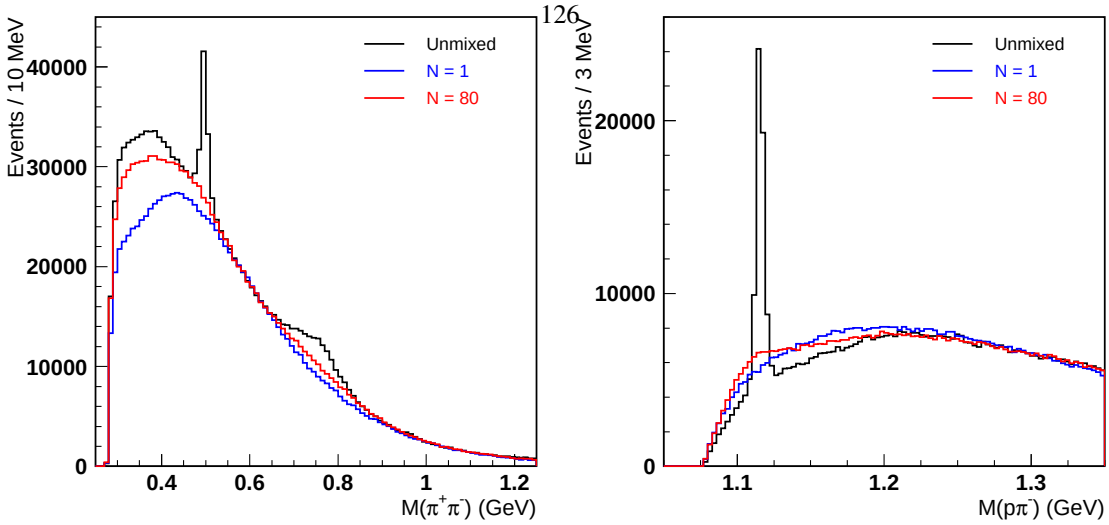

Figure 4.53: The influence of the mixing buffer on the K^0_S and ρ^0 (left panel) and Λ resonances (right panel). The mixed event distribution is shown in blue for a buffer size $N = 1$, *i.e.* when no choice can be made. The mixed event distribution in red is obtained with a buffer size $N = 80$. There is a clear improvement, in particular in the case of the K^0_S meson.

$N = 1$. The mixed event distributions with a larger buffer agree better with the unmixed invariant mass distributions, indicating the importance of avoiding kinematic mismatch. The remaining disagreement for $N = 80$ in the $M(\pi^+\pi^-)$ distribution below 0.4 GeV was explained (using Monte Carlo simulations) as η and η' meson decays to two pions.

The remaining disagreement between the unmixed distribution and the mixed event distribution with $N = 80$ for the Λ hyperon in the right panel of figure 4.53 was explained previously as the effect of mixed resonance events. By increasing the buffer size this effect will not disappear. In fact, it will become more apparent at larger buffer sizes because the smearing of the resonance peak for mixed resonance events decreases when N increases. In figure 4.54 this effect is demonstrated on the K^0_S and ρ^0 mesons for $N = 915$. For values of N larger than 300 the resonances are reproduced in the mixed event distributions.

To increase the number of events in the mixed event distribution the second closest, third closest, etc... event could be used. This leads to a degradation of the average smallest kinematic distance. When for combinatorial reasons a track is included in multiple events, this will lead to statistically correlated mixed event distributions. Another method is the use of multiple buffers which are completely disjoint. Practically the buffers would be positioned after each other. The first buffer contains the last N events, the second buffer the N events before that, and so on. The average smallest kinematic distance will be the same for all buffers and no correlations between the events in different buffers can occur.

At the STAR experiment a different method has been applied to account for differences between the mixed event distribution and the unmixed distribution, originating in correlations in the azimuthal distribution of the events in the detector [118, 119]. It is not immediately clear how the analytical method used at the STAR experiment can be extended to an experimental setup without full azimuthal coverage.

Interplay of kinematic mismatch and mixed resonance events

The two previously described effects of kinematic mismatch and mixed resonance events are related. This was already visible in figure 4.54. When the size N of the mixing buffer is chosen too large, the mixed resonance events will have a narrow distribution. For very large N the mixed resonance distribution even approaches the shape of the

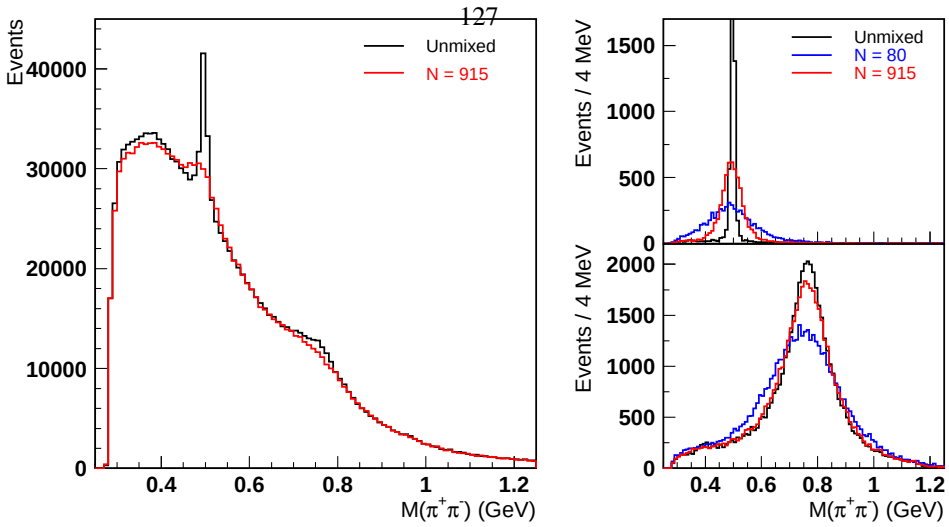

Figure 4.54: When the mixing buffer is too large, the resonances are reproduced in the mixed event background. In the left panel the distribution of the invariant mass $M(\pi^+\pi^-)$ is compared for regular (black curve) and mixed events with a buffer size $N = 915$ (red curve). In the right panels the reduced smearing of the K^0_S meson (top panel) and ρ^0 meson (bottom panel) is demonstrated for Monte Carlo events when the resonance events are mixed with a higher buffer size N.

unmixed resonance peak. This narrow distribution can be described more easily with a Monte Carlo simulation. For $N \approx 1$ the width of the mixed resonance distribution is broad and a larger number of events have to be simulated before a statistically precise description of the mixed resonance distribution is obtained. Moreover, when the mixed resonance distribution is narrow, it does not overlap with the normalization interval. In practice the buffer size should be chosen large enough to constrain the mixed resonance distribution to an invariant mass region that still allows for a suitable normalization region outside of this region, but not so large that the width of the distribution of mixed resonance events becomes comparable to the width of the unmixed resonance.

4.7.2 Demonstration of event mixing

After outlining the appropriate procedure for event mixing on the K^0_S, ρ^0 and Λ resonances, we now apply this method to some other well-established resonances.

Event mixing for the $\Xi^-(1320)$ hyperon

The $\Xi^-(1320)$ hyperon decays to a pion and a Λ hyperon. In figure 4.55 the distribution of the invariant mass $M(p\pi^-\pi^-)$ is shown in the left panel for events with at least one proton and two pions detected by the spectrometer, and in the right panel for events with an additional third pion. The mixed event distributions, when including or discarding events in the mass window of the $\Xi^-(1320)$, are statistically consistent. Therefore only the mixed event distribution for all events is shown. The low yield of resonance events in the available Monte Carlo simulations made it impossible to determine the mixed resonance distribution.

For both samples the mixed event distribution seems to be in good agreement with the expected background distribution, even without a special treatment of the mixed resonance events. In the case of the three particle final state in the left panel the Σ^- hyperon at 1385 MeV can be recognized, but an additional vertex separation requirement in the right panel suppresses this strongly decaying resonance. The excess of events at approximately 1300 MeV is

possibly due to the effect of ghost tracks (although the ghost track suppression criteria discussed in section 4.3.2 were not able to remove it completely). It also disappears when the vertex separation requirement is introduced.

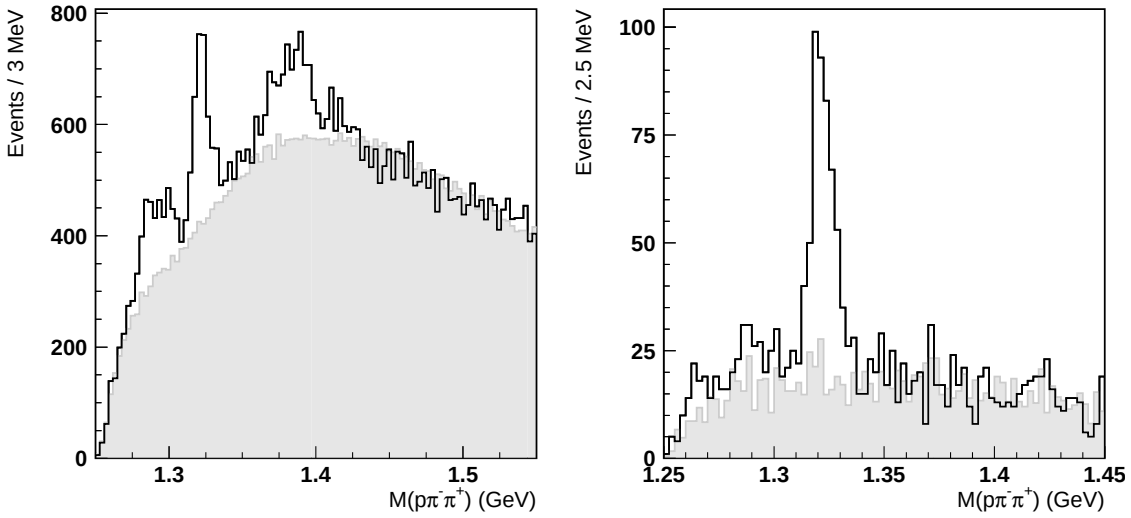

Figure 4.55: The distribution of the invariant mass $M(p\pi^-\pi^-)$ with mixed event background distribution (shaded histogram). In the left panel the distribution is obtained using events with one proton and two pions, in the right panel an additional pion was required.

Event mixing for the $\Lambda(1520)$ hyperon

For the decay of the broad $\Lambda(1520)$ hyperon to a proton and a kaon the mixed event background seems to be strongly dependent on the selection criteria, an effect that was not observed for the $\Xi^-(1320)$ hyperon. Unfortunately no Monte Carlo simulations are available because this hyperon is not included in the PYTHIA Monte Carlo generator.

The distribution of the invariant mass $M(pK^-)$ is shown in figure 4.56. The mixed event distributions, when including and discarding events in an invariant mass window around the mass of the $\Lambda(1520)$ hyperon, were again statistically consistent. Before a distance of closest approach and vertex separation requirement are introduced, the mixed event distribution agrees poorly with the unmixed distribution in the left panel. After the selection criteria are introduced in the right panel, the distribution agrees better. The disagreement when no selection criteria are applied is at present not understood.

Event mixing for the $\Xi^{0*}(1530)$ hyperon and $\Xi^{--}(1860)$ search

Already in section 4.3 the event mixing method was used in the search for the exotic baryons $\Xi^{--}(1860)$, and for the determination of the cross section of the $\Xi^{0*}(1530)$ hyperon. The distribution of the invariant masses $M(p\pi^-\pi^-\pi^+)$ and $M(p\pi^-\pi^-\pi^-)$ are shown in figure 4.57. The mixed event distributions are normalized to the unmixed distribution in the interval 1.6–2.1 GeV. The distributions seem to agree well with the expected shapes of the background distributions.[31] Moreover, there are no large differences with the results obtained by naive event mixing [5].

[31] Because completely independent analysis software was used in this section compared to section 4.3, small differences in the number of selected events are possible.

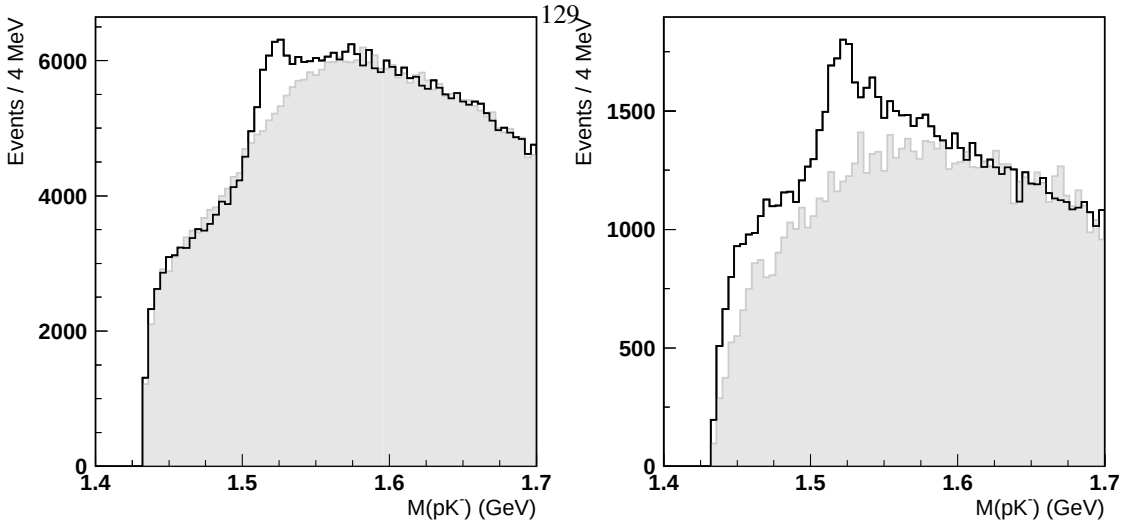

Figure 4.56: The distribution of the invariant mass $M(pK)$ with mixed event background distribution superimposed, for permissive (left panel) and more restrictive selection criteria (right panel). The mixed event distributions obtained including and discarding events in an invariant mass window around the mass of the $\Lambda(1520)$ hyperon are statistically consistent. The horizontal scale in the right panel is identical as in figure 4.9.

Event mixing for the exotic $\Theta^+(1540)$ baryon

The event mixing method was applied on the previously published analysis of the exotic $\Theta^+(1540)$ baryon [4]. In figure 4.58 the distribution of the invariant mass $M(p\pi^+\pi^-)$ is shown in the left panel for the invariant mass range used in reference [4], and a wider invariant mass range with the same binning in the right panel. The distributions are normalized to each other in the interval 1.43–1.7 GeV.

In the wider invariant mass range the mixed event distribution is substantially lower than the unmixed distribution at higher mass. This difference is possibly due to the contribution of the excited Λ^* hyperon resonances in that region. They would not be reproduced in the mixed event distributions.

4.7.3 Summary

In this section we discussed the method of event mixing to obtain an accurate description of the background shape. Event mixing allows to increase the statistical precision of the estimated background shape by an almost arbitrary factor. Several limitations of the event mixing method were discussed and solutions proposed. The effect of the selection criteria can be readily avoided at the cost of a more time-consuming event mixing procedure. Mixing of resonance events cannot be ignored, but using Monte Carlo simulations or invariant mass windows the effect can be assessed. Finally, kinematic mismatch between the original track and the track of the other event reduces the effect of the mixed resonance events.

Although accounting for these effects enhances the event mixing method, it can still generate background distributions that do not seem correct. It should therefore be used only with a lot of caution.

4.8 Overview of the search for the exotic baryon Θ at the HERMES experiment

In this section we present an overview of the search for the exotic baryon Θ^+ and its antiparticle Θ^- in all data sets collected at the HERMES experiment. These data sets are characterized by the different spectrometer configurations

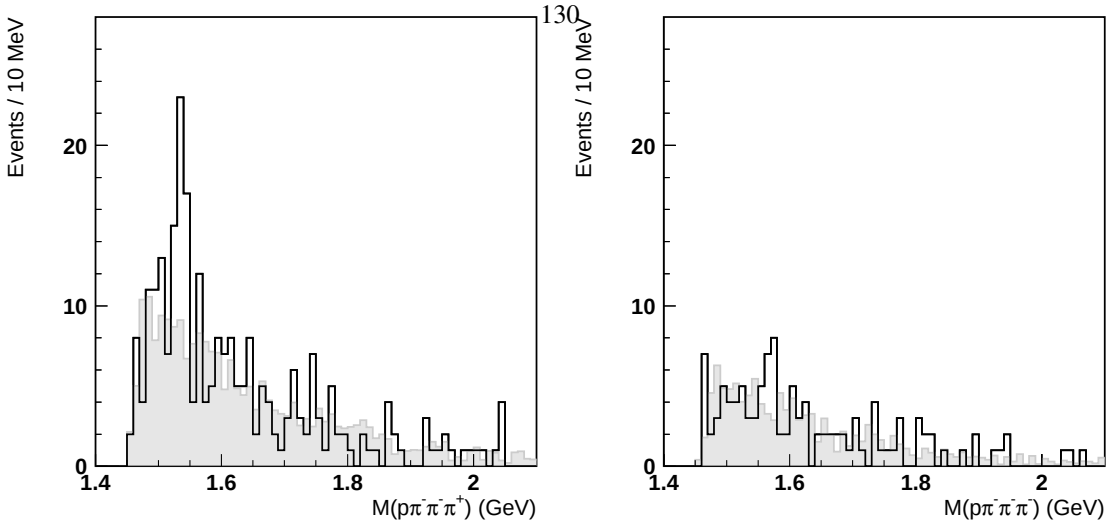

Figure 4.57: The distributions of the invariant mass $M(p\pi^-\pi^-\pi^+)$ (left panel) and $M(p\pi^-\pi^-\pi^-)$ (right panel) with mixed event background distribution.

and the various gas targets. The results of the search for the exotic baryon Θ^+ described in the previous sections are compared to the observation in the data set collected between the years 1998 and 2000, and are described in reference [4].

Although no photoproduction events are expected for the trigger configuration used during high density data taking, the invariant mass distributions for the high density data sets are included because they provide an estimate of the background from other processes.

For every data set we show a uniform set of three figures to allow for easy comparison. The distribution of the invariant mass $M(\pi^+\pi^-)$ is shown in the left panel, including only the events with a pion pair $\pi^+\pi^-$ and an additional proton p or antiproton $\overline{p}$. Events which contain a proton are shown in blue, events with an antiproton in red, and the combination of both proton and antiproton is shown in black. The number of events with a K^0_S meson and a proton or antiproton are determined, as well as the ratio of antiproton to proton events.

The distribution of the invariant mass $M(p\pi^+\pi^-)$ is shown in the middle panel between 1.41 and 1.7 GeV, and in the right panel between 1.41 and 2.52 GeV. Again the events with a proton corresponding to the decay of the Θ^+ are shown in blue, the events with an antiproton corresponding to the decay of the Θ^- in red, and the combination of both in black. For the events with a proton or antiproton in black the mixed event background distribution is shown as the shaded histogram, normalized in the region between 1.43 and 1.7 GeV indicated by the dark horizontal bar. In all cases the agreement of the mixed event background distribution with the unmixed events is poor.

The reconstructed mass, resonance width, and number of K^0_S mesons in each data set are summarized in table 4.9. The world average value for the mass is 497.65 MeV [1] and the resonance width determines the spectrometer resolution. The ratio of the number of reconstructed K^0_S mesons (associated with a proton or antiproton) to the total number of collected DIS events is used to check the consistency of the different data sets, and is influenced by the efficiency of the trigger system and the particle identification algorithms.

4.8.1 The pre-RICH period with the threshold Čerenkov counters (1996–1997)

The invariant mass distributions in the data sets collected during the years 1996 and 1997 are shown in figure 4.59 for the low density polarized hydrogen target, in figure 4.60 for the high density hydrogen target, in figure 4.61 for the high density deuterium target, and in figure 4.62 for the unpolarized nitrogen target. In none of the distributions

Table 4.9: Comparison of the reconstructed K^0_S meson for several data sets. The number of DIS events is determined using standard DIS selection criteria. The value $N_{K^0_S}$ indicates the number of K^0_S after the final event selection. For the years 2006 and 2007 the final integrated luminosity and number of DIS events are not available yet, and for the year 2007 the results were obtained with a first iteration of the data with calibrations of the previous year.

Data period	Gas type	DIS (M)	$\mathcal{L}$ (pb^{-1})	$M_{K^0_S}$ (MeV)	$\sigma_{K^0_S}$ (MeV)	$N_{K^0_S}$ (final)	$N_{K^0_S}$/DIS (k)
1996–1997	H (pol)	2.382	49.9	497.1 ± 0.05	5.9 ± 0.08	5097 ± 99	2139.9
1996–1997	H (unpol)	2.797	56.6	497.3 ± 0.12	5.9 ± 0.12	2586 ± 70	924.4
1996–1997	D (unpol)	4.511	104.5	497.1 ± 0.10	5.8 ± 0.09	3841 ± 87	851.6
1997	N (unpol)	1.919	51.4	497.5 ± 0.14	6.3 ± 0.13	2603 ± 71	1356.6
2000	H (unpol, hd)	6.850	132.5	497.0 ± 0.4	6.5 ± 0.6	198 ± 20	28.9
1998–2000	D (pol, ld)	9.407	209.2	496.7 ± 0.2	6.1 ± 0.2	1215 ± 51	129
2002–2005	H (pol, ld)	7.439	150.2	497.3 ± 0.2	6.5 ± 0.4	575 ± 37	77.3
2002–2005	D (unpol, hd)	10.29	158.1	497.1 ± 0.3	6.9 ± 0.3	978 ± 48	95.0
2006–2007	H (unpol, ld)	n.a.	n.a.	497.7 ± 0.2	7.9 ± 0.16	5290 ± 117	n.a.
2006–2007	H (unpol, hd)	n.a.	n.a.	498.3 ± 0.3	7.5 ± 0.2	1937 ± 69	n.a.
2006–2007	D (unpol, ld)	n.a.	n.a.	497.8 ± 0.3	7.8 ± 0.3	1845 ± 69	n.a.

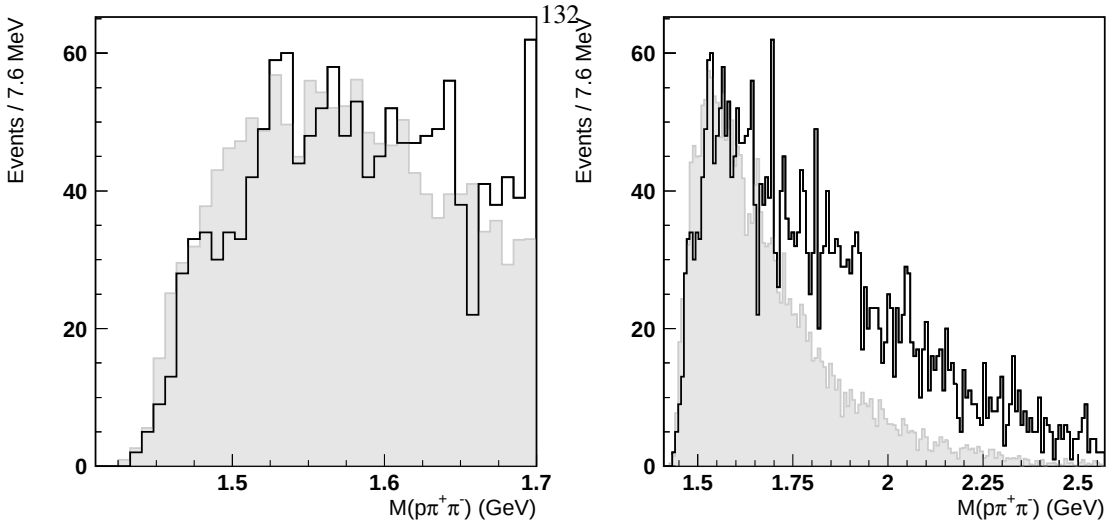

Figure 4.58: The distributions of the invariant mass $M(p\pi^-\pi^-)$ with mixed event background distribution for the mass range used in reference [4] (left panel) and for a wider mass range (right panel). The binning is identical in both panels. There are small differences in the mixed event distribution in both panels due to the separate generation of the distributions.

of the invariant mass $M(p\pi^+\pi^-)$ a prominent resonance peak can be observed in the invariant mass region around 1.53 GeV.

In the years 1996 and 1997 the HERMES experiment operated with the threshold Čerenkov counters for the identification of pions and protons. Due to the absence of the aerogel tiles of the RICH detector, the momentum resolution is better than after the installation of the RICH detector. This is reflected in the width of the K^0_S resonance, which is on average 5.9 MeV before and 6.2 MeV after the installation of the RICH detector.

The reduced particle identification capabilities are not immediately apparent in the invariant mass distribution $M(\pi^+\pi^-)$. On the contrary, there seem to be many more reconstructed K^0_S mesons which is reflected in a high value for the ratio K^0_S/DIS in table 4.9. One has to keep in mind that the events which contain these K^0_S mesons were required to contain an additional proton. Since kaons are not identified as such but rather are often identified as protons, the number of protons is inflated. The production of a K^0_S meson in association with a kaon K could even be preferred in fragmentation, because the strangeness of the kaon and the K^0_S meson can cancel each other. The seemingly large contribution of antiprotons can be explained by the misidentification of negative kaons K^- as antiprotons. Because the kaons consist of a quark and antiquark, positive and negative kaons are produced in approximately equal amounts.

Due to this misidentification of kaons as protons it is difficult to draw conclusions about the existence of the exotic baryon Θ^+ in these data sets. Since particle identification efficiencies are only poorly simulated in the available Monte Carlo simulations it is very difficult to estimate an upper limit on the production cross section.

4.8.2 The polarized deuterium period with the RICH detector (1998–2000)

After the installation of the RICH detector in 1998 the particle identification capabilities of the HERMES spectrometer improved substantially. Unfortunately the effect of the RICH detector on the momentum resolution was less beneficial. Secondary scattering in the structural and active materials, for example the aerogel tiles, lead to a deterioration in the resolution of the spectrometer reflected in the width of the K^0_S meson, as mentioned before.

Ignoring the small amounts of data collected with unpolarized high density heavy gas targets (Ne, Xe, Kr), the data collected in the years 1998, 1999 and 2000 consists of two main data sets. The results of the search for the exotic

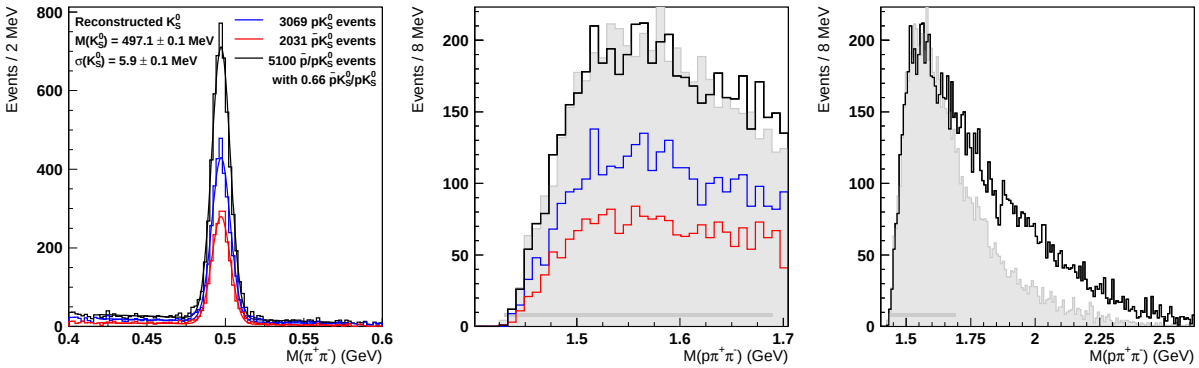

Figure 4.59: Search for the production of the exotic baryon Θ on a low density polarized hydrogen target during the years 1996 and 1997. For a description of the figures, refer to the text.

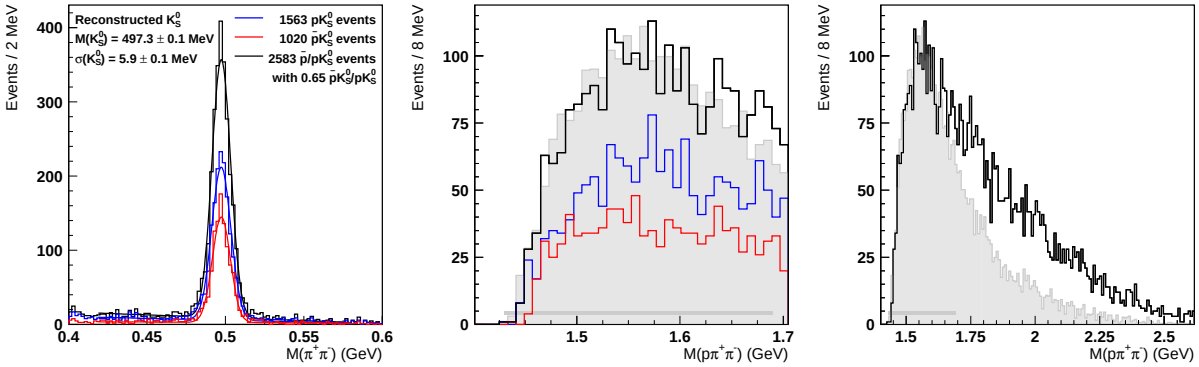

Figure 4.60: Search for the production of the exotic baryon Θ on a high density unpolarized hydrogen target during the years 1996 and 1997. For a description of the figures, refer to the text.

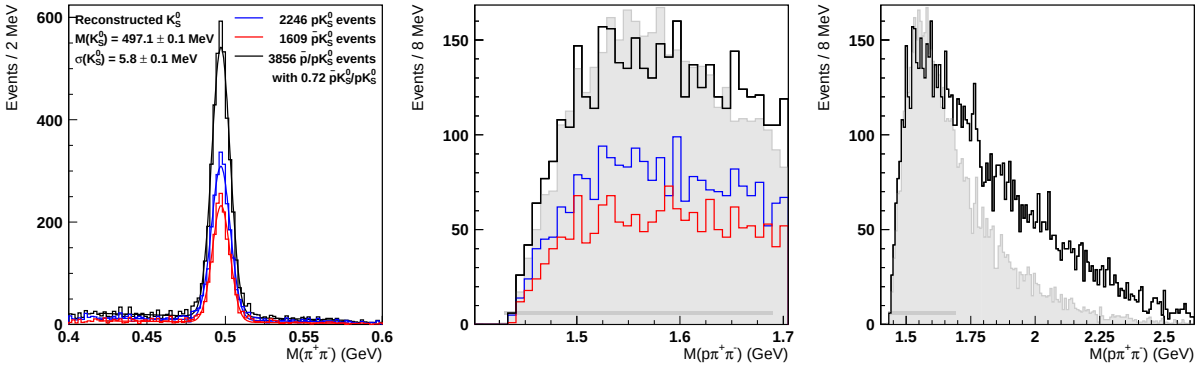

Figure 4.61: Search for the production of the exotic baryon Θ on a high density deuterium target during the years 1996 and 1997. For a description of the figures, refer to the text.

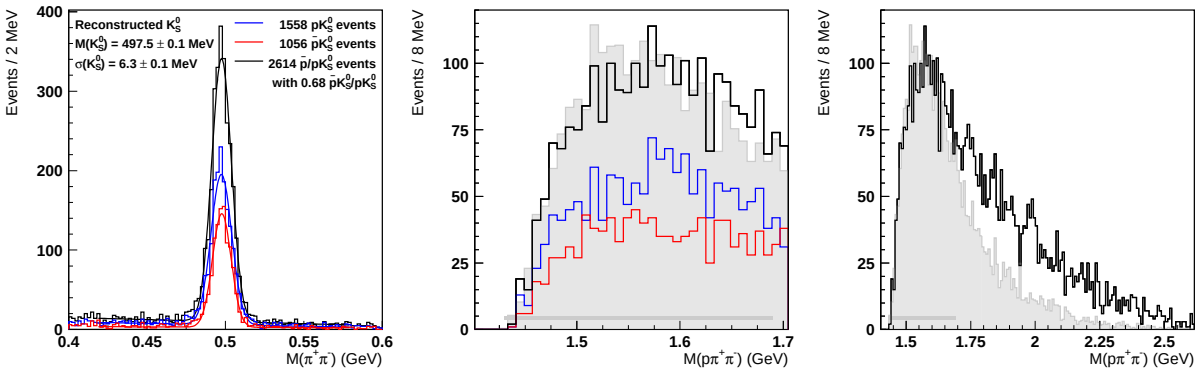

Figure 4.62: Search for the production of the exotic baryon Θ on a high density nitrogen target during the years 1996 and 1997. For a description of the figures, refer to the text.

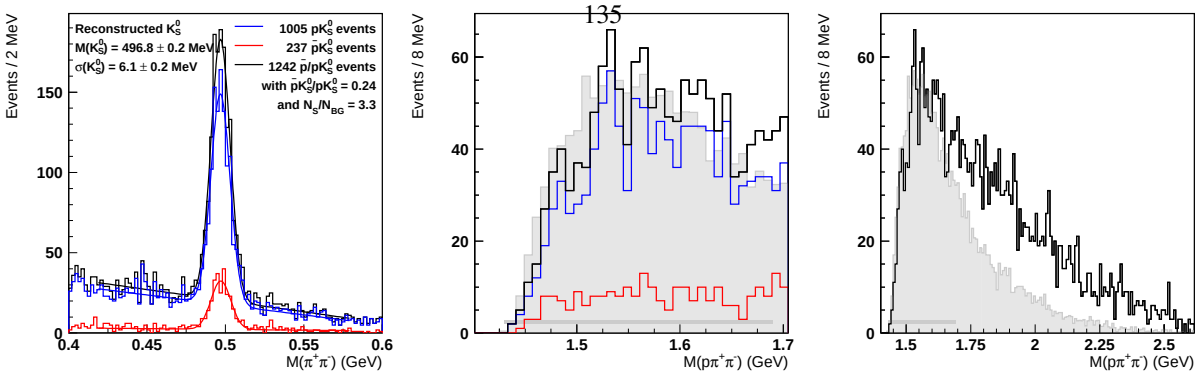

Figure 4.63: Search for the production of the exotic baryon Θ on a low density polarized deuterium target during the years 1998, 1999 and 2000. For a description of the figures, refer to the text.

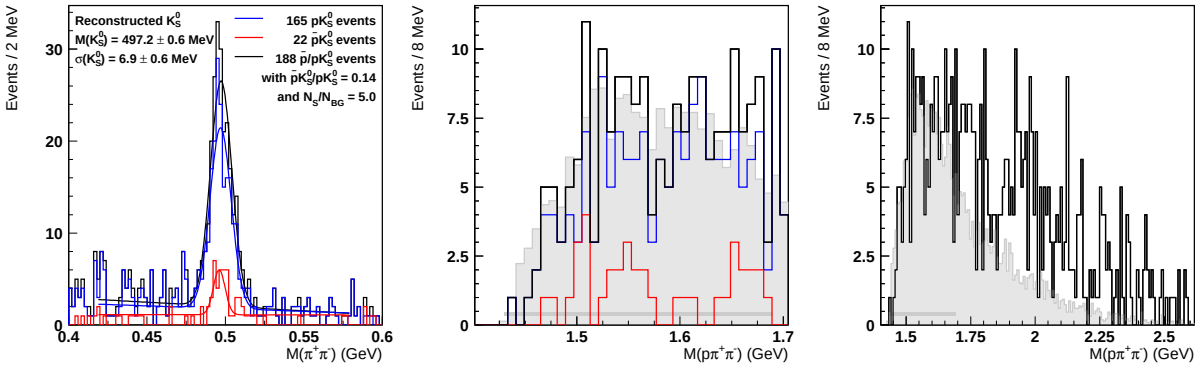

Figure 4.64: Search for the production of the exotic baryon Θ on a high density unpolarized hydrogen target during the years 1998, 1999 and 2000. For a description of the figures, refer to the text.

baryon Θ in the data collected with a polarized deuterium target are shown in figure 4.63, the results collected on the high density unpolarized hydrogen target are shown in figure 4.64.

The analysis of the data set collected on the polarized deuterium target corresponds to the published observation of the exotic baryon Θ^+ at a mass of 1528 MeV [4]. In this analysis a small fraction of events collected on the high density unpolarized deuterium target were excluded, due to the associated trigger inefficiency for photoproduction events. An additional offline calibration of the detector data necessary for the event reconstruction algorithm was used, resulting in small differences in the kinematic parameters of the used tracks. Lastly the restriction on the production vertex was changed to include the average position of the lepton beam. The originally observed structure at 1528 MeV is still present after these small adjustments.

In the data set collected on the high density unpolarized hydrogen target no prominent structure is visible that could correspond to the exotic baryon Θ, though the number of events in the distribution is small and the statistical precision low.

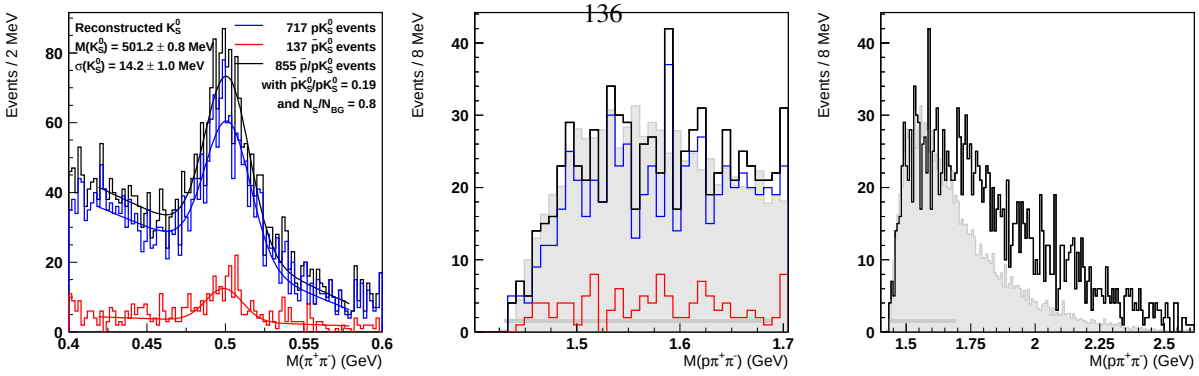

Figure 4.65: Search for the production of the exotic baryon Θ on a low density polarized hydrogen target between the years 2002 and 2005. For a description of the figures, refer to the text.

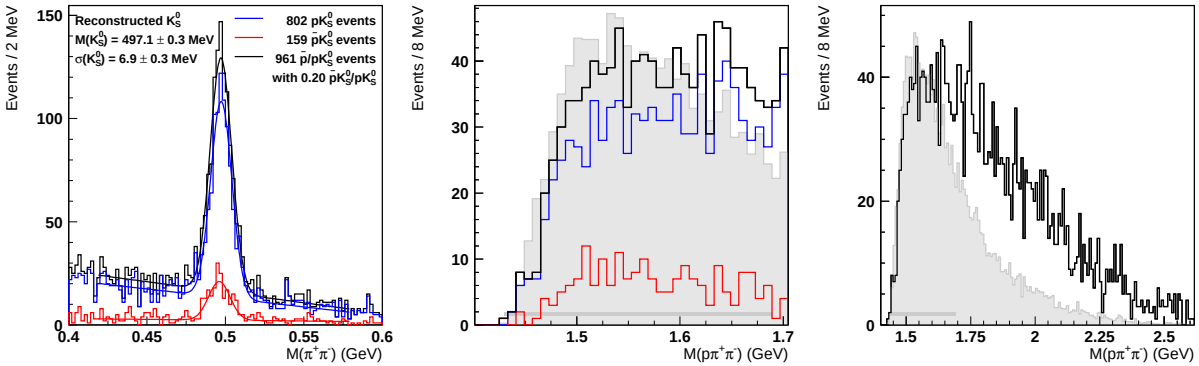

Figure 4.66: Search for the production of the exotic baryon Θ on a high density unpolarized deuterium target between the years 2002 and 2005. For a description of the figures, refer to the text.

4.8.3 The transversely polarized target period (2002–2005)

After the installation of the transverse target magnet for the transversely polarized hydrogen target in 2001, the bending effect of the magnetic field has to be corrected for. The method described in section 4.6 was applied.

The results of the search for the exotic baryon Θ in the low density transversely polarized hydrogen data set between the years 2002 and 2005 is shown in figure 4.65, the results for the data set collected on the high density unpolarized deuterium data in this period is shown in figure 4.66. For both data sets there is no structure visible at the invariant mass expected for the exotic baryon Θ.

4.8.4 The recoil detector period (2006–2007)

After the dismantling of the polarized target and the installation of the recoil detector the target densities that could be attained increased. This resulted in an increased event collection rate and an impressive amount of data the end of a two year period. The target densities during the first low density phase of every fill were still low enough for an energy

threshold of 1.4 GeV in the electromagnetic calorimeter. [137]

To accomodate the recoil detector and magnet, the dimensions of the target cell had to be changed. The length of the target cell was reduced to 15 cm, and it was moved 25 cm closer to the forward spectrometer. Using Monte Carlo simulations the effect of these changes on the acceptance for $\Theta(1540)$ decay events was investigated. Moving the target cell 12.5 cm closer to the spectrometer reduced the acceptance by a relative 20% from 0.032% to 0.025%.

In figure 4.67 the results of the search for the exotic baryon Θ in the data collected with the low density hydrogen target are shown, in figure 4.68 with the high density hydrogen target, and in figure 4.69 with the low density deuterium target. The events used for the generation of these figures were only partially calibrated. A full calibration of the data collected in the year 2007 is only expected by the end of 2006. The degradation of the resolution, visible in the width of the K^0_S meson, can be attributed to this effect.[32]

In none of the distribution of the invariant mass $M(p\pi^+\pi^-)$ a prominent structure can be observed consistent with the observation of the exotic baryon Θ^+ in figure 4.63. In particular the analysis of the data set collected on the low density deuterium target during this period, with approximately 50% more K^0_S meson candidates, does not confirm the results of the analysis on the polarized deuterium target in 1998, 1999 and 2000.

4.8.5 Combining all the collected data

Although the previous data sets were obtained in slightly different conditions, we decided to combine the distributions. In figure 4.70 the different data sets are combined. In the three panels with the combined data sets the mixed event background distribution determined only for the events collected on the low density deuterium target between the years 1998 and 2000 was used. The variations between the mixed events background distributions for different data sets are small enough to be negligible compared to the disagreement with the unmixed distributions.

In the left panel all data collected on a hydrogen target is combined. This includes the data sets collected on the low density polarized and high density unpolarized target during the years 1996 and 1997 before the installation of the RICH detector, on the high density target during the year 2000, on the low density polarized target between 2002 and 2005 with transverse magnet vertex correction, and on the low and high density target during the years 2006 and 2007. This includes data sets collected during high density data taking, for which photoproduction events is suppressed, but those data sets are only expected to contribute to background events and not to resonance events. In the combination of the data collected on hydrogen no resonance can be observed.

In the middle panel of figure 4.70 all data collected on a deuterium target is combined. This includes the data sets collected on the high density target during the years 1996 and 1997, on the low density target between the years 1998 and 2000 (corresponding to the original analysis), on the high density target between the years 2002 and 2005, and on the low density target during the years 2006 and 2007. Also here we have to point out that only the data collected between the years 1998 and 2000, and the data collected during the years 2006 and 2007 are expected to contribute to photoproduction events due to the unfavorable trigger conditions during high density data taking. The lower number of events compared to the hydrogen data leads to larger statistical fluctuations in the distribution, but no prominent resonance structures is visible. A change in slope of the distribution at approximately 1525 MeV could evoke the thought of an excess of events, but probably points rather to a loss of acceptance below 1530 MeV.

Finally, in the right panel of figure 4.70 all data collected at the HERMES experiments between the years 1996 and 2007 on hydrogen and deuterium targets is combined, including low density and high density data sets. The statistical precision of this combined data set is appreciable. No resonance structures can be observed.

[32] A small effect of the solenoidal recoil magnet field could be present and cannot be corrected for with the reconstruction method developed for the transverse magnetic field.

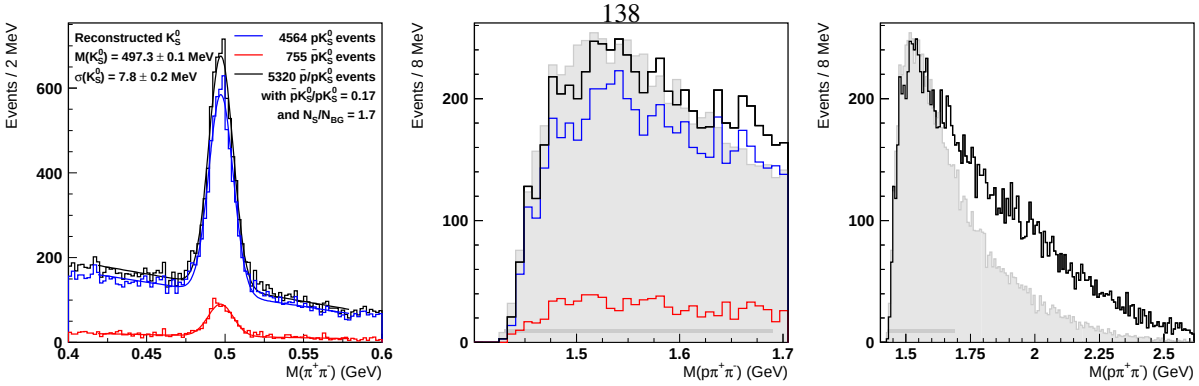

Figure 4.67: Search for the production of the exotic baryon Θ on a low density hydrogen target during the years 2006 and 2007. For a description of the figures, refer to the text.

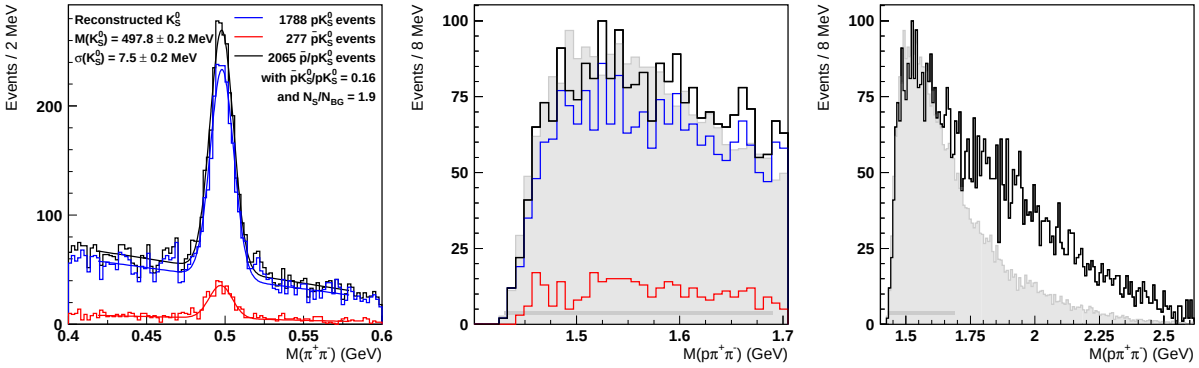

Figure 4.68: Search for the production of the exotic baryon Θ on a high density hydrogen target between the years 2006 and 2007. For a description of the figures, refer to the text.

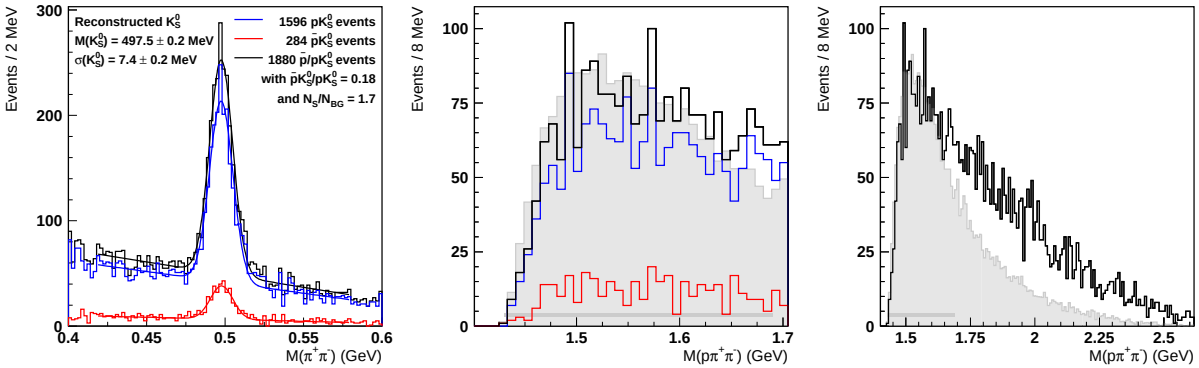

Figure 4.69: Search for the production of the exotic baryon Θ on a low density deuterium target during the years 2006 and 2007. For a description of the figures, refer to the text.

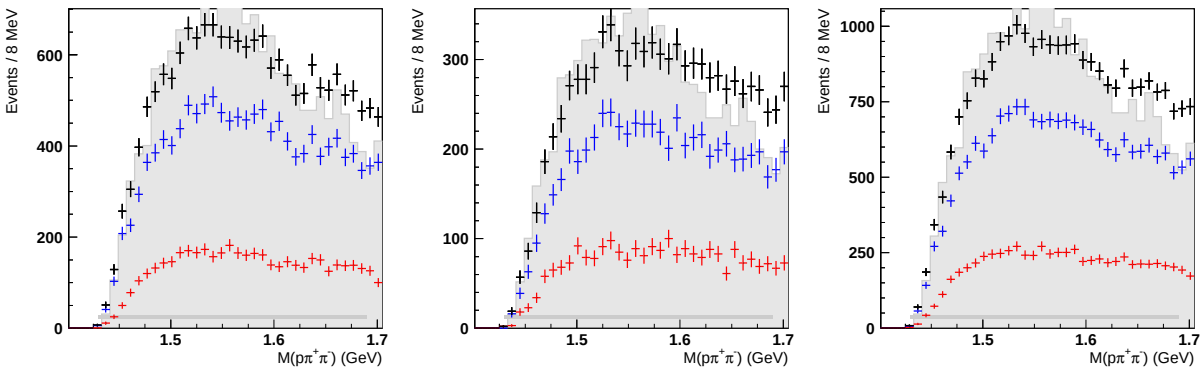

Figure 4.70: Production of the exotic baryon Θ on hydrogen and deuterium targets at the HERMES experiment. When combining all events collected on the various hydrogen targets between the years 1996 and 2007, the distribution in the left panel is obtained. Similarly, when combining all events collected on the various deuterium targets, the distribution in the middle panel is obtained. After combining all events collected on hydrogen or deuterium targets at the HERMES experiment, the distribution in the right panel is obtained. No resonance structures can be observed in the distributions.

CHAPTER V

Summary and discussion

One of the interesting questions in Quantum Chromodynamics, the theory that governs the interactions between quarks and gluons, is whether one can observe bound states that cannot be explained as a combination of a quark and an antiquark ($q\overline{q}$) or of three quarks (qqq). The theory does not exclude the existence of other *exotic* combinations of quarks and gluons, such as glue balls (gg), hybrids ($q\overline{q}g$), tetraquarks ($q\overline{q}q\overline{q}$), or exotic baryons or pentaquarks ($qqqq\overline{q}$), but such states were never unambiguously observed and could be too heavy or too wide to be observable with present experiments.

Recent calculations in the framework of the chiral quark soliton model predicted the existence of an exotic multiplet of pentaquark states, including the narrow exotic baryons Θ^+ and Ξ^{--} with minimal quark configuration $uudd\overline{s}$ and $ssdd\overline{u}$ [17]. A narrow resonance identified as the exotic baryon Θ^+ was observed by several experiments close to the predicted mass of 1530 MeV. However, none of the dedicated searches with high sensitivity for these states were able to confirm these observations. This puts the burden of proof back to the original experiments. Only one experiment has claimed the observation of the exotic baryon Ξ^{--} with a mass of 1862 MeV.

5.1 Exotic baryon search at the HERMES experiment

At the HERMES experiment a search for the exotic Θ^+ in the decay channel to pK^0_S resulted in the observation of a narrow resonance at a mass of 1528 MeV in quasi-photoproduction reactions off deuterium collected between 1998 and 2000 [4]. Due to trigger inefficiencies for 'photoproduction' events off unpolarized deuterium discovered after the publication of this result, this data set has now been slightly restricted to included only the polarized data, corresponding to a total integrated luminosity $\mathcal{L} = 209.2\,\text{pb}^{-1}$. A search for the antiparticle Θ^- in this reduced data set was unsuccessful.

Several substantial data sets have been collected after the year 2000. Between 2002 and 2005 the HERMES experiment operated with a transversely polarized hydrogen target, which resulted in an independent data set with $\mathcal{L} = 150.2\,\text{pb}^{-1}$ on hydrogen nuclei. However, the bending effect of the magnetic holding field on the charged particle tracks lead to a significantly worse resolution in the reconstruction of resonance decays. In the same period a dedicated photoproduction trigger was not able to substantially influence the efficiency for photoproduction events on the unpolarized deuterium target.

Most recently, in 2006 and 2007, another data set with an (estimated) $\mathcal{L} = 400\,\text{pb}^{-1}$ was collected on unpolarized deuterium nuclei, and approximately five times this amount on unpolarized hydrogen nuclei. The calibration of this data is still ongoing, but the uncalibrated data is available and only suffers from a somewhat reduced resolution.

Search for the exotic baryon Ξ^{--}

In this work we presented the search for the exotic baryon Ξ^{--} in the data collected between 1998 and 2000 [5]. Because the decay channel to $\Xi^-\pi^-$ with subsequent decays $\Xi^- \to \Lambda\pi^-$ and $p\pi^-$ requires four hadrons in the final state, the inclusion of low-momentum particle tracks without particle identification was necessary and increased the

number of candidate events by a factor three. Reconstruction artifacts known as ghost tracks were found in the low-momentum tracks, but were excluded from the analysis. We did not observe a resonance peak and determined an upper limit on the cross section of 2.7 nb for an exotic baryon Ξ^{--} with a mass of 1862 MeV. In the related decay channel $\Xi^0 \to \Xi^-\pi^+$ the established resonance $\Xi^{0*}(1530)$ was observed and we determined its photoproduction cross section between 10.4 nb and 28.8 nb, with an uncertainty due to the unknown production mechanism. In this channel an exotic Ξ^0 resonance at 1862 MeV with a photoproduction cross section larger than 8.1 nb is excluded.

Analysis of the $\Lambda(1520)$ hyperon and cross section

Although the search for the antiparticle Θ^- was unsuccessful in the data collected between 1998 and 2000, the HERMES experiment inherently favors particle final states over antiparticle final states due to the particle nature of the target. To characterize this effect we studied the hyperon $\Lambda(1520)$, expected to have a very similar production mechanism as the exotic baryon Θ^+ and at approximately the same mass. We assumed that the ratio of the photoproduction cross section of the antihyperon $\overline{\Lambda}(1520)$ to the hyperon $\Lambda(1520)$ is the same as for the exotic baryons Θ^- to Θ^+. The null result for the exotic baryon Θ^- is then consistent with the number of Θ^- events that are expected based on the observation of the Θ^+.

Search for the Θ^+ in the transversely polarized hydrogen data

To improve the resolution of resonances in the data collected on the transversely polarized hydrogen target between the years 2002 and 2005, we developed a method for the reconstruction of vertices in the transverse magnetic field applicable to arbitrary decay chains. The loss in the resolution of the K^0_S meson, relevant for the analysis of the exotic baryon Θ^+, could be recovered. This allowed for the first time at the HERMES experiment a search for the exotic baryon Θ^+ in data collected on a hydrogen target. No exotic resonance was observed.

Event mixing as an estimator for the background distribution

To determine the cross section or even the existence of a resonance, an accurate estimate of the distribution of background events is crucial. The event mixing method combines tracks from different events to obtain an uncorrelated sample of events, where all resonances are assumed to be absent. This is generally not true, and when resonance events are mixed they take on a distribution distinctly different from the background distribution. Using Monte Carlo simulations we showed that this easily ignored effect can have important consequences for even the most established resonances. By reducing the kinematic mismatch between the original and mixed tracks using a buffer of tracks available for selection, we significantly improved the agreement between the mixed event distribution and the unmixed distributions in the collected data in most cases. Despite these efforts the mixed event distributions do not seem to describe the background distribution of the decay channels $\Lambda(1520) \to pK^-$ and $\Theta^+ \to pK^0_S$, pointing to more fundamental difficulties with this intuitively simple method.

Overview of the analysis of all data sets collected at the HERMES experiment

In an overview of the search for the exotic baryon Θ^+ we also presented the analysis of several smaller data sets collected at the HERMES experiment. These included the period before the installation of the RICH hadron identification detector in 1998, or the analysis of low-momentum tracks below the threshold for the RICH detector and for which the alternative time-of-flight identification has to be used. Although the analysis of these data sets did not require any new technical concepts, they are an important part of the exotic baryon program at the HERMES experiment. In particular the data collected during the last two years of the experiment, in 2006 and 2007, offer an integrated luminosity that is higher than previous data sets, even if still plagued by a worse resolution. In none of the data sets a resonance peak at a mass of approximately 1540 MeV is observed.

5.2 Discussion

The initial enthusiasm about the claimed discovery of the exotic baryon Θ^+ has vanished. The null results with excellent statistical precision now outnumber the positive results. A profound skepticism or even negativism is now the general sentiment about exotic baryons, and the recent positive results are often ignored. However, it is not correct to interpret the null results as ruling out the existence of exotic baryons![1] They provide additional boundary conditions that a theoretical description of exotic baryons has to satisfy. Although the number of these boundary conditions is now becoming overwhelmingly large, there are successful theoretical efforts to reconcile the perceived contradictory results.

The result of the DIANA experiment [25] are often assumed to be contradicted by the results of the BELLE experiment [44], even though the upper limit on the width of a hypothetical Θ^+ resonance at the BELLE experiment is larger than the width observed at the DIANA experiment. High-energy scattering of proton on nuclei at the HERA-B experiment [55] and of electron on positrons at the BABAR experiment [53] saw no evidence for the exotic Θ^+, but in spite of the large statistical precision they are unable to resolve any of the established Σ^{*+} hyperons at masses of 1670 MeV and higher [1]. Theoretical efforts [36] have been successful at reconciling the null results of the CLAS experiment [33] and the positive results of the LEPS experiment [22]. Finally, interference effects may hold prospects for new observation channels, while not being in contradiction with the null results of some dedicated experiments [37, 38].

At the HERMES experiment the main goal has been to verify our earlier published results with increased statistical precision. The results presented in this thesis with the data sets collected on deuterium nuclei in 2006 and 2007 seem to indicate that the resonance observed in the data collected between 1998 and 2000 cannot be reproduced. Although the figures in this thesis were obtained without the final calibration, this conclusion is not expected to change.

In the analyzed data collected on hydrogen nuclei no exotic Θ^+ resonance could be observed either. This is in agreement with the common expectation, based on the nature of the remaining positive experiments, that the production mechanism of the exotic Θ^+ requires the presence of a neutron.

The real question is then: What did we observe in the data collected between 1998 and 2000 that could have disappeared now? A statistical fluctuation is not ruled out, especially not when combined with an underestimated background. We now know that the mixed event background estimation was incorrect, the simulated non-resonant background contribution was incomplete, and the broad Σ^{*+} hyperons seem a rather ad-hoc way of filling the remaining unexplained fraction of the background...

As said before, the hype has now ebbed away. What remains are genuine efforts at resolving the discrepancies. Maybe one by one the remaining positive results will disappear, maybe the data that will lead to undeniable confirmation still has to be taken... What we do know now is that the hundreds of experimental analyses and the thousand theoretical papers about exotic baryons written in the past four years have deepened our understanding of QCD and hadronic physics.

[1] You cannot prove a negative! From not observing a state does not follow the conclusion that it does not exist.

BIBLIOGRAPHY

BIBLIOGRAPHY

[1] Particle Data Group, W. M. Yao *et al.*, J. Phys. **G33**, 1 (2006).

[2] D. Diakonov, Prog. Part. Nucl. Phys. **36**, 1 (1996), nucl-th/9603023.

[3] D. S. Carman, J. Phys. Conf. Ser. **69**, 012011 (2007), hep-ex/0612027.

[4] HERMES, A. Airapetian *et al.*, Phys. Lett. **B585**, 213 (2004), hep-ex/0312044.

[5] HERMES, A. Airapetian *et al.*, Phys. Rev. **D71**, 032004 (2005), hep-ex/0412027.

[6] G. C. Oades, Invited review presented at Workshop on Low and Intermediate-Energy Kaon-Nucleon Physics, Rome, Italy, Mar 24-28, 1980.

[7] Particle Data Group, T. G. Trippe *et al.*, Rev. Mod. Phys. **48**, S1 (1976).

[8] Particle Data Group, M. Aguilar-Benitez *et al.*, Phys. Lett. **B170**, 1 (1986).

[9] K. Cheung, Phys. Rev. **D69**, 094029 (2004), hep-ph/0308176.

[10] M. Karliner and H. J. Lipkin, Phys. Lett. **B575**, 249 (2003), hep-ph/0402260.

[11] M. Karliner and H. J. Lipkin, (2003), hep-ph/0307343.

[12] H1, A. Aktas *et al.*, Phys. Lett. **B588**, 17 (2004), hep-ex/0403017.

[13] R. A. Arndt, I. I. Strakovsky, and R. L. Workman, Phys. Rev. **C68**, 042201 (2003), nucl-th/0308012.

[14] R. A. Arndt, I. I. Strakovsky, and R. L. Workman, Nucl. Phys. **A754**, 261 (2005), nucl-th/0311030.

[15] R. N. Cahn and G. H. Trilling, Phys. Rev. **D69**, 011501 (2004), hep-ph/0311245.

[16] S. Nussinov, (2003), hep-ph/0307357.

[17] D. Diakonov, V. Petrov, and M. V. Polyakov, Z. Phys. **A359**, 305 (1997), hep-ph/9703373.

[18] H. Z. Huang, High density matter and searches for exotics at RHIC, Presentation at International Conference on QCD and Hadronic Physics 2005, Beijing, China, 2005.

[19] T. Nakano *et al.*, Nucl. Phys. **A684**, 71 (2001).

[20] LEPS, T. Nakano *et al.*, Phys. Rev. Lett. **91**, 012002 (2003), hep-ex/0301020.

[21] T. Nakano, Int. J. Mod. Phys. **A20**, 1543 (2005).

[22] T. Nakano, J. Phys. **G32**, S77 (2006).

[23] T. Nakano, Overview of pentaquark searches, Presentation at Strangeness in Quark Matter 2006, University of California, Los Angeles, 2006.

[24] DIANA, V. V. Barmin *et al.*, Phys. Atom. Nucl. **66**, 1715 (2003), hep-ex/0304040.

[25] DIANA, V. V. Barmin *et al.*, Phys. Atom. Nucl. **70**, 35 (2007), hep-ex/0603017.

[26] W. J. Schwille *et al.*, Nucl. Instrum. Meth. **A344**, 470 (1994).

[27] SAPHIR, J. Barth *et al.*, Phys. Lett. **B572**, 127 (2003), hep-ex/0307083.

[28] F. Klein, Prog. Part. Nucl. Phys. **55**, 131 (2005).

[29] CLAS, M. Battaglieri *et al.*, Phys. Rev. Lett. **96**, 042001 (2006), hep-ex/0510061.

[30] CLAS, R. De Vita *et al.*, Phys. Rev. **D74**, 032001 (2006), hep-ex/0606062.

[31] CLAS, B. A. Mecking *et al.*, Nucl. Instrum. Meth. **A503**, 513 (2003).

[32] CLAS, S. Stepanyan *et al.*, Phys. Rev. Lett. **91**, 252001 (2003), hep-ex/0307018.

[33] CLAS, B. McKinnon *et al.*, Phys. Rev. Lett. **96**, 212001 (2006), hep-ex/0603028.

[34] CLAS, V. Kubarovsky *et al.*, Phys. Rev. Lett. **92**, 032001 (2004), hep-ex/0311046.

[35] CLAS, S. Niccolai *et al.*, Phys. Rev. Lett. **97**, 032001 (2006), hep-ex/0604047.

[36] A. I. Titov, B. Kampfer, S. Date, and Y. Ohashi, (2006), nucl-th/0607054.

[37] M. Amarian, D. Diakonov, and M. V. Polyakov, (2006), hep-ph/0612150.

[38] V. Guzey, (2006), hep-ph/0608129.

[39] NA49, C. Alt *et al.*, Phys. Rev. Lett. **92**, 042003 (2004), hep-ex/0310014.

[40] COSY-TOF, M. Abdel-Bary *et al.*, Phys. Lett. **B595**, 127 (2004), hep-ex/0403011.

[41] M. Abdel-Bary *et al.*, Phys. Lett. **B649**, 252 (2007), hep-ex/0612048.

[42] ZEUS, S. Chekanov *et al.*, Phys. Lett. **B591**, 7 (2004), hep-ex/0403051.

[43] SVD, A. Aleev *et al.*, Phys. Atom. Nucl. **68**, 974 (2005), hep-ex/0401024.

[44] Belle, K. Abe *et al.*, Phys. Lett. **B632**, 173 (2006), hep-ex/0507014.

[45] BABAR, B. Aubert *et al.*, (2004), hep-ex/0408064.

[46] J. P. Coleman, *Search for the $\Theta_5\,(1540)^+$ strange-pentaquark candidate in $e^+\,e^-$ annihilation, hadroproduction and electroproduction with the BaBar detector*, PhD thesis, Liverpool University, 2005.

[47] BaBar, K. Gotzen, Nucl. Phys. Proc. Suppl. **164**, 117 (2007), hep-ex/0510041.

[48] HyperCP, R. A. Burnstein *et al.*, Nucl. Instrum. Meth. **A541**, 516 (2005), hep-ex/0405034.

[49] HyperCP, M. J. Longo *et al.*, Phys. Rev. **D70**, 111101 (2004), hep-ex/0410027.

[50] HERA-B, K. T. Knopfle, M. Zavertyaev, and T. Zivko, J. Phys. **G30**, S1363 (2004), hep-ex/0403020.

[51] HERA-B, J. Spengler, Acta Phys. Polon. **B36**, 2223 (2005), hep-ex/0504038.

[52] BES, J. Z. Bai *et al.*, Phys. Rev. **D70**, 012004 (2004), hep-ex/0402012.

[53] BABAR, B. Aubert *et al.*, Phys. Rev. Lett. **95**, 042002 (2005), hep-ex/0502004.

[54] L3, P. Achard *et al.*, Eur. Phys. J. **C49**, 395 (2007), hep-ex/0609054.

[55] HERA-B, I. Abt *et al.*, Phys. Rev. Lett. **93**, 212003 (2004), hep-ex/0408048.

[56] SPHINX, Y. M. Antipov *et al.*, Eur. Phys. J. **A21**, 455 (2004), hep-ex/0407026.

[57] CDF, D. O. Litvintsev, Nucl. Phys. Proc. Suppl. **142**, 374 (2005), hep-ex/0410024.

[58] FOCUS, J. M. Link *et al.*, Phys. Lett. **B639**, 604 (2006), hep-ex/0606014.

[59] PHENIX, C. Pinkenburg, J. Phys. **G30**, S1201 (2004), nucl-ex/0404001.

[60] R. L. Jaffe, Phys. Rept. **409**, 1 (2005), hep-ph/0409065.

[61] M. Oka, Prog. Theor. Phys. **112**, 1 (2004), hep-ph/0406211.

[62] S.-L. Zhu, Int. J. Mod. Phys. **A19**, 3439 (2004), hep-ph/0406204.

[63] A. Chodos, R. L. Jaffe, K. Johnson, and C. B. Thorn, Phys. Rev. **D10**, 2599 (1974).

[64] A. Chodos, R. L. Jaffe, K. Johnson, C. B. Thorn, and V. F. Weisskopf, Phys. Rev. **D9**, 3471 (1974).

[65] K. Hicks, (2007), hep-ph/0703004.

[66] SVD, A. Aleev *et al.*, (2005), hep-ex/0509033.

[67] D. Strottman, Phys. Rev. **D20**, 748 (1979).

[68] R. Bijker, M. M. Giannini, and E. Santopinto, Eur. Phys. J. **A22**, 319 (2004), hep-ph/0310281.

[69] F. Buccella and P. Sorba, Mod. Phys. Lett. **A19**, 1547 (2004), hep-ph/0401083.

[70] B. G. Wybourne, (2003), hep-ph/0307170.

[71] D. Diakonov, (2004), hep-ph/0412272.

[72] T. M. Schwarz, *Thermodynamics of the chiral condensate*, PhD thesis, Technische Universität München, 2003.

[73] T. H. R. Skyrme, Proc. Roy. Soc. Lond. **A260**, 127 (1961).

[74] T. H. R. Skyrme, Nucl. Phys. **31**, 556 (1962).

[75] M. Chemtob, Nucl. Phys. **B256**, 600 (1985).

[76] A. V. Manohar, Nucl. Phys. **B248**, 19 (1984).

[77] G. S. Adkins, C. R. Nappi, and E. Witten, Nucl. Phys. **B228**, 552 (1983).

[78] M. Jezabek and M. Praszalowicz, Skyrmions and anomalies. proceedings, workshop, Krakow, Poland, World Scientific, 1987.

[79] M. Praszalowicz, Phys. Lett. **B575**, 234 (2003), hep-ph/0308114.

[80] S. Capstick, P. R. Page, and W. Roberts, Phys. Lett. **B570**, 185 (2003), hep-ph/0307019.

[81] R. L. Jaffe and F. Wilczek, Phys. Rev. Lett. **91**, 232003 (2003), hep-ph/0307341.

[82] R. L. Jaffe, Eur. Phys. J. **C35**, 221 (2004), hep-ph/0401187.

[83] D. Diakonov, V. Petrov, and M. V. Polyakov, (2004), hep-ph/0404212.

[84] R. L. Jaffe, (2004), hep-ph/0405268.

[85] M. Karliner and H. J. Lipkin, (2003), hep-ph/0307243.

[86] DESY press photo archive, 2007.

[87] A. A. Sokolov and I. M. Ternov, Sov. Phys. Dokl. **8**, 1203 (1964).

[88] Y. S. Derbenev and A. M. Kondratenko, Sov. Phys. JETP **37**, 968 (1973).

[89] J. Buon and K. Steffen, Nucl. Instr. Meth. **A245**, 248 (1986).

[90] M. Beckmann *et al.*, Nucl. Instrum. Meth. **A479**, 334 (2002), physics/0009047.

[91] HERMES, K. Ackerstaff *et al.*, Nucl. Instrum. Meth. **A417**, 230 (1998), hep-ex/9806008.

[92] C. Baumgarten *et al.*, Nucl. Instrum. Meth. **A496**, 277 (2003).

[93] HERMES, A. Airapetian *et al.*, Nucl. Instrum. Meth. **A540**, 68 (2005), physics/0408137.

[94] M. Demey, *The polarization of Λ^0 hyperons in quasi-real photoproduction*, PhD thesis, University Amsterdam, 2007.

[95] J. J. M. Steijger, Nucl. Instrum. Meth. **A447**, 55 (2000).

[96] R. Kaiser *et al.*, HERMES Report No. 02-003, 2002 (unpublished).

[97] W. Augustiniak *et al.*, HERMES Report No. 07-008, 2007 (unpublished).

[98] HERMES, A. Airapetian *et al.*, Nucl. Instrum. Meth. **A540**, 305 (2005), hep-ex/0301010.

[99] N. Akopov *et al.*, Nucl. Instrum. Meth. **A479**, 511 (2002), physics/0104033.

[100] T. Sjostrand *et al.*, Comput. Phys. Commun. **135**, 238 (2001), hep-ph/0010017.

[101] A. Airapetian *et al.*, Leading order determination of the gluon polarization from high-p_T hadron electroproduction, In preparation, 2006.

[102] A. Hillenbrand, *Measurement and simulation of the fragmentation process at HERMES*, PhD thesis, Friedrich-Alexander Universität, Erlangen-Nürnberg, 2005, DESY-THESIS-2005-035.

[103] P. Liebing, *Can the gluon polarization in the nucleon be extracted from HERMES data on single high p_T hadrons?*, PhD thesis, Universität Hamburg, 2004, DESY-THESIS-2004-036.

[104] D. P. Barber *et al.*, Nucl. Instrum. Meth. **A329**, 79 (1993).

[105] G. Bardin, C. Cavata, and J. P. Jorda, DESY-TESLA-97-03.

[106] F. M. Menden, *Determination of the gluon polarization in the nucleon*, PhD thesis, Albert-Ludwigs-Universität Freiburg, 2001, DESY-THESIS-2001-060.

[107] A. Airapetian, W. Deconinck, R. Fabbri, and B. Zihlmann, HERMES Report No. IPR-05-01, 2005 (unpublished).

[108] W. Lorenzon, EIC workshop summary, Precision Electron Beam Polarimetry Workshop for a future Electron Ion Collider, 2007.

[109] W. Deconinck and F. Giordano, Hermes Report No. 04-030, 2004 (unpublished).

[110] Particle Data Group, S. Eidelman *et al.*, Phys. Lett. **B592**, 1 (2004).

[111] M. Karliner and H. J. Lipkin, (2005), hep-ph/0506084.

[112] A. I. Titov, B. Kampfer, S. Date, and Y. Ohashi, Phys. Rev. **C72**, 035206 (2005), nucl-th/0506072.

[113] D. P. Barber *et al.*, Zeit. Phys. **C7**, 17 (1980).

[114] W. Verkerke and D. Kirkby, (2003), physics/0306116.

[115] W. Deconinck and S. Wang, Hermes Report No. 06-082, 2006 (unpublished).

[116] H. G. F. D. Drijard and T. Nakada, Nucl. Instrum. Meth. **A225**, 367 (2004).

[117] T. Nakada, (1983), CERN-EP-IR/83-10.

[118] STAR, L. Gaudichet, J. Phys. **G30**, S549 (2004), nucl-ex/0307013.

[119] L. Gaudichet, Event asymmetry effect on event mixing distributions, STAR internal note SN446, 2003.